CRISPR interference-based Functional Genetic Interaction Mapping in FTD/ALS and PD

Stewart Wynn Humble

Wolfson College
University of Oxford

A thesis submitted for the degree of
Doctor of Philosophy

Trinity 2022

Abstract

Parkinson's disease (PD) and Frontotemporal Dementia/Amyotrophic Lateral Sclerosis (FTD/ALS) are progressive neurodegenerative diseases that are neuropathologically defined by the presence of protein aggregates and the loss of specific subsets of neurons. Both diseases are associated with variants in genes that are implicated in lysosome function and proteostasis. Therefore, it is likely that converging disease pathways exist across these subsets of neurodegeneration, and the interrogation of these pathways can be used both to enhance our understanding of these disorders and lead to innovative therapeutic interventions.

Utilizing a modified i^{3}Neuron platform to facilitate systematic single and pairwise knockdown (KD) of large panels of PD and FTD/ALS-associated genes through CRISPR interference (CRISPRi) to interrogate gene-gene interactions. My efforts focus on generating the first genetic interaction maps between the major genetic causes and risk factors of PD and FTD/ALS. Most notably, our interaction screen has identified several top gene-gene interaction candidates: TARDBP-TMEM106B, CLN8-NBR1, ATP13A2-CLN8, GRN-TMEM106B, and CTSL-GRN.

TMEM106B was a component of multiple hits, and a recent study has demonstra- ted that it modifies TDP-43 pathology [1], while overexpression induces cell death and causes the cleavage of TDP-43 [2]. Additionally, it has been implicated as an interactor of *GRN* in the clinic [3, 4], and as a regulator of lysosomal function and acidification in mice [4, 5]. A remarkable trend was apparent across all interactions with *TMEM106B*, where the pH is significantly lower than the non-targeting comparison, indicating a postive overall effect on lysosomal function with knockdown.

Strikingly, there is no significant phenotype between CTSL-GRN and non-targeting controls across DQ-BSA assays or the Magic Red assay, despite the severe deficits seen in GRN single KD. Lysosomal pH, however, is decreased significantly, which indicates a potential rescue across all assays. It is known that *CTSL* cleaves *GRN* [5], but no current studies exist showing an interaction beyond that, certainly not to the degree of rescue shown by the data in this thesis. This may be an ideal target for follow-up studies as a priority interaction. These promising initial results demonstrate that identifying common pathogenic changes elicited by disease genes can help us understand the underlying converging mechanisms in PD and FTD/ALS. Through these efforts, I hope to help lay the groundwork for improved molecular understanding and therapeutic discovery.

CRISPR interference-based Functional Genetic Interaction Mapping in FTD/ALS and PD



Stewart Wynn Humble

Wolfson College

University of Oxford

A thesis submitted for the degree of

Doctor of Philosophy

Trinity 2022

Acknowledgements

I would like to thank Dr. Michael E. Ward, Professor Richard Wade-Martins, and Dr. Brent J. Ryan for their overwhelming support over the past several years. The opportunity to complete my doctoral thesis work between their labs has provided me with a truly unique experience in science between world-class institutions. To Brent specifically, who looked after me "in the trenches"–no amount of praise can equal what your mentorship has meant to me. Thank you all for the kind words, through the highs and the lows. Taking on a challenging project such as this one required confidence in me as a student and researcher–a fact that doesn't escape me.

To my family: thank you for the unending and unquestioning support. I would never have made it this far without you. To Mom, Dad, Blake, PawPaw, JuJu, and everyone else–you've all helped me achieve things someone from our small corner of Louisiana can only dream of... and despite all of the challenges along the way for all of us, we are still going strong!

To Michael, Ryan, and Rajan thank you for an amazing start to the DPhil journey at NINDS. You all are stuck with me for life, whether you like it or not! We had some great memories and here's to creating more. We all challenged each other to become stronger in the lab and achieve our scientific goals, but also were amazing companions outside of the lab. Everyone deserves friends like you three in their lives. I truly hope we stay close throughout our lives. To David and Amra, thank you for providing mentorship when mentorship was needed. Your generosity, friendship, and desire to help others above is inspiring. Having been on the receiving end, I can only say how much it meant to me as a budding PhD student. To Maia, Anne, Ling, Mari, and Jon, thank you all for the help, encouragements, and constant support at NINDS. I can only hope that I was able to make as big of an impact on you as you all have had on me.

To Peter Kilfeather. You once called me your right hand man...well right back at you! You, sir, are an amazing friend and I have the absolute utmost respect for you, not only as a friend but as a person. I truly look up to you in many ways. I hope our friendship has had the same effect on you. To Mari, Kaitlyn, Josse, 'Maine, Ana, and Raphaela, thank you all for the unending support for lab stuff, but also for all the fun we've managed to have over various points in the past few years in Oxford.

You all made my transition to Oxford much easier. To Peter H, it was an absolute pleasure getting to know you and working closely with you during your MSc project. Thank you for taking a risk on me and allowing me to be a mentor for the first time.

To Joel & Katie, Alex & Sarah, James, Miles, Ship, Eric, Erin, Nick, Ric, George, Jamie, thank you all for the close individual and shared friendships during my time in Oxford. When family are far away, you all were there for me all along. You all have been my family while in this distant land, and for that I can only say thank you and much love.

To Dje Dje: you're up next.

When I needed it most:

For God has not given us a spirit of fear, but of power, and of love, and of a sound mind.

2 Timothy 1:7 (Thanks BB)

Always remember, the Tiger was inside you the whole time and never left.

GEAUX TIGERS.



This one is for you JuJu.

veni vidi vici,



Abstract

Parkinson's disease (PD) and Frontotemporal Dementia/Amyotrophic Lateral Sclerosis (FTD/ALS) are progressive neurodegenerative diseases that are neuropathologically defined by the presence of protein aggregates and the loss of specific subsets of neurons. Both diseases are associated with variants in genes that are implicated in lysosome function and proteostasis. Therefore, it is likely that converging disease pathways exist across these subsets of neurodegeneration, and the interrogation of these pathways can be used both to enhance our understanding of these disorders and lead to innovative therapeutic interventions.

Utilizing a modified i^{3}Neuron platform to facilitate systematic single and pairwise knockdown (KD) of large panels of PD and FTD/ALS-associated genes through CRISPR interference (CRISPRi) to interrogate gene-gene interactions. My efforts focus on generating the first genetic interaction maps between the major genetic causes and risk factors of PD and FTD/ALS. Most notably, our interaction screen has identified several top gene-gene interaction candidates: TARDBP-TMEM106B, CLN8-NBR1, ATP13A2-CLN8, GRN-TMEM106B, and CTSL-GRN.

TMEM106B was a component of multiple hits, and a recent study has demonstrated that it modifies TDP-43 pathology [1], while overexpression induces cell death and causes the cleavage of TDP-43 [2]. Additionally, it has been implicated as an interactor of *GRN* in the clinic [3, 4], and as a regulator of lysosomal function and acidification in mice [4, 5]. A remarkable trend was apparent across all interactions with *TMEM106B*, where the pH is significantly lower than the non-targeting comparison, indicating a postive overall effect on lysosomal function with knockdown.

Strikingly, there is no significant phenotype between CTSL-GRN and non-targeting controls across DQ-BSA assays or the Magic Red assay, despite the severe deficits seen in GRN single KD. Lysosomal pH, however, is decreased significantly, which indicates a potential rescue across all assays. It is known that *CTSL* cleaves *GRN* [5], but no current studies exist showing an interaction beyond that, certainly not to the degree of rescue shown by the data in this thesis. This may be an ideal target for follow-up studies as a priority interaction. These promising initial results demonstrate that identifying common pathogenic changes elicited by disease genes can help us understand the underlying converging mechanisms in PD and FTD/ALS. Through these efforts, I hope to help lay the groundwork for improved molecular understanding and therapeutic discovery.

Contents

List of Figures **10**

List of Tables **16**

List of Abbreviations **18**

1 Introduction **1**

1.1 Frontotemporal Dementia/Amyotrophic Lateral Sclerosis (FTD/ALS) 2

1.1.1 Introduction 2

1.1.2 Progranulin-specific Background 3

1.2 Parkinson's Disease (PD) 5

1.2.1 Introduction 5

1.3 FTD/ALS and PD Converge at the Lysosome 6

1.3.1 Introduction 6

1.3.2 Clinical and Pathological Overlap of FTD/ALS and PD . . . 6

1.3.3 Lysosomes are a site of functional convergence between FTD/ALS and PD 8

1.4 Utilizing hiPSC-derived Neurons as a Cellular Model for Functional Genomics 15

1.4.1 CRISPR Interference (CRISPRi) 15

1.4.2 i^3Neurons 18

1.4.3 Genetic Engineering of CRISPRi into i^3Neurons 20

1.5 Aims of the Work in this Thesis 20

2 Materials and Methods **21**

2.1 Key Resources and Materials 22

2.2 Cloning 23

2.2.1 NEBuilder Hifi or InFusion Cloning 23

2.2.2 High-throughput Cloning 27

2.3 Lentivirus Production 27

2.4 Cell Culture 29

2.4.1 hiPSC Culture 29

2.4.2 hiPSC Lines 29

2.4.3 Neuron Differentiation for High-Content Applications 30

2.5 Live Cell Imaging 33

2.5.1 Live cell DQ-BSA Assay 34

2.5.2 Live Cell Ratiometric pH Assay 34

2.5.3 Live cell Magic Red CTSB Assay 35

2.5.4 Neuronal Survival and Neurite Outgrowth Assays 35

2.5.5 Transferrin Assays 36

2.6 sgRNA Validation 37

2.7 Arrayed Screening 37

2.8 Quantification and Statistical Analyses 37

3 CRISPRi sgRNA Library Generation and Validation **39**

3.1 Introduction and Aims 40

3.1.1 Preliminary FTD/ALS Sublibrary 40

3.2 CRISPRi Tool Optimization 42

3.2.1 Far-Red Protein Panel 42

3.2.2 Far-Red Optimization 46

3.2.3 sgRNA Drug Selection 49

3.3 CRISPRi sgRNA Library Generation and High-Throughput Plasmid Cloning 49

3.3.1 sgRNA Library Design and Sequence Generation 49

3.3.2 Nuclear Blue and Cytosolic Far-Red CRISPRi Plasmid Library Construction . . . 51
3.3.3 sgRNA Delivery Systems and Functional Titering . . . 54
3.3.4 Nuclear Blue and Cytosolic Far-Red sgRNA Library Functional Titering . . . 56
3.3.5 Dual Transduction of sgRNAs . . . 58
3.4 Targeted, Multiplexed RNA Sequencing for sgRNA Validation . . . 60
3.4.1 Validation of High-throughput RNA Extraction . . . 60
3.4.2 Preliminary Targeted RNA Sequencing & sgRNA Validation 61
3.4.3 High-throughput Targeted RNA Sequencing & sgRNA Validation 69
3.4.4 Transcriptomic Genetic Interactions . . . 74
3.5 Discussion . . . 75

4 Developing Assays Targeting Neuronal Function and the Lysosome 82
4.1 Introduction and Aims . . . 83
4.2 Longitudinal Imaging and Neurite Outgrowth Assays . . . 84
4.3 Transferrin Recycling and Uptake . . . 85
4.3.1 Background . . . 85
4.3.2 Transferrin recycling appears unaffected in *GRN*-KO cells . 87
4.3.3 Total transferrin uptake is decreased in *GRN*-KO cells . . . 88
4.4 Measuring Lysosomal pH . . . 89
4.4.1 Background . . . 89
4.4.2 Measuring Lysosomal pH: Transforming a low-throughput imaging assay to high-content formats . . . 90
4.4.3 Lysosomes in *GRN*-KO i^{3}Neurons have alkaline pH and fail to acidify . . . 92
4.5 Evaluating Lysosomal Proteolysis . . . 93
4.5.1 Background . . . 93
4.5.2 Optimization of the DQ-BSA Assay in i^{3}Neurons . . . 95
4.5.3 Lysosomes in *GRN*-KO i^{3}Neurons exhibit decreased active proteolysis . . . 99

4.6 DQ-BSA single knockdown CRISPRi screen reveals disease-associated lysosomal modulators and recapitulates *GRN*-KO dysfunction . . . 101
4.7 Discussion . . . 105

5 Phenotypic Screening and Genetic Interaction Mapping 114
5.1 Introduction and Aims . . . 115
5.1.1 Epistasis and Genetic Interaction Mapping . . . 115
5.1.2 Quantifying Genetic Interactions via the S-score . . . 117
5.1.3 Collaboration Acknowledgments . . . 119
5.2 Genetic Interaction Mapping . . . 120
5.2.1 Preliminary Dual Knockdown Screening . . . 120
5.2.2 Full Genetic Interaction Mapping Screen: DQ-BSA . . . 125
5.3 Genetic Interaction Validation . . . 138
5.3.1 Primary Validation: DQ-BSA . . . 138
5.3.2 Establishing Mechanistic Understanding: Magic Red and Lysosomal pH . . . 144
5.4 Discussion . . . 149

6 Discussion 156
6.1 Overview . . . 157
6.2 Molecular Biology . . . 157
6.3 Transcriptomic Interactions . . . 157
6.4 Phenotypic Assays . . . 158
6.5 Genetic Interaction Mapping . . . 159
6.6 Future Work . . . 160

Appendices

A Appendix for Chapter 3 Tables and Titers 163
A.1 List of all sgRNA sequences used for CRISPRi plasmid cloning and library generation . . . 163
A.2 Nuclear Blue Lentivirus Library Titers and Transfer Volumes . . . 173

A.3 Nuclear Blue sgRNA Lentivirus Library Titer Curves 177
A.4 Cytosolic Far-Red Lentivirus Library Titers and Transfer Volumes . 182
A.5 Cytosolic Far-Red sgRNA Lentivirus Library Titer Curves 186
A.6 Final Targeted, Multiplexed RNA Sequencing Lentivirus Titer Table 190
A.7 Final Targeted, Multiplexed RNA Sequencing Sample Table 195
A.8 Log2 Fold Change and Significance Values from Targeted RNA Sequencing 209

B Appendix for Chapter 5 Primary and Secondary Analysis Maps 211

C Appendix for Chapter 5 Tables 261
C.1 Genetic Interaction Mapping Screen Hit Table 262

References 266

List of Figures

1.1 Full-length PGRN has 7.5 GRN domains and an N-terminal secretion peptide. 3
1.2 FTD/ALS and PD Brain Pathology. 7
1.3 FTD/ALS and PD-Associated Genes Converge on the Lysosome. . 9
1.4 Transcriptional repression is achieved through CRISPR Interference. 17

3.1 Preliminary FTD/ALS Sublibrary 41
3.2 Representative plasmid maps and schematics of cytosolic and nuclear blue CRISPRi backbones. 43
3.3 Far-Red fluorescent protein panel. 45
3.4 CRISPRi Cytosolic Far-Red plasmid construct optimization. 47
3.5 Drug Selection of Co-Transduced hiPSC-Neurons. 50
3.6 CRISPRi sgRNA Library Cloning. 52
3.7 Construction of final Nuclear Blue and Cytosolic Far-Red CRISPRi libraries. 53
3.8 Acoustic Fluid Handling and Lentiviral Functional Titering. 55
3.9 Nuclear Blue sgRNA Library Functional Titering. 57
3.10 Cytosolic Far-Red sgRNA Library Functional Titering. 58
3.11 Preliminary Dual Transduction of sgRNAs. 59
3.12 Bulk RNA preparation from high content plates. 61
3.13 Preliminary Targeted RNA Sequencing, Sample Preparation. 65
3.14 Preliminary Targeted RNA Sequencing, Analysis Normalization. . . 67
3.15 Preliminary Targeted RNA Sequencing, Targeted Knockdown Analysis. 68
3.16 Final Targeted RNA Sequencing, Experimental Design & Normalization. 70

3.17 Final Targeted RNA Sequencing, sgRNA Knockdown Validation, Part I. 71
3.18 Final Targeted RNA Sequencing, sgRNA Knockdown Validation, Part II. 72
3.19 Final Targeted RNA Sequencing, Summary of sgRNA Knockdown Validation. 73
3.20 Final Targeted RNA Sequencing, Transcriptomic Interactions. . . . 76

4.1 Developing Neuronal Survival and Neurite Tracing Assays. 86
4.2 Transferrin Recycling and Total Uptake in *GRN*-KO neurons. . . . 88
4.3 Measuring Lysosomal pH: Adapting a low-throughput assay to high-content applications. 91
4.4 Lysosomes in *GRN*-KO i^{3}Neurons have alkaline pH and fail to acidify. 93
4.5 Evaluating Lysosomal Proteolysis via DQ-BSA, 3hrs uptake. 94
4.6 DQ-BSA Dose-Response to Chloroquine, 3hrs uptake. 96
4.7 DQ-BSA Assay Window Optimization, 5hrs uptake. 97
4.8 Lysosomes in *GRN*-KO i^{3}Neurons exhibit decreased active proteolysis. 100
4.9 DQ-BSA single knockdown CRISPRi screen reveals disease associated lysosomal modulators. 104
4.9 (Previous page.) DQ-BSA single knockdown CRISPRi screen reveals disease associated lysosomal modulators. 105

5.1 Translating phenotypes into interactions: Primary vs. Secondary S-scores. 118
5.2 Preliminary GI Mapping, Experimental Design and Cell-level QC. . 121
5.3 Preliminary GI Mapping, Drift Corrections and Well-level QC. . . . 122
5.4 Preliminary Genetic Interaction Mapping, Primary S-score Comparisons. 124
5.5 DQ-BSA Genetic Interaction Mapping Screen, Experimental Design & Analysis QC. 127
5.6 *GRN*: Primary and Secondary Analysis Genetic Interaction Maps. . 128

5.7 Secondary Analysis Genetic Interaction Maps for Hit-related Genes, part I. 130
5.8 Secondary Analysis Genetic Interaction Maps for Hit-related Genes, part II. 131
5.9 Secondary Analysis Genetic Interaction Maps for Hit-related Genes, part III. 132
5.10 Secondary Analysis Genetic Interaction Maps for Hit-related Genes, part IV. 133
5.11 Genetic Interaction Detection, Secondary Analysis Method. 134
5.12 Understanding Genetic Interactions: Additive vs Synergistic. 135
5.13 Genetic Interaction Detection, Tertiary Analysis Method. 136
5.14 Tertiary Genetic Interaction Map. 137
5.15 Screen Validation Overview. 139
5.16 Primary Validation, Recapitulated Positive Interactions. 141
5.17 Primary Validation, Recapitulated Negative Interactions. 142
5.18 Primary Validation, GRN Interactors. 143
5.19 Secondary Validation, Recapitulated Positive Interactions. 145
5.20 Secondary Validation, Recapitulated Negative Interactions. 146
5.21 Secondary Validation, GRN Interactors. 147

A.1 Nuclear Blue Panel A: Lentivirus titer curves with interpolation. . . 177
A.2 Nuclear Blue Panel B: Lentivirus titer curves with interpolation. . . 178
A.3 Nuclear Blue Panel C: Lentivirus titer curves with interpolation. . . 179
A.4 Nuclear Blue Panel D: Lentivirus titer curves with interpolation. . . 180
A.5 Nuclear Blue Panel E: Lentivirus titer curves with interpolation. . . 181
A.6 Nuclear Blue Panel F: Lentivirus titer curves with interpolation. . . 182
A.7 Cytosolic Far-Red Panel A: Lentivirus titer curves with interpolation. 186
A.8 Cytosolic Far-Red Panel B: Lentivirus titer curves with interpolation. 187
A.9 Cytosolic Far-Red Panel C: Lentivirus titer curves with interpolation. 188
A.10 Cytosolic Far-Red Panel D: Lentivirus titer curves with interpolation. 189
A.11 Cytosolic Far-Red Panel E: Lentivirus titer curves with interpolation. 190

B.1 *ATP13A2*: Primary and Secondary Analysis Genetic Interaction Maps. 212
B.2 *ATP6V0A1*: Primary and Secondary Analysis Genetic Interaction Maps. 213
B.3 *CHMP2B*: Primary and Secondary Analysis Genetic Interaction Maps. 214
B.4 *CLN8*: Primary and Secondary Analysis Genetic Interaction Maps. 215
B.5 *CTSD*: Primary and Secondary Analysis Genetic Interaction Maps. 216
B.6 *CTSL*: Primary and Secondary Analysis Genetic Interaction Maps. 217
B.7 *FUS*: Primary and Secondary Analysis Genetic Interaction Maps. . 218
B.8 *GALC*: Primary and Secondary Analysis Genetic Interaction Maps. 219
B.9 *GRN*: Primary and Secondary Analysis Genetic Interaction Maps. . 220
B.10 *GUSB*: Primary and Secondary Analysis Genetic Interaction Maps. 221
B.11 *HNRNPA2B1*: Primary and Secondary Analysis Genetic Interaction Maps. 222
B.12 *NBR1*: Primary and Secondary Analysis Genetic Interaction Maps. 223
B.13 *PINK1 (PARK6)*: Primary and Secondary Analysis Genetic Interaction Maps. 224
B.14 *PSAP*: Primary and Secondary Analysis Genetic Interaction Maps. 225
B.15 *SNCA (PARK1)*: Primary and Secondary Analysis Genetic Interaction Maps. 226
B.16 *TARDBP*: Primary and Secondary Analysis Genetic Interaction Maps. 227
B.17 *TAX1BP1*: Primary and Secondary Analysis Genetic Interaction Maps. 228
B.18 *TMEM106B*: Primary and Secondary Analysis Genetic Interaction Maps. 229
B.19 *UBQLN2*: Primary and Secondary Analysis Genetic Interaction Maps. 230
B.20 *VPS13C (PARK23)*: Primary and Secondary Analysis Genetic Interaction Maps. 231
B.21 *ALS2*: Primary and Secondary Analysis Genetic Interaction Maps. 232
B.22 *ANXA11*: Primary and Secondary Analysis Genetic Interaction Maps. 233
B.23 *C9orf72*: Primary and Secondary Analysis Genetic Interaction Maps. 234

B.24 *CLN5*: Primary and Secondary Analysis Genetic Interaction Maps. 235
B.25 *CRLS1*: Primary and Secondary Analysis Genetic Interaction Maps. 236
B.26 *CTSB*: Primary and Secondary Analysis Genetic Interaction Maps. 237
B.27 *GBA*: Primary and Secondary Analysis Genetic Interaction Maps. . 238
B.28 *GCH1*: Primary and Secondary Analysis Genetic Interaction Maps. 239
B.29 *KIF5A*: Primary and Secondary Analysis Genetic Interaction Maps. 240
B.30 *MAPT*: Primary and Secondary Analysis Genetic Interaction Maps. 241
B.31 *MCCC1*: Primary and Secondary Analysis Genetic Interaction Maps. 242
B.32 *NAGLU*: Primary and Secondary Analysis Genetic Interaction Maps. 243
B.33 *NDP52 (CALCOCO2)*: Primary and Secondary Analysis Genetic Interaction Maps. 244
B.34 *NEU1*: Primary and Secondary Analysis Genetic Interaction Maps. 245
B.35 *OPTN*: Primary and Secondary Analysis Genetic Interaction Maps. 246
B.36 *PARK2 (Parkin)*: Primary and Secondary Analysis Genetic Interaction Maps. 247
B.37 *PARK7 (DJ-1)*: Primary and Secondary Analysis Genetic Interaction Maps. 248
B.38 *PFN1*: Primary and Secondary Analysis Genetic Interaction Maps. 249
B.39 *SCARB2*: Primary and Secondary Analysis Genetic Interaction Maps. 250
B.40 *SETX*: Primary and Secondary Analysis Genetic Interaction Maps. 251
B.41 *SOD1*: Primary and Secondary Analysis Genetic Interaction Maps. 252
B.42 *SQSTM1*: Primary and Secondary Analysis Genetic Interaction Maps. 253
B.43 *STX17*: Primary and Secondary Analysis Genetic Interaction Maps. 254
B.44 *TBK1*: Primary and Secondary Analysis Genetic Interaction Maps. 255
B.45 *TMEM175*: Primary and Secondary Analysis Genetic Interaction Maps. 256
B.46 *VAPB*: Primary and Secondary Analysis Genetic Interaction Maps. 257
B.47 *VCP*: Primary and Secondary Analysis Genetic Interaction Maps. . 258
B.48 *VCP_mild*: Primary and Secondary Analysis Genetic Interaction Maps. 259

B.49 *VPS35 (PARK17)*: Primary and Secondary Analysis Genetic Interaction Maps. 260

List of Tables

1.1 Genes and Risk Factors Associated with PD and FTD/ALS That Have Been Implicated in Lysosomal Function. *Adapted from Wallings and Humble et al. [40]* 16

2.1 PCR Reaction 24
2.2 PCR Conditions 25
2.3 Backbone Digestion 26

3.1 Paragon Genomics CleanPlex RNA Target Enrichment Panel 62
3.2 Preliminary Targeted, Multiplexed RNA Sequencing Sample Table . 64
3.3 Transcriptomic interactions identified by targeted RNA sequencing. 75

4.1 Supplementary proteomics table, progranulin deficient lysosomes *(unpublished, courtesy of Ward Lab).* 84
4.2 Interpreting the Z-prime value. 98
4.3 Single Knockdown Hits Decreasing Lysosomal Function 103
4.4 Single Knockdown Hits Increasing Lysosomal Function 103

5.1 Selected sgRNAs for Genetic Interaction Mapping Screen 129
5.2 Top Recapitulated Hits between the Genetic Interaction Mapping Screen and Primary Validation Screen 140
5.3 Phenotypic Summaries for all Genetic Interaction Hits 148

A.1 List of all sgRNA sequences used for CRISPRi plasmid cloning and library generation. 164
A.2 Nuclear Blue Lentivirus Library Titers and Transfer Volumes 174
A.3 Cytosolic Far-Red Lentivirus Library Titers and Transfer Volumes . 183

A.4 Final Targeted, Multiplexed RNA Sequencing Lentivirus Titer Table 191

A.5 Final Targeted, Multiplexed RNA Sequencing Sample Table. 196

A.6 Log_2 Fold Change and Significance Values from Targeted RNA Sequencing. 209

C.1 Table of all interaction screening hits; hits that recapitulated in the validation screen are labeled (blue=negative, red=positive, grey=other). 262

List of Abbreviations

ALS . . . . . Amyotrophic Lateral Sclerosis

ANXA11 . . . Annexin A11

BDNF . . . . . Brain Derived Neurotrophic Factor

BSA . . . . . Bovine Serum Albumin

CDS . . . . . Coding Sequence

CQ . . . . . Chloroquine

CRISPR . . . Clustered Regularly Interspaced Short Palindromic Repeats

CRISPRi . . . CRISPR Interference

CSIMC . . . . Corrected Spot Intensity Mean per Cell

DMSO . . . . Dimethyl sulfoxide

DNA . . . . . Deoxyribonucleic Acid

Dox . . . . . Doxycycline

DQ . . . . . referring to DQ-BSA Assay

E8 . . . . . Essential 8 Stem Cell Medium

EDTA . . . . . Ethylenediaminetetraacetic Acid

ER . . . . . Endoplasmic Reticulum

ES . . . . . Embryonic Stem Cell

FTD . . . . . Frontotemporal Dementia

FTD/ALS . . Referring to the shared genetic spectrum between the two diseases

FUS . . . . . Fused In Sarcoma

G3BP1 . . . . Ras Gtpase-Activating Protein-Binding Protein 1

GRN . . . . . Granulin

HCA . . . . . High-content Analysis

HCS . . . . . High-content Screening

HEK293T . . Human Embryonic Kidney Cell Line

hiPSC-Neurons Human Induced Pluripotent Stem Cell Neurons

hnRNPA2 . . Heterogeneous Nuclear Ribonucleoprotein A2

i^{3}Neuron . . . Inducible, Integrated, Isogenic hiPSC-Neurons

iPSC . . . . . Induced Pluripotent Stem Cell

KD . . . . . Knock-down (referring to a genotype)

KO . . . . . Knock-out (referring to a genotype)

LAMP1 . . . . Lysosome-Associated Membrane Protein 1

LE . . . . . Late Endosome

LE/Lys . . . . Late Endosome/Lysosome

Lenti . . . . . Lentivirus

LRRK2 . . . . Leucine-rich repeat kinase 2

Lyso . . . . . Lysosome

mGluR . . . . Metabotropic Glutamate Receptor

mRNA . . . . Messenger RNA

miRNA . . . . Micro RNA

NEM . . . . . N-Ethylmaleimide

NES . . . . . Nuclear Export Sequence

NGN2 . . . . . Neurogenin-2

NGS . . . . . Next-Generation Sequencing

NLS . . . . . Nuclear Localization Sequence

NSA . . . . . Number of Spots per Area of cell

NT-3 . . . . . Neurotrophin-3

Oligo . . . . . Oligonucleotide

PBS . . . . . Phosphate Buffered Saline

PCA . . . . . Principal Component Analysis

PCR . . . . . Polymerase Chain Reaction

PD . . . . . Parkinson's Disease

PFA . . . . . Paraformaldehyde

PGRN . . . . Progranulin

PLO . . . . . Poly-L-Ornithine

QC . . . . . Quality Control

RBP . . . . . RNA Binding Protein

RI . . . . . Rho-Associated Coiled-Coil Containing Protein Kinase (ROCK) Inhibitor

RGC . . . . . Retinal Ganglion Cell

RNA . . . . . Ribonucleic Acid

RNP . . . . . Ribonucleoprotein

RIN . . . . . RNA Integrity Number

RIN^e . . . . . RNA Integrity Number 'equivalent'

STX . . . . . Syntaxin

TDP-43 . . . . TAR DNA Binding Protein 43

UTR . . . . . Untranslated Region

WT . . . . . Wild-Type

1 Introduction

Contents

1.1 Frontotemporal Dementia/Amyotrophic Lateral Sclerosis (FTD/ALS) 2
1.1.1 Introduction 2
1.1.2 Progranulin-specific Background 3
1.2 Parkinson's Disease (PD) 5
1.2.1 Introduction 5
1.3 FTD/ALS and PD Converge at the Lysosome 6
1.3.1 Introduction 6
1.3.2 Clinical and Pathological Overlap of FTD/ALS and PD 6
1.3.3 Lysosomes are a site of functional convergence between FTD/ALS and PD 8
1.4 Utilizing hiPSC-derived Neurons as a Cellular Model for Functional Genomics 15
1.4.1 CRISPR Interference (CRISPRi) 15
1.4.2 i^3Neurons 18
1.4.3 Genetic Engineering of CRISPRi into i^3Neurons 20
1.5 Aims of the Work in this Thesis 20

1.1 Frontotemporal Dementia/Amyotrophic Lateral Sclerosis (FTD/ALS)

Portions of this introduction have been adapted from R.L. Wallings, S.W. Humble, M.E. Ward, and R. Wade-Martins. "Lysosomal Dysfunction at the Centre of Parkinson's Disease and Frontotemporal Dementia/Amyotrophic Lateral Sclerosis". In: Trends in Neurosciences 42.12 (2019), pp. 899–912. This includes some figures which are cited appropriately. I confirm that all work is my own.

1.1.1 Introduction

Frontotemporal Dementia (FTD) and Amyotrophic Lateral Sclerosis (ALS) are adult-onset neurodegenerative diseases that are closely related clinically, pathologically, and genetically. On the surface, these two diseases seem quite distinct: FTD, primarily affecting cortical neurons in the frontal and temporal lobes and a major cause of early-onset dementia, compared to ALS, a disease of motor neurons resulting in the gradual loss of voluntary muscle movement. However, the discovery in 2011 that mutations in *C9orf72* can cause both FTD and ALS illustrates a key example of the underlying converging pathophysiology seen in FTD/ALS. These diseases have traditionally been defined by post-mortem end-points of specific neuronal loss and protein aggregates positive for α-synuclein or TDP-43/Tau/FUS and/or ubiquitin for PD and FTD/ALS, respectively.

FTD/ALS is often inherited and causal mutations are highly penetrant, indicating that these mutations have large effects on critical cellular pathways. Approximately half of the genes known to cause FTD/ALS encode proteins that regulate endolysosomal biology or play a crucial role in regulating proteostasis. Functional interactions between different FTD/ALS genes have been observed in human genetic studies (e.g. *TMEM106B* and *GRN* [3–5], *TMEM106B* and *C9orf72* [6], *PSAP* and *GRN* [7]), model organisms (e.g. *ATXN2* and *TARDBP12*), cells (e.g. *VCP* and *TARDBP* [8], *OPTN* and *TBK1* [9]).

1.1.2 Progranulin-specific Background

Frontotemporal dementia (FTD) is a devastating clinical condition characterized by a progressive degeneration of the frontal and temporal cortex. Clinically, patients can present with aphasias, lobar atrophy, as well as dementia, and are mostly middle-aged adults under 65 years of age [10, 11]. FTD has a strong inherited component that suggests a significant genetic link [12, 13]. Unlike in other neurodegenerative diseases such as Alzheimer's or Parkinson's, approximately 8.5% of all FTD/ALS patients have a family history of dementia [14], with many cases linked to mutations in RNA binding and proteostasis genes, such as *C9orf72*, *VCP*, *UBQLN2*, *GRN*, *TARDBP*, *FUS*, and *CHMP2B* [12, 15].

Mutations in the *GRN* gene, which cause a reduction in the expression of progranulin (PGRN), are a common source of inherited FTD. Homozygous-null GRN-mutations manifest as the neurodegenerative lysosomal storage disorder Neuronal Ceroid Lipofuscinosis (NCL) [12, 16–18], while heterozygotes experience early retinal degeneration accompanied by deposition of retinal lysosomal storage material [18].

Progranulin (PGRN) is a phylogenetically ancient, cysteine-rich secreted protein composed of 7.5 conserved granulin (GRN) domains, each of which is separated by linkers with cleavage sites. An individual granulin typically consists of a domain containing 12 cysteines within a 60 amino-acid motif repeated throughout the entire protein. The disulfide bonds formed by cysteine pairs within a domain help to confer stability to a structurally compact configuration that is thought to be protease resistant [19].



Figure 1.1: Full-length PGRN has 7.5 GRN domains and an N-terminal secretion peptide. C-terminal GRN-E is sufficient for neuroprotection of cortical neurons [20]. Progranulin binds Sortilin, a neuronal scavenging receptor, via three C-terminal amino acids (QLL) [20].

The functions of the various forms of PGRN (whether full-length, partially processed, or individual granulins) and their precise connections to lysosome regulation is still relatively unknown. However, it has been shown that C-terminal GRN-E is sufficient for neurite outgrowth and branching, suggesting that PGRN may require processing for adequate function [20].

Over 70 mutations in the GRN gene have been identified that cause null alleles leading to FTD with TDP-43 positive neuropathology [12, 21]. These mutations lead to haploinsufficiency in progranulin (PGRN), a secreted growth factor involved in the regulation of cellular processes such as development, wound repair, inflammation, and tumorigenesis [15, 22]. It has been established that even a partial loss of GRN causes neuronal degeneration and loss, indicating that PGRN is essential for proper neuron function and survival [12, 15, 21].

Moreover, a clinically relevant phenotype exists in homozygous-null GRN carriers that manifests as the neurodegenerative lysosomal storage disorder Neuronal Ceroid Lipofuscinosis (NCL) [12, 16, 18, 23]. NCLs are part of a larger category of disorders known as lysosomal storage diseases (LSDs), however, they typically do not have the multi-organ or multi-system involvement seen across most LSDs [24]. NCLs are more generally seen to affect the brain and retina, most commonly with childhood or infantile onset, such as in Batten disease and to a lesser incidence as adult-onset, as seen in Kufs disease [12, 24]. Intracytoplasmic inclusions of autofluorescent lipofuscin are the ultimate pathogenic hallmark of NCLs [12, 24], whereas in other LSDs the insult may cause issues in trafficking, osmolarity, export, or other lysosomal hydrolases that indeed cause progressive accumulation of non-lipofuscin substrates [25].

While markedly different than the clinical presentation of FTD patients, these findings suggest a deeper connection with late endosomal/lysosomal trafficking and processing, cellular pathways that are often dysregulated in diseases associated with lysosome function [12, 16, 23, 26]. Similar to NCL and other lysosomal storage disorders, some patients have early retinal degeneration accompanied by deposition of retinal lysosomal storage material. Ward et al observed this phenotype

in heterozygous GRN-mutation carriers and in *GRN*-KO mice, further suggesting a connection to lysosomal biology and dysregulation of normal cellular function within the CNS [12, 17, 18].

1.2 Parkinson's Disease (PD)

1.2.1 Introduction

Parkinson's disease (PD) is a neurodegenerative disease affecting 1-2% of the world's population over the age of 65 [27]. An aging population has contributed to PD becoming one of the fastest growing neurodegenerative diseases in the world [28]. The disease is characterized by the death of A9 dopaminergic neurons in the substantia nigra pars compacta (SNpc) and inclusions of α-synuclein in Lewy bodies (LBs) [29]. When seen together, these disease signatures are pathognomonic for PD, as LBs are seen in other neurodegenerative diseases, [30–32].

The majority of PD cases are sporadic, with approximately 1 in 10 patients reporting a family history of the disease [33]. However, monogenic forms of the disease have been inextricably linked to heritable mutations, such as *SNCA (PARK1/4), LRRK2 (PARK8), Parkin (PARK2), PINK1 (PARK6), DJ-1 (PARK7), and ATP13A2 (PARK9)* [33].

Clinically, PD patients present with cardinal motor symptoms such as tremor, rigidity, bradykinesia and postural instability [34], and very little can be done therapeutically, as there are minimal treatment options that are purely symptomatic, such as levodopa (L-DOPA) [35]. Due to these limitations, a growing need to search for new targets for rational drug development is currently a primary driver for researchers around the world [36].

1.3 FTD/ALS and PD Converge at the Lysosome

1.3.1 Introduction

Recent studies have started to untangle previously unknown overlaps in neurodegenerative disease etiology by identifying and characterizing similarities in neuropathological changes [37], clinical presentations [3, 38], and direct genetic connections [39, 40]. While direct genetic interactions between neurodegenerative diseases can be rare, disease-causative FTD/ALS and PD mutations share archetypal pathways such as protein misfolding [41], autophagy [42], and the lysosome [40]. Therefore, it is likely that relevant shared biological processes are converging along these disease-specific pathways, and the interrogation of these pathways can be used to enhance our understanding of FTD/ALS and PD.

1.3.2 Clinical and Pathological Overlap of FTD/ALS and PD

Nearly 20% of FTD/ALS patients can present with some form of parkinsonism [38], however, features of these symptoms can be variable. Parkinsonism is a broad term that encompasses a group of neurological conditions that share similar clinical features seen in Parkinson's disease without necessarily sharing the same disease onset or etiology [43, 44]. In fact, Parkinson's disease is the most common form of parkinsonism [43], while other common forms can be seen via drug-induced parkinsonism, vascular parkinsonism, and other related neurological diseases [43, 44]. Ultimately, the classic akinetic-ridgid syndrome is the key clinical characteristic in these patients. Certain hexanucleotide expansions of the *C9orf72* gene can even be associated with PD with or without dementia, often responsive to levodopa therapies [45]. Moreover, parkinsonism in FTD/ALS caused by the TDP-43 mutations N267S and A315E are also treatable with levodopa [46].However, not all cases present with symptoms resembling progressive supranuclear palsy (PSP) or corticobasal degeneration (CBD), which is more of an atypical parkinsonism [47].

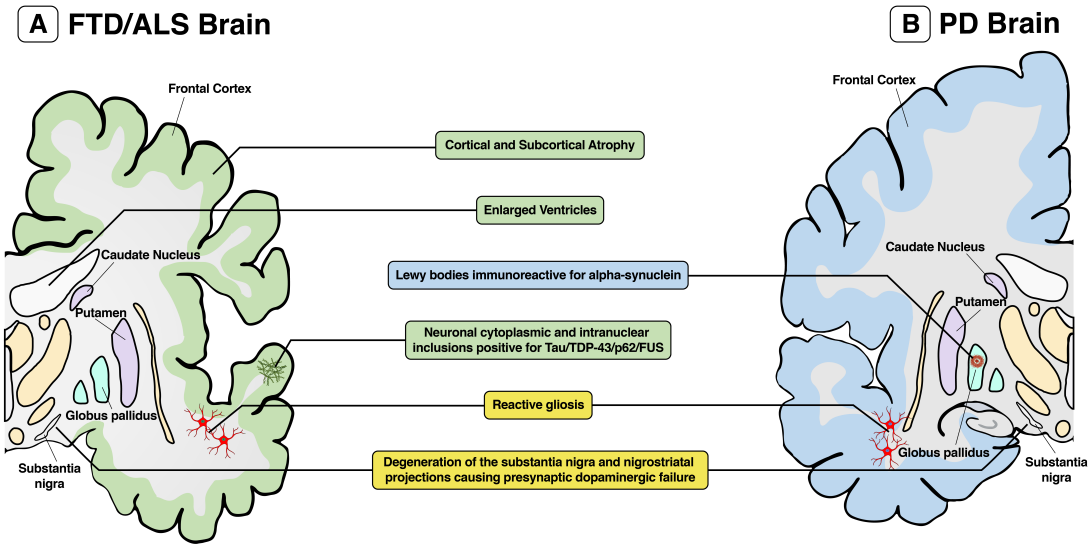


Figure 1.2: FTD/ALS and PD Brain Pathology. FTD/ALS pathology is typically characterised by cortical and subcortical atrophy, enlarged ventricles and Tar DNA-binding protein 43 (TDP-43)/Tau/p62/Fused in sarcoma (FUS)-positive inclusions. (B) Protein aggregates in the form of Lewy bodies are the defining pathological hallmark of PD. Common pathology also exists between FTD/ALS and PD, with reactive gliosis and degeneration of the substantia nigra and nigrostriatal projections observed. Green, FTD/ALS; blue, PD; yellow, FTD/ALS and PD. *Adapted from Wallings and Humble et al. [40, 46]*

Interestingly, a recent hospital-based cohort was evaluated for the frequency parkinsonism based on the differences in behavioral and cognitive features as part of a nationwide effort in South Korea. These studies showed that nearly 40% of all FTD patients presented with parkinsonism, regardless of subtype [48]. Strikingly, the behavioral disturbances were significantly more impaired in patients with parkinsonism, where these changes might signal the larger clinical progression of the disease to subcortical structures involving basal ganglia [48]. Lebedev et al. present their fMRI and DaT-SPECT research demonstrating a positive correlation between nigrostriatal dopaminergic function and executive functioning and memory testing [49], which further supports this proposed progression. Although the precise mechanisms causing features of parkinsonism in FTD is unknown, the neuropathological features showing degeneration of striatum and other subcortical structures are notable [50].

1.3.3 Lysosomes are a site of functional convergence between FTD/ALS and PD

Despite *age* being the primary risk factor for developing sporadic PD, mutations in a number of genes have been found to cause monogenic forms of PD, as well as risk-factor gene variants that contribute to sporadic forms of the disease. A subset of highly penetrant PD-associated genes encode proteins shown to play a role in lysosome homoeostasis and function, including *LRRK2*, *GBA*, *ATP13A2* and *SNCA*. Additionally, a study with candidate genes enriched for associations with autophagy and lysosomal function identified 17 new risk loci for PD [51]. Further studies also identified several rare lysosomal disorder gene variants as significant burdens associated with PD risk, all previously unknown [52]. Notably, mutations in a gene implicated in Niemann-Pick's disease, *SMPD1*, are increased in PD patients [53].

It is also known that a large proportion of FTD/ALS-causing genes are related, either directly or indirectly, to pathways that maintain protein homeostasis via lysosomes and autophagy [54]. Recent findings related to a previously unknown function of *C9orf72* in regulating the lysosomal/autophagy axis further support its importance in FTD/ALS pathology and simultaneously expands its enigmatic role as a major cause of both FTD and ALS [55, 56]. Moreover, several other key FTD/ALS genes such as *GRN*, *TBK1*, *OPTN*, *CHMP2B*, *SQSTM1/p62*, *VCP/p97* and risk factors (*TMEM106B*), center around the lysosome and protein degradation—converging pathways with increasing relevance in neurodegeneration [57].

In addition to FTD/ALS genes that are related directly to lysosomal function, other important disease-causative genes exist in functional categories linked to related pathways. Most notably, disturbances in genes that govern RNA binding and processing result from mutations in *TARDBP*, *FUS*, *MATR3*, *TIA1*, *hnRNPA1*, *hnRNA2B1*, and *C9orf72*, which is linked across multiple different functional categories related to the etiology of FTD/ALS [58]. Additionally, cytoplasmic aggregation of TDP-43 and FUS are common pathological hallmarks in both FTD and ALS [58]. Axonal trafficking has also been implicated in FTD/ALS, with many

genes such as *ALS2*, *C9orf72*, *CHMP2B*, *DCTN1*, *FUS*, *SOD1*, *TARDBP*, and *VAPB* having impact on multiple functional pathways including general trafficking and transport [59].

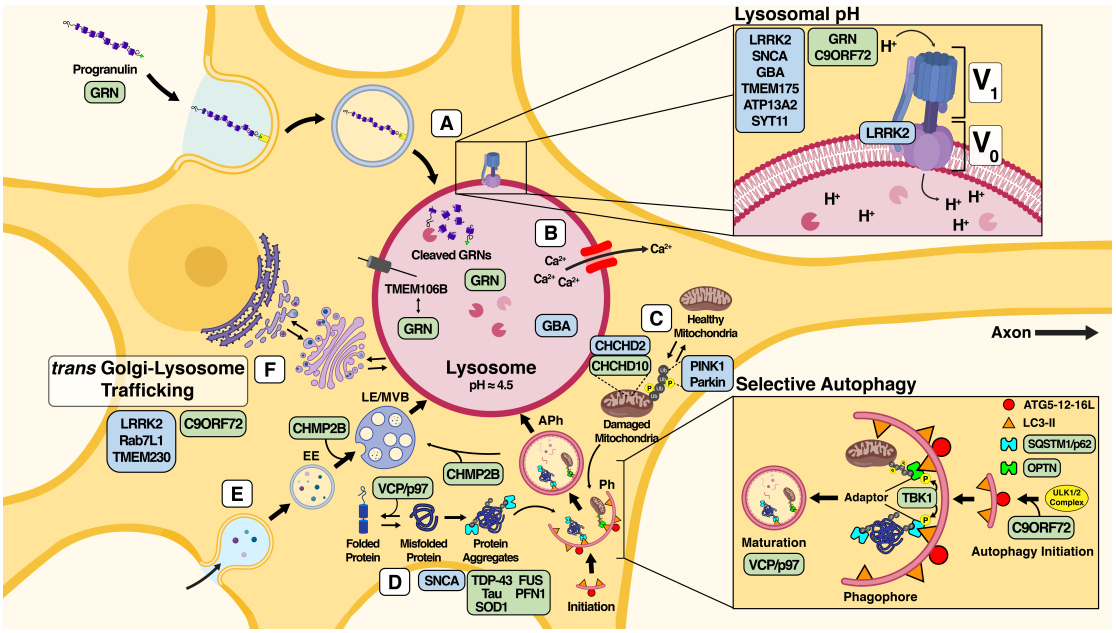


Figure 1.3: FTD/ALS and PD-Associated Genes Converge on the Lysosome. Recent findings provide evidence for a role of both PD and FTD/ALS-associated genes in multiple aspects of lysosome biology, including (A) regulation of lysosomal pH, (B) lysosomal calcium release, (C) mitophagy and selective autophagy, (D) protein quality control and macroautophagy, (E) the endolysosomal pathway, and (F) trans-Golgi-lysosome trafficking. Blue boxes, PD; green boxes, FTD/ALS. Abbreviations: APh, autophagosome; C9orf72, chromosome 9 open reading frame 72; CHCHD2/10, coiled-coil-helix-coiled-coil-helix domain containing 2/10; CHMP2B, charged multivesicular body protein 2B; EE, early endosomes; FUS, fused in sarcoma; LE, late endosomes; LRRK2, Leucine-rich repeat kinase 2; MVB, multivesicular body; Ph, phagophore; SNCA, a-synuclein; TDP-43, Tar DNA-binding protein 43; VCP, vasolin-containing protein. *Adapted from Wallings and Humble et al. [40]*

Moreover, a recently developed protein-protein interaction analysis pipeline was used to define impacted biological processes, with risk pathways identified in PD and parkinsonian syndromes, including FTD [60]. In this study, protein disposal pathways were enriched in both PD and FTD. Interestingly, the monogeneic forms of FTD/ALS that are known to have a clinical parkinsonism component are also some of the most heavily implicated in lysosomal function and/or pathways, such as *GRN*, *C9orf72*, *CHMP2B*, *VCP* [46] and *CHCHD2/10* [61]. This further

strenghtens the mechanistic link that these two diseases have key interactions centered around the lysosome.

Growing evidence suggests that several genes associated with FTD/ALS, PD, and indeed Alzheimer's disease (AD) overlap with lysosomal function and the aging process. The lysosome is the central organelle responsible for the regulation and degradation of cellular cargo and damaged proteins [62]. Furthermore, lysosomes can be deeply implicated in the aging process generally, especially in regard to neurodegenerative diseases where this complex proteolytic system is required in long-lived neurons to offset the disease-burden related to protein accumulation [62].

In the context of PD, mutations in genes such as *GBA1* is directly linked to lysosomal dysfunction. *GBA1* mutations are the most common genetic risk factor for PD and result in reduced enzymatic activity, leading to impaired lysosomal degradation [63, 64]. In FTD/ALS, mutations in the *C9orf72* gene, as mentioned earlier, have been shown to impact lysosomal function [55]. The accumulation of aberrant RNA species resulting from the C9orf72 repeat expansion disrupts lysosomal pathways and impairs protein degradation [65]. Additionally, mutations in other ALS-associated genes, such as *SQSTM1*, have been linked to lysosomal dysfunction [66], leading to impaired clearance of protein aggregates [67]. Regarding AD, several genes associated with the disease, including *APP* [68], *PSEN1* [69], and *PSEN2* [70], have been shown to influence lysosomal function. Dysfunctional lysosomes in AD contribute to the impaired clearance of amyloid-beta plaques, a hallmark feature of the disease [71].

While there is significant functional overlap between lysosomal pathways, aging, and individual neurodegenerative disorders like FTD/ALS, PD, and AD, identifying specific genes that are associated with all three disorders is challenging. However, dysregulation of the gene *TFEB*, a master regulator of lysosomal biogenesis and autophagy, has been observed in FTD/ALS [72], PD [73, 74], and AD [75], suggesting a common pathway involved in these disorders. Additionally, mutations in *VPS35*, which is involved in protein trafficking and recycling within cells, have been linked across these forms of neurodegeneration [76], with stronger direct familial ties in PD

[77, 78] where alterations in its function can lead to impaired lysosomal degradation and protein accumulation. While there are notable shared aspects of lysosomal dysfunction across FTD/ALS, PD, and AD, the specific genetic and molecular mechanisms underlying each disease can vary considerably and further understanding is needed to fully realize the complex interplay between lysosomal function and any potential common genetic factors associated with each neurodegenerative disorder.

Dysfunction in Lysosomal Pathways and Protein Aggregation

The pathognomonic hallmark of FTD/ALS and PD is the presence of protein aggregates specific to certain sub-types of each disease. This reinforces the vital role of lysosomes across these neurodegenerative diseases. Recent reports suggest that there is a difference in the response of the lysosome in PD patients with pre-aggregates opposed to patients with Lewy bodies at post-mortem. They also detected that the volume density of cathepsin D immunoreactivity was abnormally increased, and that this aspect preceded the deposition of pathologic α-synuclein [79], potentially implicating the lysosome before α-synuclein pathology is clear. Previous evidence also suggests that *GRN* functions as a chaperone for *CTSD* in the lysosome, and that the two proteins have overall neurotrophic effects [80]. Additionally, *VCP/p97* has been shown to have widespread function in protein quality control and misfolding [81].

Mutations in *GBA*, which encodes for the lysosomal hydrolase β-glucocerebrosidase (GCase), are a major genetic risk factor for PD. Loss of GCase-activity has been linked with pathogenic mutations and retention of GCase in the ER, which interrupts its normal trafficking [63, 82], and loss of *GBA* promotes α-synuclein pathology with the subsequent accumulation of glucosylsphingosine (GlcSph) [83]. Additionally, the accumulation of multilamellar bodies (MLBs) and cholesterol has been reported in lysosomes of GBA-PD patients in [63]. Interestingly, the GWAS PD risk factor *SCARB2* [84] encodes LIMP2, a cofactor required for the import of glucocerebrosidase.

ATP13A2 has been identified as the causative gene at the *PARK9* locus [85] and is currently characterized as one of a growing network of Neuronal Ceroid Lipofuscinoses (NCLs) that have severe lysosomal defects [86, 87]. This feature is also seen *ATP13A2* KO mice that exhibit typical neuropathologic findings of NCL, including the build-up of glycoproteins and glycolipids, the accumulation of Subunit c of mitochondrial ATP synthase, and delays cathepsin D maturation [88]. Additional findings suggest that *ATP13A2* loss induces mitochondrial damage and oxidative stress [89], further supporting *ATP13A2*'s role in lysosomal function.

The importance of proteostasis and lysosomal homeostasis have been emphasised with recent evidence in regards to FTD/ALS associated genes and disease models. For example, evidence of *SQSTM1/p62*'s role in FTD/ALS has been known for some time, as mutations in the gene can be causal for both FTD and ALS [90–93], in addition to its presence in protein inclusions as a pathognomonic signature in the disease spectrum [94]. A recent report highlighted a childhood-onset neurodegenerative disorder occurring due to biallelic *SQSTM1/p62* loss-of-function variants [66]. The report suggests an expansion of the *SQSTM1/p62* phenotypic spectrum, which is further supportive of dysfunction in selective autophagy pathways as a fundamental insult in neurodegeneration [66].

Whilst *SQSTM1/p62*'s precise role in FTD/ALS pathology is still being debated, its mechanism seems to be centered around protein degradation and organelle quality control, along with *VCP/p97* [95, 96]. Its functions are widespread and essential to cells across tissues, as recently reviewed by van den Boom and Meyer [81]. Nevertheless, distinct features of both knock-out and mutant *VCP/p97* include autophagic dysfunction and the mislocalization of TDP-43 to the cytosol [44]. Recent findings have suggested that *VCP/p97* plays an important role in autophagosome maturation [97], mitochondrial quality control through *UBXD1*-mediated *Parkin*-dependent mitophagy [98, 99], and the clearance of damaged lysosomes by the recruitment of the transient cofactors *UBXD1*, *YOD1*, and *PLAA* [100], further implicating certain FTD/ALS genes in crucial autophagy pathways.

Mutations in *PFN1*, an actin monomer-binding protein, have been shown to cause ALS [101]. *PFN1* has a primary role in regulating actin cytoskeleton dynamics, and gain-of-toxic-function mutations in PFN1 spur a cascade of misfolding, oligomerization, and aggregation of mutant *PFN1*, leading to the formation of cytoplasmic aggregates of sequestered TDP-43 positive for p62 and ubiquitin [102, 103]. Furthermore, lysosomal inhibition increased these cytoplasmic aggregates, highlighting the crucial role of the lysosome in clearing protein aggregation [103].

Knock-down of *C9orf72* inhibits autophagy induction and leads to *SQSTM1/p62* accumulation [104, 105] as well as aggregation of TDP-43 [105]. Neurons from patients with *C9orf72* mutations have been observed to have impaired basal autophagy [104, 106] as well as an increased sensitivity to autophagy inhibition [107]. *C9orf72*, *SQSTM1/p62*, and *FUS* may also underpin a key link to stress granule autophagy via a recognition cascade that, when defective, may lead to characteristic cytoplasmic protein inclusions seen in FTD/ALS [108]. Interestingly, it has been demonstrated that alpha-synuclein fibrils recruit *TBK1* and *OPTN*, two proteins implicated in FTD/ALS, to lysosomal damage sites and induce autophagy in microglial cells [109], implicating common pathways between FTD/ALS and PD.

Lysosomal pH

Lysosomal function requires maintaining a delicate balance of acidic luminal pH, where even moderate shifts [H+] can severely disrupt both degradative enzyme activity and endolysosomal maturation. The PD-associated proteins *LRRK2*, *TMEM175* and *ATP13A2* have all been implicated in lysosomal pH regulation. The G2019S-LRRK2 mutation has been linked to lysosomal pH and protein degradation deficits in primary astrocytes [87], and LRRK2 was recently linked as a direct interactor of *ATP6V0A1*, the subunit of the vacuolar-type ATPase H+ pump that maintains lysosomal pH [110]. Notable in this study, the expression of the R1441C mutation abolished the interaction, which caused lysosomes to alkalize and protein degradation decreased.

The lysosome-related PD risk factor *TMEM175* functions as a K+ channel in late endosomes and lysosomes. Deficiency of this gene in rat primary neurons causes decreased lysosomal catalytic activity, impaired autophagosome clearance, and overall instability in lysosomal pH [111]. Of note, loss of *TMEM175* also decreased *GBA* activity, which requires acidic pH of approximately 4-5 for proper function, highlighting a potential direct interaction between PD risk factors. Additionally, ATP13A2 has been shown to regulate SYT11, which is also associated with PD. These two genes are related at both the translational and post-transcriptional levels, as the depletion of ATP13A2 directly causes the degradation of SYT11, which leads to lysosomal alkalinization and subsequent α-synuclein accumulation [112]. This once again highlights the relationship of PD-associated genes to the lysosome and emphasizes the importance of lysosomal homeostasis in disease mechanisms.

With regards to FTD/ALS, cleaved granulins may play a part in lysosome function by impairing degradation of TDP-43 [113], which has also been shown to decrease autophagosome-lysosome fusion [114]. Indeed, it has been demonstrated that intracellular proteolysis of the progranulin protein generates stable, lysosomal granulins [115]. Furthermore, GRN has recently been implicated as a regulator of lysosomal acidification and biogenesis [116]. SNPs in *TMEM106B* have been identified as risk alleles in FTD/ALS which encodes for a transmembrane protein on the endolysosomal membrane. *TMEM106B* has been shown to interact with vATPase accessory protein 2 (AP1) and its deficiency leads to the downregulation of AP1 and V0 domain subunit expressions as well as impaired lysosomal acidification [4]. As previously mentioned, *LRRK2* has also been implicated in lysosomal pH via its interaction with vATPase subunits, highlighting once again the convergence of mechanisms at the lysosome between these two diseases. Furthermore, FTD/ALS causative *CHMP2B* has recently been shown to impair lysosomal trafficking, and reducing *TMEM106B* levels ameliorated these defects [117]. As *TMEM106B* is a risk factor for FTD/ALS caused by both *C9orf72* and *GRN* mutations, this data highlights a promising approach for treating a wide range of patients.

1.4 Utilizing hiPSC-derived Neurons as a Cellular Model for Functional Genomics

1.4.1 CRISPR Interference (CRISPRi)

In order to study relevant neuronal biology as it relates to lysosomal function in a context relevant to FTD/ALS and PD, I use a model combining two biomedical breakthroughs: 1) induced pluripotent stem cells (iPSCs) [118] and 2) the CRISPR/Cas9 system [119].

Clustered regularly interspaced short palindromic repeats (CRISPR) is a term used to denote a family of DNA sequences discovered in bacteria [120, 121], which provides adaptive immunity in prokaryotic organisms [122, 123]. This discovery and string of related breakthroughs has brought forth a revolution in modern genetic engineering. In 2005, a team of researchers found a novel cas gene, later named Cas9, that encoded a large protein with nuclease activity, along with the universal protospacer adjacent motif (PAM), a sequence required for target recognition [124]. By 2012, Gasiunas et al. were working to mechanistically characterize Cas9's mode of action in order to further harness this molecular tool [125].

This system was repurposed for genetic engineering across organisms, and a key optimization was the incorporation of a single-guide RNA (sgRNA) which merges the tracRNA-crRNA-duplex into a single molecule by including the hairpin between the two [126]. Cong et al. later demonstrate the successful use of CRISPR-Cas9 in mammalian cell lines by targeted genome cleavage in human and mouse cells [127]. This groundbreaking study showed that CRISPR-Cas9 could be programmed to target multiple genomic loci and drive homology-directed repair [127], displaying a powerful new genomic tool for precision editing in mammalian cells.

The editing process begins with the selection and design of a guide RNA (gRNA) or single-guide RNA (sgRNA) molecule that is complementary to a target DNA

Table 1.1: Genes and Risk Factors Associated with PD and FTD/ALS That Have Been Implicated in Lysosomal Function. *Adapted from Wallings and Humble et al. [40]*

Gene	Inheritance	Pathology	Functions implicated at the Lysosome
SNCA (PARK1/4)	AD	Early-onset, severe PD with Lewy bodies	Recruits FTD/ALS-associated proteins to lysosomal damage sites
Parkin (PARK2)	AR	Early-onset PD with slow progression and no Lewy bodies in most cases	Ubiquitin ligase that catalyses ubiquitin transfer to mitochondria for mitophagy
PINK1 (PARK6)	AR	Early-onset PD with slow progression and Lewy body pathology	Has an essential role in mitophagy
LRRK2 (PARK8)	AD	Typical, late-onset PD with Lewy bodies	Regulates lysosomal pH via vATPase a1 subunit
ATP13A2 (PARK9)	AR	Juvenile-onset atypical parkinsonism (Kufor–Rakeb); pathology demonstrates ceroid lipofuscinosis	Regulates lysosome pH via SYT11 and is functional in the clearance of damaged mitochondria
GBA	N/A	Typical, late-onset PD with Lewy bodies	GBA mutations lead to accumulation of cholesterol in
TMEM175	N/A	PD; not yet described	Regulates lysosomal pH
VPS35 (PARK17)	AD	Typical, late-onset PD with unknown pathology	Role in endosome–Golgi complex trafficking; mutations impair autophagy
TMEM230	N/A	Typical, late-onset PD with unknown pathology	Mutations induce autophagic dysfunction
C9orf72	AD	Adult-onset ALS/FTD with ubiquitin/p62/ TDP-43/FUS proteinopathy	Regulates autophagy induction and stress granule autophagy; acts as a GEF for 2 PD-related Rab-GTPases
GRN	AD	FTLD-TDP with ubiquitin /p62/TDP-43 proteinopathy	Chaperones cathepsin D and regulates lysosomal pH
TBK1	AD	Adult-onset ALS/FTD with ubiquitin/p62/ TDP-43/FUS proteinopathy	Required for efficient clearance of damaged mitochondria and is recruited to lysosomes by a-synuclein
OPTN	AD	Adult-onset FTD/ALS with unknown pathology	Required for efficient clearance of damaged mitochondria and is recruited to lysosomes by a-synuclein
CHMP2B	AD	Adult-onset FTD/ALS with TDP-43/ubiquitin proteinopathy	Regulates lysosomal trafficking and is an ESCRT-III component
CHCH2/10	AD	Late-onset PD or adult-onset FTD/ALS with unknown pathology	Responsible for mitochondrial quality control
TMEM106B	N/A	Adult-onset FTD with tau proteinopathy	Interacts with vATPase accessory protein 2 and regulates lysosomal pH
VCP	AD	FTD with TDP-43/ ubiquitin proteinopathy	Functional in autophagosome maturation and clearance of damaged lysosomes
SQSTM1	AD	Adult-onset FTD/ALS with TDP-43/ubiquitin/ FUS proteinopathy	Targets protein aggregates for lysosomal degradation

Abbreviations: AD, autosomal dominant; AR, autosomal recessive.

sequence in order to escort the Cas9 protein to a specific location in the genome. Once the Cas9-gRNA complex binds target DNA, Cas9 creates a double-stranded break of the genome, triggering the cell's repair mechanisms. Repair can then occur through non-homologous end joining (NHEJ), which leads to small insertions or deletions causing gene disruptions, or through homology-directed repair (HDR), which enables precise gene modifications by incorporating donor DNA templates [119, 127, 128].

CRISPR interference (CRISPRi) is a modification to the the CRISPR/Cas system that allows for the transcriptional repression of a given gene by harnessing the high precision of sgRNA/Cas protein specificity [129], shown in Figure 1.4. Other methods also achieve transcript ablation, such as RNA interference (RNAi) [130]. However, RNAi and similar methods act on the mRNA level, when transcripts have already been produced, whereas CRISPRi prevents transcription of the targeted DNA region itself by blocking transcription directly.

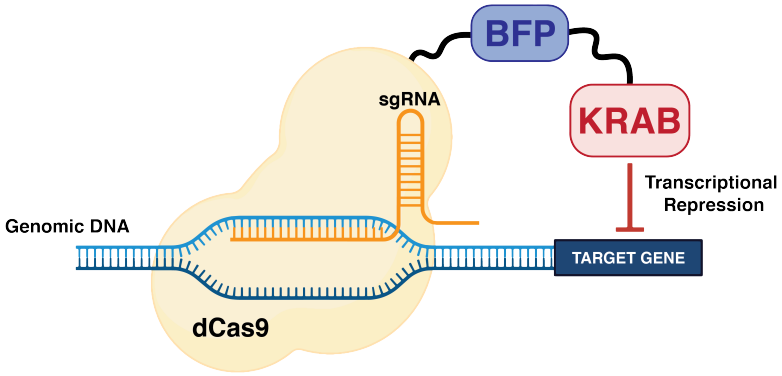


Figure 1.4: Transcriptional repression is achieved through CRISPR Interference. CRISPR interference utilizes a catalytically-dead Cas9 protein targeted to the genome via single guide RNAs (sgRNA) to deliver KRAB transcriptional repressor to a given gene locus.

The key component in CRISPRi is the catalytically-dead Cas9 protein, generated by point mutations in Cas9 that removed its endonuclease activity. However, dCas9 retains powerful genomic specificity, meaning it can still bind target loci, but does not induce a double-stranded cut in the DNA. To generate the final CRISPRi

tool, dCas9 was fused to the KRAB transcriptional repressor, which prevents the transcription of genes downstream from the sgRNA targeting sequence [131].

One advantage of CRISPRi is the flexibility of the system, as it allows for the modulation of gene expression levels without permanently altering the genome of the target model. This semi-reversible control is particularly useful in studying the functions of specific genes, as it enables researchers to observe the effects of gene silencing while leaving the possibility for normal gene function to be restored [129, 132]. Alternatively, traditional CRISPR-Cas9 involves inducing indel mutations or large deletions within the target gene, resulting in the complete loss of gene function [119]. The knockout approach is often used to study gene function by observing the consequences of complete gene loss or to generate disease models for further study, both of which may provide a more definitive assessment of gene function when studying essential genes or those with dominant roles in cellular processes [119, 133].

However, both CRISPRi and traditional CRISPR-Cas9 engineering have certain limitations such as off-target effects, where non-targeted genes may be acted on by either system due to the similarity of their DNA sequences to the intended target [133]. Additionally, the efficiency of CRISPRi and traditional CRISPR-Cas9 engineering can vary depending on the target gene and the cell type, which may require optimization for each specific application [133]. For example, the ability to assay essential genes through CRISPR knockout has been shown to been more effective than CRISPRi and shRNA/RNAi [133]. This may be, at least in part, due to potential heterogeneity arising from transgene silencing, a phenomenon where the expression of the introduced CRISPR components is gradually suppressed over time by the host cellular mechanisms [134]. This can lead to variable and unpredictable expression levels of CRISPR machinery or loss of transgene expression altogether.

1.4.2 i^{3}Neurons

The discoveries leading to the development of human induced pluripotent stem cells (hiPSCs) enabled the tangible and efficient study of isogenic human cell types in culture [135, 136]. In an effort to make the differentiation of hiPSCs more

efficient and standardized, Zhang et al. developed a method which generated cortical, glutamatergic neurons by delivering the transcription factor neurogenin-2 (NGN2) via lentivirus to hiPSCs [137].

Through single-copy integration of a doxycycline-inducible neurogenin 2 (iNGN2), Wang et al. created clonal hiPSC lines that enable simple, rapid, reproducible, and scalable production of glutamatergic cortical neurons [138]. This expanded upon the technique from Zhang et al., while avoiding viral transduction-induced toxicity and variability in NGN2 expression. The resulting hiPSCs are ***isogenic***, ***integrated*** at the AAVS1 safe-harbor, and have ***inducible*** NGN2 expression, hence the name i^{3}Neurons. This neuronal model can be differentiated through a simple two-step process over 14 days, with robust morphological, transcriptional, and functional homogeneity [138, 139].

Inducible neuronal models such as cortical i^{3}Neurons have several advantages and disadvantages in various research and application contexts when compared to more traditional differentiation methods. i^{3}Neurons and similar systems are powerful tools due to their unparalleled accessibility and reproducibility. These models can be very easily differentiated throughout a research project, enabling experimental replication, allowing for the recapitulation of disease phenotypes, identification of pathological mechanisms, and patient-specific modeling [137, 140]. However, the speed of differentiation also comes at a price, most notably with immaturity and heterogeneity in these model systems. Ward et al. sought to minimize the heterogeneity of cultures and incomplete differentiation via single copy, safe-harbor integration, as previously described [138, 139].

Despite those efforts, researchers still have to deal with the disadvantage of neuronal immaturity with inducible systems when compared to traditional differentiation methods, likely the largest disadvantage of inducible systems currently [137, 138]. No neuronal models fully capture the complexity and maturity of native neurons found in the human brain, however, inducible models such as i^{3}Neurons often resemble early-stage neurons and may lack some of the functional characteristics of mature neurons, which can limit their applicability for certain studies [137, 138, 140].

While the advancements seen with inducible neuronal models have opened up new avenues for studying neurodegenerative diseases, researchers must carefully consider their advantages and limitations in designing experiments and interpreting results.

1.4.3 Genetic Engineering of CRISPRi into i^{3}Neurons

i^{3}Neurons were further engineered by Tian et al. [140] in order to combine CRISPRi technology with the optimized neuronal differentiation method already harnessed by this model. To generate stable integration of pC13N-dCas9-BFP-KRAB [140], the dCas9-cassette was inserted into the CLYBL safe harbor locus, which allowed for CAG-promoter driven dCas9 expression. The resulting CRISPRi-i^{3}Neuron cell line, coupled with lentiviral-delivered sgRNAs, enables robust gene expression interference.

1.5 Aims of the Work in this Thesis

- **Aim 1:** Demonstrate the optimization, testing, and subcloning of relevant CRISPRi sgRNA libraries for arrayed screening
- **Aim 2:** Demonstrate the development and optimization of relevant phenotypic assays related to FTD/ALS and PD disease mechanisms
- **Aim 3:** Demonstrate the utility and application of high-content imaging and analysis in neuronal cellular models, specifically i^{3}Neurons
- **Aim 4:** Demonstrate the functional validation of sgRNA lentiviral libraries for use in high-content screening in neuronal models
- **Aim 5:** Demonstrate the development and optimization of Genetic Interaction Mapping in i^{3}Neurons for high-content screening
- **Aim 6:** Demonstrate the first Genetic Interaction Mapping screen in human iPSC-derived Neurons, utilizing the optimized DQ-BSA assay and CRISPRi

2

Materials and Methods

Contents

2.1 Key Resources and Materials 22
2.2 Cloning 23
2.2.1 NEBuilder Hifi or InFusion Cloning 23
2.2.2 High-throughput Cloning 27
2.3 Lentivirus Production 27
2.4 Cell Culture 29
2.4.1 hiPSC Culture 29
2.4.2 hiPSC Lines 29
2.4.3 Neuron Differentiation for High-Content Applications . 30
2.5 Live Cell Imaging 33
2.5.1 Live cell DQ-BSA Assay 34
2.5.2 Live Cell Ratiometric pH Assay 34
2.5.3 Live cell Magic Red CTSB Assay 35
2.5.4 Neuronal Survival and Neurite Outgrowth Assays 35
2.5.5 Transferrin Assays 36
2.6 sgRNA Validation 37
2.7 Arrayed Screening 37
2.8 Quantification and Statistical Analyses 37

2.1 Key Resources and Materials

Bacterial Strains:

- Stbl3 Chemically Competent E. coli (Thermo: C737303)

Chemicals, Assay Reagents, etc

- Chloroquine (Sigma-Aldrich, C6628)
- Bafilomycin A1 (Sigma, 19-148)
- NH4Cl (Sigma, A9434)
- Lenti-X Concentrator (Takara, 631231)

Critical Commercial Assays:

- DQ-BSA Red (Thermo, D12051)
- DQ-BSA Green (Thermo, D12050)
- Oregon Green 488 Dextran (Thermo, D7170)
- Alexa 555 Dextran (Thermo, D34679)
- Magic Red CTSB (Immunochemistry Technologies, 938)

Cell Lines:

- WTC11 hiPSC lines with doxycycline-inducible mNGN2 transgene at the AAVS1 locus (Fernandopulle et.al., 2018)
- Lenti-X 293 T (Takara, 632180)

Recombinant DNA Plasmids

- pMK1334 was a gift from Martin Kampmann (Addgene, 127,965)
- All sgRNA subclones of pMK1334 was a gift from Martin Kampmann (Addgene, 127,965)
- J72, a modified pMK1334 (EF1a-Puro-T2A-2xmycNLS-WPRE-mU6-sgRNA).
- All sgRNA subclones of J72

- MK-EF1a-Puro-T2A-MycNLS2x-mTagBFP2
- All sgRNA subclonesMK-EF1a-Puro-T2A-MycNLS2x-mTagBFP2
- J17 MK-EF1a-TDsmURF
- J18 MK-EF1a-iBlueberry
- J19 MK-EF1a-iRFP670
- J20 MK-EF1a-iRFP720
- J49 U6-1872-MK-EF1a-BSD-T2A-iRPF670 (Codon Optimized)
- J71 U6-1872-MK-EF1a-Kz-BSD-T2A-Kz-iRPF670 (Codon Optimized)

Other

- Poly-L-ornithine (Sigma P3655), BrainPhys without Phenol Red (Stemcell technologies 05791), ROCK inhibitor Y-27632 (Selleckchem S1049), Essential 8 Medium (ThermoFisher Scientific A1517001), Growth factor reduced Matrigel (BD Bioscience 35881), DMEM/F12 (ThermoFisher 11320033), N2 Supplement (ThermoFisher 17502001), NEAA (ThermoFisher 11140076), Gluta-MAX Supplement (ThermoFisher 35050061), B-27 (ThermoFisher Scientific 17504044), Recombinant Human BDNF (PeproTech 450-02), Recombinant Human NT-3 (Peprotech 450-03), Laminin Mouse protein (ThermoFisher 23017-015).

2.2 Cloning

2.2.1 NEBuilder Hifi or InFusion Cloning

Plasmids were generated with PCR and recombinase-based cloning (In-Fusion by Clontech or NEBuilder by NEB).

General outline:

Day 0:

- Design construct, order primers for insert/geneblock and sequencing primers

Day 1:

- PCR insert (4h)
- Run gel to verify single PCR product
- Pool single PCR products, purify, and quantify
- Vector (4h)
- Digest vector, purify, and quantify
- In-Fusion reaction (15 min)
- Transform bacteria (10 min)

Day 2:

- Pick colonies at 8 AM -> starter culture
- PCR-colony screening if necessary (usually only if using >2 inserts)
- Mini-prep at 1 PM
- Send plasmids to Elim for sequencing (before 5 PM)
- Spike 250 uL starter cultures into 250 mL LB for overnight cultures (only if Maxiprep needed)

Day 3:

- Check sequencing results
- Midi- or Maxi-prep DNA from sequence-verified large cultures (if needed)

Insert

Table 2.1: PCR Reaction

Component	1 x 25 uL	8 x 25uL
Q5 2x master mix	12.5 uL	100 uL
200 uM Forward primer	0.063 uL	0.5 uL
200 uM Reverse primer	0.063 uL	0.5 uL
template DNA (1ng/uL)	0.25 uL	2 uL
Nuclease free H2O	12.12 uL	97 uL

Table 2.2: PCR Conditions

STEP	Temp	Time
Initial Denaturation	98	30 sec
30-35 Cycles	98	10 sec
	56-70	30 sec
	72	30 sec/kb
Final Extension	72	2 min
Hold	12	forever

- Use PCR to generate insert, or order Geneblock (IDT)
- Design forward and reverse primers/Geneblock such that they generate exactly 20nt homologous overlaps with your digested vector on both ends (Figure 1)
- Use the Snapgene In Fusion design tool or the In-Fusion HD Cloning Kit User Manual for details of how to count overhangs. Multiple inserts can be cloned simultaneously into your digested vector, provided that they each overlap eachother by 15nt. If ordering Geneblocks, ensure that the ends are compatible with In-Fusion HD ligation.
- Don't forget to add a Kozak sequence before the ATG start
- Q5 enzyme preferred to minimize mutations (Hot-start 2x premix works well)
- Minimize template DNA (2ng total per 8 x 25uL rxns)
- Use gradient for annealing temperature to maximize chance of generating a single band (e.g. 56-70 deg over 8 tubes)
- Run 5uL of each tube on gel to determine which ones have a single band
- Pool tubes with single PCR product and purify with Qiagen PCR purification kit
- Elute with 30 uL H2O to maximize concentration
- Quantify purified PCR product via Nanodrop

Backbone Vector Digest

- Digest 5-10 ug vector the goal is to have 500 ng/ul final concentration in the digest reaction.

- Two-enzyme digestion is preferred to reduce self-ligation of vector
- Determine optimal restriction digest buffer
- Digest vector for 3 hours-overnight (use high-fidelity enzymes)
- This minimizes transformation of uncut vector
- No need to purify backbone from insert
- Heat inactivate according to NEB website for given enzymes used

Table 2.3: Backbone Digestion

Component	10uL total
10x digest buffer	1 uL
Enzyme #1	1 uL
Enzyme #2	1 uL
vector	5 ug
Millique H2O	To 10 uL

Transformation

- Best practice is to use "home-made" Mix&Go Stbl3 competent cells***
- Pre-warm ampicillin plates to 37 deg***
- Thaw bacteria on ice x 10 min
- Add 2.5 uL of In-Fusion or HiFi reaction with 25uL bacteria, flick a few times gently to mix
- Incubate on ice for 5 minutes to transform
- Spread transformed bacteria onto pre-warmed plate
- **If using Kanamycin resistant plasmids, transformed cells must recover for 1-2h in 400uL SOC on 37deg shaker prior to plating
- **We have best results with home-made Mix&Go Stbl3 E. Coli due to their good growth and reliability with viral constructs, where strains must be recombinase (-)

2.2.2 High-throughput Cloning

All sgRNA constructs were created by the ligation of BstXI and BlpI sticky ends generated by oligonucleotide annealing. Based on the desired guide RNA sequence, forward and reverse oligos were designed, created (IDT), and heated for 5 minutes at 95°C, allowed to gradually anneal to RT. This annealed oligo stock can then be placed on ice (or stored at –20°C). A 1:20 dilution of the oligo stock was prepared for use in the ligation with the gel-purified sgRNA backbone, pre-digested with BstXI and BlpI. Then transform 2.5 µl of the ligation reaction into Mix & Go STBL3 (preferred) and sequence verify across the guide region.

2.3 Lentivirus Production

To deliver sgRNAs to the cells, I used lentiviruses due to this system's ability to transduce non-dividing cells (neurons). It consists of three components: the packaging, the envelope, and the transfer plasmids. The packaging plasmids carry a mutated HIV-1 provirus un- able to package itself (for safety reasons). The envelope plasmid contains a viral envelope from a different virus dictating the types of cells the virus can infect. The transfer plasmid encode the desired transgene, in our case the sgRNA, flanked by HIV-1 long terminal repeats (LTRs) that make viral packaging and host genome integration easier.

The day before the transfection, cell dishes were coated with PLO for 1 hour at 37°C and then washed twice with water and dried. Low-passage Lenti-X HEK cells were plated at 10-12 million cells per 10cm dish. On the day of the transfection, OptiMEM (Gibco, cat. no. 31985062), pre-warmed to room temperature, was added together with LipofectamineTM 3000 (Invitrogen, cat. no. L3000001) reagent to a tube and incubated for 5-20 minutes. In a second tube, a mix of packaging plasmid (psPAX2), envelope plasmids (pMD2G), pAdvantage (translation enhancer plasmid), and plasmid DNA coding for the sgRNA, was mixed with P3000 reagent and Optimem. Tube 2 is then mixed with tube 1 and after 20 minutes, the mixture is added to the Lenti-X HEK cells dropwise.

A day after the transfection, media is changed with DMEM/FCS + Viral Boost (Alstem). Two days later, the viruses are concentrated with the Takara Lenti-X Concentrator (Clontech, cat. no. 631231 and 631232) and the media is collected. The cells are spun at 10,000g to pellet and the cell debris is removed. Viruses are stored in single vials of 12µl (one per experiment) at -80°C to avoid a decline of virus potency by thaw-freeze repeats.

Detailed concentration method:

The collected lentiviral supernatant is sterile filtered with a PVDF protein low-bind SteriFlip vacuum filter to remove cells and debris. Pool similar stocks, if desired. Clarified viral supernatant is then mixed via gentle inversion at a ratio of 3:1 (3 volumes supernatant with 1 volume concentrator) with Lenti-X Concentrator (TAKARA 631231 & 631232) and incubated for 48hrs at 4°C. The mixture is then centrifuged at 1500 x g for 45 min. at 4°C. After centrifugation, an off-white pellet will be visible. Supernatant is then carefully removed, making sure to not disturb the pellet. Residual supernatant can be removed with pipette. The pellet can then be gently resuspended in 1/10 to 1/100th of the original volume using complete DMEM, PBS, or TNE. The pellet can be somewhat sticky at first, but will go into suspension quickly. All viral sgRNA preps were concentrated 100x in sterile PBS, aliquoted in single use, individually capped PCR tubes, and immediately frozen at -80°C. One vial can then be thawed and used for transduction of target cells and functional tittering. All subsequent vials used will have matched the freeze-thaw cycles. NOTE: Centrifugation of the debris is an option, but take extra care to prevent contamination from cell debris, which may lead to contamination in your final culture. Also, a low protein binding membrane such as cellulose acetate, polyethersulfone (PES), or PVDF must be used when filtering to prevent destruction of the virus.

2.4 Cell Culture

2.4.1 hiPSC Culture

The control male WTC11 human induced pluripotent stem cells (hiPSC) line was obtained from Coriell. hiPSCs were maintained under feeder-free conditions in a 37°C, 5% CO_2tissue culture incubator on tissue culture treated dishes coated with growth factor-reduced Matrigel (BD Biosciences) and fed every 1-2 days with Essential 8 medium (Thermo Fisher Scientific), as needed. Accutase (STEMCELL Technologies) was used to enzymatically dissociate hiPSCs into single cells, and 0.5mM EDTA was used for routine dissociation to maintain colony growth. To promote cell survival during passaging, cells were passaged with the p160-Rho-associated coiled coil kinase (ROCK) inhibitor Y-27632 (10 mM: Selleckchem). hiPSCs were frozen in 90% fetal bovine serum (HyClone) and 10% DMSO (Sigma).

i^3Neurons are derived from our previously established human inducible pluripotent stem cell (hiPSC) line [139]. Stable integration of a doxycycline inducible neurogenin2 (NGN2) cassette enables rapid differentiation to glutamatergic cortical neurons (i3Neurons) within 7 days [137, 138]. hiPSCs were maintained on Matrigel (Corning Incorporated #354277) coated 10 cm tissue culture dishes and cultured in Essential 8 media (Gibco #A1517001) as previously described [139]. Once the cells were differentiated into neurons, they were maintained on poly-L-ornithine (PLO) coated plates.

2.4.2 hiPSC Lines

Major iPSC Lines:

- WTC11-NGN2 (Ward et al.)
- GRN-KO, 7/10 (WTC11-NGN2) (Ward et al.)
- NPC1-KO (WTC11-NGN2) (Prabhu and Ward et al.)
- WTC11-NGN2-dCas9 (Ward et al.)

2.4.3 Neuron Differentiation for High-Content Applications

The following steps will assume the experimenter has a 70-80% confluent 15cm dish of iPSCs with a stably integrated inducible NGN2 transgene. It is critical that the health of iPSCs be optimal prior to differentiation; poorly-maintained, spontaneously differentiated, or overly-confluent iPSC cultures tend to differentiate poorly or variably. Apart from observation under the microscope, counting, and centrifugation, all steps should be carried out in a sterile biological safety cabinet.

Induction

Day 0:

- Coat a new 15cm tissue culture dish [or T-150 flask] to be used for differentiation with 8-10mL of Matrigel solution, tilting to ensure coverage of entire surface area.
- Place in 37°C incubator for 30 min-1hr prior to beginning dissociation and re-plating (NOTE: 15cm tissue culture dishes will be used as the growth and differentiation vessels in this protocol, but the same volumes and cell numbers are applicable to T-150 flasks, as these vessels have almost identical growth surface areas.
- Amounts can also be scaled appropriately to vessels of different sizes—e.g. 10cm dishes). Prepare enough Induction Media (IM) with doxycycline (2ug/mL, or 1:1000 of stock) and ROCK inhibitor (use at 10uM, or 1:1000 of 10mM Selleckchem stock) for resuspension, plating, and media changes for 2-3 days.
- Observe iPSCs under phase contrast microscope to assess confluence and presence of cell debris. Dish should be dissociated at around 70-80% confluence (i.e. ensure 25-30 million cells per 15cm dish for replating).
- To prepare cells for Accutase dissociation, wash plate with PBS until debris is no longer visible.

- Split cells using 7-8mL of Accutase for singularizing and resuspend in 20-25 mL Induction Media (+ROCK inhibitor +doxycycline) by pipetting up and down within the 50mL conical vial
- (This is a KEY STEP: Forceful, robust pipetting is needed to ensure proper singularizing of the iPSCs, as this prevents clumping in the final neuronal culture. However, if you are too forceful—you can cause cell damage/death).
- Pellet cells (KEY STEP), When using PBS as the primary fluid for resuspension, you MUST also include 5-6mL of a relevant media*** for proper pelleting.
- NOTE: if you want to replate iPSCs at this stage do not resuspend in Induction media, but rather E8 or E8+RI for the first spin, and subsequent resuspension in Induction media after the second spin.
- Resuspend and count cells, aspirate Matrigel solution from NEW 15cm dish, plate iPSC-Induction media suspension on NEW 15cm dish at 20-25 million cells per dish or scale up/down as needed.
- Observe cells under microscope to ensure even distribution and high proportion of live cells (identified by light halo around each cell) vs dead cells and debris (darker and smaller than live cells), and place in 37°C incubator and gently slide dish side-to-side and front-to-back to distribute cells.

Days 1-2:

- On the following day, the first check should be the color and clarity of Induction media on the cells.
- Check cells under microscope.
- NORMAL: Induction media is Orange or Yellow, but clear.
- ABNORMAL: Induction media is Orange or Yellow, but cloudy (indication of possible cell death or contamination).
- Nascent neuritic extensions should begin to be evident after about 24 hours of doxycycline exposure.

- Aspirate old media and Replace with fresh Induction media; wash step is optional but not necessary (we usually do not wash with PBS for Induction media changes).

Day 3:

- Check cells under microscope.
- Neurites should be obvious by this time. If neurites are not present or cells appear misshapen or otherwise unhealthy, cells should be discarded and the protocol re-attempted with a new batch of d0 iPSCs.
- Make up new IM media with fresh doxycycline and ROCK inhibitor.
- Once cells are confirmed to be healthy, cells should be dissociated with accutase and either frozen or re-plated onto final dishes for neuronal maturation and experimental manipulation.

High Content Plate Production

Coating Dishes:

- Prepare stock of PLO, and add approximately half culture volume of 1x solution to the tissue culture dishes to be used for plating day 3 partially-differentiated hiPSC-neurons.
- Gently tilt the plate to ensure full coverage. (Recommended for 96—100uL, Recommended for 384—20uL minimum). For best results, incubate dishes overnight in a 37°C incubator.
- Aspirate coating solution, then wash dishes with sterile water.
- Repeat 2x for 3 total washes (Recommended wash volume for 384—20uL minimum).
- Aspirate water and let dishes dry completely in a BSC (typically requires 30 min-1hr).
- To accelerate the drying process, stand the dishes on their sides and lean them against the back of the sterile hood or tap/shake remaining liquid onto a clean paper towel in the sterile hood.

- Lids may also be left askew to allow better airflow.
- When producing large batches of 96 or 384 well plates, optimizing the robotic washer settings to aspirate as much fluid as possible will help accelerate drying as well.
- The PE CCUs (96 or 384) have deeper wells than other plates in their respective classes, this puts the optical surface closer to the imager, but may prevent robotic washers from completely aspirating a well.
- Finding a balance between the remaining volume and drying time is a key step and necessary when planning your experiments.
- Coated and dried dishes should be used immediately or wrapped in aluminum foil and stored at 4°C for up to 1 week, although fresh use is greatly preferred.
- Optional: Faster neurite outgrowth and increased neuronal survival during replating may be achieved by additionally coating plates with laminin prior to plating.
- Dilute laminin to 15µg/mL in PBS, and add ½ culture volume of this solution to the polymer-coated dishes. Incubate at 37°C for 1 hour before aspirating and plating neurons.
- NOTE: Having an automated or partially automated PLO coating and washing procedure in place will greatly assist in your ability to scale experiments and increase throughput, especially for high-content applications where many plates will be needed.

2.5 Live Cell Imaging

Live cell imaging was carried out in phenol red free neuronal culture medium, where possible. Most screens were done in normal phenol-red-containing Brainphys base medium plus supplements.

High content imaging was performed using a PerkinElmer HCSS Opera Phenix, with 20X water, 40X water, and 63X water objectives; images were processed using Harmony Analysis software (PerkinElmer).

2.5.1 Live cell DQ-BSA Assay

Live cell DQ-BSA measurements were made in order to assess the formation of autolysosomes in WT and PGRN-KO i3Neurons, relying on the cleavage of self-quenched DQ Red BSA substrate within acidic cellular compartments. WT and PGRN-KO i3Neurons were plated on 384-well dishes with regular media changes occurring every other day until day 9, including pre-treatment of a small subset of wells with 30µM Chloroquine (CQ) 8-12hrs. before DQ-BSA loading to induce lysosomal alkalinization as a control. On day 10, neurons were loaded with 45µg/mL DQ-BSA Red (Invitrogen, #D12051) as a media change and incubated for 5 hours to allow for substrate endocytosis. Live-cell spinning disk confocal microscopy was performed via PerkinElmer's Opera Phenix HCS System; control and sample wells were imaged at 40X and counterstaining with NucBlue Live ReadyProbes Reagent (Invitrogen, #R37605) to count and segment nuclei. All analysis was performed via PerkinElmer's Harmony HCA Software.

2.5.2 Live Cell Ratiometric pH Assay

Live cell ratiometric lysosomal pH measurements were made using a modified method from Saric et al. [141], further optimized for high content imaging and analysis. WT and PGRN-KO i3Neurons were plated on 96-well dishes with regular media changes occurring every other day until day 8-9. On day 9-10, neurons were loaded with 50 µg/mL ph-sensitive Oregon Green-488 dextran (Invitrogen, #D7171), and 50 µg/mL ph-insensitive/loading control Alexa-555 red dextran (Invitrogen, #D34679) for 4 hours and chased overnight with neuronal media after 3-4 washes with PBS the day before imaging. Dextrans are not broken down by human lysosomes, so will therefore accumulate in the terminal endolysosomes of the cell, allowing for precise measurements of these compartments.

Physiological buffers of known pH (ph 4-pH 8) containing 10µg/mL nigericin were then placed on some of the wells of WT neurons in order to generate a calibration curve from the images of these wells. Live-cell spinning disk confocal microscopy was performed via PerkinElmer's Opera Phenix HCS System; calibration and

sample wells were imaged at 63X, counterstaining with NucBlue Live ReadyProbes Reagent (Invitrogen, #R37605) to count and segment nuclei. As pH increases, the intensity of the Oregon Green-488 dextran in calibration well lysosomes also increases due to the action of nigericin to equilibrate the pH of all cellular compartments. Bafilomycin A1 (Sigma, 19-148) was also used as a postive experimental control. When used in tandem with pH-insensitive Alexa-555 red dextran, a ratiometric measurement can be made from captured images of sample lysosomes (488/555), with subsequent back-calculation of the pH of those compartments based on the corresponding calibration curve. All analysis was performed via PerkinElmer's Harmony HCA Software.

2.5.3 Live cell Magic Red CTSB Assay

Live cell Magic Red measurements were made in order to assess active proteolysis in i3Neurons, relying on the CTSB substrate reaching acidic cellular compartments. i3Neurons were plated on 384-well dishes with regular media changes occurring every other day until day 9, including pre-treatment of a small subset of wells with 30µM Chloroquine (CQ) 8-12hrs. before Magic Red loading to induce lysosomal alkalinization as a control. On day 10, neurons were loaded with Magic Red CTSB (Immunochemistry Technologies, 938) as a media change and incubated for 1 hour to allow for substrate entry, then washed well with normal media for imaging. Live-cell spinning disk confocal microscopy was performed via PerkinElmer's Opera Phenix HCS System; control and sample wells were imaged at 40X and counterstaining with NucBlue Live ReadyProbes Reagent (Invitrogen, #R37605) to count and segment nuclei. All analysis was performed via PerkinElmer's Harmony HCA Software.

2.5.4 Neuronal Survival and Neurite Outgrowth Assays

GFP-only neurons were split and pre-combined with GFP-mApple neurons positive for an sgRNA (cytosolic BFP) before replating procedures on re-plating day, then immediately imaged (time 0h) and every day thereafter until day 8 (time 192h). 5k or 15k neurons per well plating density and 5%, 15%, or 25% transduced

subpopulation. Subsequent cell count analysis and neurite tracing analysis was performed via GE InCell HCA software.

2.5.5 Transferrin Assays

3 Day post-dox Neuron Transferrin Recycling: Thaw 3 vials of day 3 post-dox iPSC derived neurons (approx 12-15m cells) per genotype; experiment was done on G3 (WT) and 7/10 (PGRN-KO) neurons. Cells were pooled and resuspended in 2.6 mL of starve medium (brainphys, no supplements) for 30mins. 500uL of cells were then put into ice tube [unlabeled sample]. Tubes were pelleted 300g for 3 mins at 4C and resuspended in 300ul ice PBS ready for FACS. Remaining cells were pelleted 300g 5 mins RT, resuspended with 2.1 mL starve supplemented with Transferrin 488 (1:200). Samples were offset by 30 seconds. 17 min incubation (12 at 37 in metal bath and 5 at RT in centrifuge), cells were resuspended in complete Brain Phys (2.1 mL), 500uL/sample immediately added to tube on ice [0 min chase] with further samples taken at 5, 10 and 20 min. Filtered in FACS tubes; Taken to FACS machine on ice and minimum of 50k cells counted.

5 Day post-dox Neuron Transferrin Recycling: 2 million neurons per sample (3 day) were plated into a matrigel coated 35mm dish (5 x G3 WT and 5 x 7/10 PGRN-KO). 3 days later media was replaced with 'starvation medium' (brainphys, no supplements) for 30 mins. Unlabeled put on ice. Tfn-488 was added to cells (1:200: 40 ug/ml). Incubated 15 mins. Replaced with chase medium, and put on ice 1 by 1. Washed in ice cold PBS. Time points: 0, 5, 10, 20 post-chase. Lifted with accutase on ice 7 mins. Cells were pelleted, resuspended in ice cold PBS. Taken to FACS machine on ice and minimum of 50k cells counted.

3 Day post-dox Neuron Transferrin Uptake: 2 million 3-day post-dox iPSC derived neurons per sample were thawed and resuspended (total 16 million cells per genotype). Cells were incubated in 4.2 mL of starve medium. After 30 mins, 500ul was added to 500ul ice cold PBS (unlabeled control). Remaining cells were pelleted (0.2g for 5 mins) and resuspended in 1.85mL starve medium supplemented with 40ug/ml Tf-488 (to retain volumetric ratio with unlabeled sample). Initial

sample was taken immediately (250ul) and added to 750ul ice cold PBS to stop uptake. Cells were incubated in a water bath for remaining time with 250ul being taken every 2.5 mins and added to ice cold PBS as above. WT and PGRN-KO cells were staggered by 30 seconds to allow for precise timepoints. After samples were added to PBS they were pelleted and resuspended in 300ul ice cold PBS and filtered for FACS analysis (on ice).

2.6 sgRNA Validation

To extract RNA from multi-well sample plates, we used the Direct-zolTM-96 RNA (Zymo research, cat. no. R2054) protocol. This allows the efficient extraction of RNA from samples arranged in a 96- well plate. First, the cells are lysed in TRIzol, added into columns binding the RNA, and washed with various buffers. Finally, the RNA was eluted using DNase/RNase-free water.

The RNA was then quantified using the RiboGreen RNA Assay Kit (ThermoFisher, cat. no R11490) and then the total concentration of RNA was normalized to a concentration of 0.5ng/uL with DNase/RNase-free water.

2.7 Arrayed Screening

Multi-well plates of i^{3}Neurons generated via the method described earlier for high-content applications are replated and transduced with sgRNA libraries using the Echo Acoustic Fluid Handling method explained in Chapter 3 on either day 2 or day 3. From there, virus-containing media is changed the following day (16-24hrs after transduction) using the CyBio Felix Fluid Handling robot. All further media changes and assay reagent incubations are handled in the same way. Plates are then run through multiple end-point assays, either live cell, fixed, or RNA extraction.

2.8 Quantification and Statistical Analyses

Statistical analysis was carried out on GraphPad Prism where possible. Statistical tests used and the significance values found are discussed in the figure legends.

Single cell and well level outliers were screened out in the analysis pipeline via robust Inter-quartile range (IQR) outlier detection. Data are expressed as mean ± SD unless otherwise stated. For secondary analysis maps, the median absolute deviation (MAD) cutoffs were: MAD > 1 for weak hits, MAD > 2 for strong hits. The analysis for all primary validation and secondary mechanistic validation follow up assays were performed in R, using multiple t-tests with corrections:

- ns: $P > 0.05$
- *: $P \leq 0.05$
- **: $P \leq 0.01$
- ***: $P \leq 0.001$
- ****: $P \leq 0.0001$

3

CRISPRi sgRNA Library Generation and Validation

Contents

3.1 Introduction and Aims 40
3.1.1 Preliminary FTD/ALS Sublibrary 40
3.2 CRISPRi Tool Optimization 42
3.2.1 Far-Red Protein Panel 42
3.2.2 Far-Red Optimization 46
3.2.3 sgRNA Drug Selection 49
3.3 CRISPRi sgRNA Library Generation and High-Throughput Plasmid Cloning 49
3.3.1 sgRNA Library Design and Sequence Generation 49
3.3.2 Nuclear Blue and Cytosolic Far-Red CRISPRi Plasmid Library Construction 51
3.3.3 sgRNA Delivery Systems and Functional Titering 54
3.3.4 Nuclear Blue and Cytosolic Far-Red sgRNA Library Functional Titering 56
3.3.5 Dual Transduction of sgRNAs 58
3.4 Targeted, Multiplexed RNA Sequencing for sgRNA Validation 60
3.4.1 Validation of High-throughput RNA Extraction 60
3.4.2 Preliminary Targeted RNA Sequencing & sgRNA Validation 61
3.4.3 High-throughput Targeted RNA Sequencing & sgRNA Validation 69
3.4.4 Transcriptomic Genetic Interactions 74
3.5 Discussion 75

3.1 Introduction and Aims

Functional genomics platforms require robust, precise molecular tools to determine a particular gene's function and/or involvement in specific molecular pathways. Achieving these endpoints requires the perturbation of a gene, set of genes, or genome-wide target libraries through the means of a molecular tool that can induce predictable genomic changes in a target biological system or model, as well as a delivery system adequate for repeated, reproducible experimentation. A key step in building such a platform is library generation, usually in the form of lentiviral particles ready for transduction into the target cell type.

The type and quality of these molecular tools (e.g. sgRNA/dCas9, shRNA, siRNA) and preparation of a screening library (e.g. cDNA, lentivirus) will directly influence any phenotypic results downstream, particularly the sensitivity to which phenotypes can be analyzed. Additionally, arrayed screening requires the separation of library components before screening takes place, unlike in pooled screening, where library components are initially combined, and targets are differentiated downstream by genetic barcoding or other means [142].

Aims of this chapter

- Demonstrate the optimization, testing, and subcloning of relevant Nuclear Blue and Cytosolic Far-Red sgRNA libraries for arrayed screening
- Demonstrate the lentiviral packaging and functional titering of these libraries
- Demonstrate the functional validation of these libraries

3.1.1 Preliminary FTD/ALS Sublibrary

Near the start of my DPhil studies, the Ward Lab initiated the creation and validation of an FTD/ALS-focused CRISPRi library consisting of several key disease-causative genes, risk factors, and known interactors seen in Figure 3.1A.

This library was cloned into the lentiviral backbone featuring a selection cassette of EF1a-Puro-T2A-mTagBFP2 (Figure 3.2A), which does not target the translated fluorescent protein to a particular subcellular compartment. Due to the lack of a targeting sequence, this tool translates the cassette and labels the cytoplasm of transduced cells brightly blue, as shown in the schematic in Figure 3.2B.

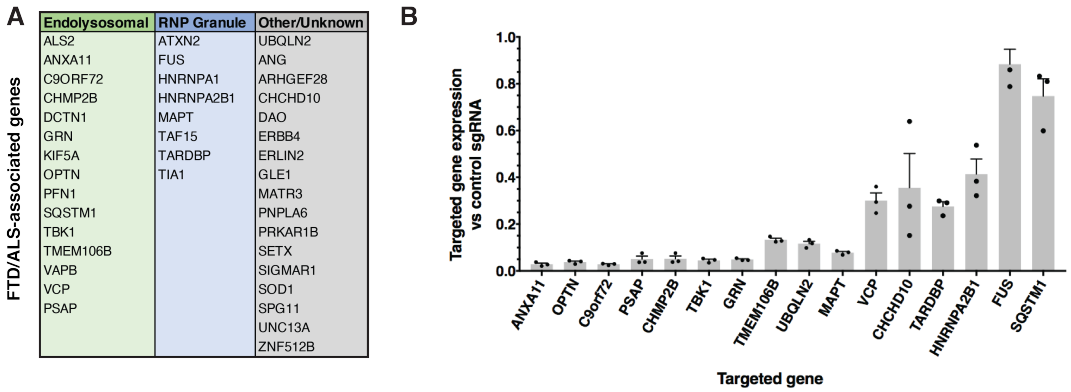


Figure 3.1: Preliminary FTD/ALS Sublibrary. A.) Genes that when mutated cause FTD/ALS vs their putative general functions. B.) Validation of CRISPRi sgRNAs targeting 16 FTD/ALS genes via RT-qPCR. *Table in panel A courtesy of M.E. Ward. RT-qPCR results of selected sgRNA targets in panel B courtesy of M. Gachechiladze*

A subset of the proposed targets in Figure 3.1A were chosen as targets related to lysosomal biology for downstream experimentation and screening. Subsequent validation via RT-qPCR was undertaken by M. Gachechiladze, as shown in Figure 3.1B. This preliminary library was effective at the suppression of most gene targets and served as an initial validation of several key FTD/ALS sgRNAs. However, the cytosolic blue backbone used to clone this library has drawbacks when scaling up to an arrayed screen. For example, most high-content assays require the segmentation of nuclei and cell cytoplasm as a first step to more intricate analysis, such as spot detection and tracking. While the cytosolic blue backbone would have very accurate cytoplasm detection for neurite and cell body segmentation, the system would have sub-optimal nuclear detection and require alternative nuclear stains such as DRAC5 opposed to blue/DAPI, which is a preferred method across live cell imaging assays.

3.2 CRISPRi Tool Optimization

In order to utilize CRISPRi tools more effectively in the downstream high-content microscopy and analysis my project required, further optimization and tool generation was needed. This optimization came in two distinct steps: 1) the implementation of a new CRISPRi tool that targets the selection marker to the nucleus (Figure 3.2C) and 2) the design, creation, and optimization of a new CRISPRi tool for cytosolic labeling with a far-red fluorescent protein. The nuclear blue plasmid was developed by a collaborator lab and subsequently gifted to the Ward Lab (pMK1334)[140], providing a new CRISPRi tool that was equally effective at target transcript suppression and cell selection, but more ideal for most microscopy endpoints, as the double nuclear localization sequence (2xNLS) provides a clear nuclear label without leakage into the cytoplasm, as shown in the schematic in Figure 3.2D.

Additionally, functional genomics screening requiring the ablation of more than one gene requires a second, complementary sgRNA delivery mechanism that will ensure robust confirmation of the second sgRNA's lenti-transduction. Due to the experience I was gaining in high-content imaging, I proposed a dual sgRNA delivery system that would harness the strength of existing tools and optimize a second tool for high-content applications. As the nuclear BFP system solved the nuclear segmentation issue needed for downstream analysis, the proposed cytosolic far-red system would provide an alternative selection cassette, including the new fluorescent marker and an alternative drug resistance protein in order to allow for selection of the second sgRNA. When combined, these two tools would provide a powerfully tuned high-content CRISPRi system that would achieve dual-gene ablation, rapid nuclear counts and cytoplasm tracing without the need for counter-staining, as well as open RFP and GFP channels for various assays to be performed.

3.2.1 Far-Red Protein Panel

The initial step I took to generate the new far-red cytosolic system was to identify an ideal candidate fluorescent protein that met the following key criteria: 1) could be packaged and expressed via lentivirus, 2) would express in the correct subcellular

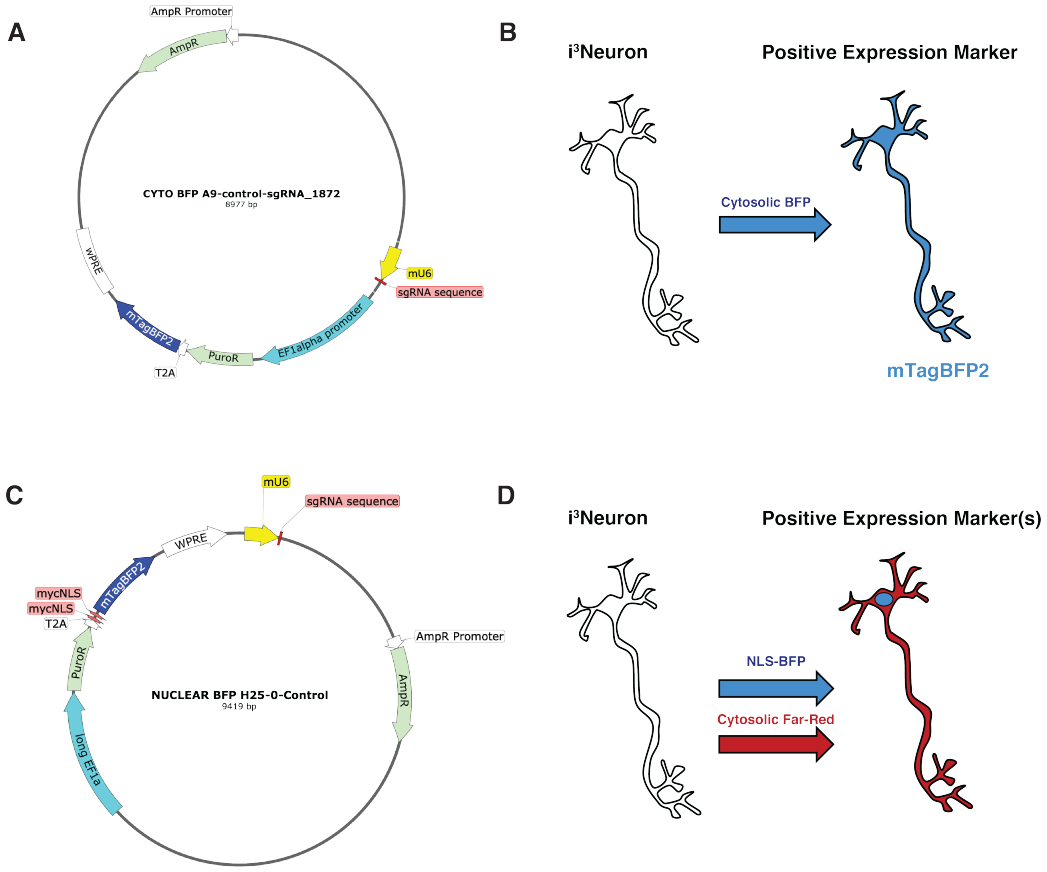


Figure 3.2: Representative plasmid maps and schematics of cytosolic and nuclear blue CRISPRi backbones. A.) Plasmid map of the cytosolic BFP CRISPRi backbone. Note the selection cassette Puro-T2A-mTagBFP2 driven by the long EF1a promoter. B.) Representative schematic showing BFP in the cytoplasm of lenti-transduced i^{3}Neurons. C.) Plasmid map of the nuclear BFP CRISPRi backbone. Note the selection cassette Puro-T2A-2xNLS-mTagBFP2 driven by the long EF1a promoter. D.) Representative schematic showing BFP in the nucleus of lenti-transduced i^{3}Neurons. Also shown is the concept of a cytosolic far-red marker for dual sgRNA delivery and confirmation.

compartment, and 3) would fluoresce brightly enough to serve as a cytoplasm marker and potentially trace neurites. The development of new far-red/near-IR fluorescent proteins is currently in high demand for multiple applications, including *in-vivo* models and *in-vitro* cellular cultures. Candidate proteins were chosen from a range of characteristics such as oligomeric state (e.g. monomeric, dimer, tandem-dimer), reliance on cofactors, predicted brightness, and potential ease of molecular cloning. The candidates were TDsmURF (tandem-dimer), iBlueberry (monomeric), iRFP670

(dimer), and iRFP720 (dimer) [143–145]. Ideally, a monomeric variant could be used, as they are very efficient for cloning and lentiviral packaging purposes. However, the entire family of far-red/near-IR fluorescent proteins, which are based on phytochrome and phycobiliproteins [143–145], have a key flaw in that they require the biliverdin [146] as a cofactor in order to fluoresce. Biliverdin (BV), a byproduct of the breakdown of heme, provides the expressed protein with the necessary chromophore [147]. The fluorescence of a far-red/near-IR protein is tied to bioavailablity of BV, and it is thought that various proteins within the family have different dependencies on BV. Ultimately, the BV content of your model must be adequate for the protein of interest to fluoresce and/or exogenous BV can be supplied. However, this may be a limiting factor in a high-content screen.

Subsequently, the four far-red/near-IR fluorescent proteins TDsmURF, iBlueberry, iRFP670, and iRFP720 were all cloned and transduced into our hiPSC-neurons in order to test for cytosolic expression and brightness. Downstream phenotypic assays will require a two-vector sgRNA delivery approach, meaning two channels will be reserved for nuclear and cell body/neurite segmentation. Utilizing the far-red, or 647nm/670nm (Ex/Em), channel for at least one of the delivery vectors will allow for more flexibility for screening assays.

No expression of TDsmURF or iBlueberry was seen across any wells, while both iRFP670 and iRFP720 were both expressed well, as shown in Figure 3.3B. These results may indicate that the iRFP/dimer subfamily respond better to the BV available in our i^{3}Neuronswhen compared to the other species. However, this line of inquiry was outside of the purpose of this panel, so was not pursued further. iRFP670 and iRFP720 were both sufficient far-red/near-IR proteins to take forward into further optimization. Quantification of the efficiency of transduction can be seen in Figure 3.3A, where both iRFP670 and iRFP720 had near 75% positive neurons per well. Additionally, both had very similar mean intensities, with both nearly 2-fold above background from initial testing before optimization.

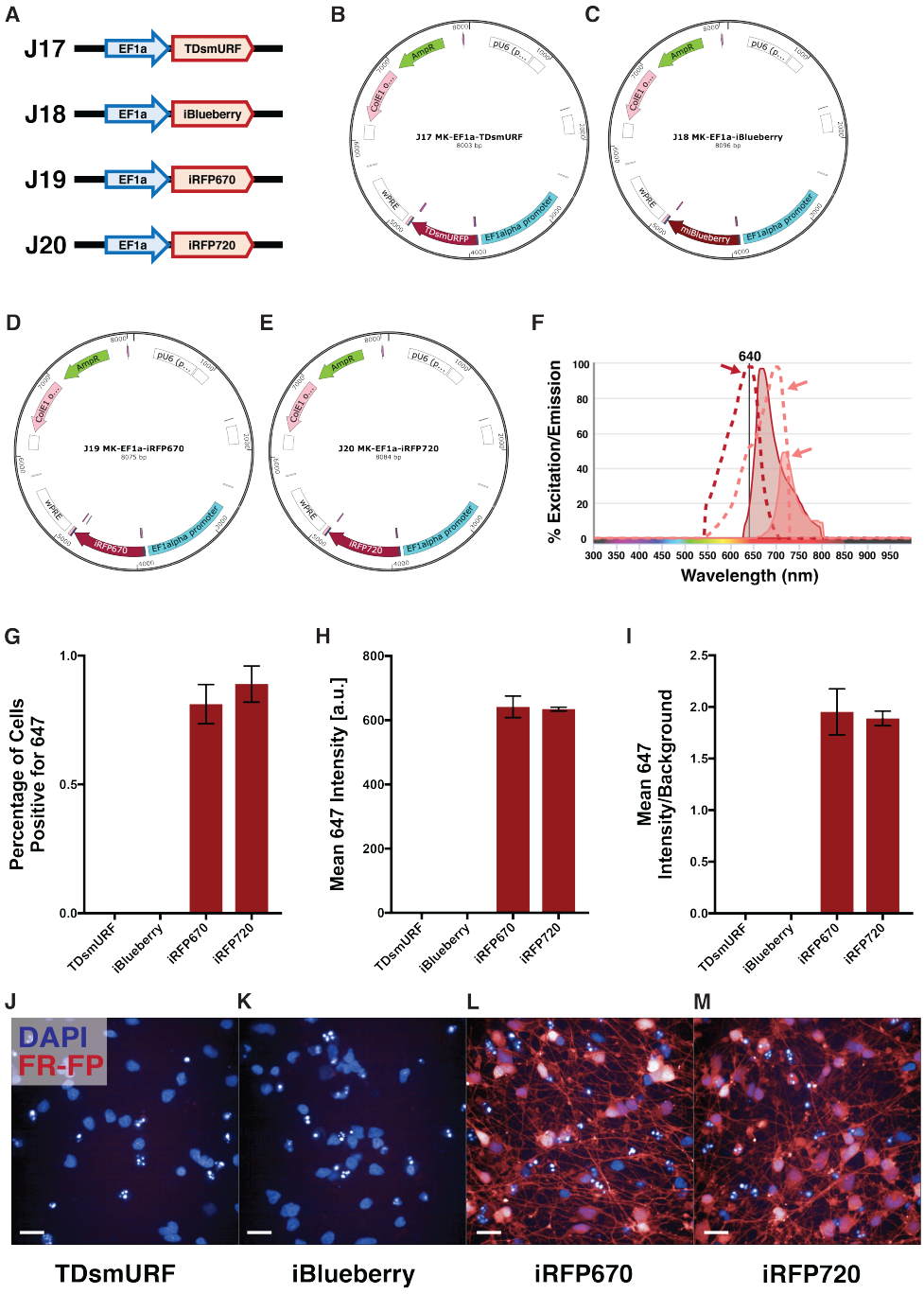


Figure 3.3: Far-Red fluorescent protein panel. Four far-red/near-IR fluorescent proteins were chosen for testing and optimization in hiPSC-neurons—TDsmURF, iBlueberry, iRFP670, and iRFP720. A.) Representative schematics of plasmid constructs J17, J18, J19, and J20 generated to test the various far-red fluorescent proteins in the panel. B.) Plasmid map of J17. C.) Plasmid map of J18. D.) Plasmid map of J19. E.) Plasmid map of J20. F.) Predicted excitation/emission spectra for iRFP670 (dark red) and iRFP720 (light red); predicted peak emission spectra are normalized to the Opera Phenix's 640nm laser. G.) Quantification of percentage of positive cells, H.) mean fluorescent intensity [a.u.], and I.) mean intensity/background, respectively, for each protein expressed cytosolically. J.) Representative images of each protein expressed in i^{3}Neurons, scale bar = 20µm (FR-FP = Far-Red Fluorescent Protein).

iRFP670 was chosen for further CRISPRi tool construction in order to achieve optimized imaging parameters. Figure 3.3F highlights the drop in (Ex/Em) efficiency with iRFP720 when compared to iRFP670 based upon the far-red laser available (640nm) in the PerkinElmer Opera Phenix, which will be used for downstream screening and analysis.

3.2.2 Far-Red Optimization

Each plasmid construct we utilize for guide delivery with CRISPRi has similar features, consisting of a U6 promoter for sgRNA production, along with a long-EF1a promoter that expresses our selection cassette. The selection cassette is a two-part system: drug selection-T2A-fluorescent protein, as shown in Figure 3.2A and Figure 3.2C.

After selecting the candidate far-red/near-IR fluorescent protein, I rapidly generated a new CRISPRi construct, J49, which included two key changes to previous iterations: 1) a new drug selection protein, blasticidin (BSD) and 2) iRFP670 without a targeting sequence. These new tools were generated as a T2A sequence with BSD in position 1 and iRFP670 in position 2, in order to take advantage of a key molecular tool known as 2A self-cleaving peptides [148, 149]. T2A peptides are widely used in molecular biology, as they allow for multiple proteins to be expressed from a single promoter [148, 149]. 2A peptides induce ribosomal skipping during translation, and were utilized on previous iterations of CRISPRi tools in order to separate the drug selection protein from the fluorescent protein marker. When initially designing the cytosolic far-red construct, I chose to stick with the same approach proven by our other CRISPRi tools, where the first protein is for drug selection , and the second is the fluorescent protein, iRFP670.

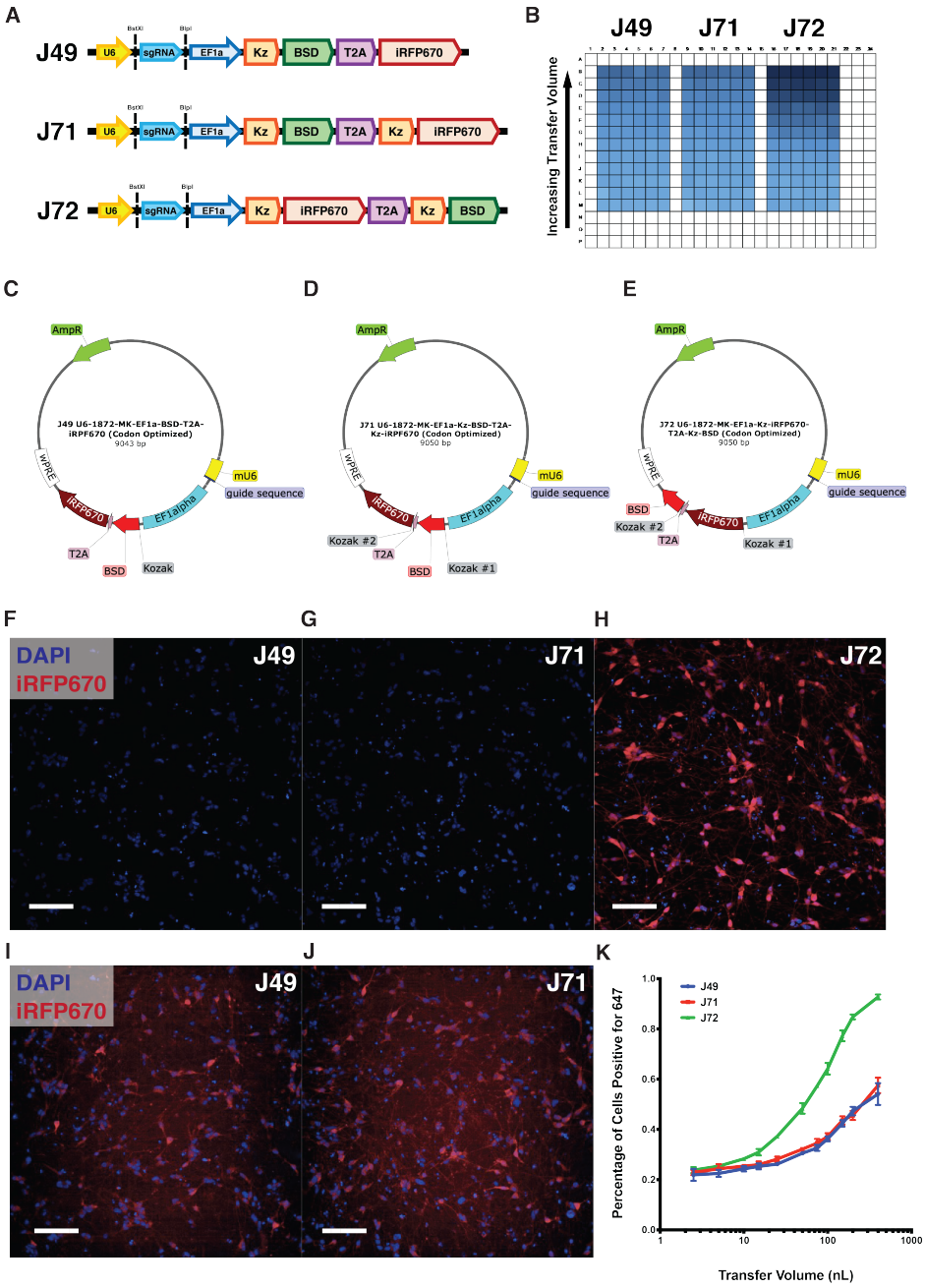


Figure 3.4: CRISPRi Cytosolic Far-Red plasmid construct optimization. A.) Representative schematics of plasmid constructs J49, J71, and J72 generated to optimize the expression of iRFP670 as a selection marker. B.) Heatmap displaying the percentage of detectable far-red-positive neurons when comparing the expression of iRFP670 across the variants. C.) Plasmid map of J49, note the single kozak and iRFP670 at position 2. D.) Plasmid map of J71, note the double kozak and iRFP670 at position 2. E.) Plasmid map of J72, note the double kozak and iRFP670 at position 1. F-H.) Representative images of the three constructs and their relative expression of the desired cytosolic far-red fluorescent protein, iRFP670; scale bar = 20µm. I-J.) Representative images of two constructs, J49 and J71, with the dynamic range scaled down to visualize the lower expression of iRFP670, note the high background; scale bar = 20µm. K.) Quantification of (B), showing the detectable transduction across J49, J71, and J72; n=6 wells for each transfer volume.

With only a limited number of efficient eukaryotic selection tools available, blasticidin was chosen primarily because it would integrate well with other CRISPRi tools currently in use. For example, any sgRNA made with the BSD-T2A-FarRed system would not interfere with either marker in the the puromycin/mTagBFP2 CRISPRi tools, nor other tools under development in the Ward Lab at the time, which deliver dCas9 plus a hygromycin B drug selection cassette.

While long-term complementarity with other molecular tools was my primary focus, there was a key failure with the J49 construct that required a fundamental change. Upon transduction of J49 into i^{3}Neurons, my preliminary results showed sub-optimal expression of iRFP670 and reduced the overall sensitivity of our far-red functional titering experiments, as shown in Figure 3.4. To address this issue, I designed additional constructs shown in Figure 3.4A that altered key features that would potentially increase iRFP670 expression. Upon further research into the issue, the position of your proteins of interest around the T2A peptide is very important, as expression is favored for the first protein, and expression of the second protein may be considerably lower [148, 149]. J49, our original construct, was based off of previous variants: EF1a-Kz-BSD-T2A-iRFP670. As shown in Figures 3.4F-H and Figures 3.4I-K, the performance of J49 was sub-optimal, with minimal expression of iRFP670 leading to images with higher than anticipated S/N ratio. In the design for J71 (3.4A), we added an additional kozak consensus sequence before the second protein, a technique that had shown some efficacy in *Bombyx mori* embryonic (BmE) cells[149].

However, this did not seem to increase overall iRFP670 expression, with nearly indistinguishable results from J49 shown in Figure 3.4F when compared to Figure 3.4G and Figure 3.4I when compared to Figure 3.4J. In the design for J72, the positions of the drug selection protein and iRFP670 were inverted in relationship to the T2A peptide. This placed iRFP670 as the first protein, with the drug selection protein coming after the T2A. The J72 variant worked quite well, as shown in 3.4H, with much greater iRFP670 expression, allowing for a much greater

sensitivity in our functional titering experiments and downstream segmentation. *J72 was later published in Carling et al. [74].*

3.2.3 sgRNA Drug Selection

The last phase of tool optimization was to confirm that both drug selection proteins were functioning properly. Control lentiviruses harboring non-targeting sgRNA sequences for both the nuclear blue and cytosolic far-red systems were transduced separately into i^{3}Neurons. Upon expression of their respective selection cassettes, neurons were treated with either puromycin (low = [1µg/mL], high = [15µg/mL]) or blasticidin (low = [3µg/mL], high = [30µg/mL]), as shown in Figure 3.5A and Figure 3.5B, respectively.

A preliminary co-transduction experiment was also performed, where both non-targeting lentiviruses were expressed in tandem, showing that both fluorescent markers could be simultaneously expressed to fully label i^{3}Neurons. These successfully co-transduced i^{3}Neurons survived rigorous drug selection with media combined with both puromycin and blasticidin, at the same concentrations as above, shown in Figure 3.5C. The population of neurons that survived were highly enriched for both fluorescent markers.

3.3 CRISPRi sgRNA Library Generation and High-Throughput Plasmid Cloning

3.3.1 sgRNA Library Design and Sequence Generation

For a given target gene, a 20bp DNA sequence is required to serve as the template sgRNA for dCas9-BFP-KRAB localization. This sequence must be upstream and unique to the canonical transcription start-site of the target gene locus. Horlbeck et al. generated a database of potential sgRNAs by training a machine learning classifier to derive unique DNA sequences that would provide the highest predicted chance for successful knockdown of every human gene [150]. I utilized this database to filter, design, and implement the first joint FTD/ALS and PD sgRNA library for use in arrayed CRISPRi high-content screening.

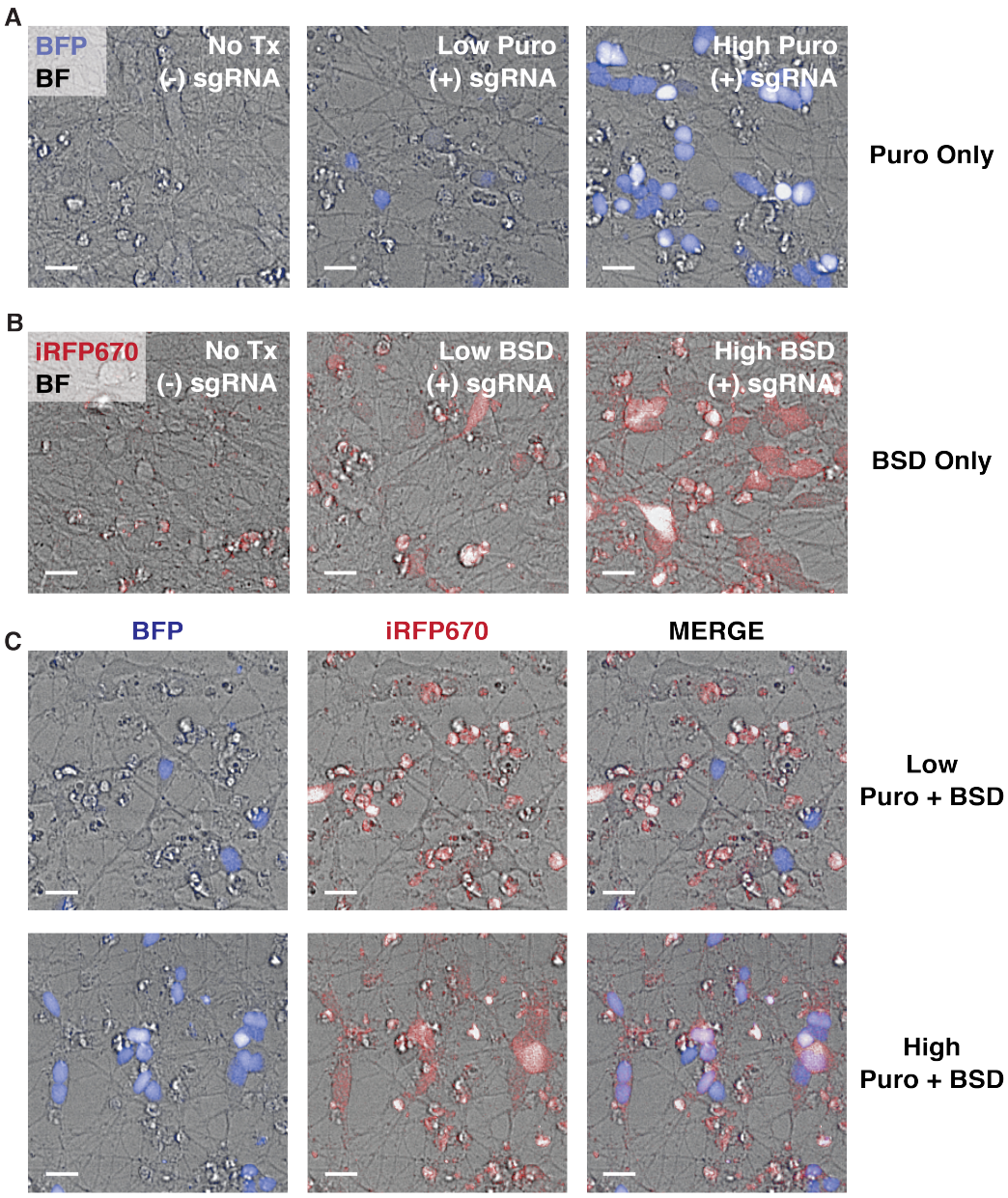


Figure 3.5: Drug Selection of Co-Transduced hiPSC-Neurons. Preliminary co-transduction experiment showing that both fluorescent markers and drug selection tools are functional. A.) i^{3}Neurons +/- transduction with non-targeting nuclear blue CRISPRi lentivirus plus no drug treatment, low puro treatment [1µg/mL], and high puro treatment [15µg/mL]. B.) i^{3}Neurons +/- transduction with non-targeting cytosolic far-red CRISPRi lentivirus plus no drug treatment, low BSD treatment [3µg/mL], and high BSD treatment [30µg/mL]. C.) Successfully co-transduced i^{3}Neurons with low puro [1µg/mL] + low BSD [3µg/mL] treatment, and high puro [15µg/mL] + high BSD [30µg/mL] treatment. Cells that survived were enriched for both fluorescent markers (MERGE).

This library exists in several forms, including at the *in silico* design level, the DNA oligo level, within multiple plasmid systems (e.g. nuclear blue and cytosolic far-red), and as transducible lentiviruses. The most fundamental form is at the DNA oligo stage, as the annealed oligos referenced in Table A.1 can rapidly be sub-cloned into any vector system.

Previously validated sgRNA sequences by the Ward Lab are listed in Table A.1 and were validated in iPSCs and i^3Neurons. These sgRNAs were re-validated throughout the work of this thesis. Those sgRNAs shown in the table with multiple sequences represent 1) newly chosen sgRNAs for validation and 2) those sgRNAs previously shown to achieve *at least* partial knockdown, and therefore more than one was brought forward into further validation and screening. Validating multiple sgRNAs minimizes the risk off-target effects for a given target.

Newly selected sgRNA sequences were chosen in pairs as the top two predicted guides from the database. As a naming convention, the two sgRNAs for a gene X were named X-1 and X-2, e.g. CTSD-1 and CTSD-2 for the gene CTSD. In addition to gene-targeting sgRNAs, there are nine "non-targeting" sgRNAs that have no specificity to any gene locus in the human genome.

3.3.2 Nuclear Blue and Cytosolic Far-Red CRISPRi Plasmid Library Construction

After selecting and annealing the oligo library, further construction of the plasmid libraries could begin. Figure 3.6 is an abridged summary of the ligation cloning process required to produce a new gene-targeting CRISPRi plasmids. The previously arrayed and annealed oligos form sticky ends for BstXI and BlpI and are diluted in parallel for all gene targets, shown in Figure 3.6A. From there, diluted oligos are arrayed on 96-well formats for ligation to a pre-linearized CRISPRi vector backbone. This was a key step in my thesis work, as high-throughput cloning allowed for the generation of multiple CRISPRi libraries in parallel and within manageable timescales. All ligation reactions were then transformed,

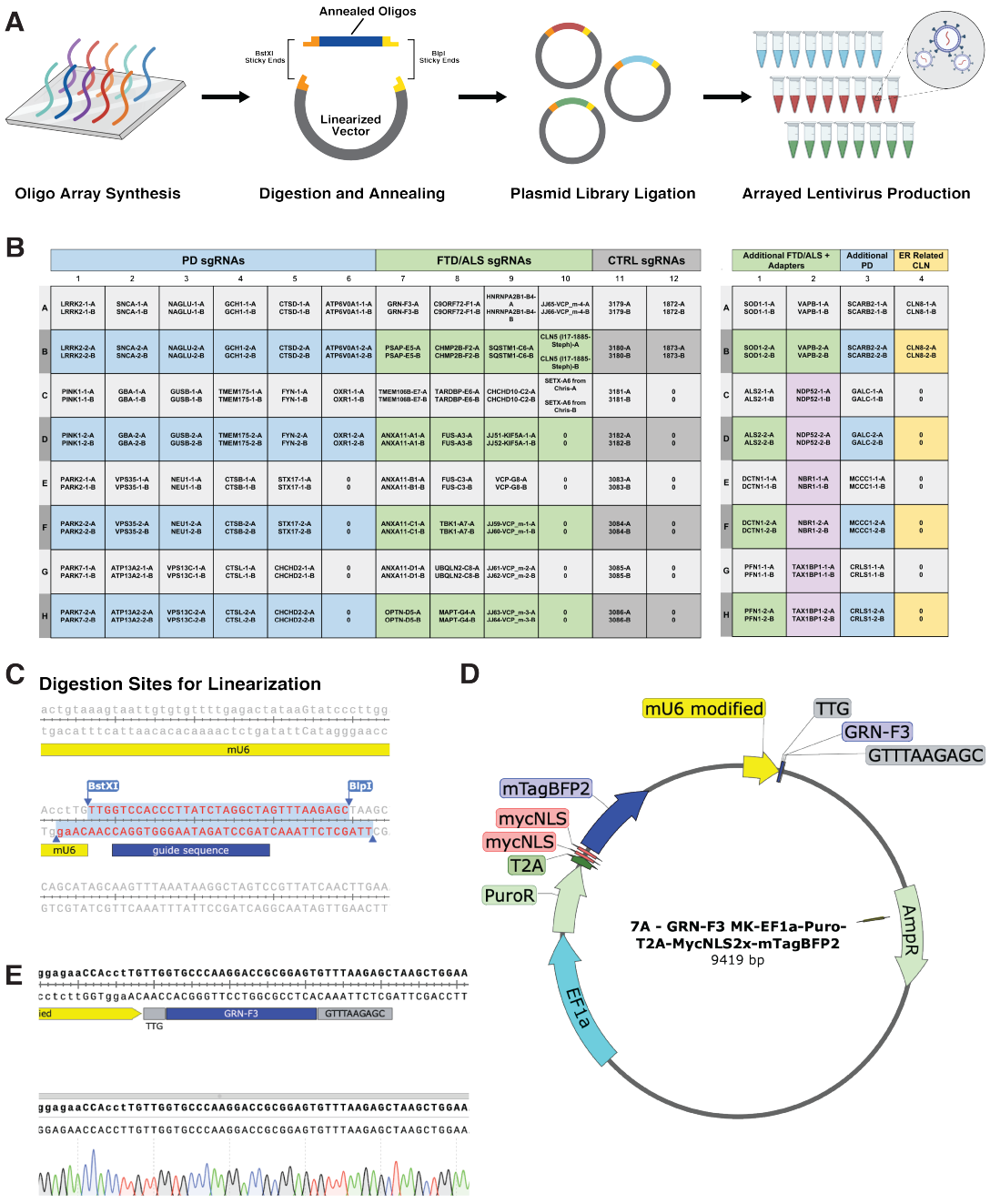


Figure 3.6: CRISPRi sgRNA Library Cloning. A.) Schematic overview detailing the major steps in the construction of sgRNA Libraries. B.) Annealed DNA Oligo Library Plate Map summarizing gene targets and plate location for high throughput cloning. C.) DNA sequence illustrating the "guide sequence region" that is digested from the base vector plasmids for ligation cloning of new annealed oligos downstream. D.) Plasmid map for construct 7A, the Nuclear Blue vector harboring the sgRNA sequence for GRN. E.) sgRNA sequence verification for GRN, as a representative example.

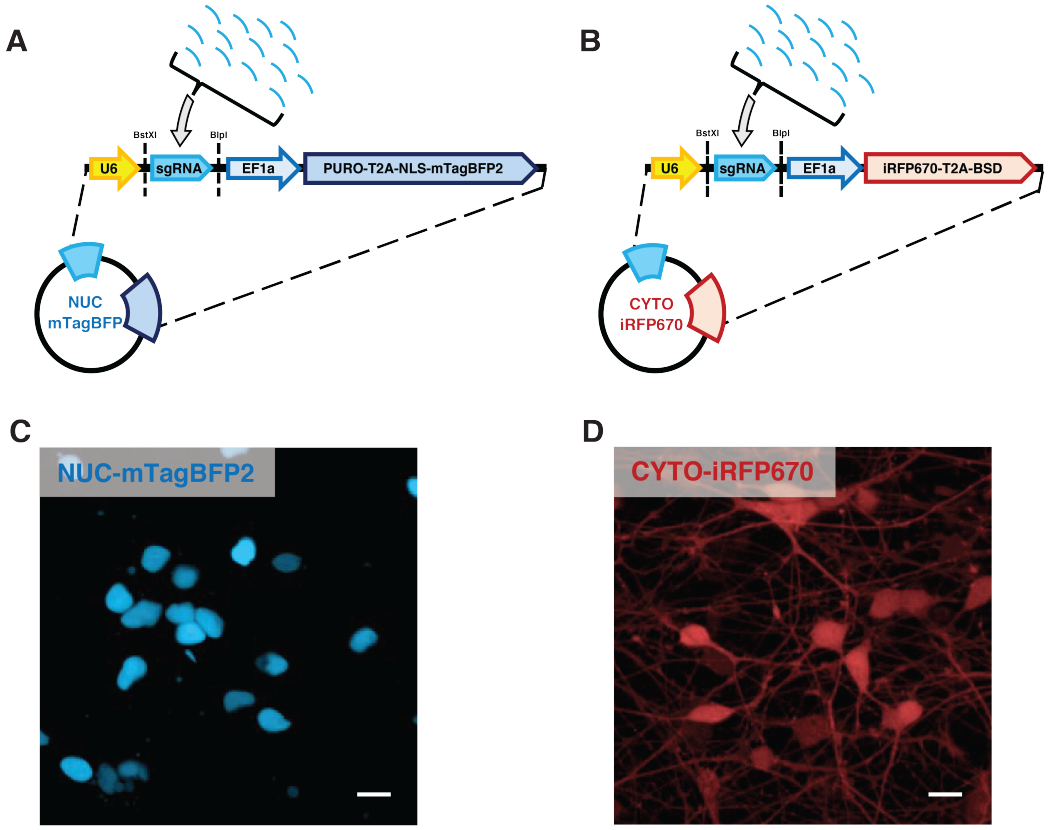


Figure 3.7: Construction of final Nuclear Blue and Cytosolic Far-Red CRISPRi tools. A.) The insertion of an sgRNA library (annealed oligos) into the nuclear blue plasmid CRISPRi construct. B.) The insertion of an sgRNA library (annealed oligos) into the Cytosolic far-red plasmid CRISPRi construct. C.) Example image of i^3Neurons expressing lenti-delivered selection cassette Puro-T2A-2xNLS-mTagBFP2; scale bar = 10µm. D.) Example image of i^3Neurons expressing lenti-delivered selection cassette EF1a-iRFP670-T2A-BSD; scale bar = 10µm.

followed by DNA extraction, and subsequent sgRNA sequence validation. Once final libraries existed in sequence-verified DNA formats, lentiviral production was performed. Final, "ready-for-transduction" preps of each verified sgRNA were arrayed across multiple sample tubes to prevent freeze-thaw losses, as described in Chapter 2.

Figure 3.7 displays an example schematic of sgRNA plasmid library generation, where the library of annealed oligos is inserted into both the Nuclear Blue and Cytosolic Far-Red systems. To assess if the final plasmid systems were functioning as designed, lentiviruses from each tool harboring the non-targeting sequence *1872*

were transduced into i^{3}Neurons. The resulting images in Figure 3.7C and Figure 3.7D show the expression of the selection cassettes *EF1a-Puro-T2A-2xNLS-mTagBFP2* and *EF1a-iRFP670-T2A-BSD* (J72), respectively. Strong, stable expression is seen across both systems and will provide the necessary sensitivity for downstream segmentation algorithms

3.3.3 sgRNA Delivery Systems and Functional Titering

Another major challenge to overcome was sufficient, reproducible delivery of our sgRNA lentiviral libraries to our target neurons. Initially, I was considering pre-arraying the viruses in high-content plates (e.g. 96-well or 384-well plates), which could then be transferred to i^{3}Neurons by hand or with a multi-tip fluid handler. However, this method would be burdensome and time-consuming without any fluid-handling options, especially for the level of arrayed screening I was aiming to achieve. Additionally, it would prevent downstream flexibility in experimental layout and require one plate of pre-arrayed lentivirus *per experiment* to avoid freeze-thaw cycle losses.

The solution was to repurpose a key piece of lab equipment normally used to transfer chemical compounds for screening. The Labcyte Echo (Figure 3.8A) is regularly used by the Wade-Martins lab for compound screening and has the ability to deliver fluid from a source plate to a destination plate using acoustic sound waves, as shown in Figure 3.8B. Despite most compounds being dissolved in DMSO, the device also has the ability to deliver fluid dissolved in water.

The titration seen in Figure 3.8C was our first attempt to deliver a commercially available lentivirus harboring GFP to a destination plate that had i^{3}Neurons in culture. As shown, the neurons in culture successfully expressed the GFP marker, and there is a clear indication of an increase in GFP intensity from the minimal transfer volume of 2.5nL up to 200nL total transfer volume per 384 well (Figure 3.8D-E).

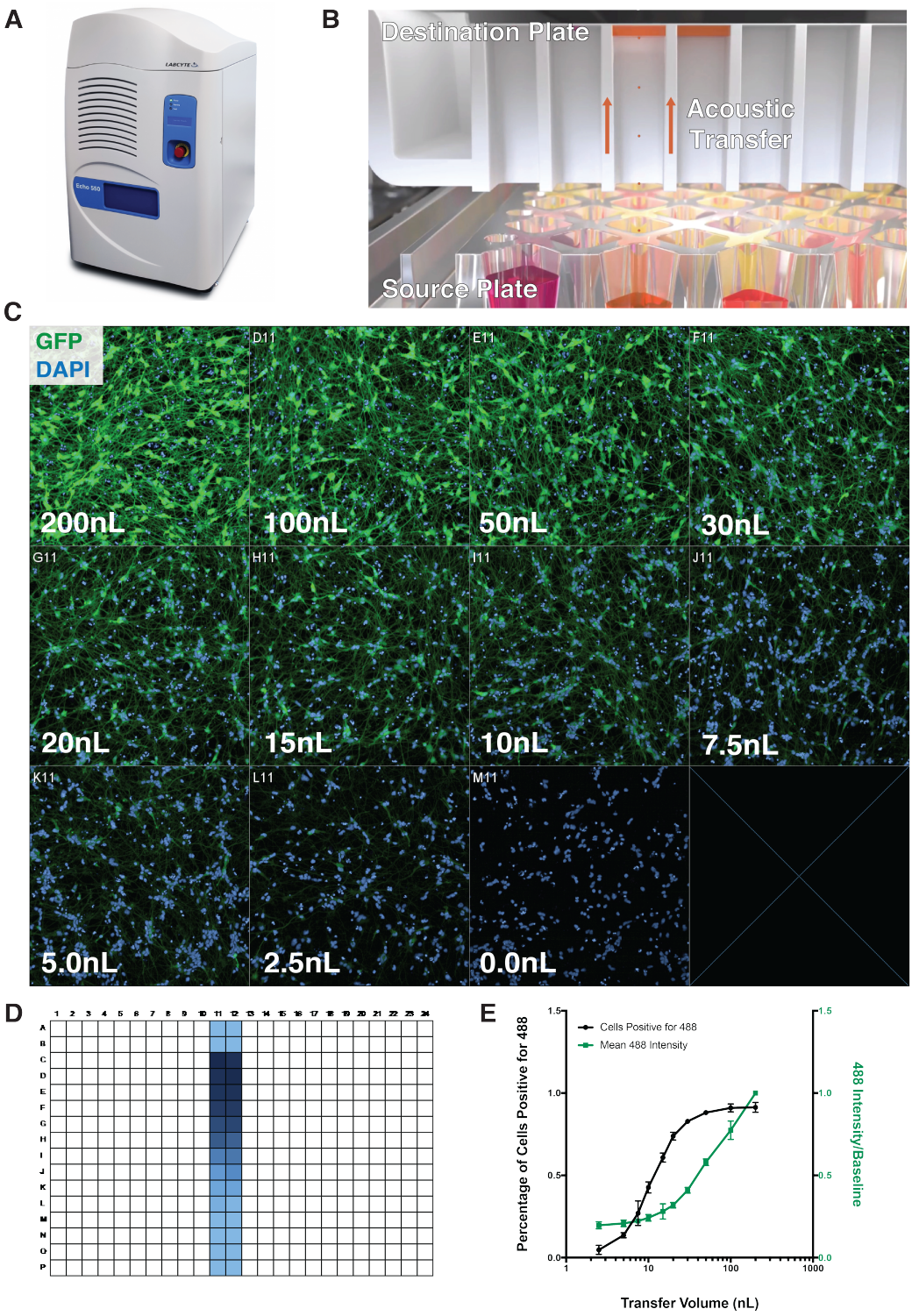


Figure 3.8: Acoustic Fluid Handling and Lentiviral Functional Titering. A.) Labcyte Echo 550 Acoustic Fluid Handler. B.) Animated representation of fluid transfer from source plate to destination plate, each droplet is 2.5nL of the source fluid; adapted from Labcyte. C.) Delivering a test lentivirus harboring GFP; a titration was performed from 0-200nL. D.) Representative heatmap of panel C. E.) Dual-axis quantification of C, including the percentage of positive cells (left axis) and the increase in intensity (right access) across the experiment.

3.3.4 Nuclear Blue and Cytosolic Far-Red sgRNA Library Functional Titering

With the sgRNA lentiviral libraries produced and delivery system optimized, I needed to analyze the potency of each virus to be used in high-content imaging. I chose to use a functional titering method for all lentiviruses from our sgRNA libraries. Overall, we can see reliable transduction across the various batches of lentivirus, with consistent titer levels shown (Section A.3 and Section A.5). Nearly all viruses titered range from 15-25% transduction efficiency at the lowest transfer volumes, up to 85-95% transduction efficiency at the highest transfer volumes, as shown in the selected examples in Figure 3.9 and Figure 3.10.

The results in Figure 3.9B and Figure 3.10B include titer curves for sgRNAs targeting GRN, PSAP, TMEM106B, TARDBP, CHMP2B, and H25 (GFP/non-targeting) depicting the percentage of positive cells at a given viral transfer volume. Heatmap results from the Nuclear Blue and Cytosolic Far-Red systems are shown in Figure Figure 3.9C and Figure 3.10C, respectively. Figure 3.9A shows representative images of i^{3}Neurons transduced with virus containing the Nuclear Blue sgRNA of interest, resulting in a BFP positive nucleus. Co-staining was performed with Nuc647 in order to compare the BFP-positive population of neurons with the total population. Figure 3.10A shows representative images of i^{3}Neurons transduced with virus containing the Cytoplasmic Far-Red sgRNA of interest, resulting in a far-red/near-IR positive cytoplasm. Co-staining was performed with DAPI in order to compare the iRFP670-positive population of neurons with the total population.

The production of the lentiviral libraries for both the Nuclear Blue and Cytosolic Far-Red systems was performed across several batches. To ensure the quality across batches, titration curves for all viruses were compared across batches and analyzed for optimal transfer volumes for downstream experimentation. All calculated transfer volumes to achieve 65%-85% sgRNA-positive populations for 10-12k cells per 384 well can be seen in Table A.2 for Nuclear Blue and Table A.3 for Cytosolic Far-Red Lentiviral Libraries. All individual titer curves can be seen in Appendix A (Section A.3 and Section A.5).

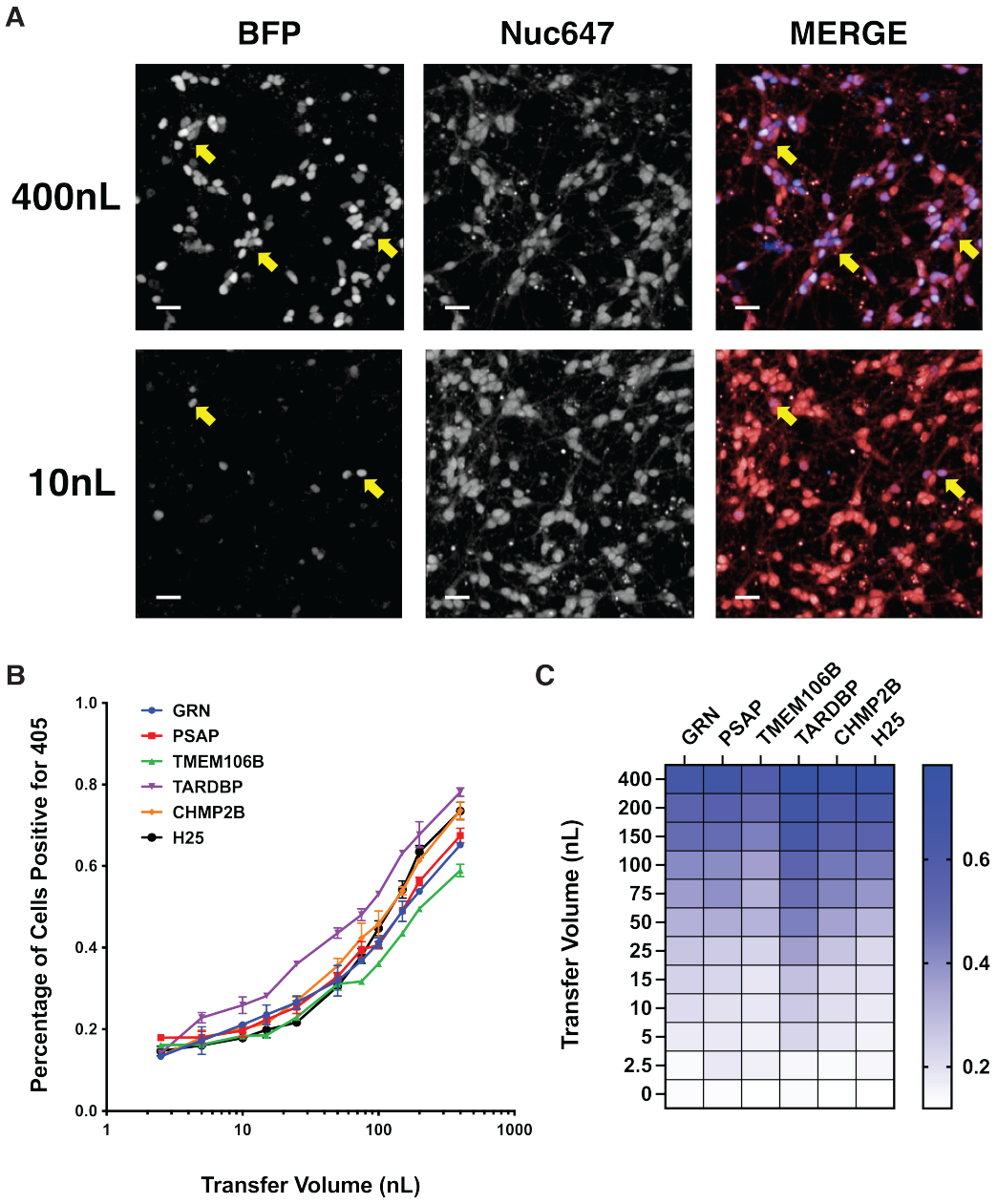


Figure 3.9: Nuclear Blue sgRNA Library Functional Titering. A.) Representative images from Nuclear Blue virus functional titering at 400nL and 10nL transfer volumes, with yellow arrows highlighting positive BFP expression; Nuc647 staining for all live nuclei; scale bar = 20µm. B.) Titer curves quantified from the selected examples, displaying the percentage of cells positive for BFP expression; n=3 wells. C.) Representative heatmap of the results from B.

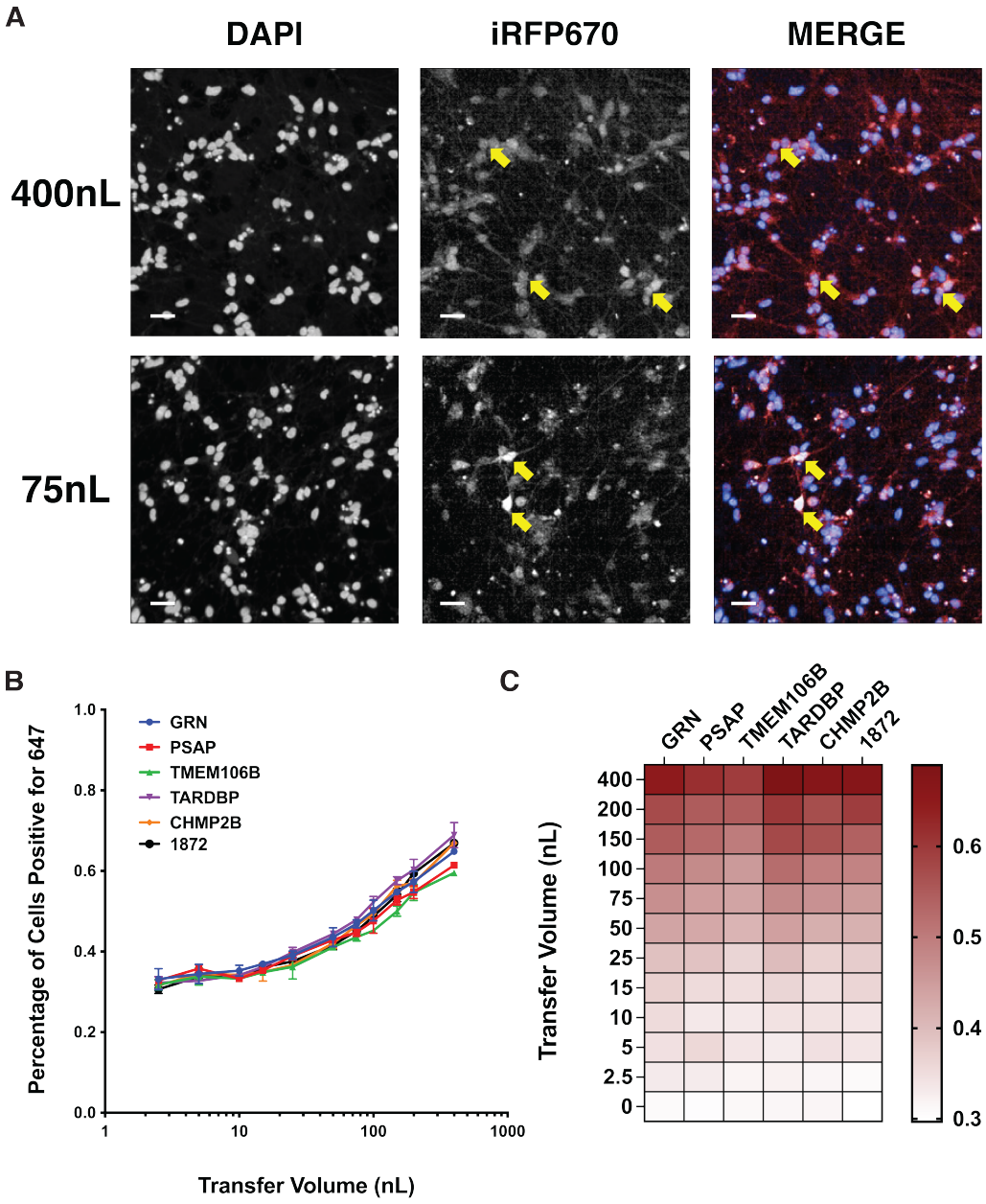


Figure 3.10: Cytosolic Far-Red sgRNA Library Functional Titering. A.) Representative images from Cytosolic Far-Red virus functional titering at 400nL and 10nL transfer volumes, with yellow arrows highlighting positive iRFP670 expression; DAPI staining for all live nuclei; scale bar = 20µm. B.) Titer curves quantified from the selected examples displaying the percentage of cells positive for iRFP670 expression; n=3 wells. C.) Representative heatmap of the results from B.

3.3.5 Dual Transduction of sgRNAs

Before further assay development and screening, I first wanted to validate that two sgRNAs could be simultaneously delivered to i^{3}Neurons on 384-well plates.

Two methods were attempted for this experiment: 1) where I Echo-delivered two sgRNAs directly to wells with neurons in culture and 2) where I Echo-delivered the same volume of sgRNAs to wells containing only neuronal media, requiring a second, hand-transfer step to the cell plate.

Lentiviruses harboring a GFP marker or an iRFP670 marker were transduced into our i^{3}Neurons. The GFP lenti was delivered at three increments: 10nL, 20nL, or 30nL. The iRFP670 lenti was delievered across a broader spectrum from 100-400nL transfer volume. The results in Figure 3.11A and Figure 3.11B compare these two methods, where the echo to media method had fewer dual-positive neurons across all transfer volumes. In Figure 3.11A, there were significantly more dual-positive i^{3}Neurons when directly delivering the sgRNAs opposed to delivering to media with the intermediate step in Figure 3.11B, especially at higher transfer volumes. Ultimately, this helped solidify our methods going forward into further phenotypic experiments.

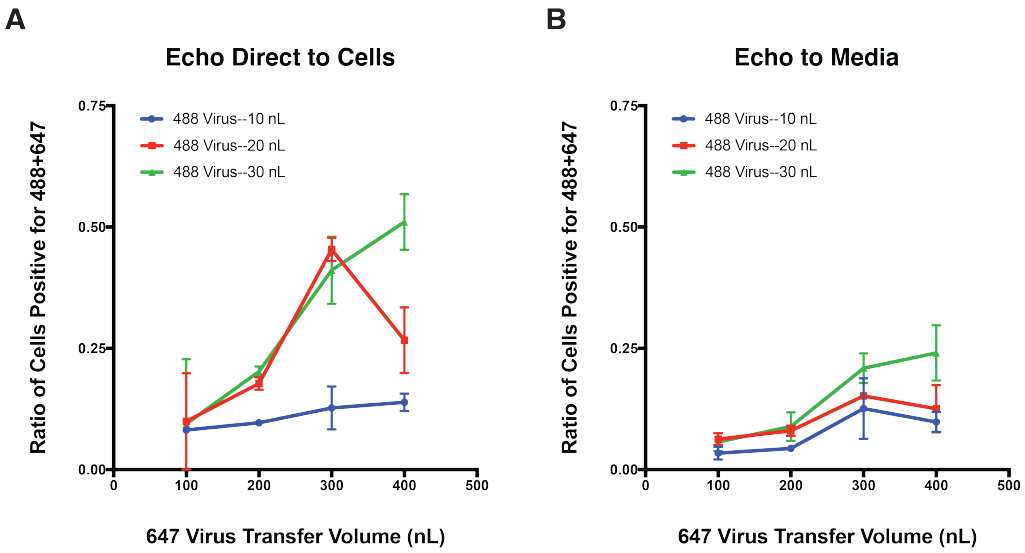


Figure 3.11: Preliminary Dual Transduction of sgRNAs. A.) Dual sgRNA delivery direct to cells. B.) Dual sgRNA delivery to neuronal media, requiring intermediate transfer step.

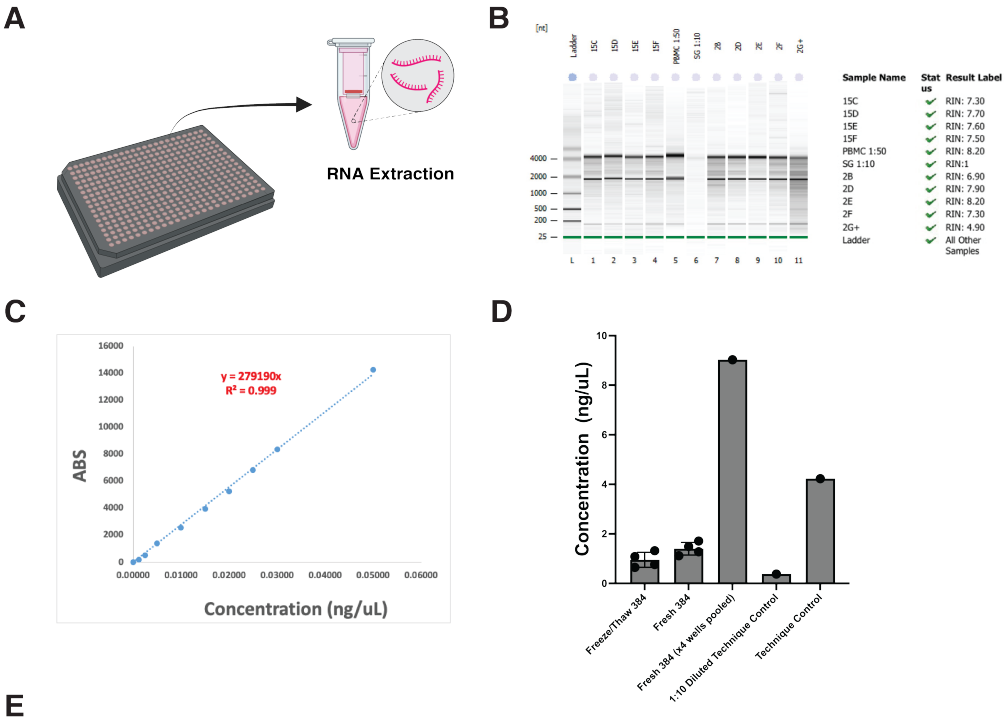
3.4 Targeted, Multiplexed RNA Sequencing for sgRNA Validation

3.4.1 Validation of High-throughput RNA Extraction

In order to further validate our sgRNA libraries, confirmation of target gene knockdown was necessary. Previously used methods for this process were low throughput, usually on 6-well dish formats with sgRNA transduction and drug selection performed ahead of any RNA extraction. Additionally, RNA extraction on this level is usually very straightforward and concern for RNA recovery is quite low. However, choosing a delivery method that optimized our ability to array sgRNAs on high-content formats meant further optimization was needed for the generation and handling of knockdown i^{3}Neurons in such as way that we could 1) deal with the vast quantity of samples and 2) could do so in a reproducible manner with confidence in the performance of the sgRNA knockdown, as each knockdown line is re-transduced and regenerated for each specific experiment.

A targeted, multiplexed RNA sequencing method was chosen for sgRNA validation across our library of disease genes. In order to examine the efficiency of RNA preparation from a very small sample of i^{3}Neurons I performed a preliminary experiment as a proof-of-concept for RNA recovery from high content plates. The results from the bioanalyzer runs in Figure 3.12B showed very promising results with high RIN values for samples when compared to controls. We were also able to quantify the yield of each sample, calibration curve and results shown in Figures 3.12C-E.

Despite the low concentrations of RNA seen from a single well of neurons on 384-scale, the quality was more than acceptable across samples. Additionally, Figure 3.12D shows mild, if any differences in yield between the frozen or fresh 384 neuron samples, as well as a marked increase in RNA yield when pooling four 384 wells together pre-extraction.



E

Sample Name	ABS Value	ng/uL	pg/uL	Sample Type
15C	1840	1.3181	1318.10	Freeze/Thaw 384
15D	1512	1.0831	1083.13	Freeze/Thaw 384
15E	903	0.6469	646.87	Freeze/Thaw 384
15F	1065	0.7629	762.92	Freeze/Thaw 384
PBMC 1-10	25904	18.5565	18556.54	RNA Control (independent sample)
SG 1-10	528	0.3782	378.24	1:10 Diluted Technique Control (Qiagen Micro)
2B	2083	1.4922	1492.17	Fresh 384
2D	2387	1.7099	1709.95	Fresh 384
2E	1785	1.2787	1278.70	Fresh 384
2F	1564	1.1204	1120.38	Fresh 384
2G+H+I+J	12607	9.0311	9031.13	Fresh 384 (x4 wells pooled)
SG	5906	4.2308	4230.81	Technique Control (Qiagen Micro)

Figure 3.12: Bulk RNA preparation from high content plates. A.) Concept schematic of extracting RNA from a 384-well plate. B.) Bioanalyzer gel showing the sample runs and corresponding RIN values. C.) RiboGreen calibration curve validating post-QC RNA quantification method. D.) Quantification of the results in E, comparing the sources of RNA samples. E.) Sample table summary of RiboGreen results and sample type.

3.4.2 Preliminary Targeted RNA Sequencing & sgRNA Validation

After optimization of the RNA extraction methods, I was able to focus attention on the sgRNA validation itself. A custom, targeted RNA sequencing panel was purchased from Paragon Genomics to enrich each knockdown sample for the genes we were targeting in our sgRNA library – a few additional genes were chosen as

Table 3.1: Paragon Genomics CleanPlex RNA Target Enrichment Panel

FTD/ALS Group	PD Group	Other	Oxidative Stress	Housekeeping Controls
ALS2	*ATP13A2 (PARK9)*	*ATP6V0A1*	*GSTO1*	*ACTB*
ANXA11	*CHCHD2*	*CLN5*	*HMOX1*	*C1orf43*
C9orf72	*CRLS1*	*CLN8*	*NQO1*	*GAPDH*
CHCHD10	*FYN*	*CTSB*		*HMBS*
CHMP2B	*GALC*	*CTSD*		*PSMB4*
DCTN1	*GBA1*	*CTSL*		
FUS	*GCH1*	*NBR1*		
GRN	*GUSB*	*NDP52 (CALCOCO2)*		
HNRNPA2B1	*LRRK2 (PARK8)*	*OXR1*		
KIF5A	*MCCC1*	*PSAP*		
MAPT	*NAGLU*	*STX17*		
OPTN	*NEU1*	*TAXBP1 (TAX1BP1)*		
PFN1	*PARK2 (Parkin)*	*TMEM106B*		
SETX	*PARK7 (DJ-1)*			
SOD1	*PINK1 (PARK6)*			
SQSTM1	*SCARB2*			
TARDBP	*SNCA (PARK1)*			
TBK1	*TMEM175*			
UBQLN2	*VPS13C (PARK23)*			
VAPB	*VPS35 (PARK17)*			
VCP				

a transcriptomic readout for oxidative stress and as housekeeping controls (Table 3.1). Additionally, *UBQLN2* had to be removed from the panel, as it is only a single exon and therefore would not fit in with Paragon's method for multiplexing. However, it was previously validated in the Ward Lab and was kept in the library for downstream phenotypic screening. In total, 61 genes were in the targeted RNA sequencing panel, across the FTD/ALS, PD, other interactors, oxidative stress, and housekeeping genes.

The purpose of the targeted panel is to more efficiently use next-generation sequencing methods by multiplexing many samples onto a single sequencing chip. As the panel is only enriching and barcoding our target genes, this method allowed me to very rapidly identify changes in transcriptomic expression across multiple samples, while also focusing the NGS reads on the specific subset of the human genome that we needed to validate the sgRNA library.

Figure 3.13A is an abridged summary of the targeted, multiplexed RNA sequencing process. After sample RNA extraction and cDNA conversion, the targeted NGS

panel is used for multiplexed PCR reactions that enrich all target genes, followed by indexing PCR reactions that systematically barcode all enriched transcripts, giving a unique marker per sample for post-sequencing analysis. Following sample collection and RNA extraction, RNA sample quality checks and quantification were carried out, as shown in Figures 3.13B-F and Figures 3.13G-H. While the RIN values for all samples were adequate, the concentrations quantified in Figure 3.13G were lower for the first two batches of samples compared to the final three batches of samples. This pattern can be seen in the heatmap of Figure 3.13H, indicating a potential batch effect. The sample summary in Table 3.2 has been labeled by batch, with the color indicating another potential co-variate, the time of prep (dark blue = early round, light blue = late round). The differences in concentrations seem to line up with whether or not the RNA preps happened in the early round of preps (RNA Preps 1 and 2) vs the late round of preps (RNA Preps 3, 4, and 5).

Post-sequencing transcript count quality control and normalization analysis was then performed. Figure 3.14A shows a series of scatter plots displaying the read counts across all samples for each of the housekeeping control genes ACTB, C1orf43, GAPDH, HMBS, and PSMB4. These control genes were chosen as the best representatives to serve as reference genes within iPSC and iPSC-derived cellular models [151]. One benefit of utilizing multiple reference or "housekeeping" genes is the ability to normalize across different levels of expression. For example ACTB is expressed very highly, while HMBS has much lower expression levels (Figure 3.14A).

Table 3.2: Preliminary Targeted, Multiplexed RNA Sequencing Sample Table

Sample Name	ABS Value	ng/uL	RIN	sgRNA Ref Name	sgRNA Short Name	Gene Target	Batch
B2	1435	0.963	8.70	LRRK2-1	1A	LRRK2	RNA Prep 1
B3	2143	1.438	8.80	LRRK2-1	1A	LRRK2	
B4	907	0.609	8.40	LRRK2-1	1A	LRRK2	
B5	882	0.592	9.00	LRRK2-1	1A	LRRK2	
E2	391	0.262	8.40	PINK1-1	1C	PINK1	
E3	319	0.214	7.70	PINK1-1	1C	PINK1	
E4	208	0.140	7.60	PINK1-1	1C	PINK1	
E5	313	0.210	7.30	PINK1-1	1C	PINK1	
F2	373	0.250	7.60	PARK2-1	1E	PARK2	
F3	2063	1.384	8.80	PARK2-1	1E	PARK2	
F4	57	0.038	7.90	PARK2-1	1E	PARK2	
F5	88	0.059	8.00	PARK2-1	1E	PARK2	
H2	3077	2.065	8.50	PARK7-1	1G	PARK7	RNA Prep 2
H3	2066	1.386	7.70	PARK7-1	1G	PARK7	
H4	471	0.316	8.20	PARK7-1	1G	PARK7	
H5	351	0.236	7.30	PARK7-1	1G	PARK7	
J2	518	0.348	7.60	SNCA-1	2A	SNCA	
J3	683	0.458	8.30	SNCA-1	2A	SNCA	
J4	1831	1.229	7.00	SNCA-1	2A	SNCA	
J5	844	0.566	7.90	SNCA-1	2A	SNCA	
L2	587	0.394	7.60	CHCHD2-1	5G	CHCHD2	
L3	625	0.419	8.30	CHCHD2-1	5G	CHCHD2	
L4	705	0.473	8.50	CHCHD2-1	5G	CHCHD2	
L5	1488	0.998	8.80	CHCHD2-1	5G	CHCHD2	
D7	5125	3.439	9.10	GBA-1	2C	GBA	RNA Prep 3
D8	3525	2.365	9.00	GBA-1	2C	GBA	
D9	4374	2.935	9.00	GBA-1	2C	GBA	
D10	2777	1.863	8.30	GBA-1	2C	GBA	
G7	3258	2.186	8.30	VPS35-1	2E	VPS35	
G8	3488	2.340	9.00	VPS35-1	2E	VPS35	
G9	3514	2.358	8.20	VPS35-1	2E	VPS35	
G10	3688	2.475	8.30	VPS35-1	2E	VPS35	
J7	3478	2.334	9.80	ATP13A2-1	2G	ATP13A2	
J8	3802	2.551	8.90	ATP13A2-1	2G	ATP13A2	
J9	3415	2.291	8.10	ATP13A2-1	2G	ATP13A2	
J10	2706	1.816	8.40	ATP13A2-1	2G	ATP13A2	
M7	3229	2.167	7.40	ATP6V0A1-1	6A	ATP6V0A1	RNA Prep 4
M8	3616	2.426	8.20	ATP6V0A1-1	6A	ATP6V0A1	
M9	2755	1.849	8.80	ATP6V0A1-1	6A	ATP6V0A1	
M10	3053	2.049	8.20	ATP6V0A1-1	6A	ATP6V0A1	
D12	2453	1.646	7.70	GRN-F3	7A	GRN	
D13	4476	3.003	8.00	GRN-F3	7A	GRN	
D14	3575	2.399	8.90	GRN-F3	7A	GRN	
D15	3554	2.385	8.50	GRN-F3	7A	GRN	
G12	4366	2.930	8.40	3086	11H	Non-targeting	
G13	2383	1.599	8.70	3086	11H	Non-targeting	
G14	4173	2.800	9.00	3086	11H	Non-targeting	
G15	3109	2.086	9.80	3086	11H	Non-targeting	
I12	4424	2.968	8.90	1872	12A	Non-targeting	RNA Prep 5
I13	2700	1.812	9.40	1872	12A	Non-targeting	
I14	5581	3.745	8.10	1872	12A	Non-targeting	
I15	3897	2.615	8.30	1872	12A	Non-targeting	
L12	3175	2.130	8.10	H25	H25	GFP	
L13	3765	2.526	8.90	H25	H25	GFP	
L14	3460	2.322	6.80	H25	H25	GFP	
L15	2506	1.682	-	H25	H25	GFP	

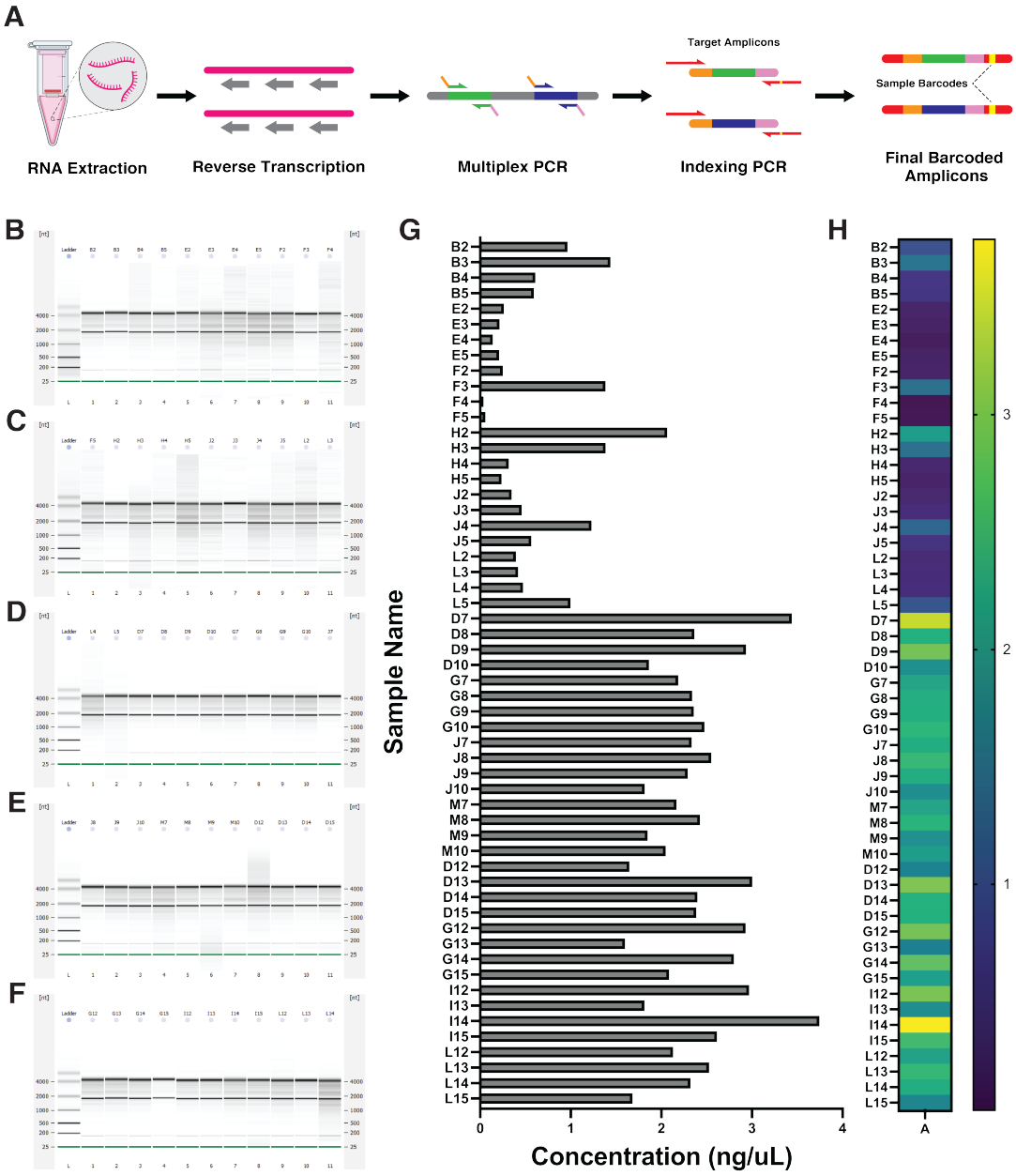


Figure 3.13: Preliminary Targeted RNA Sequencing, Sample Preparation. A.) Schematic overview detailing the major steps in the pipeline for Targeted, Multiplexed RNA Sequencing. B-F.) Bioanalyzer gels showing the sample runs, corresponding RIN values can be found in Table 3.2. G.) RiboGreen quantification of RNA concentrations corresponding to the samples in Table 3.2 and Bioanalyzer gels in B-F. H.) Representative heatmap of RiboGreen quantification of RNA concentrations in G.

Figure 3.14B is an enlarged version of the GAPDH plot in Figure 3.14A that highlights the bi-modal population of GAPDH counts across all samples. This bimodal population corresponds to the time of batch prep, as mentioned previously and shown in Table 3.2 and the RNA quantification in Figures 3.13G-H. The PCA in Figure 3.14C shows that the major contribution of variance in PC1 seems to be the GAPDH counts in the samples. There are two major clusters and when the GAPDH count is overlayed as a heatmap from dark blue to light blue, the differences are indicative of the batch effect. These findings further supported the need to normalize our read counts across the experiment.

Two methods of normalization were tested: 1) normalizing via housekeeping control genes and 2) median ratios normalization (via DESeq2). The box plots in Figure 3.14D display the median read counts across all samples before normalization, whereas Figure 3.14E and Figure 3.14F show the same box plots following normalization from housekeeping and median ratios methods, respectively. The variance across median counts in all samples was greatly reduced with either method, but the median ratios method was chosen to proceed through further quantification.

After the normalization method was confirmed and applied across the samples in the experiment, sgRNA knockdown could be validated. The results from the preliminary experiment included knockdown results from the following sgRNAs: LRRK2-1, PINK1-1, PARK2-1, PARK7-1, SNCA-1, CHCHD2-1, GBA-1, VPS35-1, ATP13A2-1, ATP6V0A1-1, GRN-F3 (positive control, previously validated), and 1872 (non-targeting control), a full summary of the samples can be seen in Table 3.2.

The scatter plots in Figures 3.15A-J show the normalized transcript counts for a given gene of interest across the entire sample set, where the samples in red were transduced with an sgRNA targeting that particular gene and the samples in blue were transduced with either a non-targeting sgRNA or an sgRNA targeting a different gene. These plots give a clear indication of the effect of an sgRNA targeting a gene of interest and illustrates knockdown efficiency. The bar graph in Figure 3.15K shows a summary of the knockdown efficiency of the submitted

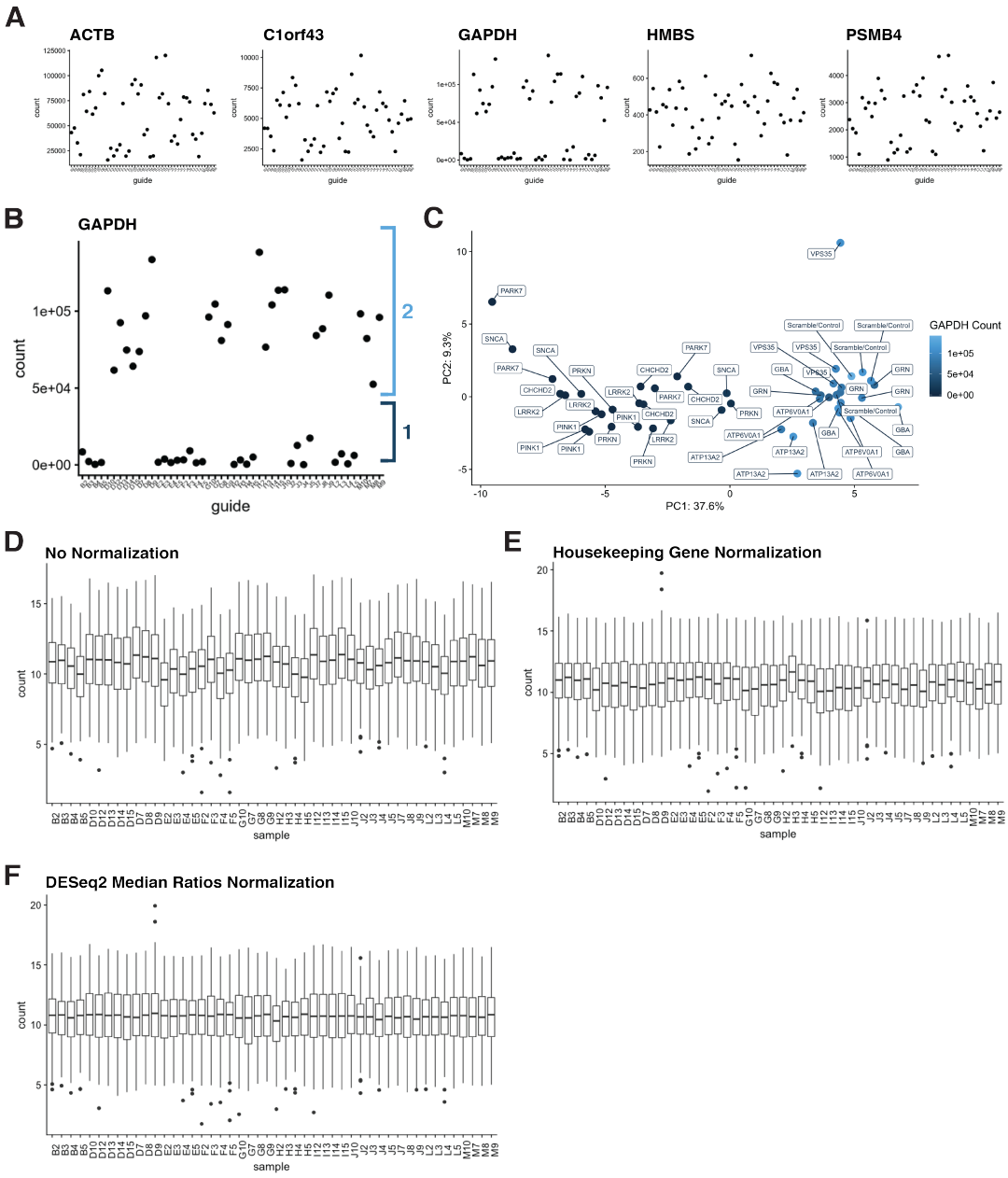


Figure 3.14: Preliminary Targeted RNA Sequencing, Analysis Normalization. A.) Scatter plots of read counts across all samples for each of the housekeeping control genes ACTB, C1orf43, GAPDH, HMBS, and PSMB4. B.) Enlarged scatter plot of GAPDH read counts, annotated with "time of prep" batch information. C.) Non-normalized PCA showing all samples overlayed with GAPDH count information as indicated by color; samples with high GAPDH counts are colored light blue, samples with low GAPDH counts are colored dark blue. D.) Box plots of median read counts across all samples before normalization. E.) Box plots of median read counts across all samples after normalization via housekeeping genes. F.) Box plots of median read counts across all samples after normalization via DESeq2 median ratios method.

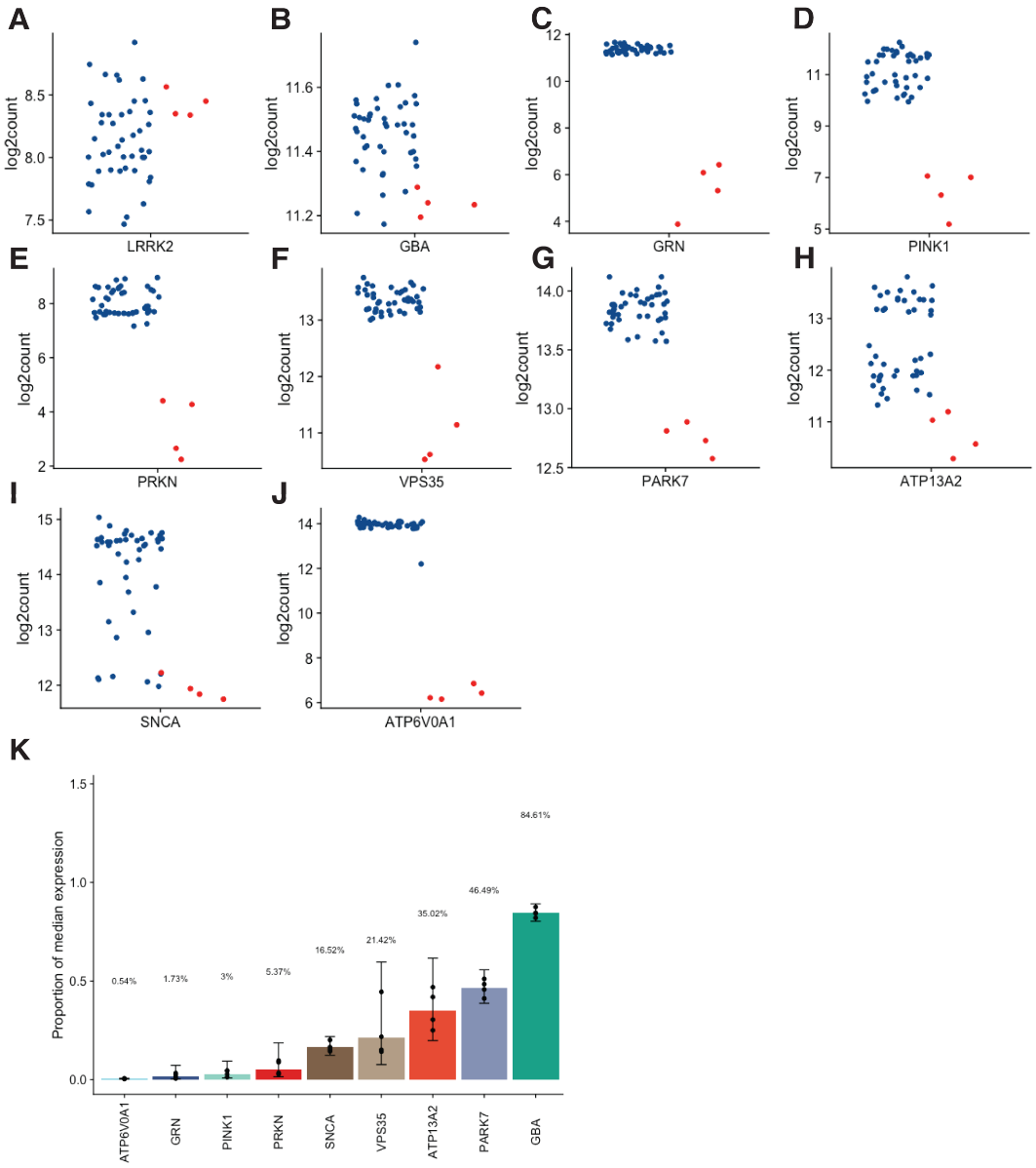


Figure 3.15: Preliminary Targeted RNA Sequencing, Targeted Knockdown Analysis. Scatter plots showing the normalized transcript counts for a given gene of interest, samples in red were transduced with the sgRNA targeting that particular gene; A.) *LRRK2*, B.) *GBA*, C.) *GRN*, D.) *PINK1*, E.) *PRKN (PARK2)*, F.) *VPS35*, G.) *PARK7*, H.) *ATP13A2*, I.) *SNCA*, and J.) *ATP6V0A1*. K.) Bar graph summary showing the knockdown efficiency of the submitted sgRNAs, n=4.

sgRNAs, where ATP6V0A1-1, PINK1-1, PARK2-1, SNCA-1, and VPS35-1 all show promising initial knockdown results when compared to the positive control, GRN-F3. ATP13A2-1, PARK7-1, and GBA-1 had slightly less efficient performances, achieving partial knockdowns for their gene targets. LRRK2-1 is not shown, as knockdown was unsuccessful in i^{3}Neurons which have very low or no LRRK2 expression.

3.4.3 High-throughput Targeted RNA Sequencing & sgRNA Validation

Following the preliminary targeted RNA sequencing experiment, I was able to further optimize the experimental design and approach to make the high-throughput sgRNA validation more efficient and robust. To help avoid batch effects, all 96 sgRNAs assigned random 'code' that determined their plate position and biological replicates were spread across multiple plates, as seen in Figure 3.16A. Example Tapestation gels for RNA quality control checks in Figure 3.16B and Figure 3.16C utilize RIN^e values instead of the more traditional RIN [152]. Raw RIN and RIN^e values for all experimental submissions can be found in Table A.5, and all normalized titer transfer volumes for this experiment can be found in Table A.4. Figure 3.16D and Figure 3.16E once again demonstrate the favored normalization method, median ratios from DESeq2, which was optimized in the preliminary experiment.

The primary results from our final targeted, multiplexed RNA sequencing experiment included knockdown results from all sgRNAs in my library (refer back to Table A.1 for all sgRNA information). The knockdown validation data is summarized as a heatmap split into two parts, seen in Figure 3.17 and Figure 3.18. These heatmaps show high transcript expression as red (hot) and low transcript expression as blue (cold). The most noticeable feature of the heatmaps in Figure 3.17 and Figure 3.18 are the regular dark blue insets, which in most cases represent samples that received the sgRNA that corresponds to the gene with low transcript counts, validating the CRISPRi-mediated repression.

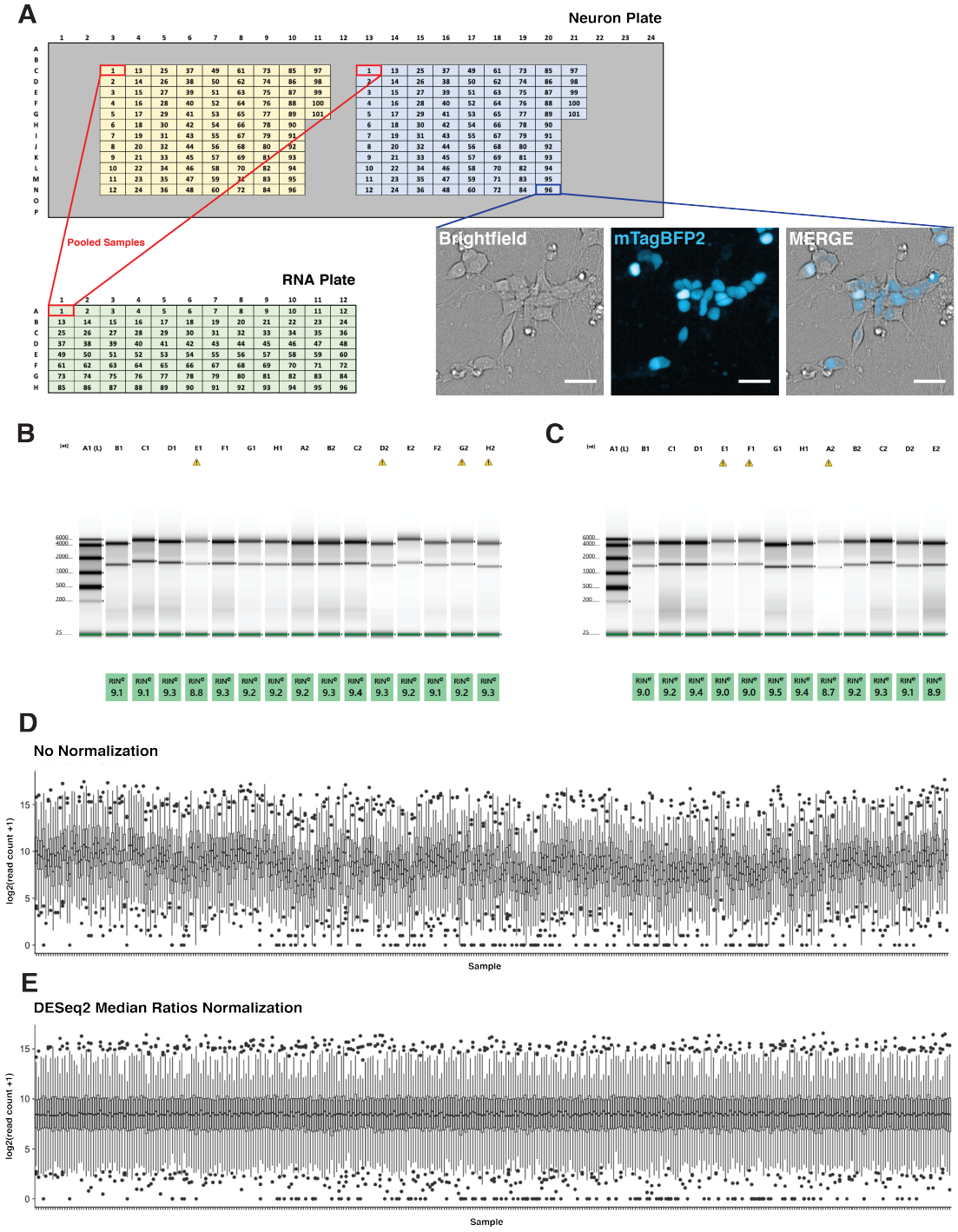


Figure 3.16: Final Targeted RNA Sequencing, Experimental Design and Normalization. A.) Schematic of the plate layout and experimental design for the final targeted RNA sequencing experiment; left inset shows how pooled neuronal samples are organized on the final RNA sample plates; right inset shows an example of the puro-selected final samples from pre-harvest plate checks, scale = 20µm. B-C.) Example TapeStation gels showing the characteristic sample runs, corresponding RIN^e values can be found in Table A.5. D.) Box plots of read counts across all samples before normalization. E.) Box plots of read counts across all samples after normalization via DESeq2 median ratios method.

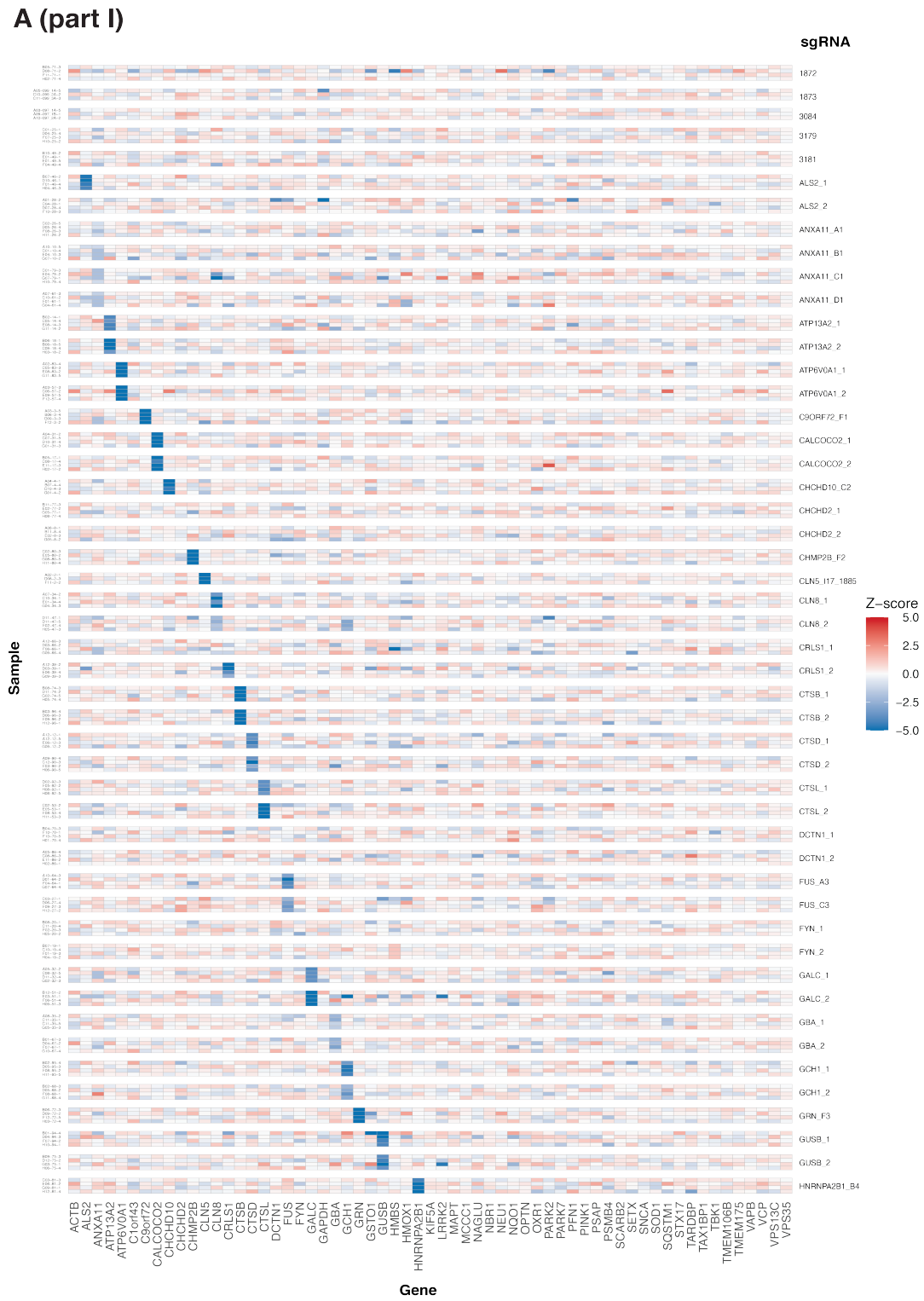


Figure 3.17: Final Targeted RNA Sequencing, sgRNA Knockdown Validation, Part I. A.) Part I: Representative heatmap of non-targeting sgRNAs and sgRNAs targeting panel genes A-H.

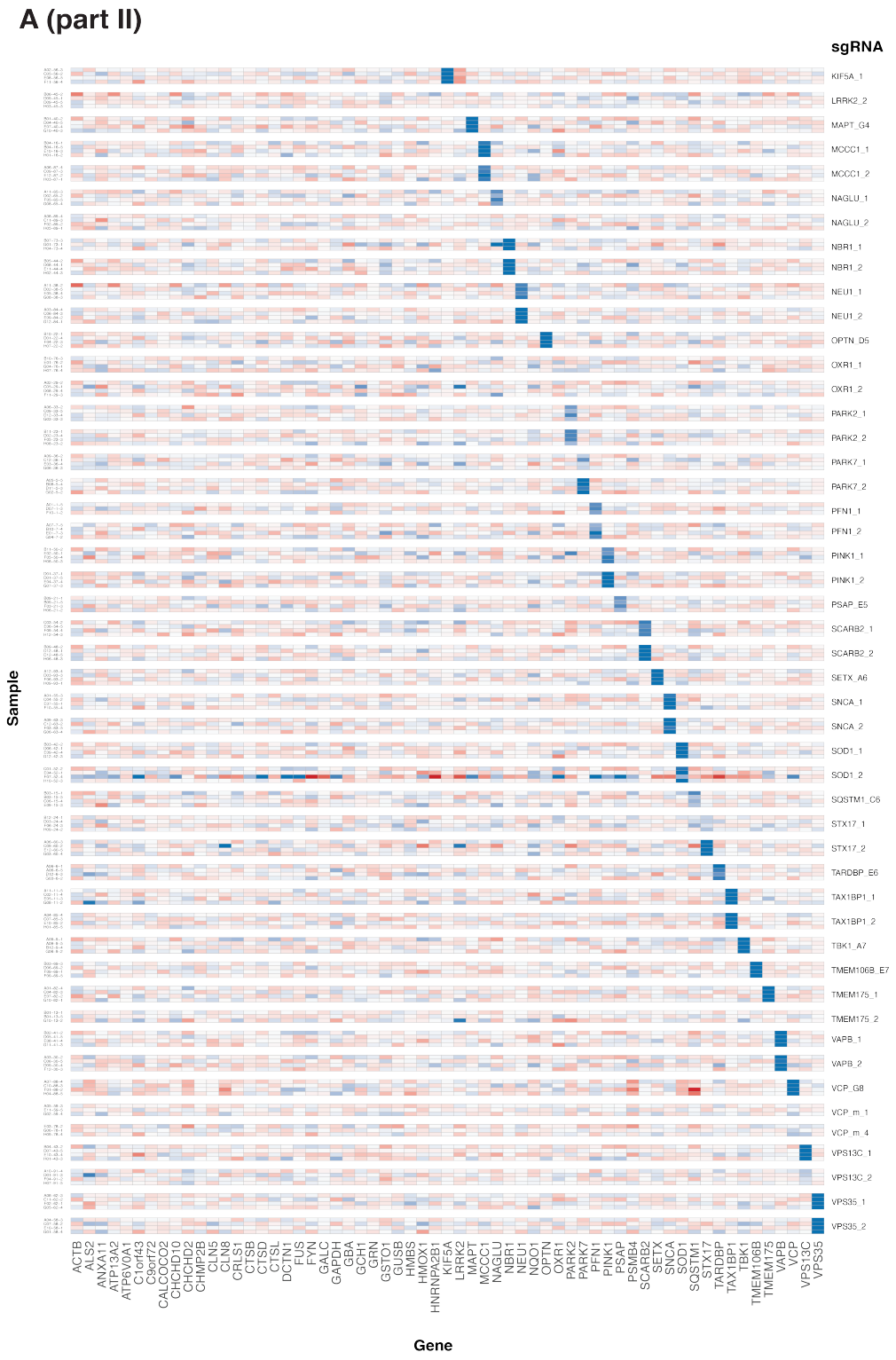


Figure 3.18: Final Targeted RNA Sequencing, sgRNA Knockdown Validation Part II. A.) Part II: Representative heatmap of sgRNAs targeting panel genes K-V.

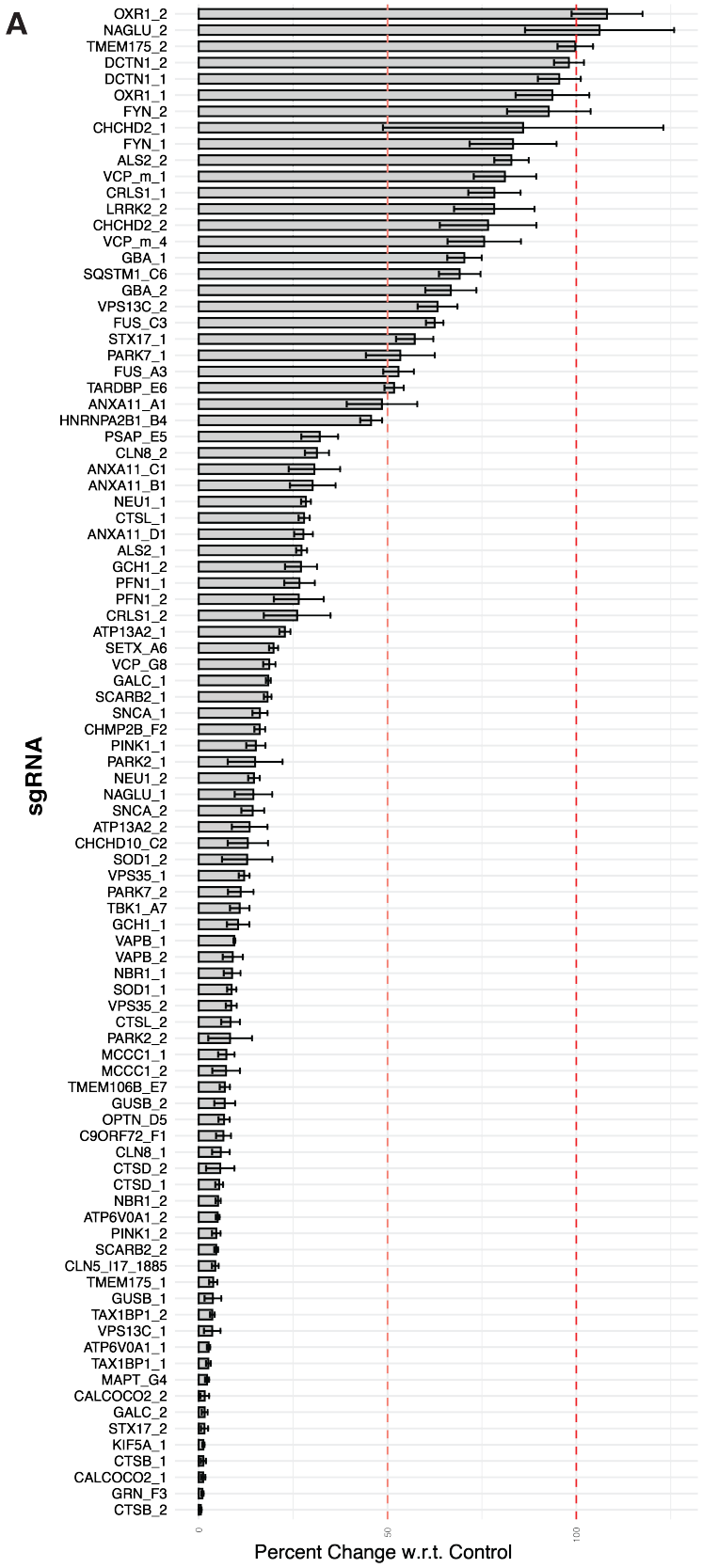


Figure 3.19: Final Targeted RNA Sequencing, Summary of sgRNA Knockdown Validation. A.) Quantification of each sgRNA knockdown as percent change with respect to non-targeting controls.

The sgRNAs CHCHD2_1, CHCHD2_2, DCTN1_1, DCTN1_2, FYN_1, FYN_2, LRRK2_1, LRRK2_2, OXR1_1, and OXR1_2 all failed validation, therefore, no sgRNAs were able to ablate transcripts for the genes *CHCHD2*, *DCTN1*, *FYN*, *LRRK2*, or *OXR1*. ALS2_2, CRLS1_1, NAGLU_2, and TMEM175_2 also failed validation, but the alternate guides that target their gene of interest all successfully repressed target transcripts. This still allowed me to target *ALS2*, *CRLS1*, *NAGLU*, and *TMEM175* in down stream phenotypic assays. ANXA11_A1, ANXA11_B1, ANXA11_C1, ANXA11_D1, VCP_m_1, and VCP_m_4 all showed mild knockdown and were very close to significance, so I still brought them through to the phenotypic screening. Moreover, VCP_m_1 and VCP_m_4 were both designed to achieve a mild knockdown [153]. All other sgRNAs successfully knockdown their target transcripts, either partially or robustly, referring to those above or below the 50% threshold in Figure 3.19, respectively. Log_2FoldChange and significance values for all targeted gene knockdowns and the corresponding sgRNA can be found in Table A.6.

3.4.4 Transcriptomic Genetic Interactions

While RT-qPCR is an effective method at sgRNA validation, the targeted RNA sequencing method was chosen to provide further information about our genes of interest in these knockdown samples. Post-sequencing analysis provides a dataset containing the unique expression changes for the entire targeted library across each sample, which would allow for the transcriptomic profiling of disease-relevant gene interactions.

Figure 3.20A shows the concept behind this process, where a "Gene C knockdown" sample is generated, but can also be analyzed for transcript expression changes in "Gene A" also in the panel. If significant expression changes are detected, this may suggest a transcriptomic-level or gene regulatory connection between two disease genes.

The results in Figure 3.20B, Figure 3.20C, and Figure 3.20D show heatmaps of some of the top transcriptomic interactions I was able to detect: *KIF5A*/*LRRK2*,

CLN8/*GCH1*, and interactions with *VCP*, respectively. Figure 3.20B demonstrates that when *KIF5A* transcripts were ablated, *LRRK2* transcripts were upregulated. When *CLN8* transcripts were ablated, *GCH1* transcripts also went down, as shown in Figure 3.20C. However, this effect primarily was seen with sgRNA CLN8_2, not CLN8_1. The *VCP* knockdown samples had the most potential interactions detected, shown in Figure 3.20D. *ALS2*, *CLN8*, *SOD1*, and *SQSTM1* were all upregulated when transcripts for *VCP* were ablated. The non-targeting control 1872 is shown for reference in all heatmaps.

Table 3.3: Transcriptomic interactions identified by targeted RNA sequencing.

Gene	sgRNA	Mean Counts	log2FoldChange	padj
GCH1	CLN8_2	42.04	-1.83	8.59077E-10
SQSTM1	VCP_G8	635.05	0.58	2.58009E-05
CLN8	VCP_G8	31.60	0.87	0.003
SOD1	VCP_G8	828.09	0.79	0.003
PARK2	CALCOCO2_2	21.37	1.00	0.005
CHCHD2	VPS13C_2	17.10	-2.84	0.006
LRRK2	KIF5A_1	28.47	0.97	0.010
ALS2	VCP_G8	98.84	0.44	0.015
GSTO1	NBR1_2	57.06	-0.82	0.021
LRRK2	CTSB_2	28.47	-0.93	0.047

3.5 Discussion

In Chapter 3, I successfully demonstrated arrayed CRISPRi sgRNA library development and implemented robust methodology leading to fully optimized high-throughput plasmid ligation cloning, lentivirus production, and sgRNA validation platforms. From *in silico* sgRNA sequences to ready-to-transduce lentiviral libraries, this chapter focused on the many technical issues arising during an early stage of my DPhil project that required fine tuning in order to implement a functional genomics screen reliant on high-content microscopy.

CRISPRi Tool Optimization

The generation and optimization of J72, the cytosolic far-red system published in Carling et al. [74], was a necessary component for accomplishing dual sgRNA

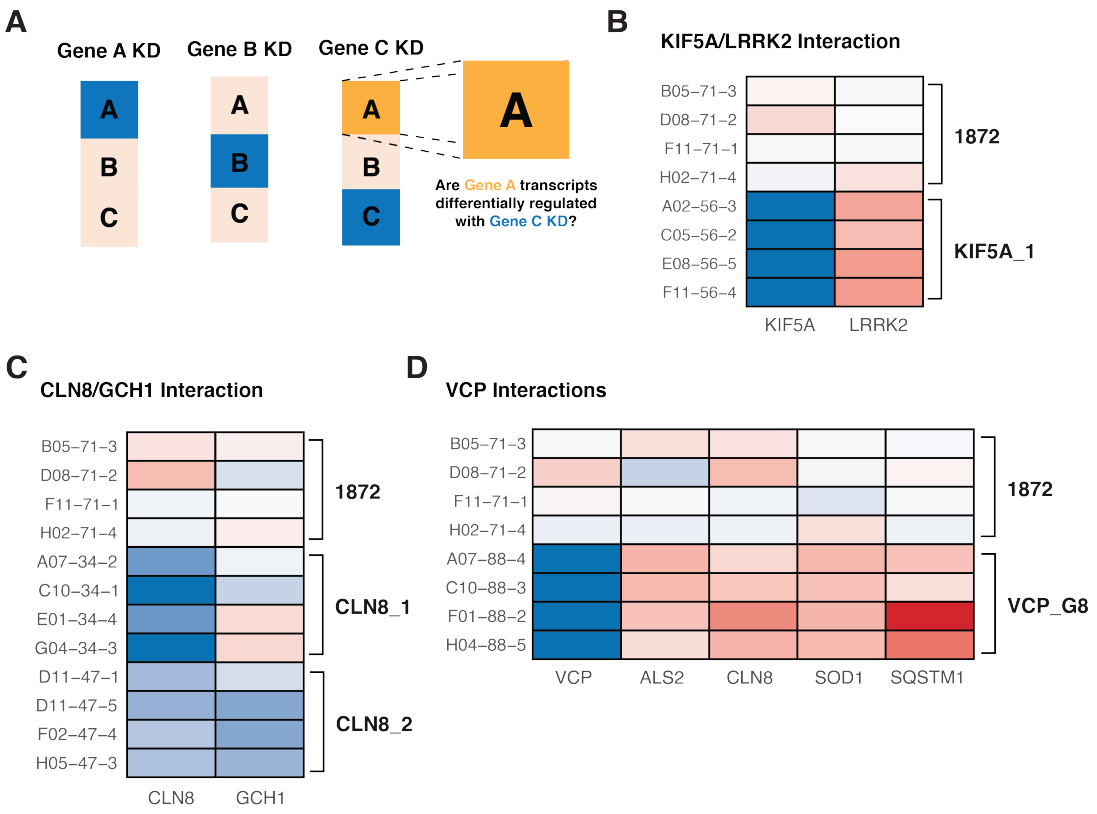


Figure 3.20: Final Targeted RNA Sequencing, Transcriptomic Interactions. A.) Schematic representing the concept behind discovering transcriptomic-level interactions. Transcript expression heatmaps for the B.) *KIF5A/LRRK2* interaction, C.) *CLN8/GCH1* interaction, and D.) *VCP* interactions.

delivery for downstream high-content imaging. Up to that point, no CRISPRi tools existed other than those harboring BFP fluorescent markers, which meant there was no efficient way of confirming if two sgRNAs had been successfully delivered to a single cell. The fundamental goal of creating a novel functional genomics platform capable of high-content, imaged-based screening required reproducible, pairwise knockdown of two target genes, therefore *confirmation* and *selection* for two different sgRNAs was necessary.

From my experiences with high-content imaging, the two most fundamental segmentation markers required for most phenotypic assays are 1) a nuclear marker and 2) a cell body marker. When transduced into cells, J72 expresses a cytosolic Far-Red fluorescent protein and blasticidin resistance that allows for the quick and

accurate identification of positively transduced cells. When used in conjunction with a second sgRNA-lenti in our nuclear blue system containing a puromycin resistance protein, we can identify and enrich for co-transduced cells that contain both sgRNAs of interest, silencing the expression of both gene targets. These tools are dual-purpose and provide the most efficient way to knockdown your target(s) of interest, while simultaneously providing your cell model with the necessary accessory markers for most major assays utilizing the 488nm (GFP) and 555nm (RFP) excitation channels.

CRISPRi sgRNA Library Generation

Establishing a fully optimized ligation cloning platform was another key step, as our sgRNA library had to be created in duplicate to achieve systematic pairwise knockdown of our target genes. The sgRNA sequences had to be *ligated into* and *sequence verified* in both the nuclear blue and cytosolic far-red systems, ready for lentivirus production. This would require double the necessary preparation, incubation, and validation time and effort from the onset, so optimization of this pipeline was necessary. The most impactful modifications came from the efficient use of multi-well formats for oligo arraying, oligo annealing, ligation, and transformation steps. Generally, the commitment to high-throughput cloning methods where applicable streamlined the generation of the arrayed sgRNA plasmid libraries needed for my project, without the need for commercial assistance.

Functional titering of the sgRNA lentiviral libraries also gave me an advantage in downstream microscopy assays, as we will be able to normalize the transduction of all sample wells based on fluorescent marker expression, while also ensuring enough iPSC-neurons are sgRNA-positive for downstream quantification. The Echo has proven to be a robust delivery mechanism for our lentiviruses, and provided great reproducibility when quantifying our functional titers across multiple wells and batches. When combined with optimized i^{3}Neuron cell plating, this tool has helped me to effectively miniaturize CRISPRi cell line generation to 384-well formats. With this pipeline, it is now possible to generate as many single and/or dual knockdown i^{3}Neuron cell lines as needed for a given experiment, making it a very powerful tool and platform for scalable, imaged-based phenotypic screening.

Targeted, Multiplexed RNA Sequencing for sgRNA Validation

All individual guides must be validated for optimal target knockdown via gene expression analysis methods such as RT-qPCR. However, due to the scope and scale of my project, an alternate approach was chosen: targeted, multiplexed RNA sequencing. With the same upfront sample preparation, this approach allowed me to examine two key questions: 1) is the target gene knocked down and 2) what transcriptomic profile does that knockdown produce with respect to other disease-relevant genes in our target library? With RT-qPCR, we would only be able to address the first question, and potentially miss any interesting transcriptomic-level interactions due to target knockdown.

Unexpectedly, I was able to utilize the platform I established for functional titering and knockdown i^3Neuron cell line generation to generate the samples for RNA sequencing. This process combined nearly all of the tool and pipeline optimization I had accomplished up to that point, including the sgRNA delivery methods via acoustic fluid handling, drug-selection for sgRNA-positive i^3Neurons, and sample RNA extraction from 384-well formats. This culminated in the preliminary sgRNA validation experiment performed on a subset of the sgRNA library, in order to find any weak points in our experimental design before the full scale-up.

Validation of our general approach was achieved, but there was a batch effect identified that was most likely due to the lack of a proper normalization step before sequencing samples were run. How the samples were processed through RNA extraction was also a factor that indicated need for further optimization. For example, instead of breaking the biological replicates up across RNA extractions, I harvested all biological replicates for a subset of the knockdown samples and repeated that until all samples had been extracted. Unfortunately, this mean that some samples had all biological replicates in the high GAPDH/high RNA concentration group and some samples had all biological replicates in the low GAPDH/low RNA concentration group. Despite the fact that no proper normalization was done due

to a miscommunication with the core performing the sequencing, these potential sources of error could have been reduced by a small alteration in experimental design.

These optimization steps were introduced for the final targeted RNA sequencing experiment, generating a high-quality RNA seq. dataset consisting of 384 CRISPRi samples that were treated with 96 sgRNAs in biological quadruplicate. The design of the final experiment allowed for all 96 different samples to be extracted as a single group on multi-well formats, serving as a single biological replicate per condition. That process was repeated across 4-5 total replicates of each knockdown condition to abolish any batch effect due to RNA extraction technique, which also allowed me to harvest and prep all four biological replicates in parallel using multichannel-level throughput. Samples were also subsequently normalized by concentration and submitted for sequencing.

I was then able to validate whether a given sgRNA adequately abolished the transcripts of its target gene. Of the 54 genes targeted, only 5 had no validated sgRNAs, meaning the two sgRNAs selected per gene failed to induce transcript repression in i^{3}Neurons. An additional 4 genes had a combination of one validated sgRNA, and one failed sgRNA. All other genes had at least partial repression detected, with many achieving a large decrease in target transcript levels, indicating successful knockdown. Despite the lack of sgRNA knockdown validation for *LRRK2* and *CHCHD2*, it is worth noting that these genes are not highly expressed in i^{3}Neurons, and may require validation in a more disease-specific cellular model, such as dopaminergic neurons. Essentially, if a transcript is not present, an sgRNA designed to prevent it's expression cannot be validated. Therefore, the failure of the *LRRK2* and *CHCHD2* guides is conditional to the biological system in which they are used.

The sgRNA validation summary seen in Figure 3.19 helps to reveal the overall performance of the library. For those guides under the 50% threshold (light red), performance appears to be quite robust and reliable across samples for a given sgRNA. Those guides above the 50% threshold are achieving partial knockdown, with most appearing reliable across replicates. Throughout my experience using

this CRISPRi platform I've observed that, in most cases, a transcript's expression can be altered reliably, which makes this technology so powerful. However, in genes where normal function is essential or involve some non-redundant pathway, knockdown can be hard to achieve and/or lead to decreases in fitness. The partial knockdown in these *essential genes* can still have phenotypic effects in downstream assays, which supports the use "weaker" sgRNAs, despite their expression readouts.

Transcriptomic Genetic Interactions

The identification of transcriptomic-level interactions have the potential to reveal previously unknown pathway connections and convergence between disease-causative genes in FTD/ALS and PD. By utilizing targeted RNA sequencing, I have a readout of all disease-relevant genes for every sample submitted for sequencing. Due to this experimental design, I have been able to look for transcriptomic interactions such as those highlighted in Table 3.3 and Figure 3.20.

The *KIF5A*/*LRRK2* interaction looks promising from a technical perspective, as *LRRK2* is not highly expressed in many cell types and cortical neurons are no exception [154], though *LRRK2* protein is present in brain tissues [155]. Therefore, detection sensitivity is relatively high for this gene in this model, as I normally do not see these transcripts expressed to this degree. Figure 3.20B demonstrates a clear up-regulation of *LRRK2* transcripts in response to *KIF5A* knockdown, which indicates the two genes might be linked on some fundamental pathway or regulatory level.

Expression data also indicated that *GCH1* was down-regulated with *CLN8* knockdown, suggesting another potential interaction. However, this is a slightly different case where of the two sgRNAs tested, one guide showed the interaction and one did not, which lowers the overall confidence that this would be a true transcriptomic interaction. Figure 3.20C illustrates these results, indicating a change in *GCH1* expression with the CLN8_2 guide only. CLN8_1 was the stronger performing sgRNA when it came to CLN8 knockdown and was brought forward for screening. Further experimentation will be needed to properly assess the potential for off-target effects with the CLN8_2 guide.

The *VCP* interactions shown in Figure 3.20D display an increase in transcript expression of ALS2, CLN8, SOD1, and SQSTM1. VCP is an important gene with multiple functions along shared molecular pathways with *SOD1* and *SQSTM1* such as proteostasis [40], calcium regulation [156], and neuronal trafficking [157], so initially it makes sense that knockdown of this gene might overlap with several forms of cellular dysfunction. There is less current evidence for a direct interaction between VCP and ALS2 or CLN8. The sgRNA VCP_G8 was previously validated by the Ward Lab (Figure 3.1), and so no further VCP guides are in the screen to validate the current findings other than VCP_m_1 and VCP_m_4, which achieve only mild repression. For all the potential interactions in Table 3.3, the expression analysis was able to detect changes in transcript levels, but further validation with these and perhaps other guides will be needed for confirmation of any gene-gene transcriptomic-level interactions.

The overarching goal of Chapter 3 has been to highlight the creation of a multipurpose platform that enables high-throughput knockdown line generation across numerous experimental endpoints. The use of this platform will not only enable me to perform downstream arrayed screening with various phenotypic assays, but also a specific technique in functional genomics known as Genetic Interaction Mapping. Genetic interaction maps measure the extent to which a phenotype caused by knockdown of one gene is modified by the knockdown of a second gene, thus revealing functional relationships between pairs of genes. The next stages of this thesis will consist of assay development and optimization in order to generate mechanistic data and map converging pathways within FTD/ALS and PD.

4

Developing Assays Targeting Neuronal Function and the Lysosome

Contents

4.1 Introduction and Aims 83
4.2 Longitudinal Imaging and Neurite Outgrowth Assays 84
4.3 Transferrin Recycling and Uptake 85
4.3.1 Background 85
4.3.2 Transferrin recycling appears unaffected in *GRN*-KO cells 87
4.3.3 Total transferrin uptake is decreased in *GRN*-KO cells . 88
4.4 Measuring Lysosomal pH 89
4.4.1 Background 89
4.4.2 Measuring Lysosomal pH: Transforming a low-throughput imaging assay to high-content formats 90
4.4.3 Lysosomes in *GRN*-KO i^{3}Neurons have alkaline pH and fail to acidify 92
4.5 Evaluating Lysosomal Proteolysis 93
4.5.1 Background 93
4.5.2 Optimization of the DQ-BSA Assay in i^{3}Neurons . . . 95
4.5.3 Lysosomes in *GRN*-KO i^{3}Neurons exhibit decreased active proteolysis 99
4.6 DQ-BSA single knockdown CRISPRi screen reveals disease-associated lysosomal modulators and recapitulates *GRN*-KO dysfunction 101
4.7 Discussion 105

4.1 Introduction and Aims

FTD/ALS and PD are incurable neurodegenerative diseases, and numerous failed clinical approaches indicate a need to more fully understand the root biological causes underlying these disorders in order to develop effective therapies. The alternative strategy I aim to implement relies on the identification of pathways that are dysregulated in both FTD/ALS and PD, and to utilize functional genomics screening platforms to interrogate associated cellular phenotypes. One key pathway I have chosen to target is lysosomal function, as several genes associated with both disorders have been implicated in the dysfunction of this pathway and related autophagic processes [40].

Proximity labeling of lysosomes deficient in *GRN*, a causative FTD gene, revealed potential alterations in several key processes related to endolysosomal pathways, including transferrin recycling, lysosomal acidification, and lysosomal transport (Table 4.1). It is known that these properties of endosomal trafficking and lysosomal function are important for normal homeostasis and are implicated in other neurodegenerative diseases [69, 158, 159].

These key findings pushed my project toward developing phenotypic assays aimed at better understanding the disruption of lysosomal biology seen across these neurodegenerative diseases. This chapter will layout several key milestones throughout my DPhil project that have pushed me to optimize these assays for high-content imaging, allowing for downstream screening and Genetic Interaction Mapping by combining HCS/HCA approaches with the CRISPRi functional genomics platform from Chapter 3.

Aims of this chapter

- Demonstrate the development and optimization of relevant phenotypic assays
- Demonstrate the utility and application of high-content imaging and analysis in neuronal cellular models, specifically i^{3}Neurons
- Demonstrate the *phenotypic* functional validation of sgRNA lentiviral libraries for use in high-content screening

Table 4.1: Supplementary proteomics table, progranulin deficient lysosomes *(unpublished, courtesy of Ward Lab).*

Gene ID	pFDR[A]	Ratio[B]	# Peptides[C]	Go Term Enrichment
ANXA11	1.05E-05	-9.4	16	Calcium-dependent Protein Binding
ANXA6	2.82E-03	-1.7	31	
MYO1D	1.00E-16	<-100	5	
MYO5A	7.45E-03	1.7	55	
S100A10	1.00E-16	<-100	2	
SYN1	4.76E-05	-2.5	12	
MGRN1	2.88E-03	2.2	4	Endosome to Lysosome Transport
RHOB	2.84E-02	1.4	7	
TRAK1	2.10E-03	4.9	13	
TSG101	2.36E-02	1.6	16	
VIPAS39	1.46E-02	2	8	
ATP6V1A	3.37E-03	1.4	27	Transferrin Endocytosis and Recycling; Ferric Iron Transport; Hydrogen-Exporting ATPase Activity
ATP6V0A1	8.02E-03	1.3	22	
ATP6V1A	3.37E-03	1.4	27	
ATP6V1H	7.15E-04	1.5	13	

[A] FDR corrected p-value between GRN KO vs. WT neurons
[B] Upregulated: positive ratio; Downregulated: negative ratio
[C] # of peptides detected for the protein in LC-MS/MS platform

4.2 Longitudinal Imaging and Neurite Outgrowth Assays

Assessing longitudinal survival and neurite outgrowth are common approaches used to evaluate overall neuronal health, with some groups now incorporating cutting-edge image capture and analysis techniques such as super-resolution [160] and machine learning [161]. While most of my phenotypic assays will be organelle-level resolution, I wanted to incorporate these readouts as a more general assessment of neuronal function.

My initial approach was to image a polyclonal i^{3}Neuron cell line expressing a cytosolic mApple marker delivered via lentivirus, which would be bright enough to achieve robust neurite segmentation. A preliminary time-lapse experiment, shown in Figure 4.1A, shows how we can resolve neurites in i^{3}Neurons from the complete absence of neurites on re-plating day (time 0h) to very complex neurites on day 8 (time 192h), and beyond.

Figure 4.1B lays out a graphical representation of the various cell lines required for the longitudinal assays that I was developing. With high-content and CRISPRi applications in mind, I needed a multi-modal system that could be utilized for 1) cell count analysis and 2) neurite tracing analysis. To accomplish this, I utilized tools generated in the Ward Lab to target mNeonGreen, a robust fluorescent marker, to the nucleus of i^{3}Neurons to generate a polyclonal lentivirus-derived differentiating line that could be utilized for cell counts. I then implemented the tool from Figure 4.1A to target mApple to the cytosol. The resulting cell line is multi-purpose and can serve as a foundation line for longitudinal neuronal assays. Once the GFP+mApple line is transduced with a cytosolic BFP sgRNA lentivirus, as in Figure 4.1B-C, the line harbors 3 total fluorescent markers and can be utilized for cell counts and neurite tracing.

Example images of these lines are shown in Figure 4.1C; yellow arrows highlight cell-count control GFP-only neurons, white arrows highlight neurite length control GFP+mApple neurons, orange arrows highlight GFP-mApple neurons positive for an sgRNA (cytosolic BFP), appearing purple on the merge; a variant of this assay was used in [140].

Figure 4.1D is a preliminary cell count analysis that reaffirmed the need for a general neuronal health readout. The quantified results show selective vulnerability of *GRN*-KO neurons to oxidative stress after 2h Na Arsenite [500μM] treatment. To assess neurites, we needed to determine how greatly neuron density affected any potential analysis. Figure 4.1E extracted neurite length data across a range of conditions, including 5k or 15k neurons per well plating density and 5%, 15%, or 25% transduced subpopulation.

4.3 Transferrin Recycling and Uptake

4.3.1 Background

Transferrin (Tf) is the major iron delivery protein for neurons and the microvasculature within the brain, supporting the importance of homeostasis in this

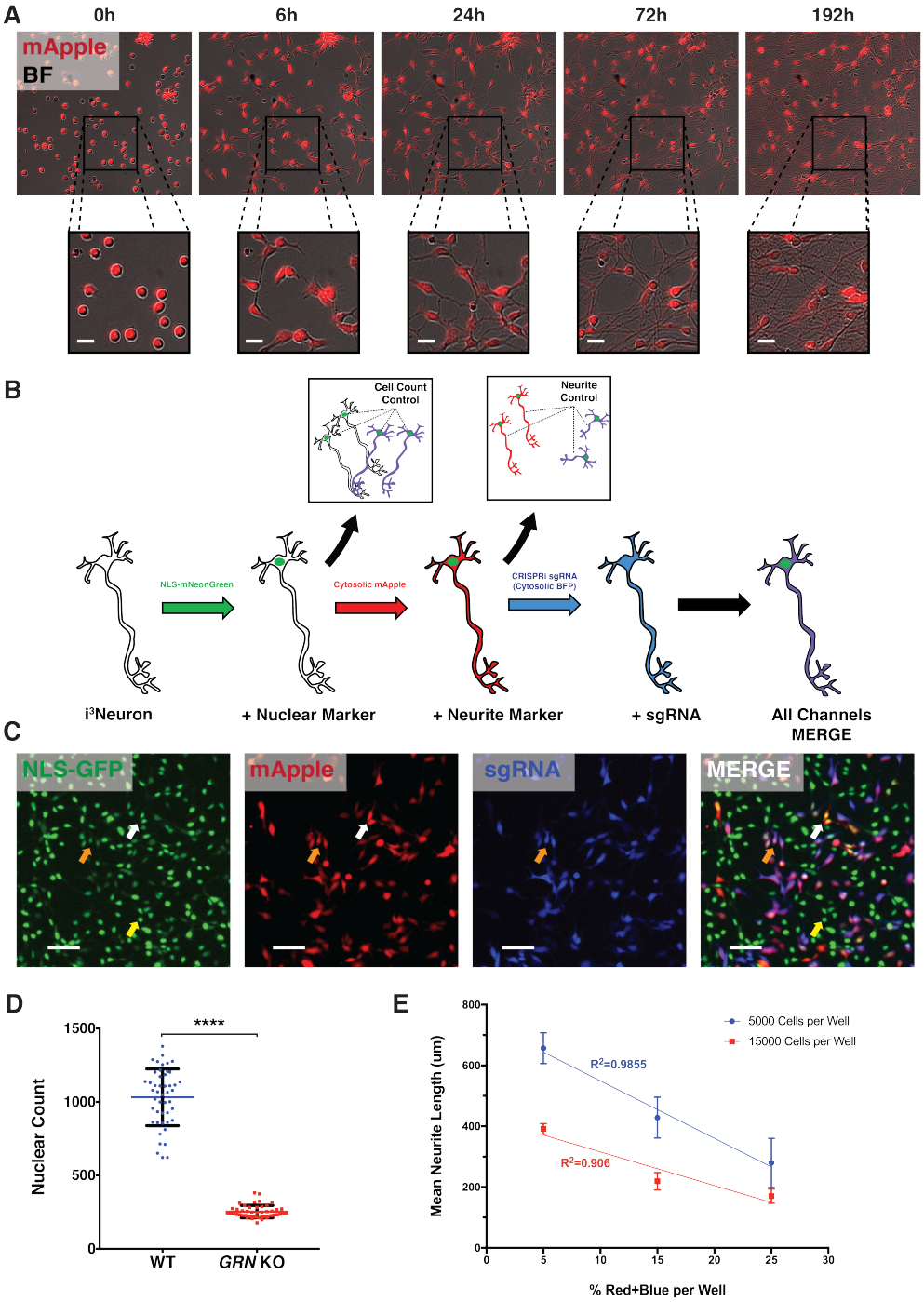


Figure 4.1: Developing Neuronal Survival and Neurite Tracing Assays. A.) Time-lapse images of i^{3}Neurons expressing cytosolic mApple from 0h to 192h in culture showing the progression of early neurite growth; BF = brightfield, scale bars = 20µm. B.) Representative schematic of i^{3}Neuron cell line generation for longitudinal survival and neurite tracing assays. C.) Example images of the lines in use; yellow arrows = GFP-only neurons, white arrows = GFP+mApple neurons, orange arrows = GFP+mApple neurons positive for cytosolic BFP sgRNA, appearing purple on the merge; scale bars = 50µm. D.) Quantification of preliminary cell count shows selective vulnerability of *GRN*-KO neurons after 2h Na Arsenite treatment; n=48 wells. E.) Quantification of preliminary neurite outgrowth analysis comparing plating density and percentage of positive cells.

pathway [162]. Alterations in the availability of the transferrin receptor (TfR), proper recycling through the endocytic pathway, and dysregulation of local iron homeostasis in various forms of neurodegeneration have been implicated in disorders such as Huntington's Disease and Parkinson's Disease [159, 163, 164].

Transferrin machinery has been identified as one of the potentially dysregulated pathways in our proximity-labeling-based proteomics analysis of iPSC-derived neurons, seen in Table 4.1. In order to validate and further understand the effect that *GRN* loss in iPSC-derived neurons has on transferrin uptake and recycling, a number preliminary experiments were planned. Initial studies using fluorescently tagged Tf and live-cell spinning disk microscopy showed no obvious differences. In order to more quantitatively analyze this pathway, a number of flow cytometry experiments were performed.

4.3.2 Transferrin recycling appears unaffected in *GRN*-KO cells

Initially, I analyzed the effects of *GRN* loss on TfR recycling by performing the uptake of tagged Tf in 3-day post-doxycycline, resuspended i^{3}Neurons. This allowed me to perform the experiment in a shared pool of cell culture medium. After 15 mins uptake with Tf conjugated to Alexa 488, the cells were chased with complete medium for 0, 5, 10 and 20 mins. Cells were washed with ice cold PBS at their respective time points, filtered, and analyzed by flow cytometry.

When background fluorescence is removed and the cells normalized by the total Tf-488 load, there appears to be no or little difference in the recycling of transferrin when comparing WT and *GRN*-KO i^{3}Neurons in Figure 4.2A. This experiment, however, was performed in 3-day post-doxycycline i^{3}Neurons, which are still under development from induced pluripotent stem cells to cortical, glutamatergic neurons. These neurons are only beginning to develop processes, yet are locked into the cortical neuron pathway via transcription factor induced differentiation. However, it is possible that Tf recycling pathways are different in fully matured neurons which have unique endocytic machinery. To rule out a potential difference, we

repeated the experiment in 6-day post-doxycycline neurons, which are further along the differentiation process and have more matured processes.

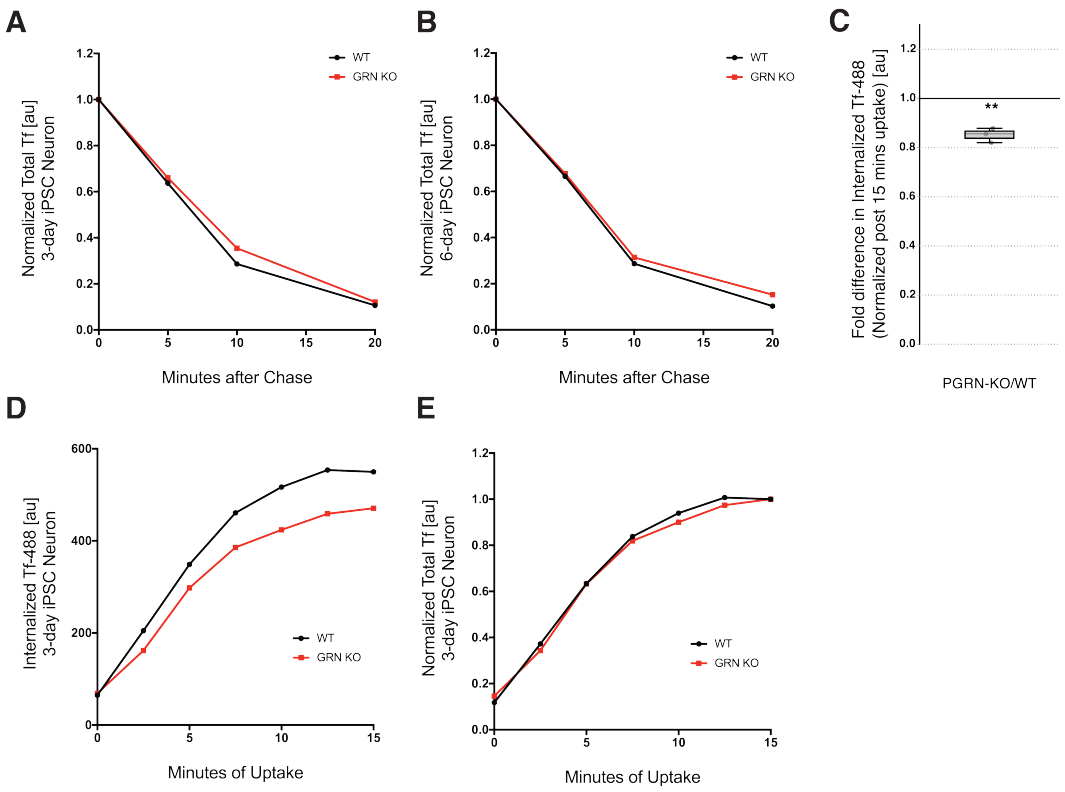


Figure 4.2: Transferrin uptake and recycling in *GRN*-KO neurons. A.) Tf-488 was added to either WT or *GRN*-KO 3-day post-doxycycline neurons for 15 mins before being chased for indicated times. The plot represents the geometric mean of Alexa 488–Tf intensity for the population of cells (p ≥ 35,000 cells) as a function of time. B.) As in A, with 6-day post-doxycycline neurons (p ≥ 5000 cells). C.) Fold difference of internalized Tf-488 in *GRN*-KO neurons compared to WT; Combined data of 3 repeats of Tf uptake after 15 mins from either WT or *GRN*-KO day-3 and day-6 post-dox neurons. Data was normalized within each experiment to WT uptake after 15 mins (3 repeats with a minimum of 5000 cells per experiment, significance calculated using Student's t test, **p ≤ 0.01). D.) Tf-488 was added to either WT or *GRN*-KO 3-day post-doxycycline neurons over the course of 15 mins, with samples removed every 2.5 mins at the indicated times. The plot represents the geometric mean of Alexa 488–Tf intensity of the population (p ≥ 75,000 cells) as a function of time. E.) As in D, with data normalized to the last time point, 15 mins (p ≥ 75,000 cells).

4.3.3 Total transferrin uptake is decreased in *GRN*-KO cells

After removing background fluorescence and normalizing by total Tf-488 load, there also appears to be no or little difference in the recycling of labeled transferrin

when comparing 6-day post-dox neurons, as shown in Figure 4.2B. However, I also observed in three cases that at time 0 there was less labeled Tf in the *GRN*-KO neurons than the WT, which implies a difference in the total Tf uptake. When all data after 15 mins uptake is combined, this difference is statistically significant ($p = 0.006$, Figure 4.2C).

To investigate this claim further, I performed an experiment to test Tf-488 uptake rather than recycling. After adding exogenous Tf-488 to the cells, I arrested further uptake at different time points (0, 2.5, 5, 7.5, 10, 12.5, 15 mins), and subsequently probed the rate and overall uptake of labeled Tf in the neurons. Cells were washed, filtered, and analyzed by flow cytometry in Figures 4.2D-E. As shown in Figure 4.2D, I observed a difference in the total Tf uptake into the neurons as before in Figure 4.2C; when combined with results from Figures 4.2A-B, the difference is statistically significant ($p = 0.006$, Figure 3C). However, Figure 4.2D shows that the rate of uptake is comparable between WT and *GRN*-KO i^{3}Neurons.

4.4 Measuring Lysosomal pH

4.4.1 Background

Perturbations of lysosomal acidification have been shown to play a major role in certain neurodegenerative diseases, such as lipid accumulation in Niemann-Pick type C1 (NPC1) and inhibition of autophagy in Presenilin 1-related Alzheimer's Disease [69, 158]. Proteomic results generated by the Ward Lab implicated potentially dysregulated pathways, such as the acidification of endocytic components (recycling endosome, late endosomes, and/or lysosomes) as well as cellular and/or lysosomal calcium homeostasis (Table 4.1).

To measure lysosomal acidification, we chose a technique modified from Saric et al. [141], which utilizes a pH-*sensitive* green probe (Oregon Green-488 dextran), by adding a loading control also serving as a pH-*insensitive* probe (Alexa-555 red dextran). These dextrans accumulate in the terminal endocytic compartments following an overnight chase, and measurement of their fluorescence will allow

for ratiometric calculations of pH within individual lysosomes. Combining these measurements with an *in-situ* calibration using solutions of known pH enables accurate measurements of pH within the lysosome.

4.4.2 Measuring Lysosomal pH: Transforming a low-throughput imaging assay to high-content formats

Both dextran probes were loaded onto i^{3}Neurons in an 8-well glass slide for 4 hours and chased with neuronal media overnight the day before imaging, shown diagrammatically in Figure 4.3A. The initial results from our pulse-chase ratiometric method for measuring lysosomal pH are quantified in Figures 4.3B-C. The assay requires an initial calibration step, where several wells of WT i^{3}Neurons are individually exposed to solutions of known pH containing nigericin and subsequently imaged. The intensity of the pH-sensitive Oregon green dextran and pH-insensitive Alexa 555 dextran are analyzed in a ratiometric fashion across the various pH exposures and later used to generate the calibration curve seen in Figure 4.3B.

In parallel, experimental sample wells were also imaged and analyzed, at which point the ratiometric values can be back calculated to pH. The preliminary data from the low-throughput lysosomal pH experiments, quantified in Figure 4.3C, showed only a mild difference in lysosomal pH between WT and *GRN*-KO i^{3}Neurons, which did not reach statistical significance. This finding pushed me toward further assay optimization by scaling up the entire assay to 96-well formats and high-content imaging, shown in Figure 4.3D.

After optimizing plating and experimental parameters, my first high-content imaging assay for lysosomal pH was performed and the quantification, shown in Figure 4.3E, reached significance. Figure 4.3E shows that the lysosomal pH of *GRN*-KO neurons is significantly elevated compared to WT counterparts (n=5 wells per condition, p-value < 0.0001).

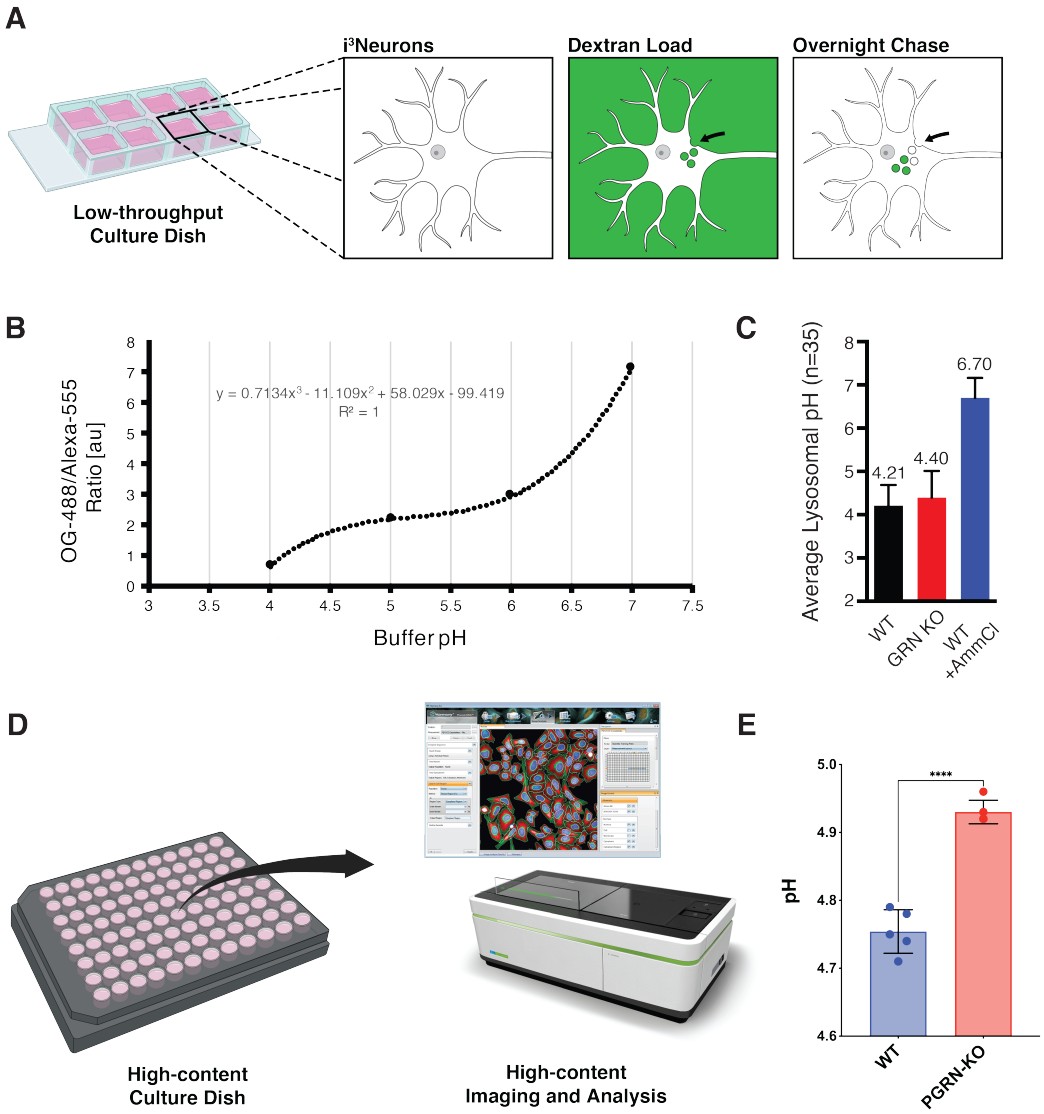


Figure 4.3: Measuring Lysosomal pH: Adapting a low-throughput assay to high-content applications. Preliminary lysosomal pH assay showing A.) Representative schematic of a pulse-chase experiment, where pH-sensitive dextrans are loaded into i^{3}Neurons on low-throughput culture dishes. B.) Calibration curve fitted to ratiometric intensity measurements in neurons exposed to solutions of known pH. C.) Quantification and preliminary results from the low-throughput analysis method; n=35 lysosomes per condition. D.) Representative schematic showing an example high-content culture dish and tools used for HCA and HCS. E.) Quantification and preliminary results from the high-content imaging and analysis methods; n=5 wells per condition, p-value < 0.0001.

4.4.3 Lysosomes in *GRN*-KO i^{3}Neurons have alkaline pH and fail to acidify

In order to confirm the initial findings that *GRN*-KO i^{3}Neurons were unable to acidify their lysosomes, I performed a series of repeat experiments to validate the phenotype and replicate my findings from the high-content optimization. Figure 4.4A shows a series of images from WT control wells that were clamped at the corresponding pH. The increase in fluorescent signal from the pH-*sensitive* dextran probe can be visualized in this panel alongside the increase in pH of the control solutions.

Dextran probes were loaded onto WT and *GRN*-KO i^{3}Neurons in 96-well plates for 4 hours and chased with neuronal media overnight. An example calibration curve generated to analyze sample wells for one of the plates is shown in Figure 4.4B. Quantification of our high content imaging data, shown in Figure 4.4C, demonstrated that the mean lysosomal pH observed across all experiments in WT and *GRN*-KO i^{3}Neurons was approximately 4.3 and 4.8, respectively. These findings indicate an average significant difference of approximately 0.5 pH units between the lysosomes of WT vs *GRN*-KO neurons, where *GRN*-KO neurons have highly alkalinized lysosomes (n=3 repeat experiments, p-value < 0.0001). While this may seem like a subtle change, the concentration of protons in the lysosomal compartment of *GRN*-KO neurons had a nearly three-fold decrease compared to WT counterparts ([H+] in WT $\approx$ 50µM, *GRN*-KO $\approx$ 16µM).

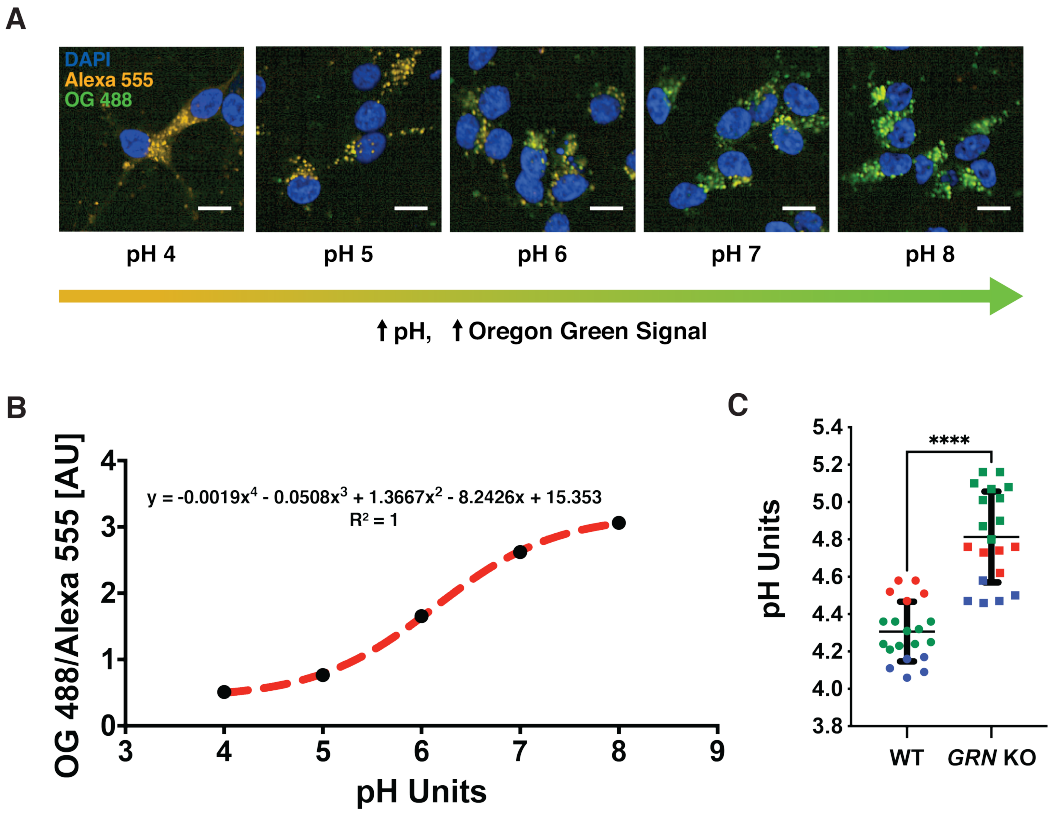


Figure 4.4: Lysosomes in *GRN*-KO i^{3}Neurons have alkaline pH and fail to acidify. A.) Representative images displaying the increase in Oregon Green 488 intensity within the control wells containing known pH solutions; scale bars = 10µm. B.) Quantification of A, shown as a 4th order calibration curve used to calculate pH in sample wells. C.) Lysosomal pH measurements performed in WT vs. *GRN*-KO i^{3}Neurons; three independent experiments were performed, each represented by a different color, where each dot represents a biological replicate; p-value < 0.0001.

4.5 Evaluating Lysosomal Proteolysis

4.5.1 Background

In response to the findings that lysosomes within *GRN*-KO i^{3}Neurons are highly alkalinized, I predicted that these lysosomes would also have decreased degradative properties. To further interrogate this, I performed an orthogonal lysosomal assay utilizing the DQ-BSA Red and DQ-BSA Green reagents in order to measure active proteolysis within the lysosomes of neurons. This assay produces a readout of the degradative capacity of a cell via fluorescence, as shown in the Figure 4.5A schematic.

Upon uptake of DQ-BSA substrate, the BODIPY fluorophores conjugated to bovine serum albumin (BSA) molecules are initially self-quenched due to their close spatial proximity. As the DQ-BSA reagent proceeds through endocytic pathway, trafficking vesicles mature and eventually fully acidify by fusing with terminal lysosomes. These acidic compartments are actively degradative and lead to the complete digestion of BSA molecules and subsequent dequenching of the fluorophores. This allows for an increase in fluorescence intensity in those compartments, providing for several outcome measurements to be made. An example image of DQ-BSA puncta in i^{3}Neurons can be seen in Figure 4.5B. Carling et al. previously used this assay as a phenotypic readout for lysosomal function in SH-SY5Y-based high-content compound screens [74].

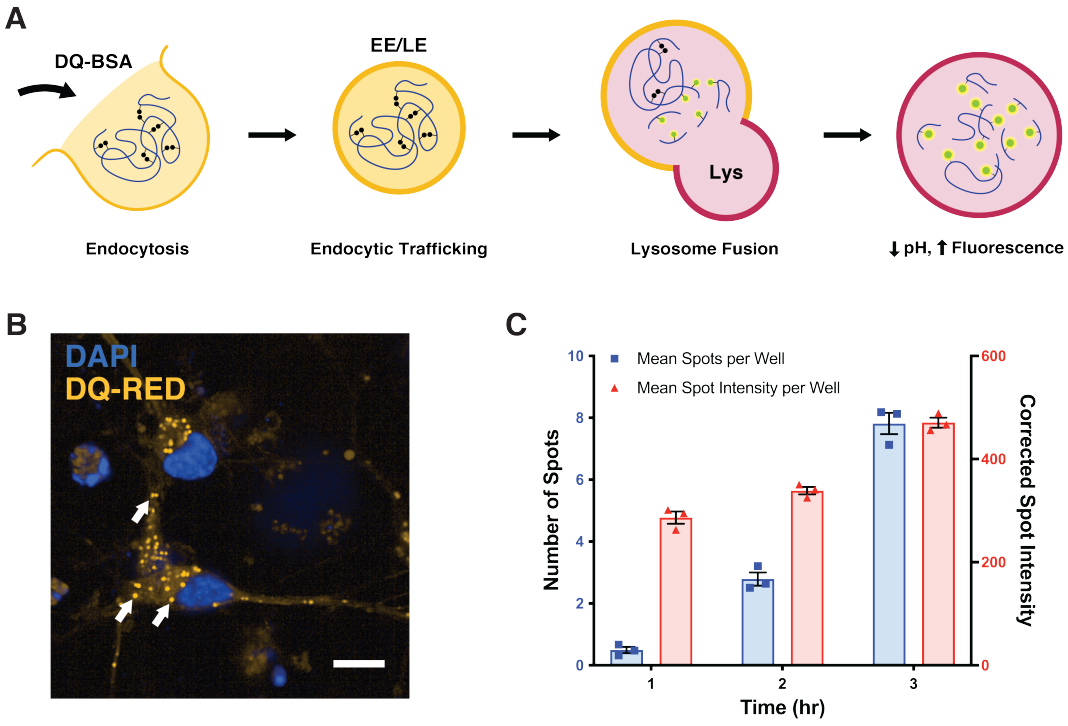


Figure 4.5: Evaluating Lysosomal Proteolysis via DQ-BSA, 3hrs uptake. Preliminary DQ-BSA assay showing A.) Representative schematic of the DQ-BSA assay and how the reporter is processed through the endocytic pathway. B.) Representative image of DQ-BSA Red assay showing DQ-labeled acidic compartments in i^{3}Neurons, intensity of the compartments correlates to the degradative capacity of the cell. C.) Quantification of DQ-BSA activity outcome measures *Number of Spots* and *Corrected Spot Intensity* averaged per cell per well, after 1, 2, and 3 hours uptake; n=3 wells per condition.

4.5.2 Optimization of the DQ-BSA Assay in i^{3}Neurons

The DQ-BSA assay has several potential endpoints that can be quantified. Two of the most commonly used are spot intensity and number of spots, as they are reliable endpoints and represent different aspects of lysosomal function or activity. Quantification of these two measures in a preliminary DQ-BSA experiment are shown in Figure 4.5C.

These measures can be significantly reduced pharmacologically by the lysosomal inhibitor Chloroquine (CQ) [74, 165, 166]. Chloroquine acts as a strong positive control for decreased lysosomal activity in the DQ-BSA assay because the compound is a lysosomotropic agent that prevents acidification in lysosomal compartments, inhibiting lysosomal enzymes and cargo degradation.

In Figure 4.6, i^{3}Neurons treated with increasing concentrations of CQ show a clear reduction in lysosomal activity, confirming the assay is functioning and that assay windows can be determined. The white arrows in Figure 4.6A point out the absence of red puncta at the higher end of the dose-response curves compared to untreated WT i^{3}Neurons, quantified in Figure 4.6B and Figure 4.6C. Both phenotypic outcome measures showed clear dose-responses when treated with CQ, Figure 4.6B representing the response in Corrected Spot Intensity, and Figure 4.6C representing the response in Number of Spots.

A direct comparison of the results for untreated i^{3}Neurons vs the 50μM CQ treatment at 1hr, 2hrs, and 3hrs uptake incubation can be seen in Figure 4.6D and Figure 4.6E. The largest difference is observed at the 3hrs uptake time-point, indicating the assay window is tightly related to overall incubation time and can be further optimized.

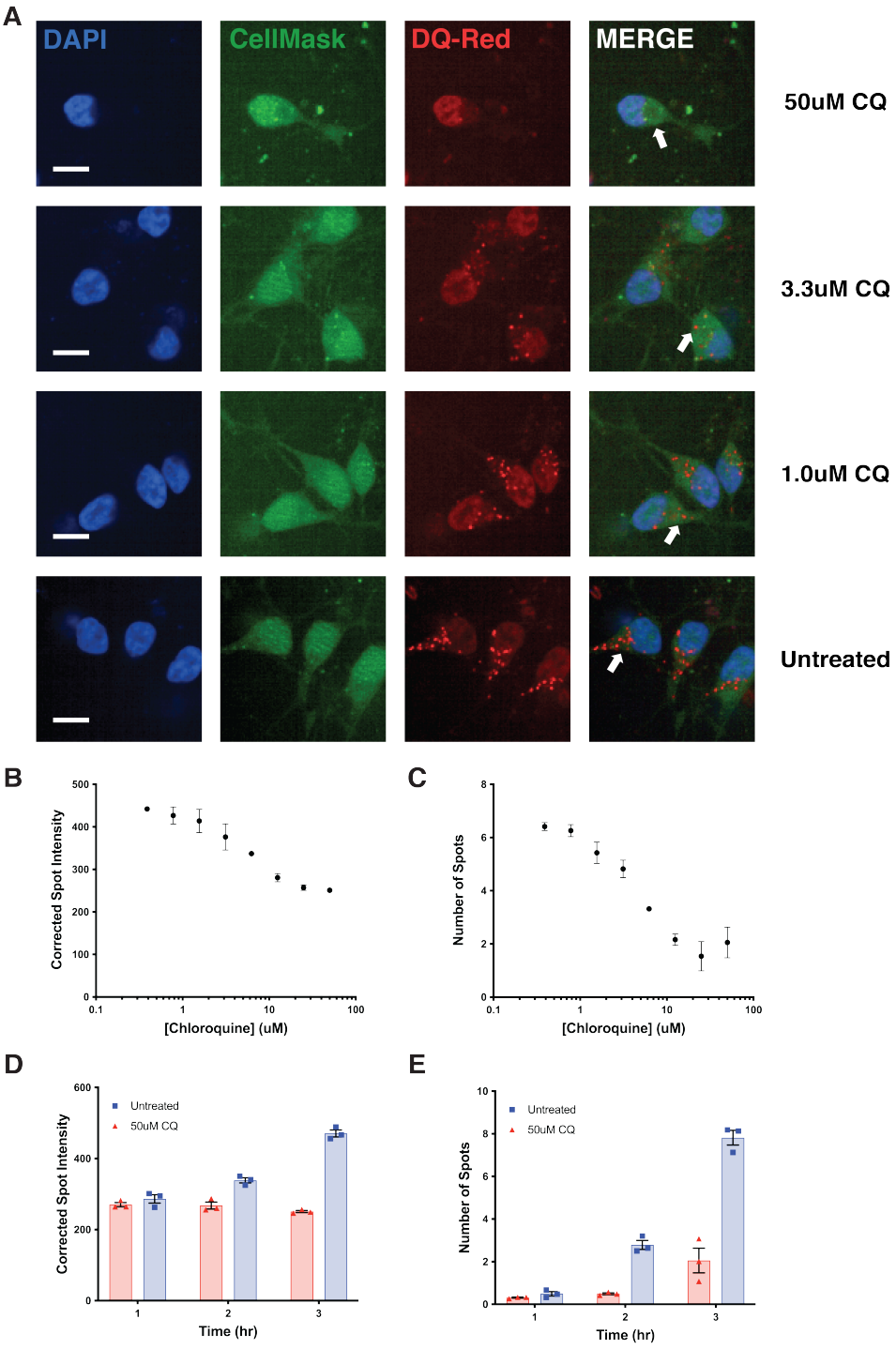


Figure 4.6: DQ-BSA Dose-Response to Chloroquine, 3hrs uptake. A.) Representative images of Chloroquine dose-response after overnight treatment; scale bar = 10µm. B.) Quantification of Corrected Spot Intensity per cell per well in response to the concentration of Chloroquine treatment. C.) Quantification of Number of Spots per cell per well in response to the concentration of Chloroquine treatment. D.) Quantification of DQ-BSA activity outcome measures 'Number of Spots' and 'Corrected Spot Intensity' averaged per cell per well, after 1, 2, and 3 hours uptake; n=3 wells per condition. E.) Quantification of DQ-BSA activity outcome measures 'Number of Spots' and 'Corrected Spot Intensity' averaged per cell per well, after 1, 2, and 3 hours uptake; n=3 wells per condition.

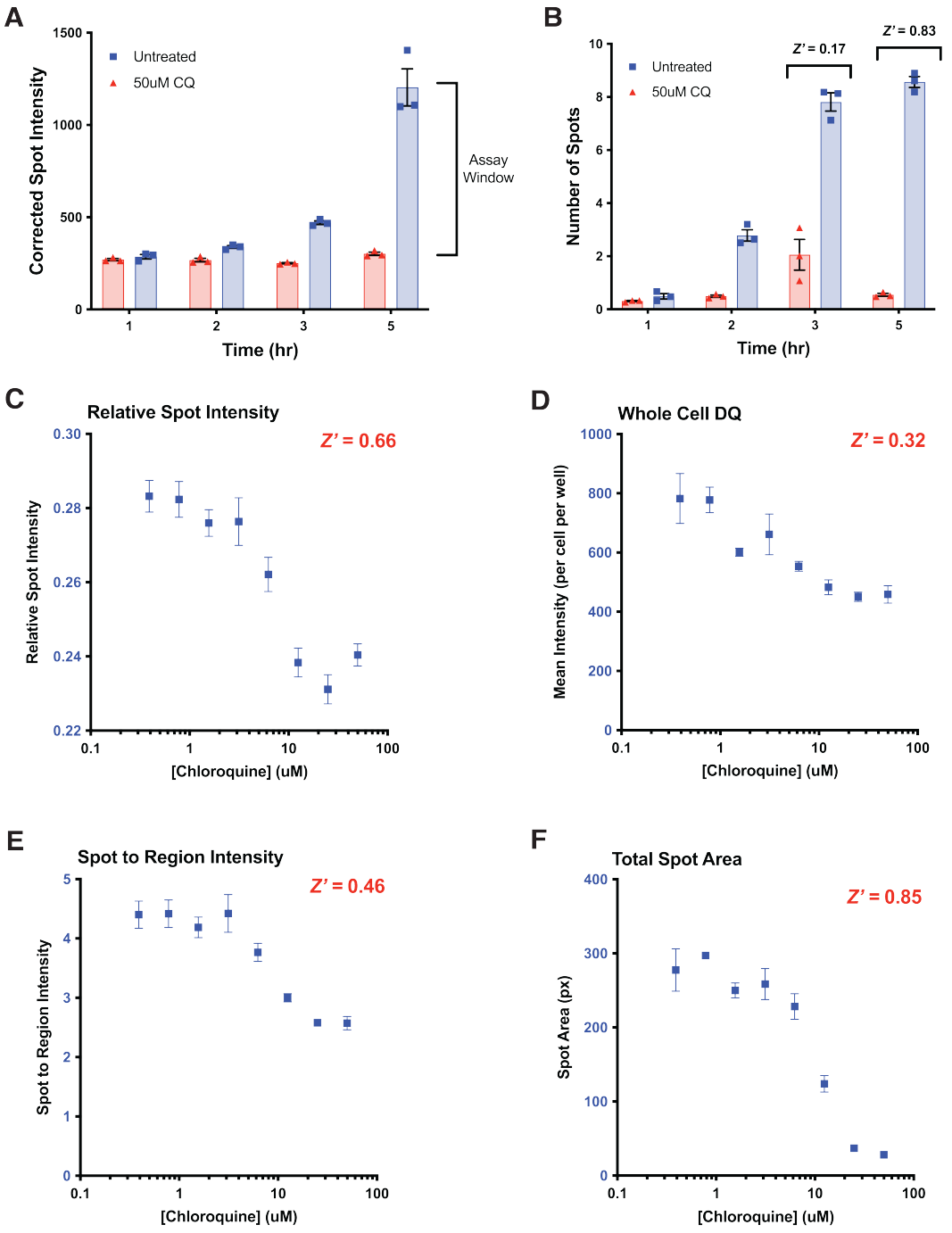


Figure 4.7: DQ-BSA Assay Window Optimization, 5hrs uptake. Preliminary DQ-BSA assay showing A.) Corrected Spot Intensity and B.) Number of Spots quantification for untreated vs 50µM CQ treated i^{3}Neurons over a time course of 5 hours; the *z'* value for Number of Spots per cell per well increased from 0.17 to 0.83 when measured at 5hr vs 3hr time-point; n=3 wells per condition. C.-F.) Other outcome measures were also quantified with a dose-response to chloroquine in order to determine reliable readouts, *Z'* values shown; n=3 wells per condition.

The results from the 3-hour time-point DQ-BSA experiments were determined not to have a large enough assay window for phenotypic screening but were still very informative. Therefore, I expanded the time course to 5 hours in order to allow for additional DQ-BSA loading and separation between the untreated and CQ treated conditions. This separation can clearly be seen in Figure 4.7A and Figure 4.7B, where both spot intensity and number of spots have a much greater Δ *outcome* between untreated and CQ groups in the 5-hour time-point vs. the 3-hour time-point.

The z-prime of a particular assay *(Z')* is defined in terms of four parameters: the positive control mean (μ_p) and standard deviation (σ_p), and the negative control mean (μ_n) and standard deviation (σ_n).

$$Z' = 1 - \frac{3(\sigma_p + \sigma_n)}{|\mu_p - \mu_n|}$$

The *Z'* value for number of spots at the 3-hour time-point was only 0.17, whereas the 5-hour timepoint scored much higher at 0.83. Other endpoints were measured in Figures 4.7C-F, where total spot area (Z'=0.85) and relative spot intensity (*Z'*=0.66) were the top performers.

Table 4.2: Interpreting the Z-prime value.

Z-prime (*Z'*)	**Interpretation**
1.0	Ideal, Z-factors can never exceed 1
between 0.5 and 1.0	An excellent assay
between 0 and 0.5	A marginal assay
less than 0	Overlap between the positive and negative controls for the assay is too high

4.5.3 Lysosomes in *GRN*-KO i^{3}Neurons exhibit decreased active proteolysis

After the initial assay optimization was complete, I carried out a series of experiments aimed at 1) utilizing DQ-BSA to further validate the lysosomal pH phenotype established in *GRN*-KO i^{3}Neurons shown in Figure 4.4 and 2) increasing the throughput of my high-content imaging assays by expanding our neuronal cultures to 384-well imaging formats. Figure 4.8A lays out the concept map for the increase in throughput. 384-well formats allow for an expanded experimental design, including more well replicates, more experimental conditions, and higher statistical confidence per experiment. A key breakthrough in my DPhil has been the complete optimization of i^{3}Neuron culture and maintenance on these high-content and high-throughput applications, which has ultimately allowed for the arrayed CRISPRi functional genomics screens to proceed.

In order to further validate our lysosomal pH findings, I chose to incorporate another disease cell lineage into these experiments, as a positive control. Figure 4.8B compares the lysosomal pH of *NPC1*-KO and *GRN*-KO i^{3}Neurons to WT. These *NPC1*-KO neurons were generated by a collaborator to the Ward Lab and exhibit clear disease pathology, as shown by Prabhu et al. [167]. Both *NPC1*-KO and *GRN*-KO neurons have elevated lysosomal pH when compared to WT i^{3}Neurons (n=10 wells per condition; $p < 0.0001$).

The results in Figure 4.8C show that *GRN*-KO neurons had a significant decrease in corrected spot intensity, while *NPC1*-KO neurons show a subtle decrease (ns) similar to the results seen in the lysosomal pH assay (Figure 4.8B). Neither *GRN*-KO neurons or *NPC1*-KO neurons showed significant changes in number of spots when compared to WT, shown in Figure 4.8D. However, the *NPC1*-KO neurons in Figure 4.8E showed a significant increase in lysosomal spot area compared to WT, while *GRN*-KO neurons had a subtle decrease in spot area.

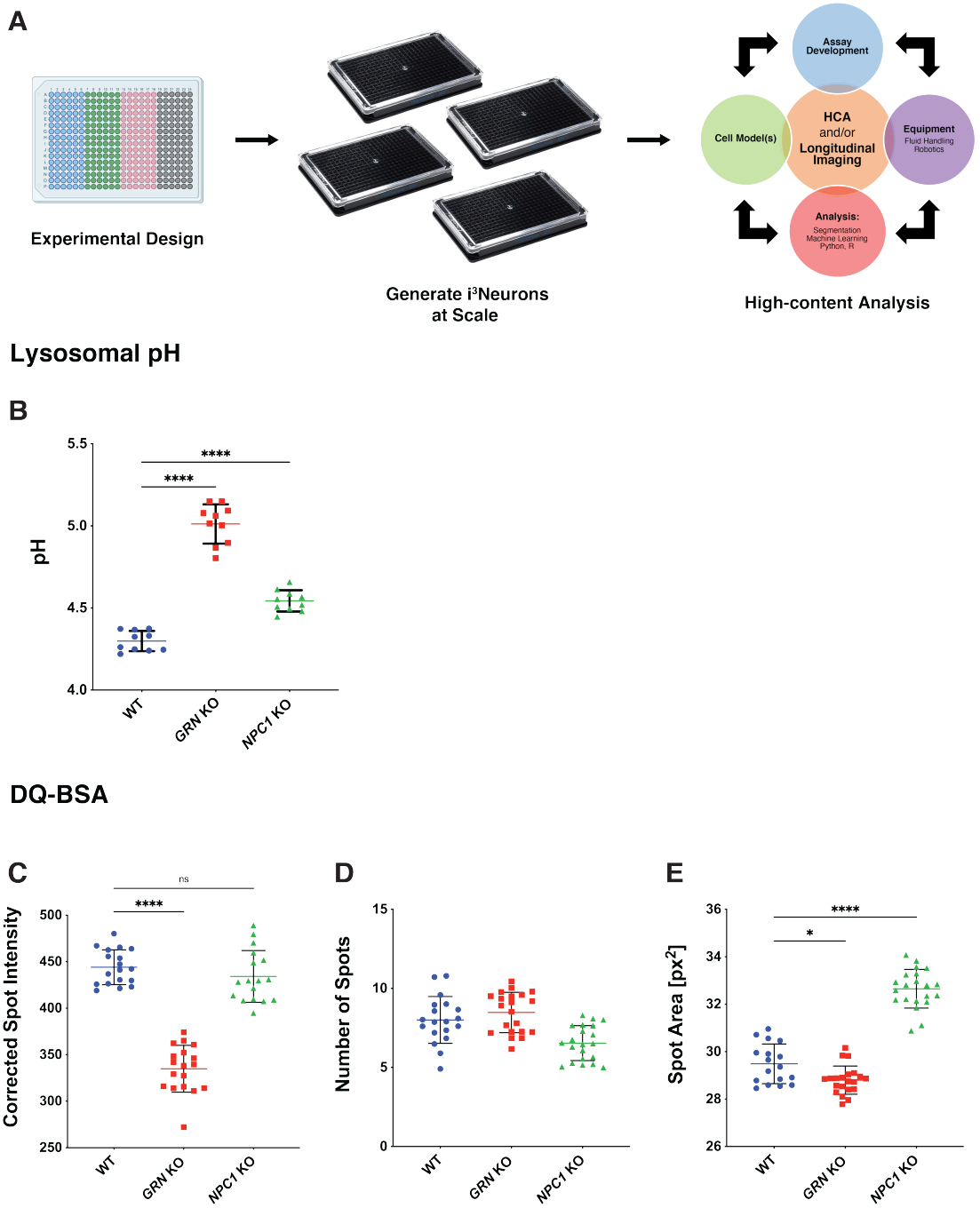


Figure 4.8: Lysosomes in *GRN*-KO i^{3}Neurons exhibit decreased active proteolysis. A.) Concept map for utilizing high-content imaging and high-throughput cell culture formats. B.) Lysosomal pH measurements performed in WT, *GRN*-KO, and *NPC1*-KO i^{3}Neurons; n=10 wells per condition, p-values < 0.0001. Quantification of DQ-BSA assay endpoints C.) Corrected Spot Intensity, D.) Number of Spots, and E.) Spot Area to assess lysosomal function; n=18 wells per condition, *p-value <0.05, ****p-values < 0.0001.

4.6 DQ-BSA single knockdown CRISPRi screen reveals disease-associated lysosomal modulators and recapitulates *GRN*-KO dysfunction

Throughout much of assay optimization, I have utilized key i^{3}Neuron *knockout* lines that enabled me to gauge analysis methods and assay windows while probing for potential phenotypes related to *GRN* biology, as this gene is a focus of the Ward Lab. Following the successful implementation of the DQ-BSA assay in knockout i^{3}Neuron lines, I was ready to attempt a preliminary CRISPRi screen that would only knockdown a single gene per sample. This coincided with the final targeted RNA sequencing sample generation in Chapter 3, Figure 3.16 and Tables A.5-A.4.

Figure 4.9B represents a previous experiment where DQ-BSA was loaded onto WT and *GRN*-KO i^{3}Neurons in 384-well plates for 5 hours and imaged to analyze the fluorescent puncta in each cell. The resulting quantification demonstrated that the corrected spot intensity observed across all experiments in *GRN*-KO iPSC-derived neurons was significantly decreased when compared to WT counterparts (Figure 4.9B, p-value < 0.0001).

Remarkably, the quantification of the DQ-BSA assays for a subset of the single knockdown screen samples, shown in Figure 4.9C, recapitulate the findings in the *GRN*-KO lines. *GRN* knockdown and and *GRN* knockout are both indicating a decrease in decreased active proteolysis. Surprisingly, *TMEM106B* and *CTSL* knockdown both showed the opposite phenotype in the assay, suggesting that active proteolysis had increased in those lines.

Using the arrayed CRISPRi screening platform established in Chapter 3, I generated 3 identical high content plates that systematically knocked-down each target gene of interest via the nuclear blue system (see Table A.2 for sgRNA list). These plates were screened through the DQ-BSA assay, measuring any changes to lysosomal function in each knockdown cell line, shown in Figure 4.9D.

Those hits above the cutoff z-score of +3 represent an increase in lysosomal activity, those below a z-score of -3 represent a decrease in lysosomal activity as a phenotypic readout of DQ-BSA corrected spot intensity. Some hits across the

screen were very high-performing, such as CTSL-1/CTSL-2 both having z-scores of approximately +10, while ATP6V0A1-1 performed well to deacrease lysosomal activity with a z-score of approximately -10. Non-targeting controls are seen in grey at the far left of the hit map, grouping near 0. Chlororquine (CQ) was positive control sample for decreases in lysosome activity, with a z-score between -5 and -10.

The value of the z-score represents the magnitude and direction between a measurement and the population mean, put in terms of the standard deviation of the measurement. A particular z-score will be positive when the raw score is above the mean, negative when below. The z-score of a particular measurement *(z)* is a standardized score that describes the relationship of value to the mean of a group of values, as defined in terms of three parameters: the observed value *(x)*, the sample mean (μ), and the sample standard deviation (σ), as shown in the equation:

$$\text{z-score: } z = \frac{x - \mu}{\sigma}$$

The most significant hits for decreased lysosomal activity were from sgRNAs targeting *ATP6V0A1*, *VPS35*, *SCARB2*, *GRN*, *PSAP*, *CRLS1*, *FUS*, *KIF5A*, *SOD1*, *TAX1BP1*, and *VCP*. The most significant hits for increased lysosomal activity were from sgRNAs targeting *CTSL*, *TMEM106B*, *CLN8*, *ATP13A2*, and *PFN1*. Interestingly, targets related to *GRN* through either direct or indirect interaction were enriched in the hits seen both above and below the cutoffs; these were *CTSL*, *TMEM106B*, and *PSAP*.

Summaries of the corresponding sgRNAs and their z-scores can be seen in ranked order in Table 4.3 and Table 4.4 on the next page.

Table 4.3: Single Knockdown Hits Decreasing Lysosomal Function

sgRNA	**z-score**
ATP6V0A1-1	-11.5
VPS35-2	-8.3
VPS35-1	-7.1
SCARB2-1	-6.3
GRN-F3	-5.7
TAX1BP1-1	-5.4
CRLS1-2	-5.0
SCARB2-2	-4.9
PSAP-E5	-4.6
SOD1-1	-4.3
VCP-G8	-4.2
FUS-C3	-3.7
KIF5A-1	-3.7

Table 4.4: Single Knockdown Hits Increasing Lysosomal Function

sgRNA	**z-score**
CTSL-2	12.1
CTSL-1	12.0
TMEM106B-E7	10.3
CLN8-2	6.9
CLN8-1	6.8
ATP13A2-2	3.4
PFN1-1	3.1

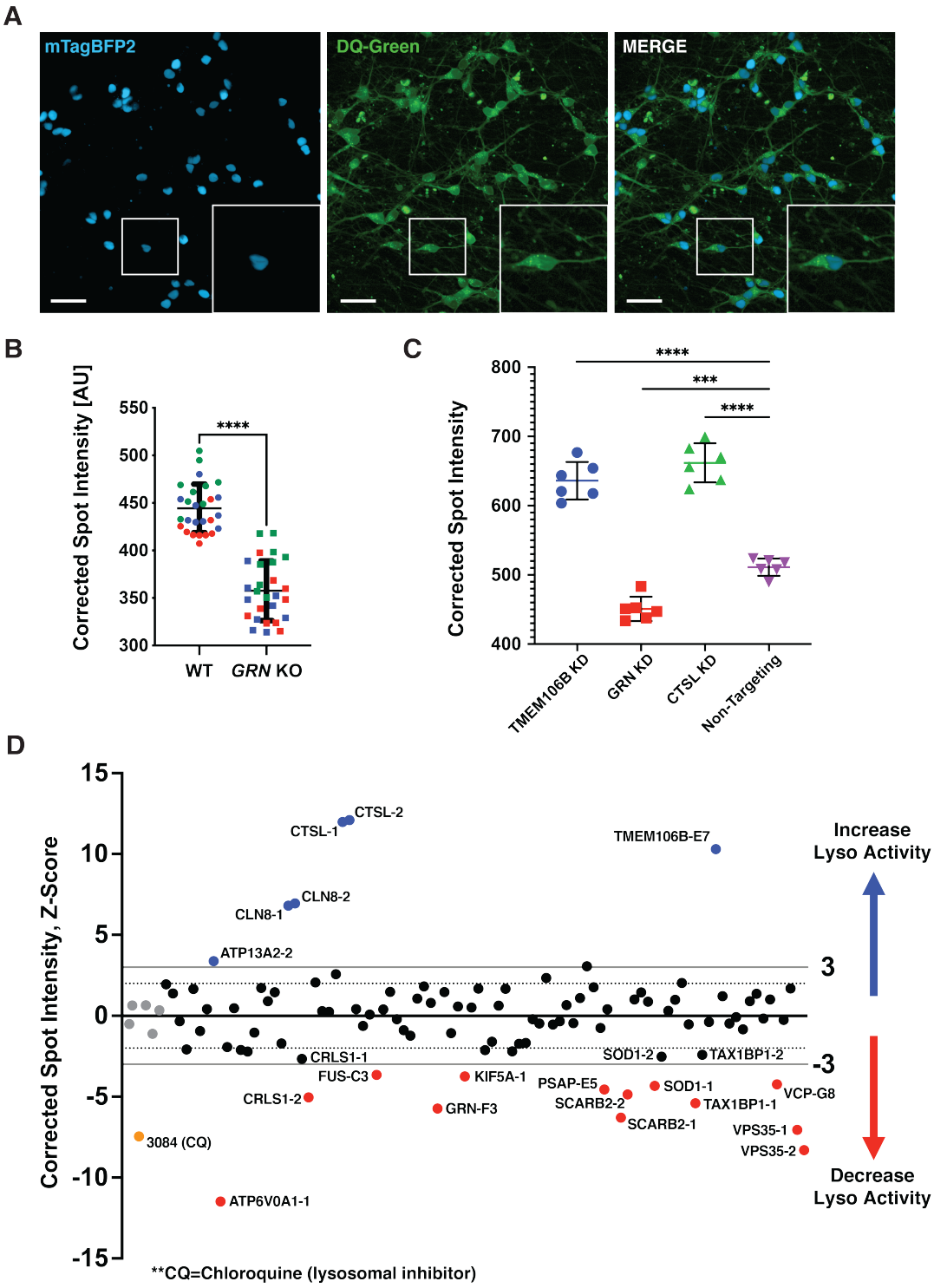


Figure 4.9: DQ-BSA single knockdown CRISPRi screen reveals disease associated lysosomal modulators. (Caption next page.)

Figure 4.9: (Previous page.) DQ-BSA single knockdown CRISPRi screen reveals disease associated lysosomal modulators. A.) Representative images of the DQ-Green assay in i^{3}Neurons transduced with an sgRNA from the nuclear blue CRISPRi system; scale bar = 30µm. B.) Quantification of DQ-BSA assay endpoint Corrected Spot Intensity, measurements performed in WT and *GRN*-KO i^{3}Neurons; three independent experiments were performed, each represented by a different color, where each dot represents a biological replicate; p-value < 0.0001 C.) Quantification of DQ-BSA assay endpoint Corrected Spot Intensity, chosen from (D) showing all replicates from measurements performed in CRISPRi i^{3}Neurons transduced by non-targeted, TMEM106B, GRN, and CTSL nuclear blue sgRNAs; n=6, 2 technical replicates on each of 3 plates, ***p-value <0.001, ****p-value < 0.0001. D.) Single KD Screening Hits, Corrected Spot Intensity outcome measure; each point represents the mean z-score from 3 separate plates of single gene knockdown cell lines. Dotted lines mark the cutoff of ± 2σ from the control mean; n=6, 2 technical replicates on each of 3 plates.

4.7 Discussion

In Chapter 4, I successfully demonstrated the development and optimization of several key neuronal assays, including longitudinal survival and neurite outgrowth, transferrin recycling and uptake, as well as key lysosomal activity assays that measure pH and active proteolysis. These assays were also adapted to multi-well formats, including high-throughput 384 well screening dishes, and thoroughly vetted for application into high-content imaging screens and analysis. Of these, assessing lysosomal proteolysis via DQ-BSA was chosen as the most robust and reproducible for screening, culminating in the functional validation of many of our sgRNAs in the first of a series of CRISPRi-based phenotypic screens.

Neuronal Survival and Neurite Outgrowth

My preliminary neurite tracing experiments demonstrated that it was possible to set up the expression tools needed to perform precise neurite outgrowth tracing without the need for further dyes or reagents. The system I developed also allows for repeated measurements, both for neurite outgrowth and nuclear counts, across time requiring only routine neuronal maintenance.

Figure 4.1A and Figure 4.1E showed that neurite length increases very quickly and early on in i^{3}Neuron development, and that increases in labeled neurite populations increases complexity, such as branch points, nodes, and other advanced

neuronal features (Figure 4.1A), while equally decreasing the sensitivity for detection of features such as overall length (Figure 4.1E). However, relative neurite length comparisons seemed to be maintained no matter the cell density, an important finding that is favorable for high-content screening. This makes sense, as when you increase the overall neuronal population it will become harder and harder to resolve individual neurites and overall length measurements. The results in Figure 4.1E suggest that relative measurements of overall neurite length are quite robust, but that more accurate measurements would depend on the overall seeding density. Untangling these features in future analysis will provide many outcome measurements from a single assay.

Another key observation relates to the potential weaknesses of the assay, referring to the mix of labeled populations of neurons. This potential heterogeneity can be harnessed as a tool, instead of being ignored or seen as a flaw, as shown in Figure Figure 4.1B. A delicate balance must be achieved in this assay that 1) allows for proper neuron seeding density so cultures do not collapse and 2) provides enough labeled neurites for phenotypic detection. This is not immediately straightforward, as I have optimized cell densities for 96 and 384-well platforms that permit i^{3}Neurons to thrive, but if a single population of GFP+mApple neurons were used, then the assay window for relative neurite length would likely not exist. Moreover, the percentage of neurons positive for your sgRNA of interest are also determined by the route of transduction, efficiency of your lentivirus preps, and other factors. Lentiviral transductions are often incomplete, leaving a sub-population of cells with your expression vector and a sub-population of cells without.

Therefore, it is necessary to seed each well with all three sub-populations consisting of the base GFP-only, GFP+mApple line, and GFP+mApple+BFP (sgRNA postive) line. The GFP-only line provides the necessary padding for overall seeding density without interfering with the neurite assay, while simultaneously providing an in-well WT control line for nuclear counts. The GFP+mApple line may or may not simply represent the "non-transduced" population of neurons in culture, depending on the method of transduction. However, these "missed" cells

can provide an in-well neurite length control, if needed. Lastly, the actual reporter line for the phenotypic assay will be the sgRNA-positive BFP neurons, but having these sub-populations present assist with confidence in any results.

Transferrin

Much of our understanding of endocytic recycling has come from studies regarding the transferrin receptor. A potential flaw in such a fundamental aspect of the endocytic pathway may point to an additional (albeit indirect) role of *GRN* in cellular homeostasis. One potential functional consequence would be decreased iron availability for neurons, which may reduce survivability. Moreover, perhaps the vATPases required for late endosome/lysosome acidification and mobilization of transferrin from its receptor play a role in this process (Table 4.1). However, our initial experiments seem to demonstrate intact rates of uptake and recycling, with only overall uptake being reduced (Figure 4.2), and glial cells do not appear to depend upon Tf for iron uptake [162].

Our preliminary findings suggest that Tf recycling pathways are unaffected, while overall uptake seems to be decreased in *GRN*-KO i^{3}Neurons. A difference in total Tf-488 between WT and *GRN*-KO which is independent of the rate of Tf uptake may be due to 3 potential reasons: decreased cell surface binding of the Tf to the receptor, decreased total transferrin receptor in the cell, or decreased export of TfR from the ER/Golgi to the endocytic recycling system. Further experiments will be needed to distinguish between these three hypotheses.

Iron homeostasis has been directly implicated in neurodegenerative diseases, yet the importance of Tf in this process seems to be underappreciated. Several connections between neurodegeneration and iron overload currently exist, as opposed to iron deficiency or decreased Tf/TfR [163]. With total Tf uptake reduced, we must begin to postulate whether there is decreased cell surface binding of Tf to the receptor, decreased total TfR in the cell, or decreased export of TfR from the ER/Golgi to the endocytic recycling system. A combination of western blot for total protein and immunofluorescence will help to determine overall levels of TfR and its cellular distribution. These experiments will be key in validation of

this potential phenotype, and will help determine the cause of decreased Tf-488 uptake in the absence of *GRN*.

Lysosomal pH

Ion homeostasis in acidic organelles, primarily lysosomes, is a fundamental process for many of the "housekeeping roles" that these organelles perform within a cell. Specifically, the regulation of protons (H^+) in these organelles is closely intertwined with other tightly regulated ions like calcium (Ca^{2+}), sodium (Na^+), and potassium (K^+) [25, 168]. Understanding if there are any functional differences within a disease model will help to elucidate the roles of these important ions, if any, in disease etiology. For example, it has been shown that Presenilin 1 is essential for proper vATPase assembly, leaving these cells unable to acidify their lysosomes properly, and causing a net calcium efflux from these compartments [69]. As vATPase pumps ferry protons into the organelle lumen in order to acidify lysosomes, the subsequent gradient serves to transport calcium into the lumen via Ca^{2+}/H^+ exchange, demonstrating how dysregulation in one particular ion can have a large effect on another in these tightly regulated systems.

Precise measurements of the pH in lysosomal compartments within living cells can be quite challenging and difficult to reproduce, but is essential to properly evaluating the degradative capacity of these organelles. It has been known for some time that lysosomal function is severely disrupted with the loss of *GRN* [18], leading to lysosomal storage defects and the eventual classification as CLN11 in rare cases of *GRN* homozygous-null patients [16]. This made the Ward Lab's *GRN*-KO i^3Neuron cell line an ideal model system to functionally demonstrate perturbations in this pathway.

Initially, my findings suggested a potential deficit in lysosomal pH, but it wasn't until I adapted the low-throughput imaging assay to high-content formats that I was able to confirm the phenotype. The low-throughput analysis method was completely manual, severely limited by user input and hindered by potential biases. High-content analysis (HCA) has no such issue, allowing near infinite analysis capabilities in comparison, limited only by computing power and knowledge of

the particular software at hand. To demonstrate the differences directly, the low throughput method sampled a total of 35 lysosomes per condition, whereas the HCA analysis pipeline could sample many hundreds, if not thousands of neurons and thousands upon thousands of lysosomes. This key decision to convert the assay and vastly increase the sample size of the experiment was a key milestone in my DPhil, and demonstrates the strength that these technologies can bring to functionally interrogating an otherwise unrealized biological phenomenon.

Ultimately, *GRN*-KO neurons are unable to adequately acidify their lysosomes (Figure 4.4) despite an increase in the regulation of acidification machinery shown in our proteomics data (Table 4.1). These results suggest *GRN* plays an important role in maintaining lysosomal pH, with v-ATPases either contributing to that effect or providing a compensatory role for that effect. Recent studies demonstrate that progranulin, which is processed by the lysosome, plays a role in lysosomal fusion [169] and pH [116].

I would like to note that the findings in Tanaka et al. [116] agree with my own independent findings implicating GRN biology and the regulation of lysosomal pH, and that my initial findings occurred before the time of their publication and in neuronal cell models.

Lysosomal Proteolysis

Loss of *GRN*, resulting in progranulin deficiency in i^{3}Neuron models, not only impaired lysosomal pH, but also negatively altered lysosomal degradative properties. The DQ-BSA assay has proven to be an effective method to further validate these deficits and is highly adaptable to high-content screening. My preliminary results from Figure 4.8, summarized in independent experimental repeats shown in Figure 4.9B, suggest that *GRN*-KO lysosomes have significantly hindered degradative capacity. The dysregulated lysosomal pH and obstructed proteolysis seen in our *GRN*-KO i^{3}Neurons further supports our understanding that *GRN* plays a key role in normal lysosomal function, which in turn affects other neurodegeneration-associated genes suggested in Table 4.1.

Figure 4.9B provides additional evidence for the significance of these phenotypic findings, as the *NPC1*-KO i^{3}Neurons I utilized as a positive control for the experiment accurately model a lysosomal storage disorder known to have lysosomes with increased pH [167]. Once analyzed, the *NPC1*-KO neurons displayed a significant increase in pH, however, the *GRN*-KO displayed an *even larger increase* in pH. This suggests that the loss of *GRN* in these neurons greatly disrupts the acidification of lysosomes to a larger degree than anticipated. Moreover, these findings directly translated into the DQ-BSA assay in Figures 4.8C-E, with *GRN*-KO neurons showing a clear deficit in DQ intensity measurements, while *NPC1*-KO neurons had a subtle effect that didn't reach significance. Interestingly, the *NPC1*-KO neurons did have a large phenotype related to spot area. A known feature and hallmark of Niemann Pick type C1 are the lipid and cholesterol-engorged lysosomes of the disease [158, 167], further suggesting that the DQ assay can be retrofitted for multiple endpoints. Neither *GRN*-KO neurons or *NPC1*-KO neurons showed significant changes in number of spots when compared to WT, suggesting that lysosomal biogenesis is still intact.

These results suggest that there are indeed defects in lysosomal function in both *GRN*-KO and *NPC1*-KO hiPSC-neurons, and that the DQ-BSA assay reaches a threshold sensitivity in detecting disease-relevant lysosomal phenotypes through high content applications. However, while the DQ-BSA assay can measure multiple endpoints, the effect size due to dysfunction in lysosomal acidification decreased in comparison to the lysosomal pH assay, supporting the need to have multiple robust, orthogonal screening assays for lysosomal function for downstream applications and as a form of biological validation.

Single KD CRISPRi Screen

The assay development and library preparation work leading up to this initial CRISPRi screen culminated in a key set of experiments, shown in Figure 4.9B and Figure 4.9C, where you can observe the recapitulation a lysosomal phenotype seen in *GRN*-KO neurons in *GRN*-KD neurons. This was another key milestone, where

I was able to phenocopy the KO phenotype via CRISPRi, while also validating the entire high-content functional genomics screening platform.

In the preliminary screen of single-knockdown targets, I've identified that depletion of the vATPase A1 subunit, *ATP6V0A1*, completely diminishes lysosomal activity (Figure 4.9D. Interestingly, this gene lies within a PD GWAS locus [51], along with other key hits *CRLS1*, *SCARB2*, and *VPS35* [170, 171], further emphasizing the genetic link between lysosomal dysfunction and PD. Additionally, knockdown of *GRN* and known interactors *PSAP*, *CTSL*, and *TMEM106B* has revealed clear roles as a lysosomal modulators, as our preliminary data show a significant positive shifts in activity with *CTSL* or *TMEM106B* knockdown, and significant negative shift in activity with *GRN* or *PSAP* knockdown. These promising initial results demonstrate that identifying common pathogenic changes elicited by disease genes can help us understand the underlying converging mechanisms in PD and FTD/ALS.

Due to this emerging evidence, it will be imperative to further analyze the function of these interactors, especially those which unexpectedly increased lysosomal activity. For example, *CTSL* is the cathepsin responsible for cleaving progranulin into individual granulins in the lysosomal compartment [115, 172, 173]. Despite this connection with *GRN*, *CTSL* also has a key regulatory role in connection with other key lysosomal proteases [174]. *TMEM106B*'s involvement with *GRN* is a well-documented clinical phenotype, which reduces the penetrance of FTD in *GRN* mutation carriers [3], but evidence for its true mechanistic role in the cell is still developing. Recent studies in mice suggest a key role in regulating lysosomal pH [4], and there is emerging evidence that it plays a key role in *CHMP2B* [117] and perhaps an even larger role in neurodegeneration, as *TMEM106B* fibrils have been implicated as a central player across TDP-43-, Tau-, and Synuclein-related proteinopathies via c-terminal fragment accumulation and subsequent amyloid fibril seeding [175–178]. This recently discovered fibrillization pathway highlights *TMEM106B* as common and widespread structural target that may be implicated in neurodegeneration [176, 179].

*For the following arguments, the z-scores and log_2FoldChange values will have the following format: (**z-score, log_2FoldChange**). Summaries of z-scores can be found in Table 4.3 and Table 4.4, while summaries of log_2FoldChange values can be found in Table A.6*

In some cases, both sgRNAs targeting a given gene have the same phenotypic readout, whereas in other cases a there may be slight divergence in the phenotype for a given sgRNA pair for this particular assay. The activity of each sgRNA in the screen was directly compared to data from the targeted RNA-seq validation, and in nearly all cases where there was phenotypic divergence, the degree of knockdown directly correlated with that change. The most clear examples of this effect can be observed for the Δ s-score and Δ log_2FoldChange between ATP6V0A1-1(-11.5, -5.22)/ATP6V0A1-2(-1.9, -4.36), CRLS1-1(-2.7, -0.36)/CRLS1-2(-5.0, -1.51), SOD1-1 (-4.3, -3.54)/SOD1-2 (-2.5, -2.82), and TAX1BP1-1 (-5.4, -5.21)/TAX1BP1-2 (-2.4, -4.72), where the guide with the lower knockdown efficiency dropped below the ±3 z-score cutoff. This confirmed that where divergence occurred, as seen in Figure 4.9, the sgRNA with more-efficient knockdown showed the stronger phenotype.

There were some unique cases such as CLN8-1 (6.8, -4.71) and CLN8-2 (6.9, -1.84), where both sgRNAs show the same phenotype despite one guide providing more robust knockdown, here both exhibit large increases in DQ/lysosomal activity. A similar effect is seen between SCARB2-1(-6.3, -2.46)/SCARB2-2(-4.9, -4.49), CTSL-1 (12.0, -1.87)/CTSL-2 (12.1, -3.68), and VPS35-1(-7.1, -3.05)/VPS35-2 (-8.3, -3.73) where both guides have a robust phenotype despite ranging differences in knockdown efficiency. Moreover, there were cases where sgRNAs with very similar knockdown efficiency showed different phenotypic scores, such as with ATP13A2-1 (0.4, -2.16)/ ATP13A2-2 (3.4, -2.77) and PFN1-1 (3.1, -1.96)/PFN1-2 (1.8, -1.86). Out of all the above scenarios, I would be least confident in these phenotypes due to a combination of their proximity to the lower threshold cutoff for significance, very similar knockdown performance, and large differences in z-score.

Ultimately, sgRNA performance is not black and white, and wholly dependent on features such as knockdown efficiency and the phenotype being measured. Whether

or not a given gene target is essential for neuronal survival and the penetrance of that gene into a particular pathway, which may or may not be directly implicated in a particular assay measurement, are factors that must be considered into the screening process. Validation of the sgRNA phenotypic findings related to lysosomal function must be established through independent replication, assay control selection, and further orthogonal phenotypic characterization in order to establish any final conclusions. Further studies will be needed to both confirm any single knockdown phenotypes shown in this preliminary experiment, and also to better understand the specificity of a particular guide to its target before even considering how other complex biological processes and pathways might be contributing to differences in sgRNA performance.

5

Phenotypic Screening and Genetic Interaction Mapping

Contents

5.1 Introduction and Aims 115
5.1.1 Epistasis and Genetic Interaction Mapping 115
5.1.2 Quantifying Genetic Interactions via the S-score 117
5.1.3 Collaboration Acknowledgments 119
5.2 Genetic Interaction Mapping 120
5.2.1 Preliminary Dual Knockdown Screening 120
5.2.2 Full Genetic Interaction Mapping Screen: DQ-BSA . . . 125
5.3 Genetic Interaction Validation 138
5.3.1 Primary Validation: DQ-BSA 138
5.3.2 Establishing Mechanistic Understanding: Magic Red and Lysosomal pH 144
5.4 Discussion 149

5.1 Introduction and Aims

The findings from the preliminary single knockdown screen in Chapter 4 implicated lysosomal dysfunction as a central pathophysiological consequence of mutations causing FTD/ALS and PD. In Chapter 5, I propose to unite the functional genomics tools, methods, and validation work from Chapter 3 with the phenotypic assay development and high-content imaging techniques from Chapter 4 to systematically generate high-quality genetic interaction maps of FTD/ALS and PD genes in i^{3}Neurons. Single and pair-wise knockdowns of genes will be performed in 384-well formats using our CRISPRi screening platform to identify common pathogenic changes elicited by disease genes related to key lysosomal processes.

Aims of this chapter

- Demonstrate the development and optimization of Genetic Interaction Mapping in i^{3}Neurons for high-content screening
- Demonstrate the first Genetic Interaction Mapping screen in human iPSC-derived Neurons, utilizing the optimized DQ-BSA assay and CRISPRi
- Demonstrate primary and secondary screening validation of pairwise hits from the Genetic Interaction Mapping Screen

5.1.1 Epistasis and Genetic Interaction Mapping

The fundamental principle in genetic interaction mapping is that a phenotype caused by the loss or knockdown of one gene can be modified by the loss or knockdown of a second gene, this is known as **epistasis** [180–182]. Genetic interactions can be sensitizing, in which the phenotype of dual gene knockdowns is more severe than expected, or alleviating, in which dual gene knockdowns result in a phenotype that is less severe than expected when compared to single gene knockdowns [183, 184].

Early researchers looked to identify strong *qualitative* differences between related gene-pairings to find evidence of complementary or converging pathways [181].

However, gene-gene interactions are not simply all-or-nothing phenomena, and a continuum of genetic interaction strengths exist for a given pathway or set of related genes [185]. Interrogation of this continuum requires a *quantitative* approach to go beyond the qualitative *"up, down, no-change"* analysis of gene-gene interactions. Moreover, a quantitative approach has several distinct advantages such as the ability to interrogate the full interaction spectrum, and an overall increase signal-to-noise as the frequency of genetic interactions is higher with a set of rationally chosen genes that all function in related pathways [181, 185].

As a general overview, a genetic interaction (ε_{AB}) can be defined between gene A and gene B in terms of any quantitative phenotype P as the difference between the observed phenotype of the dual knockdown ($P_{AB}^{observed}$) and the expected phenotype of the dual knockdown ($P_{AB}^{expected}$) [181].

$$\varepsilon_{AB} = P_{AB}^{observed} - P_{AB}^{expected}$$

$$\text{where: } P_{AB}^{expected} = P_{A}^{observed} + P_{B}^{observed}$$

This equation, but more practically the underlying concept of a gene interaction, heavily depends on the ability to accurately compute the single gene knockdown conditions $P_{A}^{observed}$ and $P_{B}^{observed}$ in order to derive the "expected" dual knockdown condition $P_{AB}^{expected}$ [181]. The derivation of the expected dual phenotype relies upon the generation of a model that can empirically represent the combined effect across the gene set, and may take any of multiple forms [181, 182]:

$$\text{multiplicative: } P_{AB}^{expected} = P_{A}^{observed} \times P_{B}^{observed}$$

$$\text{additive: } P_{AB}^{expected} = P_{A}^{observed} + P_{B}^{observed}$$

$$\text{empirical (mixture): } P_{AB}^{expected} = P_{A}^{observed} + | - | \times | \div P_{B}^{observed}$$

The utility of these techniques have been demonstrated repeatedly, most commonly in yeast [183, 185], but also in mammalian cells [183], and more recently using CRISPRi as a tool for the functional genomics side [186]. To my knowledge, however, genetic interaction mapping has not yet been performed at subcellular resolution with organelle-specific phenotypic assays in advanced neuronal models. My primary aim is to achieve this endpoint by measuring the effect of single versus pairwise knockdowns using the rationally-derived sgRNA library (Table A.1) generated in Chapter 3, which centers upon key lysosomal pathways in FTD/ALS and PD.

5.1.2 Quantifying Genetic Interactions via the S-score

In order to generate quantitative interaction scores, I chose the S-score method developed by Collins et al. which produces a quantitative score representing the overall strength of an interaction by deriving the direction and magnitude of a given dual knockdown when compared to controls or other interaction pairs [185]. The S-score represents a modification to the traditional t-value score, the population medians of interaction pairs and controls are utilized instead of their means.

The S-score between two interaction pairs is defined in terms of 5 parameters: the *median* phenotypic value ($\mu_{Experiment}$) and number of measurements ($n_{Experiment}$) for the experimental sample interaction, the *median* phenotypic value ($\mu_{Control}$) and number of measurements ($n_{Control}$) for the control interaction pair, and the s_{Var}, a shared variance estimate derived from the variance of both the $\mu_{Experiment}$ and $\mu_{Control}$ measurements [185].

$$\text{S-score: } S = \frac{\mu_{Experiment} - \mu_{Control}}{\sqrt{\frac{s_{Var}}{n_{Experiment}} + \frac{s_{Var}}{n_{Control}}}}$$

S-scores are generated relative to the control interaction pair or condition. However, it is also possible to plug-in another interaction pair into the control positions in the S-score equation, repositioning the reference frame. In the results of this chapter, I incorporated this process to generate two distinct forms of S-score

analysis: Primary (1°) and Secondary (2°) (Figure 5.1). These two variants of the the same interaction data allow for you to both compare the entire dataset to a control phenotype "true zero" baseline, while also considering single KD phenotypes as another baseline for comparison. Figure 5.1 lays out this concept in more detail, where the single KD phenotype for Gene 1 has different primary and secondary s-scores: a primary s-score of +4 with true zero as the baseline, and a secondary s-score of 0 because the single KD phenotype is the baseline. This becomes clearer when considering an interaction pair. The interaction pair reciprocals Gene1-Gene2 and Gene2-Gene1 all have similar primary s-scores near true zero. However, they are mildly negative when compared to the Gene 1 single KD baseline and highly positive when compared to the Gene 2 single KD baseline, as the secondary s-scores have placed the phenotypic scores of these interactions *in terms of* Gene 1 and Gene 2, respectively. Figure 5.6 shows primary and secondary s-scores across the entire sgRNA library in an example related to *GRN* KD.

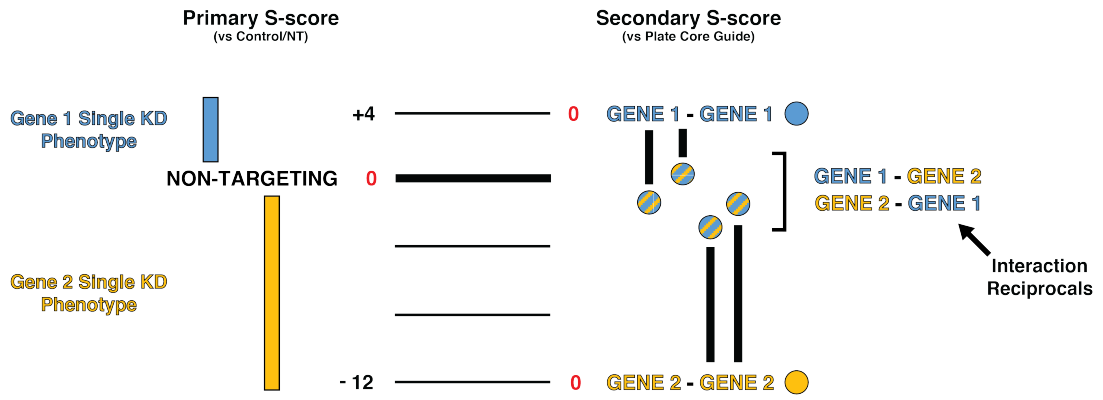


Figure 5.1: Translating phenotypes into interactions: Primary vs. Secondary S-scores.

5.1.3 Collaboration Acknowledgments

Several portions of Chapter 5 are based on joint work with key collaborators in order to facilitate the complex bioinformatics analysis required by this project. I generated all the experimental data and experimental designs under the guidance of my mentors Michael E. Ward, Richard Wade-Martins, and Brent J. Ryan. All bioinformatics-based analysis was completed in collaboration with Endre Sebestyen of the Bioinformatics CRO, Peter Kilfeather of the Wade-Martins Lab, and Sean Collins of the University of California, Davis. Endre Sebestyen and Peter Kilfeather both assisted in the primary and secondary analysis pipeline generation and automation seen in Figures 5.2 through 5.10. Sean Collins assisted with tertiary analysis, interaction detection and hit formulation, as well as general troubleshooting as an expert in the field, seen in Figure 5.13 and Figure 5.14. Endre Sebestyen also assisted with follow-up validation analysis and figure generation, seen in Figures 5.16 through 5.21. Peter Kilfeather also assisted with the generation of all figures in Appendix B.

5.2 Genetic Interaction Mapping

5.2.1 Preliminary Dual Knockdown Screening

Building from the single knockdown DQ-BSA screen, shown in Figure 4.9 from Chapter 4, I performed a preliminary screen with dual knockdown. A specific experimental design was chosen for this experiment, shown in Figure 5.2A, where sgRNAs were arrayed in a 7x7 matrix (Figure 5.2D) to produce the necessary combinations across our preliminary sub-library. This matrix design produces single and pair-wise knockdown (by genotype) of a small set of *GRN* interactors and *CLN8* and *ATP6V0A1*, which both showed strong single KD phenotypes in the single KD screen.

In this preliminary experiment, "single KDs" were generated by the same sgRNA from both virus systems (e.g. 1872-FR + 1872-NB, GRN-FR + GRN-NB). All samples analyzed in the genetic interaction screens within this chapter were treated with two viruses, one in Nuclear Blue (NB) and one Far Red Cytoplasmic (FR), as described in Chapter 3. Genetic interaction pairs were transduced in duplicate, and single-cell level data obtained from high-content analysis.

Single-cell data is difficult to wrangle and requires quality control (QC) clean up and normalization. Figure 5.2E and Figure 5.2F represent the first step in analysis, outlier detection and removal. Figure 5.2E shows the distribution of single-cell results, grouped by well or by sgRNA pair (i.e. shared genotype), detected to be an outlier or not, or an NA value. Figure 5.2F is the fraction of Figure 5.2E that are outliers for each outcome measure, most are not useful beyond analysis QC; primary outcome measures are Corrected Spot Intensity Mean per Cell (CSIMC) and Number of Spots per Area of cell (NSA). Once outliers are removed, the long upper tail of the distributions seen in Figure 5.2G density plots are no longer present.

Both the preliminary screen and the larger genetic interaction mapping screen will require nearly full 384-well plates to efficiently assay all of the experimental combinations. As the DQ-BSA is a no-wash assay and there are limitations on imaging speed, I predicted that there would be some form of assay drift

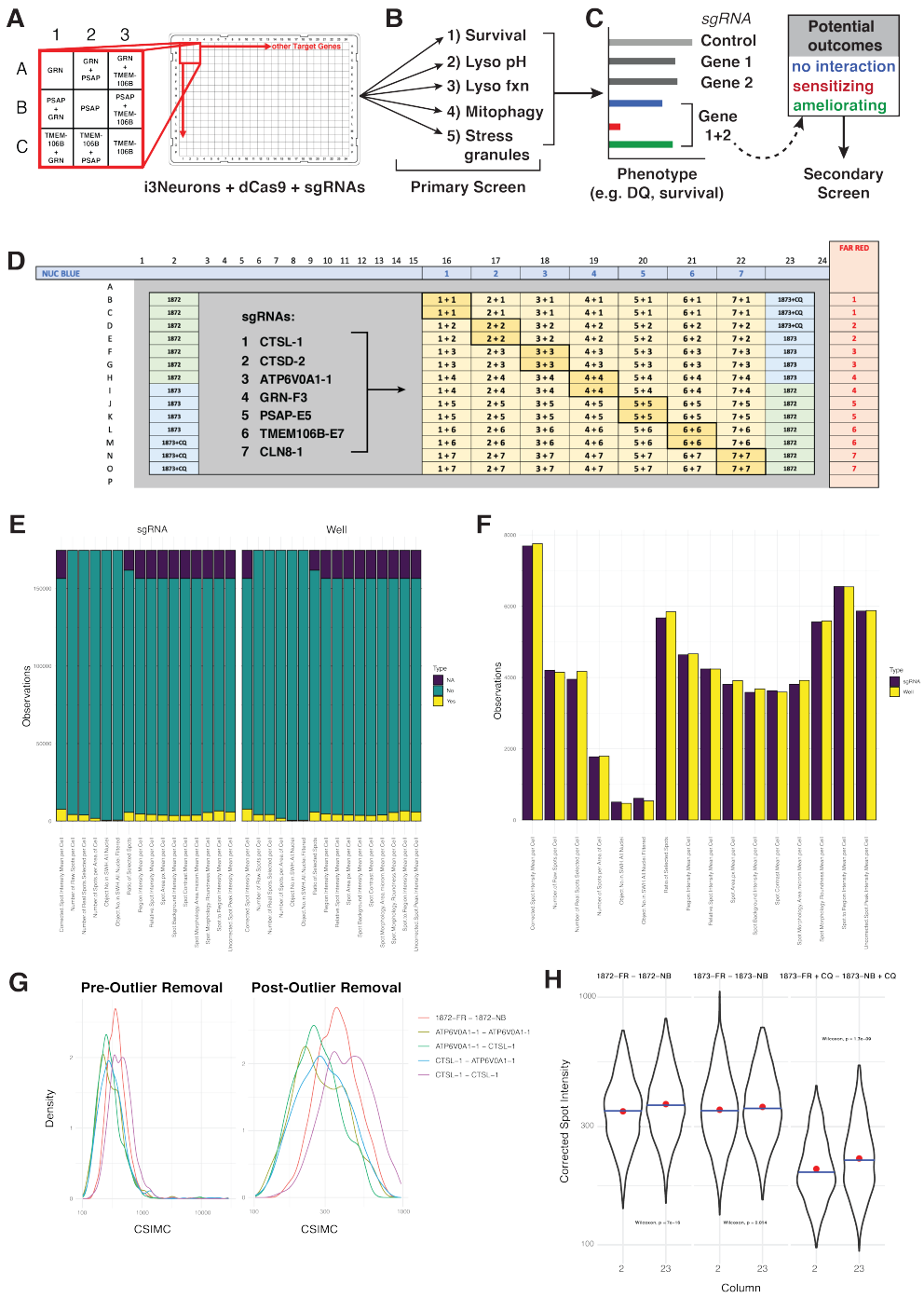


Figure 5.2: Preliminary GI Mapping, Experimental Design and Cell-level QC. Representative concept map of A.) Genetic Interaction Mapping combined with B.) high-content primary screening assays and C.) quantification of potential outcomes for secondary screen analysis. D.) Experimental design of the preliminary experiment, including a list of sgRNAs used in the experiment. E.) Quantification and sorting of single-cell outlier results when grouped by sgRNA or Well, all outcome measures. F.) Outlier-only fraction of (E), all outcome measures. G.) Density plots of selected examples pre- and post-outlier removal (single-cell level); CSIMC = Corrected Spot Intensity Mean per Cell. H.) Violin plots quantifying CSIMC results of controls; samples flank the experiment and produce a left/right difference.

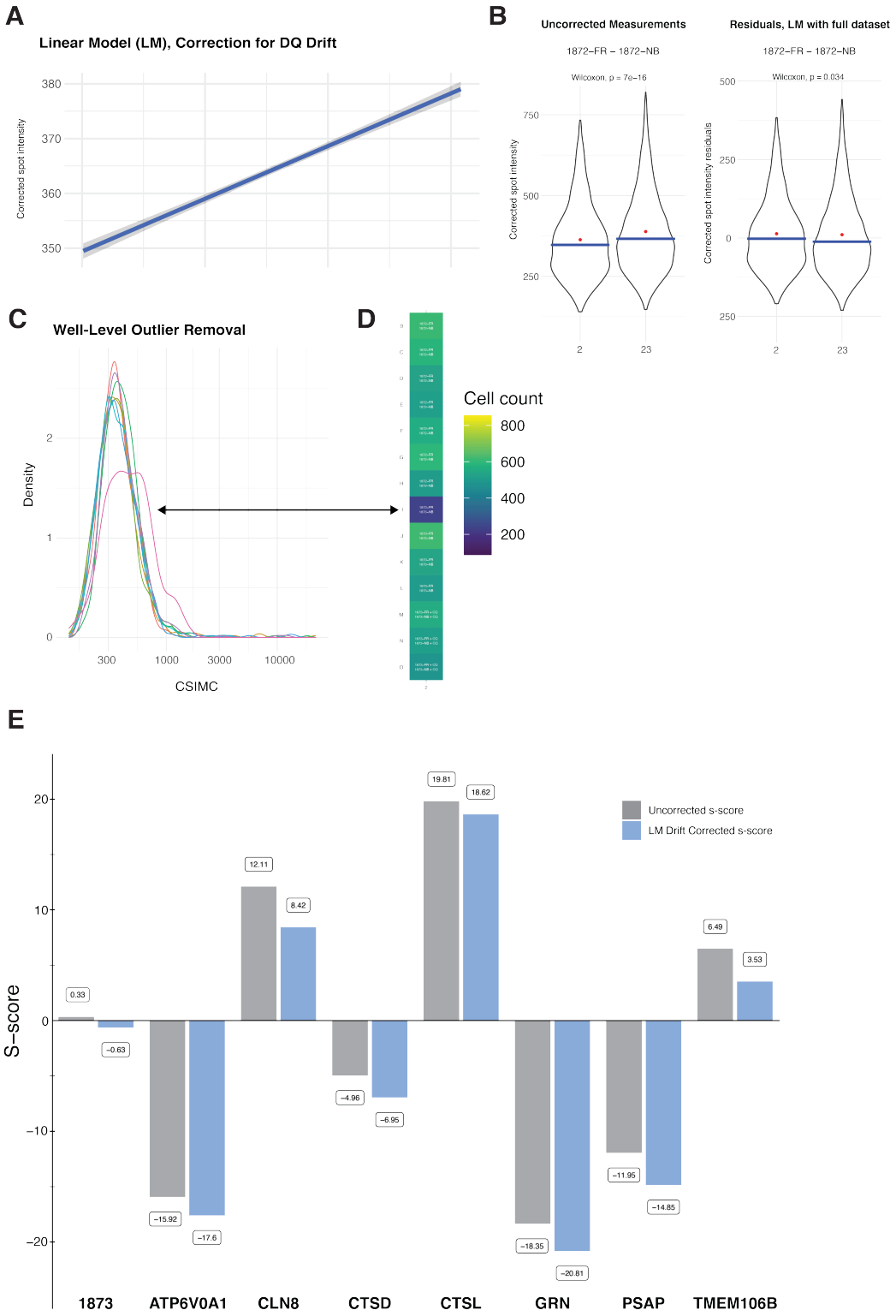


Figure 5.3: Preliminary GI Mapping, Drift Corrections and Well-level QC. A.) A linear model was used to correct for the drift in the DQ-BSA assay shown in the violin plots in B.) comparing uncorrected raw measurements and drift-corrected residuals. C.) Density plots of the 1873-1873 control wells indicating a major difference in one of the wells, row I. D.) Representative heatmap of cell counts corresponding to the wells of 1873-1873, explaining the outlier/bad well. E.) Primary S-score comparisons of single KD combinations.

when imaging a plate. This was confirmed in Figure 5.2H, where the flanking controls in the first and last column imaged were statistically different ; for 1872-1872 controls, p-value=7e-16; for 1873-1873 controls, p-value=0.014 (columns 2 v 23; mean = red dot, median = blue line).

To address this issue, a linear model was generated (Figure 5.3A) to correct for DQ drift by calculating the relationship between the increases in DQ intensity across the order of capture (by well), show as approximately Δ30 corrected intensity units across the plate. Figure 5.3B shows the resulting violin plots of the 1872-1872 populations in column 2 vs column 23 before and after drift correction, with post-drift correction measurements represented as residuals. Figure 5.3C and Figure 5.3D demonstrate the well-level QC steps, in this case removal of an outlier well, still needed after single-cell cleanup, outlier removal, and drift corrections. Confirmed that multiple levels of QC checks and cleanup would be required for the larger screen.

Primary S-scores were then systematically calculated between all sample combinations and controls in the final filtered dataset, in this experiment 1872-1872 served as the S-score control. Single KD results are shown in Figure 5.3E, both uncorrected and LM drift corrected versions are present. There was no major difference between the 1873-1873 combination and 1872-1872 combination, indicating no difference between the two sets of non-targeting controls. There were large S-scores for several of the single KD combinations, including: strongly negative phenotypes for *ATP6V0A1* (-17.6, corrected), *GRN* (-20.81, corrected), and *PSAP* (-14.85, corrected); strongly postive phenotypes for *CLN8* (8.42, corrected) and *CTSL* (18.62, corrected); mildly negative and postive phenotypes for *CTSD* (-6.95, corrected) and *TMEM106B* (3.53, corrected), respectively.

Other key interaction pairs with *GRN* were analyzed and plotted in Figure 5.4. CLN8 KD has a strongly positive phenotype, as shown in the single KD scores from Figure 5.3E and in the combinations with TMEM106B KD (Figure 5.4D), where positive s-scores are amplified, or in the combinations with GRN KD (Figure 5.4A), where the negative s-scores are somewhat alleviated when compared to GRN KD only.

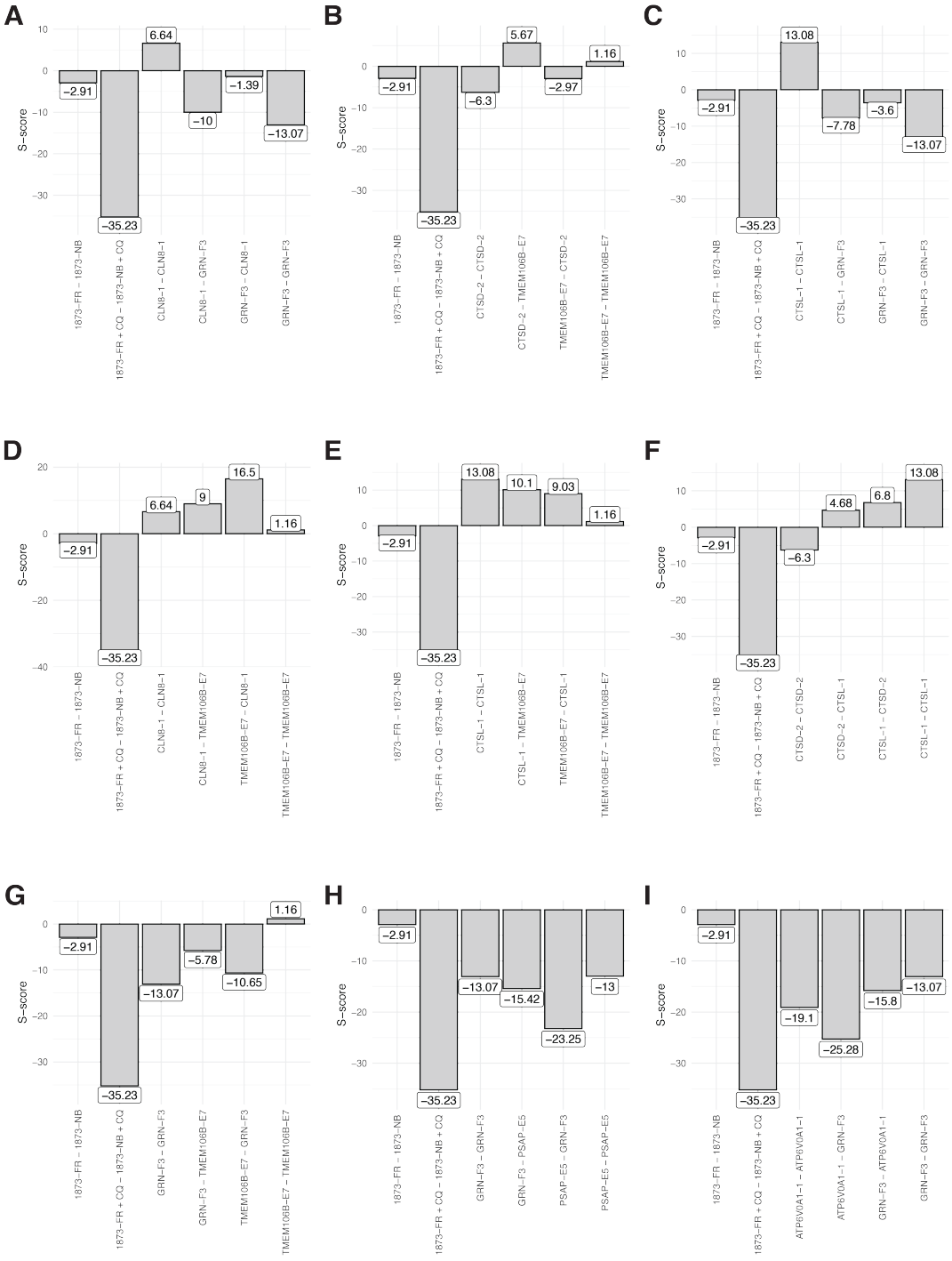


Figure 5.4: Preliminary Genetic Interaction Mapping, Primary S-score Comparisons. Primary S-scores for the interaction pairs A.) CLN8-GRN B.) CTSD-TMEM106B C.) CTSL-GRN D.) CLN8-TMEM106B E.) CTSL-TMEM106B F.) CTSD-CTSL G.) GRN-TMEM106B H.) GRN-PSAP I.) ATP6V0A1-GRN

This also occurs in the GRN-CTSL (Figure 5.3C), GRN-TMEM106B (Figure 5.3G), and CTSD-CTSL (Figure 5.3F) combinations. Another strong phenotype is seen with ATP6V0A1 KD (Figure 5.3I), further sensitizing the GRN KD phenotype. This also occurs in the GRN-PSAP (Figure 5.3H) combination, where the combined s-score is lower than each of the single KD conditions on their own.

5.2.2 Full Genetic Interaction Mapping Screen: DQ-BSA

The final genetic interaction mapping screen implemented key experimental design optimizations compared to the preliminary dual KD screen. The largest change is in the experimental layout itself, as shown in Figure 5.5A, where a "core guide" layout replaces the "knockdown matrix" seen previously. This new format changes how we consider the entire screening structure, instead shifting focus to an individual sgRNA, or "core guide" and forming a miniature interaction screen with all other sgRNAs, or "auxiliary guides", systematically combined against the core. All validated sgRNAs selected for the genetic interaction mapping screen are listed in Table 5.1.

The core guide format also allows for primary and secondary s-scores to be more carefully accounted for, providing 1) flanking and drift controls that can be used to generate primary s-scores for all combinations local to a plate and 2) single KD combinations derived from the core guide and it's reciprocal auxiliary guide (e.g. GRN-NB + GRN-FR) for secondary s-score analysis. This method standardizes the secondary s-score analysis and localizes all possible dual KD combinations to a single plate including all reciprocals, allowing for the generation of secondary s-score interaction maps that show which genes interact with the core guide phenotype most significantly. Moreover, this new experimental design also allowed for additional single KD combinations derived from targeting and non-targeting combinations (e.g. GRN-NB + 1872-FR and/or 1872-NB + GRN-FR), giving a more complete profile for the single KD conditions.

The schematic in Figure 5.5B highlights the key points in the optimized analysis pipeline, such as the outlier detection and removal in Figure 5.5C and Figure 5.5D,

respectively. With additional drift controls in place, a more precise linear model could be implemented (Figure 5.5G) to correct for the increase in DQ intensity across the order of image capture, seen in the violin plots of CSIMC measurements in Figure 5.5E, and corrected residuals in Figure 5.5F.

Upon completion of the assay and imaging components screen, all image data was quantified and run through the analysis pipeline. Figure 5.6 is a representative example of Primary and Secondary S-score analysis results and interaction "maps" that were generated using the *GRN* plate results. Primary S-scores are plotted as a hitmap in Figure 5.6A and as a barchart in Figure 5.6B, showing general trends across the combinations for this plate. Most of the interaction combinations in the GRN plate have negative primary s-scores.

Representative hit plots, or secondary interaction maps, of the secondary s-scores for the outcome measures CSIMC and NSA can be found in Figure 5.6C and Figure 5.6D, respectively. These scatter-plots take all secondary scores for a given outcome measure, calculated in terms of the a GRN-GRN baseline, and plot them on a coordinate system based on reciprocal guide orientation. Interaction combinations that have GRN sgRNA in Far Red have their s-score as the X-position, while interaction combinations that have GRN sgRNA in Nuclear Blue have their secondary s-score as the Y-position, combining interaction reciprocals as one point in X,Y space. Those reciprocals with concordant secondary s-scores are closer to the diagonal line, representing reproducibility between guide combinations from both sgRNA systems. The GRN "single KD" combinations (secondary controls) consisting of GRN-control or control-GRN are represented by the orange dots, weak hits are shown in grey, and strong hits are red (positive=hot) or blue (negative=cold). The black dotted lines represent the spread of the secondary controls in orange and the orange dotted line marks the mean/center of all secondary controls.

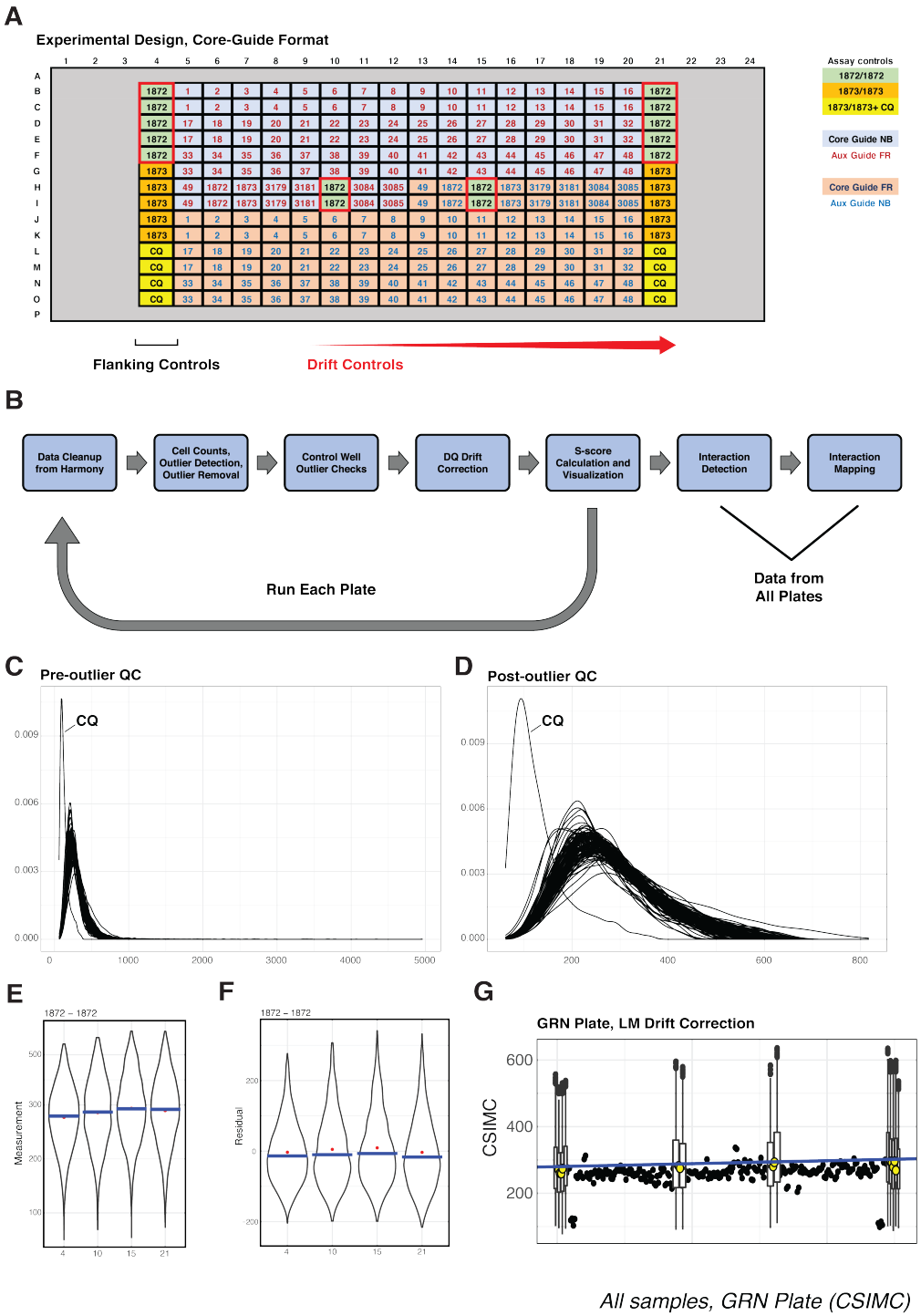


Figure 5.5: DQ-BSA Genetic Interaction Mapping Screen, Experimental Design & Analysis QC. A.) Representative schematic of the full interaction screen experimental design, with core guide reciprocals labeled by cell fill color and auxiliary guides labeled by font color. Flanking and Drift controls shown. B.) Representative diagram of the optimized analysis pipeline. *GRN* plate results as density plots C.) pre-outlier quality control and D.) post-outlier quality control. E.) Violin plots quantifying CSIMC results of controls placed in key locations across the plate layout to analyze DQ drift. F.) Same control samples from (E), shown as violin plots of drift-corrected residuals. G.) Linear model used to analyze drift across the 1872-1872 controls across the *GRN* plate.

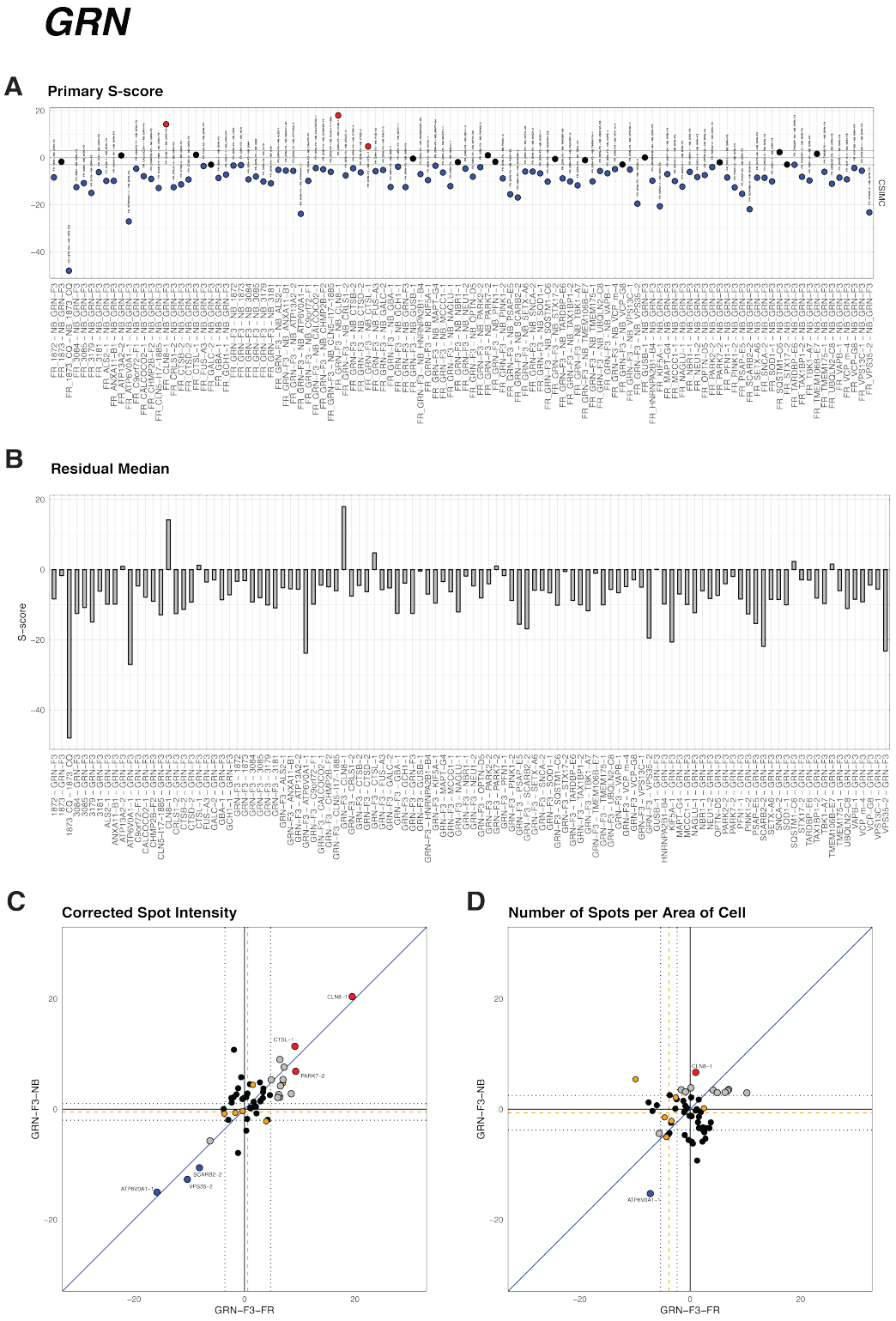


Figure 5.6: *GRN*: Primary and Secondary Analysis Genetic Interaction Maps. A.) Representative hitmap of Primary S-scores for all *GRN* combinations; Red = increase in DQ CSIMC, Blue = decrease in DQ CSIMC. B.) Alternative barchart representation of A; all primary s-scores are calculated from the residual median data (drift-corrected median of single-cell population). Secondary S-score interaction maps for *GRN* KD combinations, C.) CSIMC outcome measure and D.) NSA outcome measure.

Table 5.1: Selected sgRNAs for Genetic Interaction Mapping Screen

Validated sgRNAs	Screening Batch	Nuc Blue Virus Code	Nuc Blue Virus 70% Titer (nL)	Far Red Virus Code	Far Red Virus 70% Titer (nL)
PINK1-2	2	NB1	275	FR1	163
PARK2-2	2	NB2	270	FR2	128
PARK7-2	2	NB3	260	FR3	168
SNCA-2	2	NB4	255	FR4	135
GBA-1	2	NB5	333	FR5	143
VPS35-2	2	NB6	333	FR6	118
ATP13A2-2	2	NB7	305	FR7	453
NAGLU-1	2	NB8	305	FR8	150
GUSB-1	2	NB9	310	FR9	140
NEU1-2	2	NB10	418	FR10	113
VPS13C-1	2	NB11	240	FR11	143
GCH1-1	2	NB12	193	FR12	145
TMEM175-1	2	NB13	260	FR13	185
STX17-2	2	NB14	330	FR14	178
MAPT-G4	2	NB15	415	FR15	155
CLN5-I17-1885	2	NB16	345	FR16	340
SETX-A6	2	NB17	535	FR17	280
CALCOCO2-1	2	NB18	453	FR18	680
NBR1-1	2	NB19	555	FR19	380
TAX1BP1-2	2	NB20	628	FR20	393
SCARB2-2	2	NB21	648	FR21	240
GALC-2	2	NB22	753	FR22	228
MCCC1-1	2	NB23	583	FR23	335
CRLS1-2	2	NB24	735	FR24	248
CTSB-2	1	NB25	298	FR25	223
CTSL-1	1	NB26	218	FR26	138
CTSD-2	1	NB27	215	FR27	100
ATP6V0A1-1	1	NB28	200	FR28	108
GRN-F3	1	NB29	475	FR29	148
PSAP-E5	1	NB30	398	FR30	108
TMEM106B-E7	1	NB31	478	FR31	138
ANXA11-B1	1	NB32	535	FR32	190
OPTN-D5	1	NB33	423	FR33	173
C9orf72-F1	1	NB34	443	FR34	128
CHMP2B-F2	1	NB35	385	FR35	123
TARDBP-E6	1	NB36	430	FR36	100
FUS-A3	1	NB37	513	FR37	320
TBK1-A7	1	NB38	520	FR38	143
UBQLN2-C8	1	NB39	408	FR39	123
HNRNPA2B1-B4	1	NB40	373	FR40	165
SQSTM1-C6	1	NB41	325	FR41	185
KIF5A-1	1	NB42	548	FR42	223
VCP-G8	1	NB43	438	FR43	180
VCP_m-4	1	NB44	375	FR44	228
SOD1-1	1	NB45	655	FR45	235
ALS2-1	1	NB46	435	FR46	485
PFN1-1	1	NB47	315	FR47	375
VAPB-1	1	NB48	595	FR48	383
CLN8-1	1	NB49	580	FR49	103
1872	both	NB1872	565	FR1872	168
1873	both	NB1873	488	FR1873	240
3084	both	NB3084	510	FR3084	473
3085	both	NB3085	583	FR3085	230
3179	both	NB3179	490	FR3179	270
3181	both	NB3181	525	FR3181	238

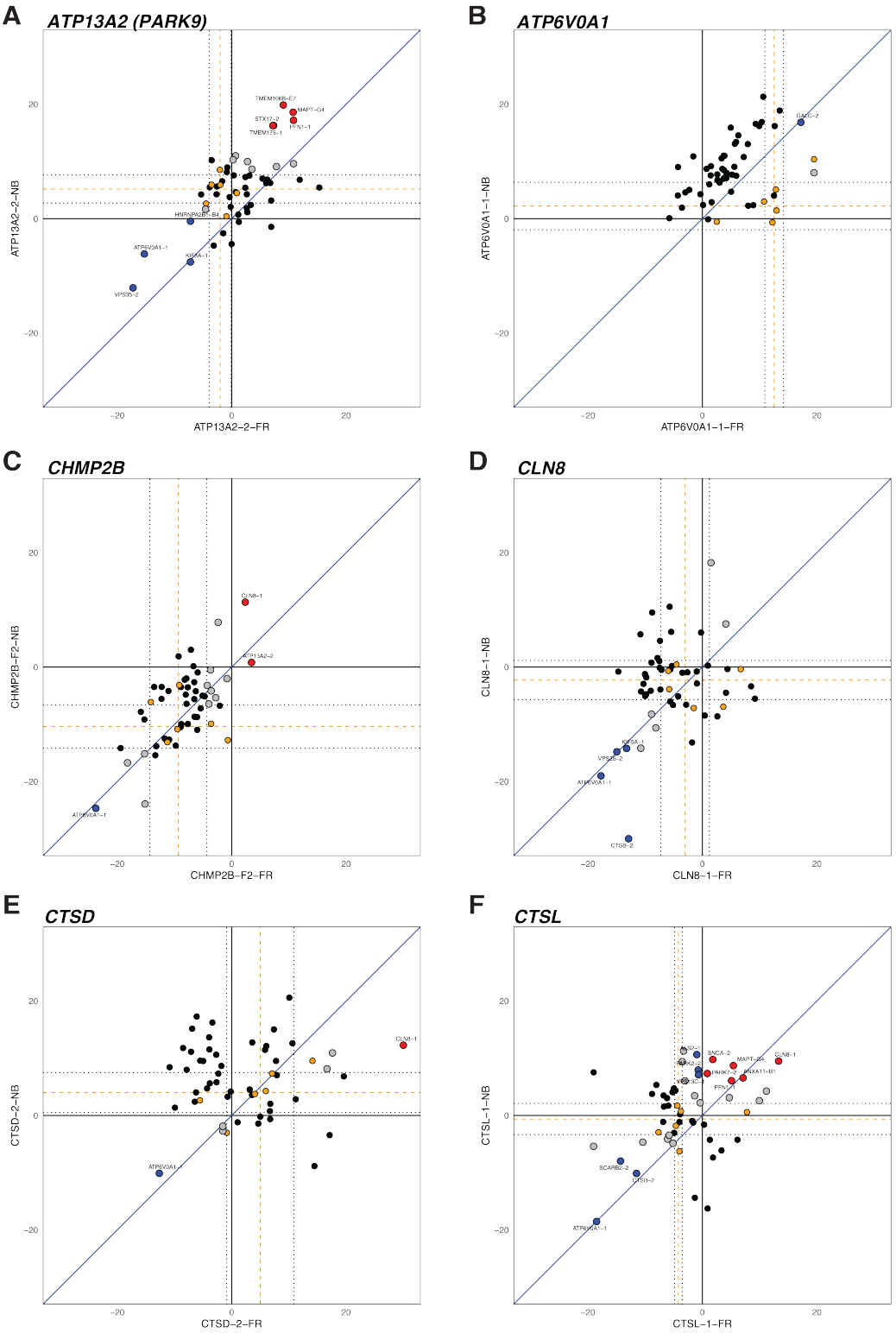


Figure 5.7: Secondary Analysis Genetic Interaction Maps for Hit-related Genes, part I. Secondary Interaction Plots for A.) ATP13A2, B.) ATP6V0A1, C.) CHMP2B, D.) CLN8, E.) CTSD, and F.) CTSL.

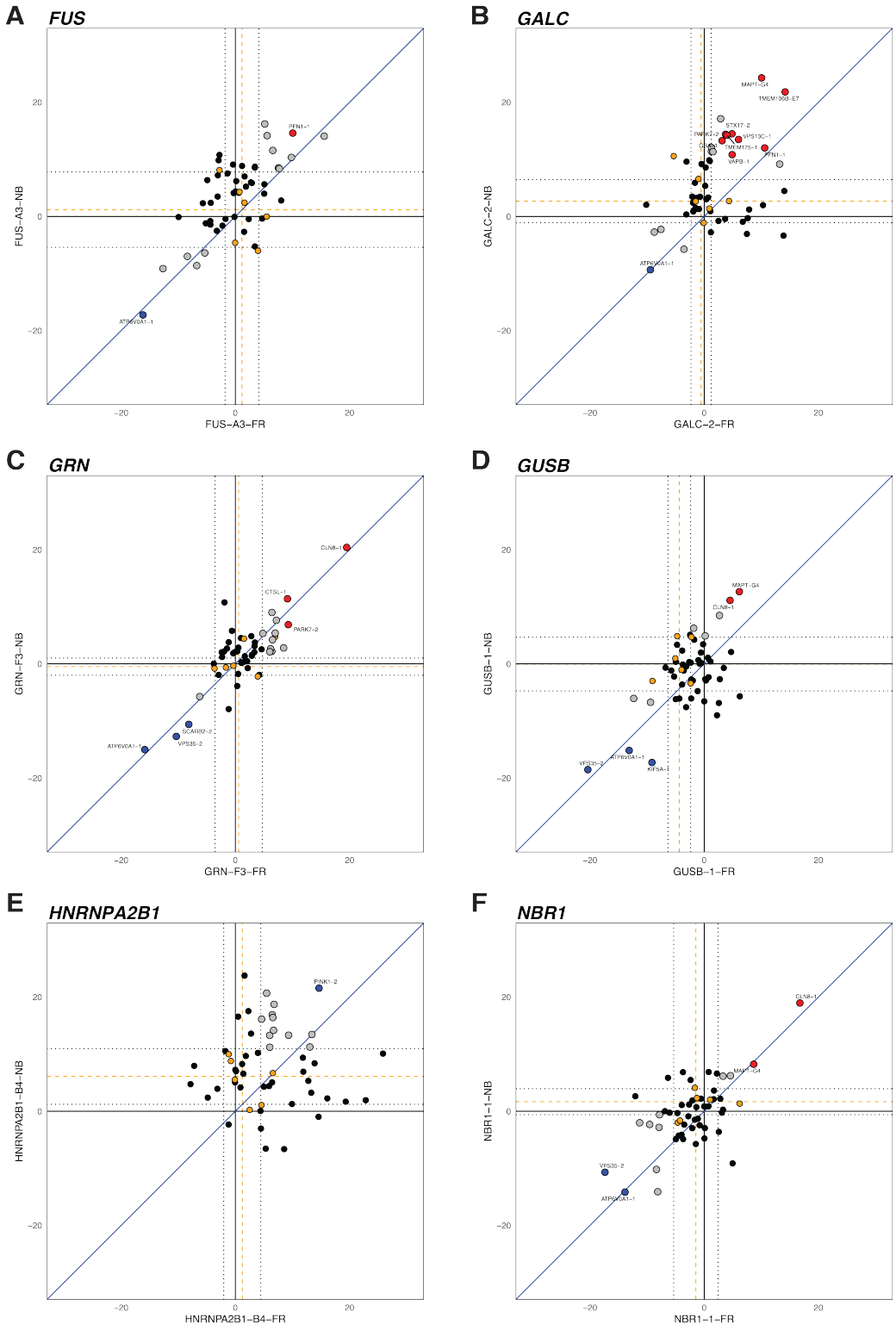


Figure 5.8: Secondary Analysis Genetic Interaction Maps for Hit-related Genes, part II. Secondary Interaction Plots for A.) FUS, B.) GALC, C.) GRN, D.) GUSB, E.) HNRNPA2B1, and F.) NBR1.

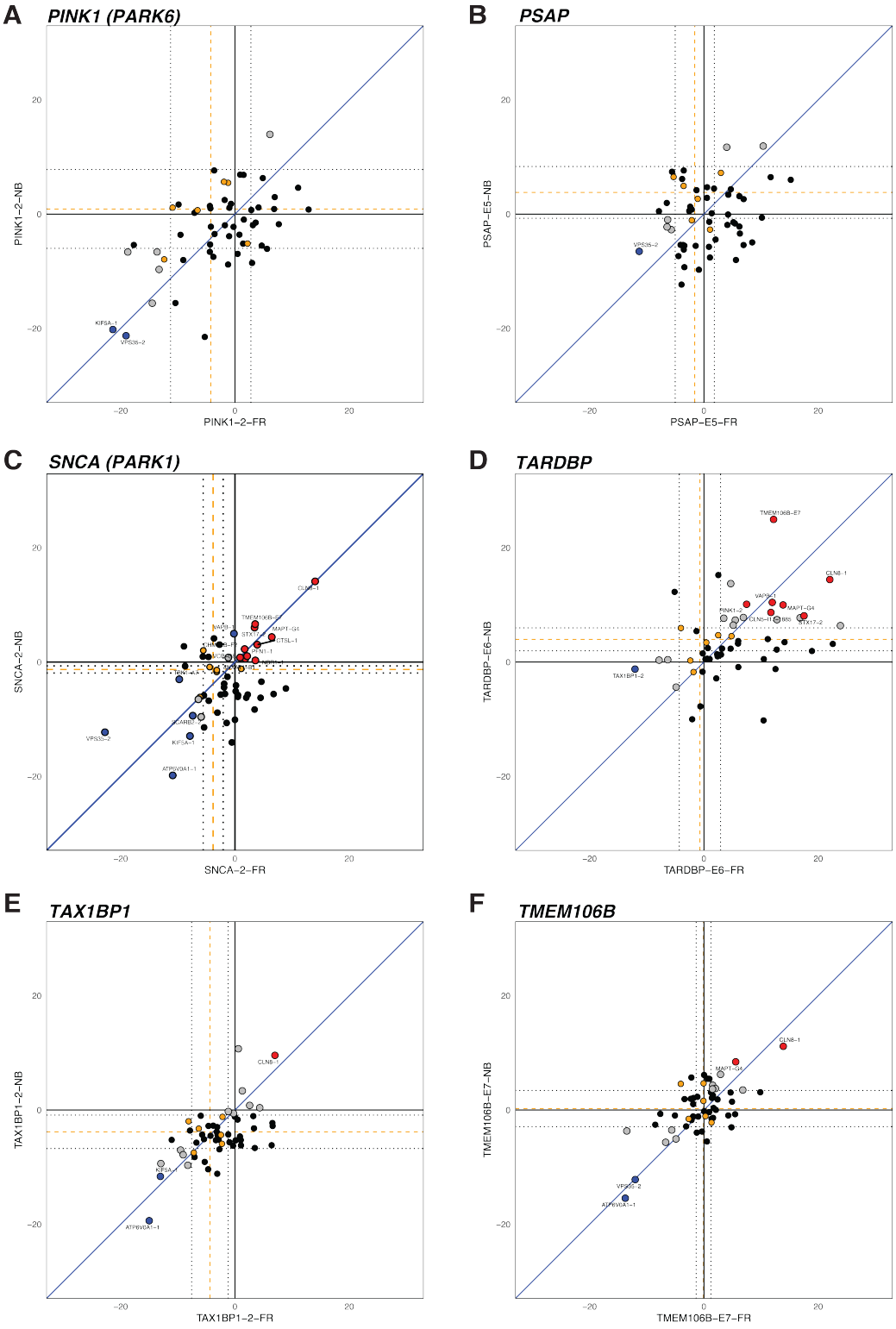


Figure 5.9: Secondary Analysis Genetic Interaction Maps for Hit-related Genes, part III. Secondary Interaction Plots for A.) PINK1, B.) PSAP, C.) SNCA, D.) TARDBP, E.) TAX1BP1, and F.) TMEM106B.

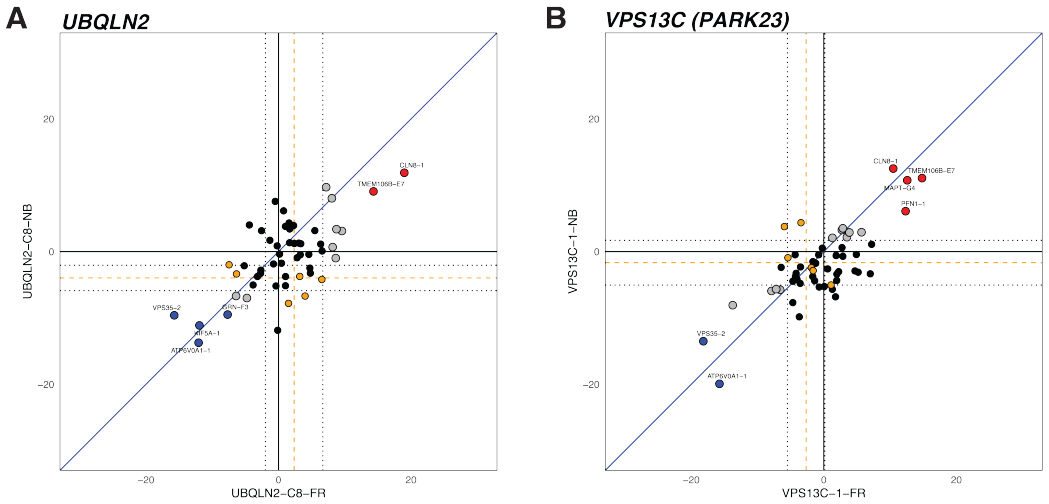


Figure 5.10: Secondary Analysis Genetic Interaction Maps for Hit-related Genes, part IV. Secondary Interaction Plots for A.) UBQLN2 and B.) VPS13C.

Secondary interaction maps for the CSIMC outcome measure can be seen in Figure 5.7, Figure 5.8, Figure 5.9, and Figure 5.10 for all genes that were detected in "hit" interactions brought forward for further validation (to be presented in a later figure). All primary and secondary analysis genetic interaction maps across the 49 plates can be found in Appendix B.

Figure 5.11 outlines the first of two interaction detection methods used to generate a potential list of hits for follow-up validation. The method is summarized in the Figure 5.11A schematic relied upon the primary and secondary analysis only, where weak and strong secondary hits from all plates were brought forward (Figure 5.11C) and filtered for the strongest outcome measure, CSIMC. The 555 hits were then filtered for the most concordant primary s-score reciprocals, shown in Figure 5.11D and Figure 5.11E, leaving 334 total hits where the scores agreed across the plates. The remaining hits were then analyzed using interaction equation mentioned previously in Section 5.1.1 and shown in Figure 5.11B, and filtered for the largest volume of interactions that I could bring to primary validation (repeat of DQ-BSA).

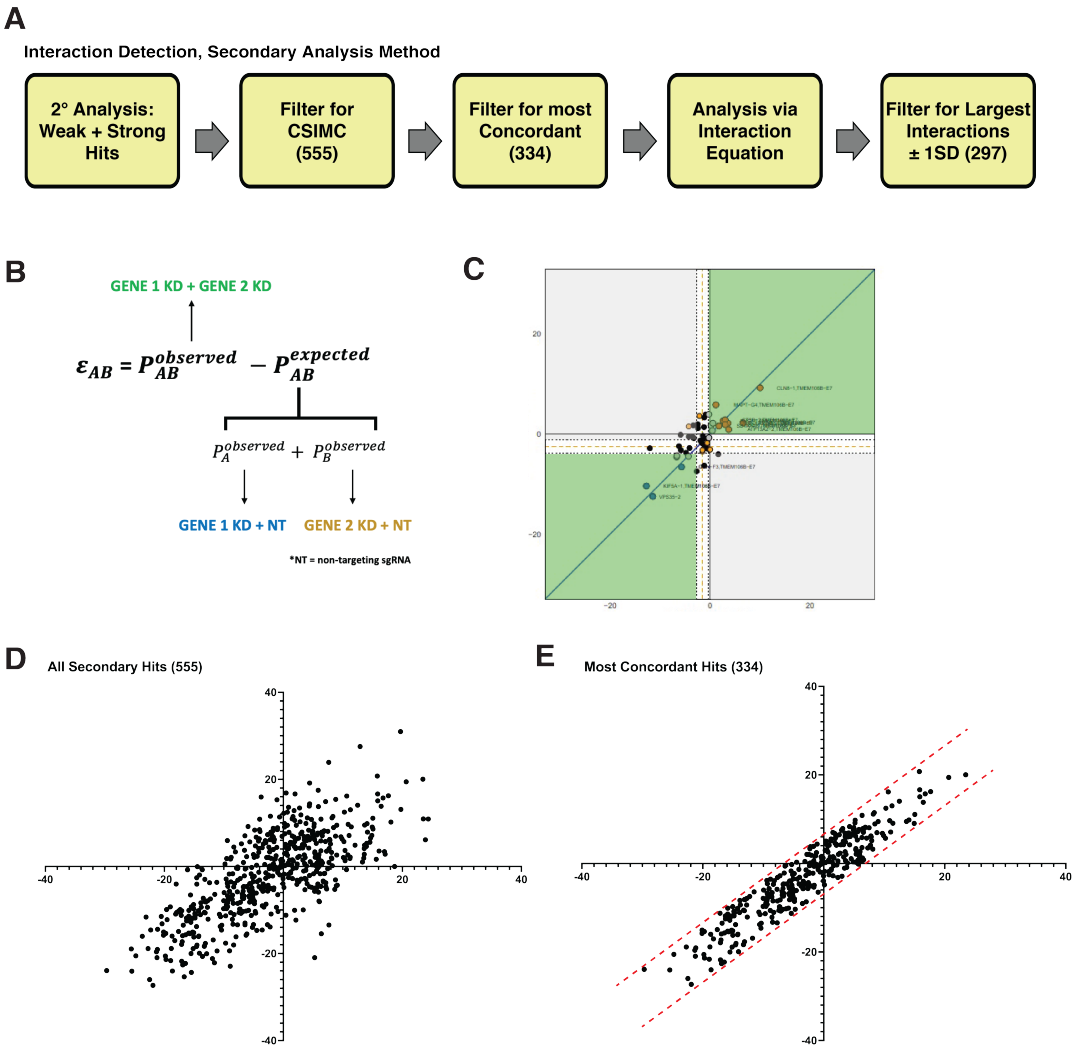


Figure 5.11: Genetic Interaction Detection, Secondary Analysis Method. A.) Representative diagram of the Secondary Interaction Detection method and narrowing of hits. B.) Interaction equation from Section 5.1.1, where components of the equation are labeled according to the screen design. C.) Example of the first step in this method, where all strong and weak secondary hits are brought forward. Scatterplots D.) and E.) represent the narrowing of hits based on reciprocal concordance.

Another key concept is the interpretation of the results from the interaction equation shown in Section 5.1.1 and Figure 5.11B, which helps to compare a given interaction combination to its single KD components. Combination KDs with the highest scores may or may not be a real, synergistic interaction due to the effects of strong single KDs on a given interaction pair. To address this, all related comparisons must be considered via the interaction equation to calculate

ε_{AB} values, where additive interactions: $\varepsilon_{AB} = 0$, negative synergistic interactions: $\varepsilon_{AB} \ll 0$, and positive synergistic interactions: $\varepsilon_{AB} \gg 0$. Good examples of this are demonstrated in Figure 5.12, where the example interaction pairs PARK2-VCP and TARDBP-TMEM106B each have results suggesting their interactions are additive and positive synergistic, respectively. Further validation would be needed to confirm any synergistic interactions, but the example is clear.

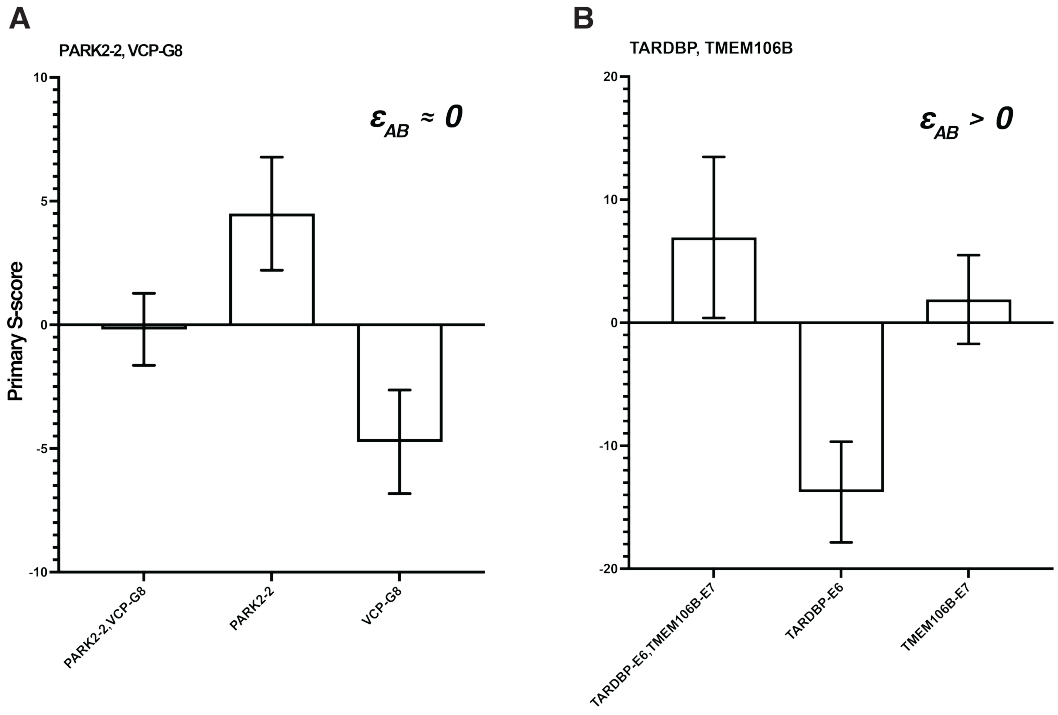


Figure 5.12: Understanding Genetic Interactions: Additive vs Synergistic. Primary S-score data from the Genetic Interaction Mapping screen, with interplate reciprocals combined for each condition. A.) The interaction pair PARK2-VCP, as an example additive interaction ($\varepsilon_{AB} \approx 0$). B.) The interaction pair TARDBP-TMEM106B, as an example positive, *potentially synergistic* interaction ($\varepsilon_{AB} > 0$).

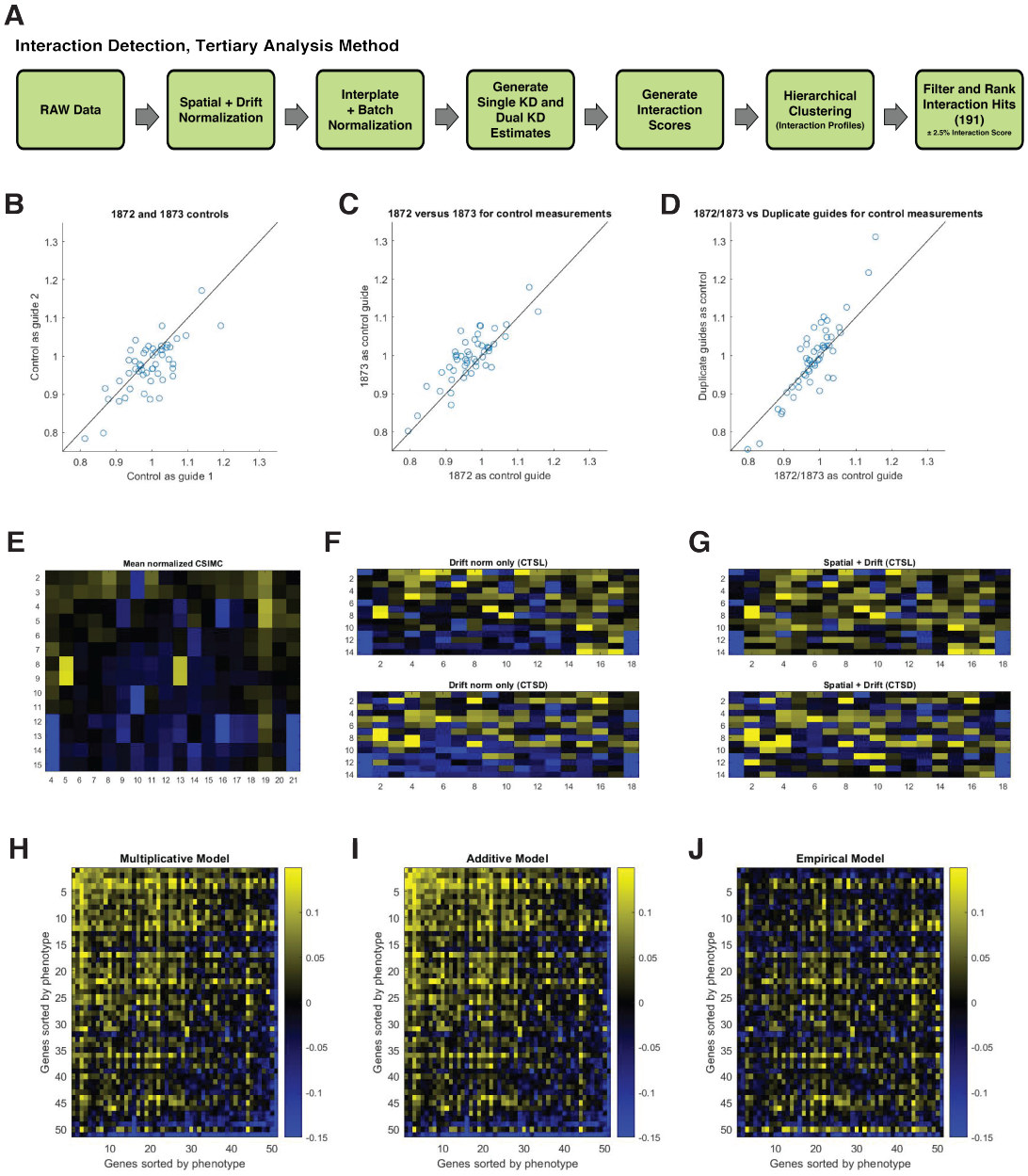


Figure 5.13: Genetic Interaction Detection, Tertiary Analysis Method. A.) Representative diagram of the Tertiary Interaction Detection method and narrowing of hits. Well-level scatterplots comparing B.) 1872-1872 and 1873-1873 control wells, which highly correlate; C.) 1873 vs 1872 used as the control in a gene-control interaction pair, there is a slight elevation in phenotypic score in the 1873-gene or gene-1873 combinations; and D.) 1872-Gene/1873-Gene vs Gene-Gene single KD combinations, at the extremes there seems to be a dosage effect of getting "double delivery" of targeting sgRNA. Representative heatmaps of E.) All well replicates superimposed into their screen layout positions, representing the "floor" of a given single KD phenotype; F.) Drift-only corrected plate layout with visible top/bottom biases, prompting G.) Spatial normalization to reduce this effect. H.) Multiplicative model, I.) Additive model, and J.) Empirical model, for predicting dual KD phenotypes for downstream scoring.

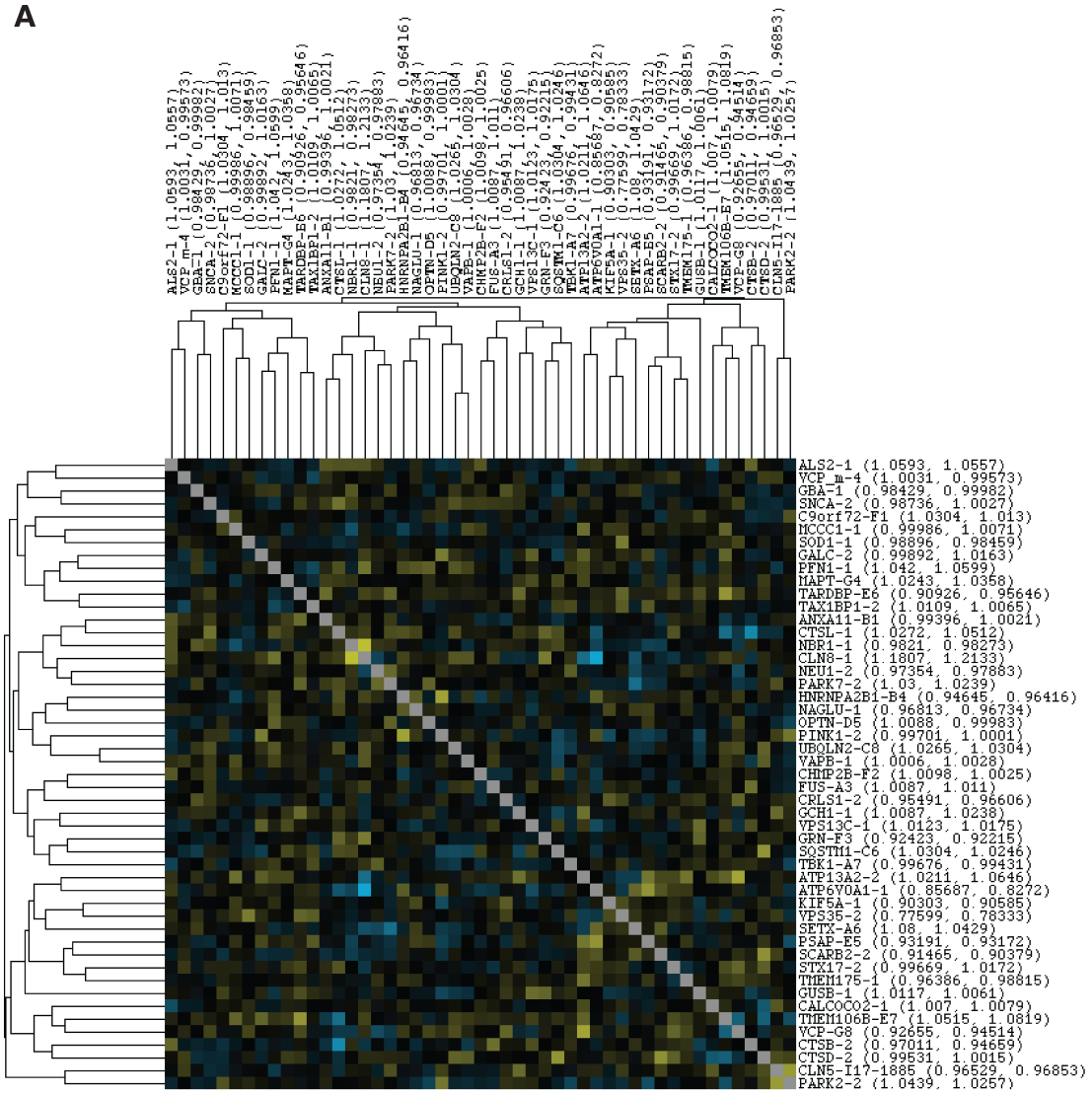


Figure 5.14: Tertiary Genetic Interaction Map. A.) Representative dendrogram of all pairwise gene-gene interactions from the screen. Those genes clustering together represent similar interaction profiles across the screen, regardless of known function. Yellow denotes a positive interaction, Blue denotes a negative interaction.

Figure 5.13 outlines the second interaction detection method used to generate a potential list of hits for follow-up validation. This method is completely disconnected from the Primary and Secondary S-scores, instead starting back at the well-level raw data, after removal of single-cell outliers. "Tertiary" interaction detection is summarized in the Figure 5.13A schematic, including batch (Figure 5.13E), drift (Figure 5.13F), and spatial (Figure 5.13G) normalization steps. After normalization, several models for predicting dual KD phenotypes are compared in Figures 5.13H-J in

order to generate interaction scores based on the observed and expected phenotype scores. Hierarchical clustering could then be performed to generate a Tertiary Genetic Interaction Map between all gene-gene combinations, shown in Figure 5.14.

The narrowing of hits to 191 was performed based on Tertiary analysis, with cutoffs set at ±2.5% interaction effect sizes. Additional interaction pairs were added as hits: 1) known interactors of GRN if not currently a hit, to complete the interaction network, 2) most significant PD interactors not currently a hit, and 3) add the most significant interactions from the secondary analysis method that were not currently in the hits to test the sensitivity of the previous method. This allowed for the largest volume of interactions (218) that I could bring through to primary validation (repeat of DQ-BSA). The full list of all interaction screening hits can be reviewed in Appendix C, with those hits that recapitulated in the validation screen labeled 1) blue for top negative interactions, red for top positive interactions, and grey representing the other groups (e.g. GRN interactors).

5.3 Genetic Interaction Validation

5.3.1 Primary Validation: DQ-BSA

Phenotypic hits must be validated to account for any potential missed noise or biological variation that could not be accounted for due to the nature of high-content screening. The genetic interaction screen I performed cannot be validated in precisely the same fashion as a normal compound screen, but many fundamentals are the same, such as increasing the number of biological replicates where possible and including more control groups. The primary challenge associated with the validation of the interaction screen is the exponential growth of the necessary controls needed as your hit list increases. For the validation I was planning, there were 4-6 control comparisons, whether non-targeting or single KD comparisons, needed in biological quadruplicate per interaction in order to properly interrogate a given interaction combination. This equates to between 16-24 wells per interaction, and there were 218 interactions to bring through primary validation.

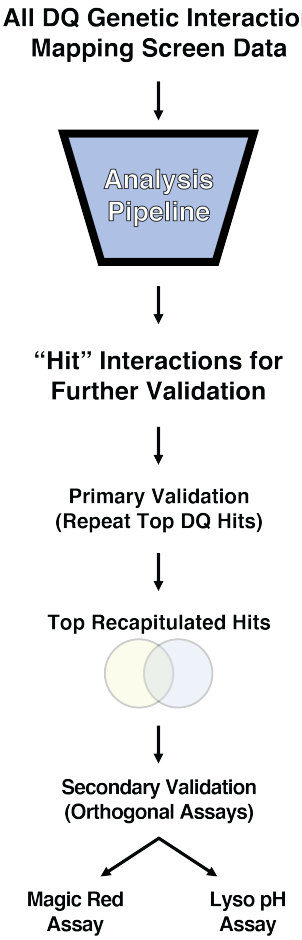


Figure 5.15: Screen Validation Overview.

The concept map in Figure 5.15 lays out the plans and the overall path I took from the screen analysis, through to interaction detection, and all subsequent validation experiments. After completion the main Genetic Interaction Mapping screen, a repeat set of DQ-BSA validation experiments were performed. These experiments repeated the same assay for each of the 218 hits, so was considered a "primary validation", as it is not a true secondary screen. Due to the complex nature of the main screen, it was important to narrow the scope of secondary screening downstream by demonstrating that the highest yield hits would recapitulate their phenotypes in an experimentally independent fashion.

After completing the primary validation experiments, interaction scores were

once again generated using the interaction equation, where the top 5 positive, top 5 negative, and a few additional interactors relevant to *GRN* biology were chosen for secondary validation experiments, shown in Table 5.2. Several *GRN* interactors did recapitulate phenotypically, but were lower down the hit list than the top 5 positive or negative hits.

CSIMC measurements and drift-corrected primary S-scores across all recapitulated hits were plotted with corresponding non-targeting controls and single KD comparisons, shown in Figure 5.16, Figure 5.17, and Figure 5.18. Each figure represents all hits from each major category in Table 5.2: Figure 5.16 represents the positive interactions group, Figure 5.17 represents the negative interactions group, and Figure 5.18 represents the *GRN* interactors. Interaction combinations are stacked in columns for quick comparison between the CSIMC plots on the top row with the primary S-Scores on the bottom row. All results have been pooled as a phenotypic summary in Table 5.3.

Table 5.2: Top Recapitulated Hits between the Genetic Interaction Mapping Screen and Primary Validation Screen

Top Recapitulated Hits	Category
CTSD-2-TMEM106B-E7	top_negative
HNRNPA2B1-B4-UBQLN2-C8	top_negative
CHMP2B-F2-FUS-A3	top_negative
CTSL-1-TMEM106B-E7	top_negative
ATP13A2-2-CLN8-1	top_negative
CTSD-2-CTSL-1	top_negative
CLN8-1-NBR1-1	top_positive
ATP6V0A1-1-PINK1-2	top_positive
CTSL-1-SNCA-2	top_positive
TAX1BP1-2-PSAP-E5	top_positive
VPS13C-1-GALC-2	top_positive
TARDBP-E6-TMEM106B-E7	top_positive
GRN-F3-TMEM106B-E7	grn_interactors
CTSL-1-GRN-F3	grn_interactors
CTSD-2-GRN-F3	grn_interactors
GRN-F3-GUSB-1	grn_interactors

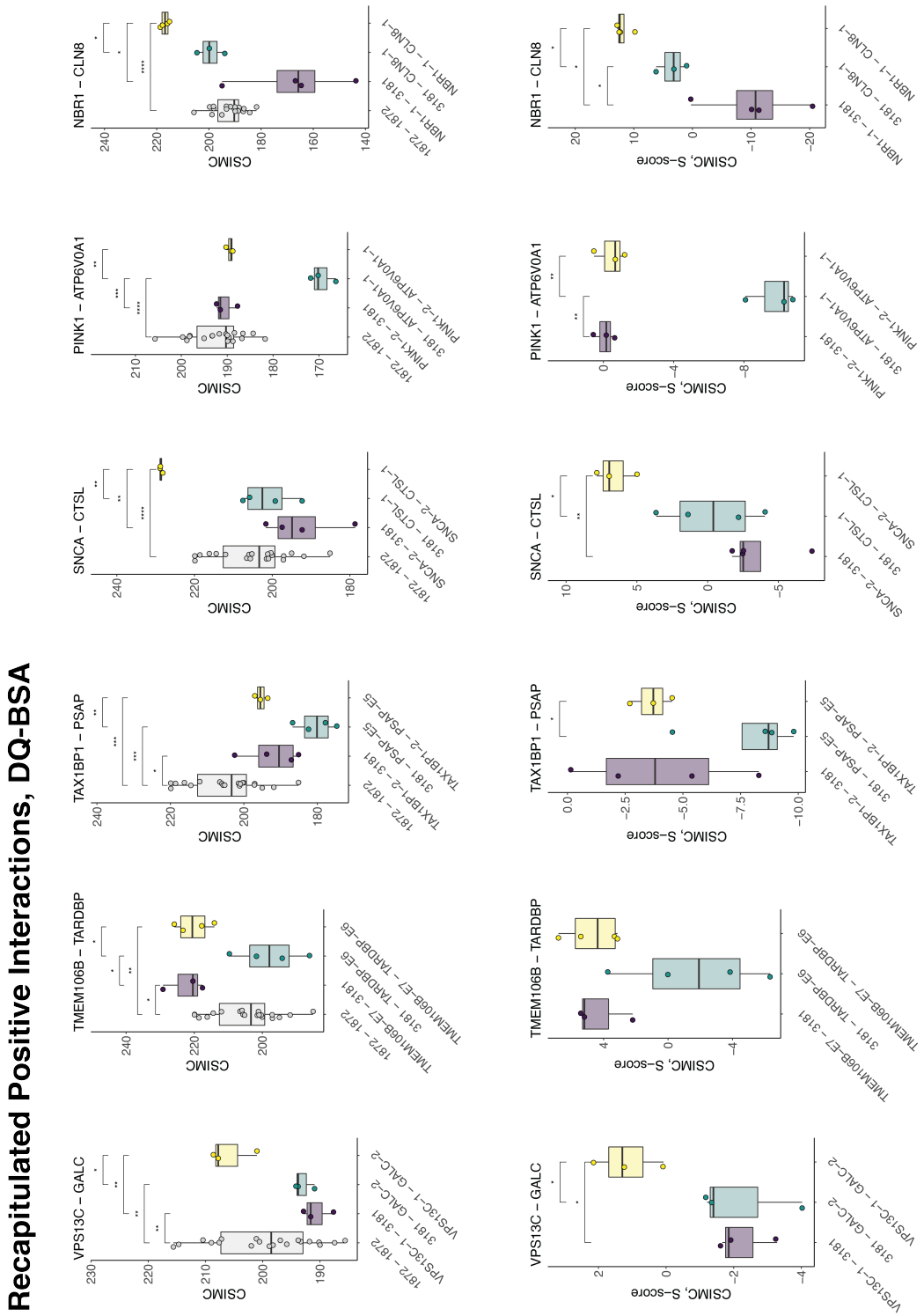


Figure 5.16: Primary Validation, Recapitulated Positive Interactions. VPS13C-GALC, TARDBP-TMEM106B, TAX1BP1-PSAP, CTSL-SNCA, ATP6V0A1-PINK1, and CLN8-NBR1.

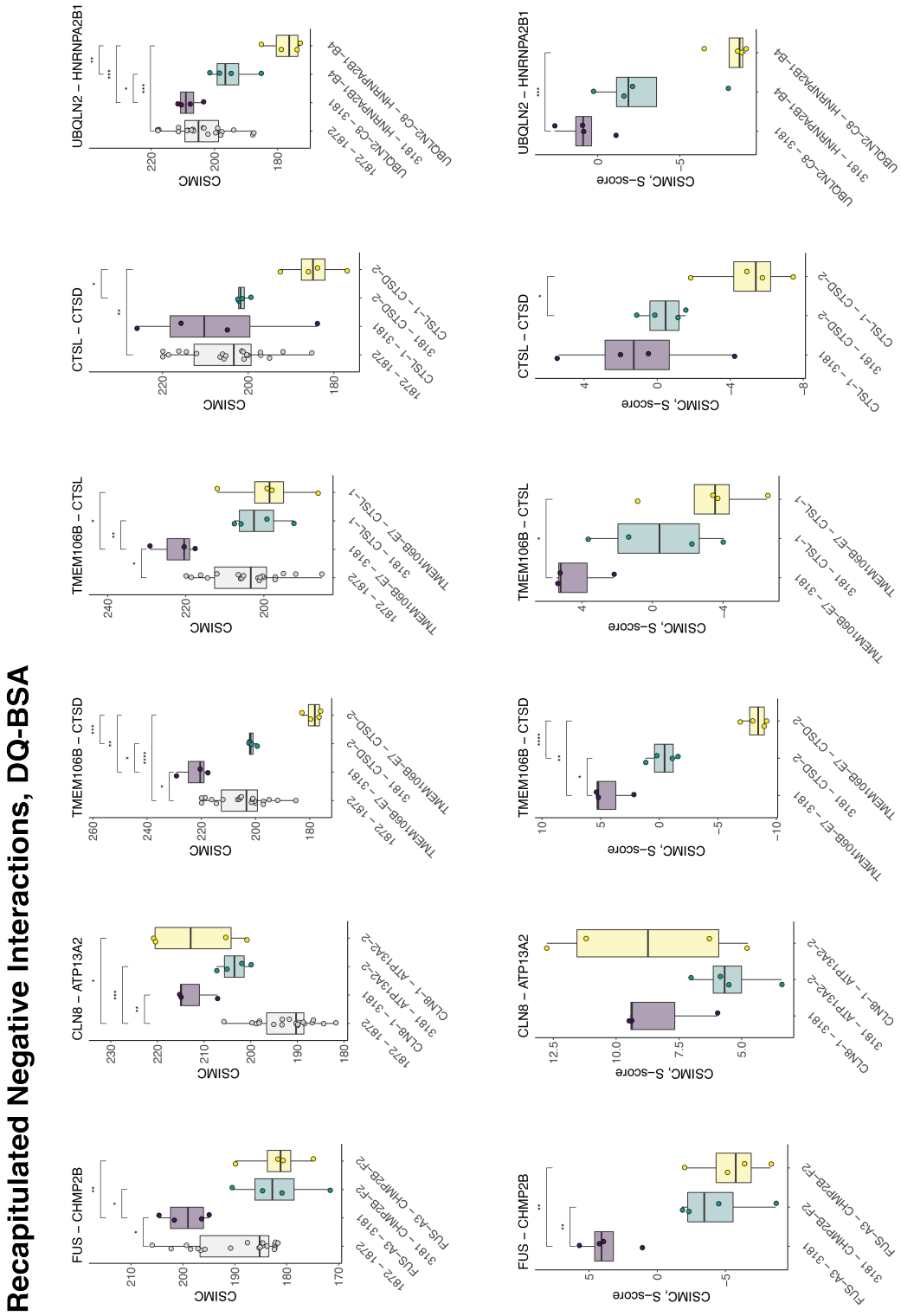


Figure 5.17: Primary Validation, Recapitulated Negative Interactions. CHMP2B-FUS, ATP13A2-CLN8, CTSD-TMEM106B, CTSL-TMEM106B, CTSD-CTSL, and HNRNPA2B1-UBQLN2.

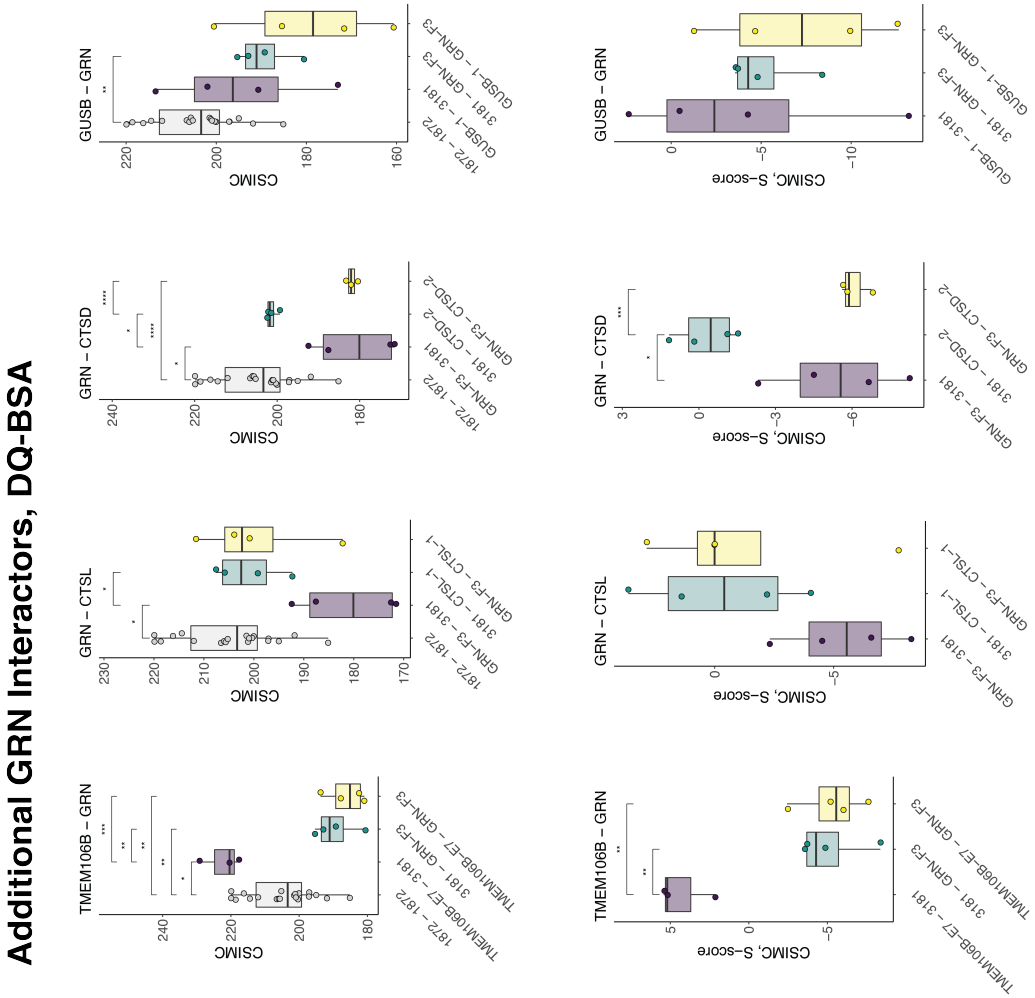


Figure 5.18: Primary Validation, GRN Interactors. GRN-TMEM106B, CTSL-GRN, CTSD-GRN, and GRN-GUSB.

5.3.2 Establishing Mechanistic Understanding: Magic Red and Lysosomal pH

Referring back to the screening validation overview in Figure 5.15, top recapitulated hits in across the DQ-BSA assays of the main genetic interaction mapping screen and the primary validation experiments require further *mechanistic, biological validation* to better understand the phenotypes present across single and dual KD combinations for a given interaction pair. The primary purpose of the secondary validation experiments is to begin to understand which lysosomal pathways the hit interactions have greatest influence. These assays do not represent a full mechanistic follow-up, but will 1) confirm any potential biological relevance along lysosomal pathways and 2) direct and inform future mechanistic studies related to the hit interactions.

Two orthogonal assays will be utilized for secondary validation: the Magic Red Cathepsin B Activity assay and the well-characterized lysosomal pH assay, featured in Chapter 4, Figure 4.3, Figure 4.4, and Figure 4.8. The Magic Red assay was chosen as another readout for lysosomal proteolysis that has been well characterized [166], and has multiple variations in substrates, such as a CTSL variant [165], which can be utilized in future studies. Additionally, the CTSB variant of Magic Red has previously been used in tandem with DQ-BSA as a complementary readout for lysosomal degradation [187]. Moreover, the dye-based assay could be quickly retrofitted for the pipelines already in place within my high-content imaging platform, and is very similar to the DQ-BSA assay in terms of methodology and image acquisition.

The 16 recapitulated hits from Table 5.2, along with associate control and single KD comparisons, were brought forward for the secondary validation experiments. Interaction scores were generated for the Magic Red assay, but the lysosomal pH assay requires another analysis method and does not suffer from any assay drift, so was handled separately. Drift-corrected primary S-scores and Lysosomal pH values for all 16 hit combinations were plotted with corresponding non-targeting controls and single KD comparisons, shown in Figure 5.19, Figure 5.20, and Figure 5.21.

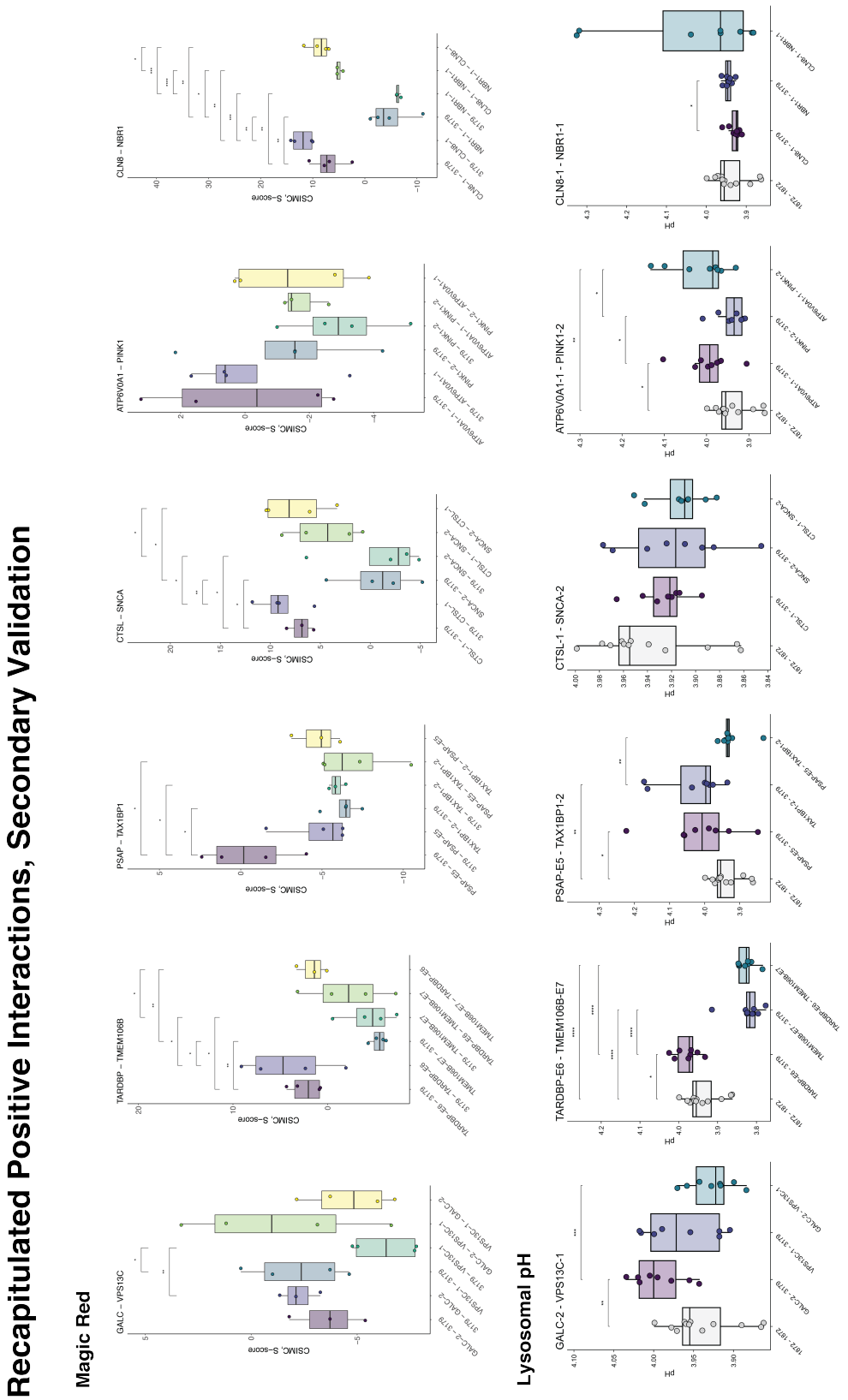


Figure 5.19: Secondary Validation, Recapitulated Positive Interactions. VPS13C-GALC, TARDBP-TMEM106B, TAX1BP1-PSAP, CTSL-SNCA, ATP6V0A1-PINK1, and CLN8-NBR1.

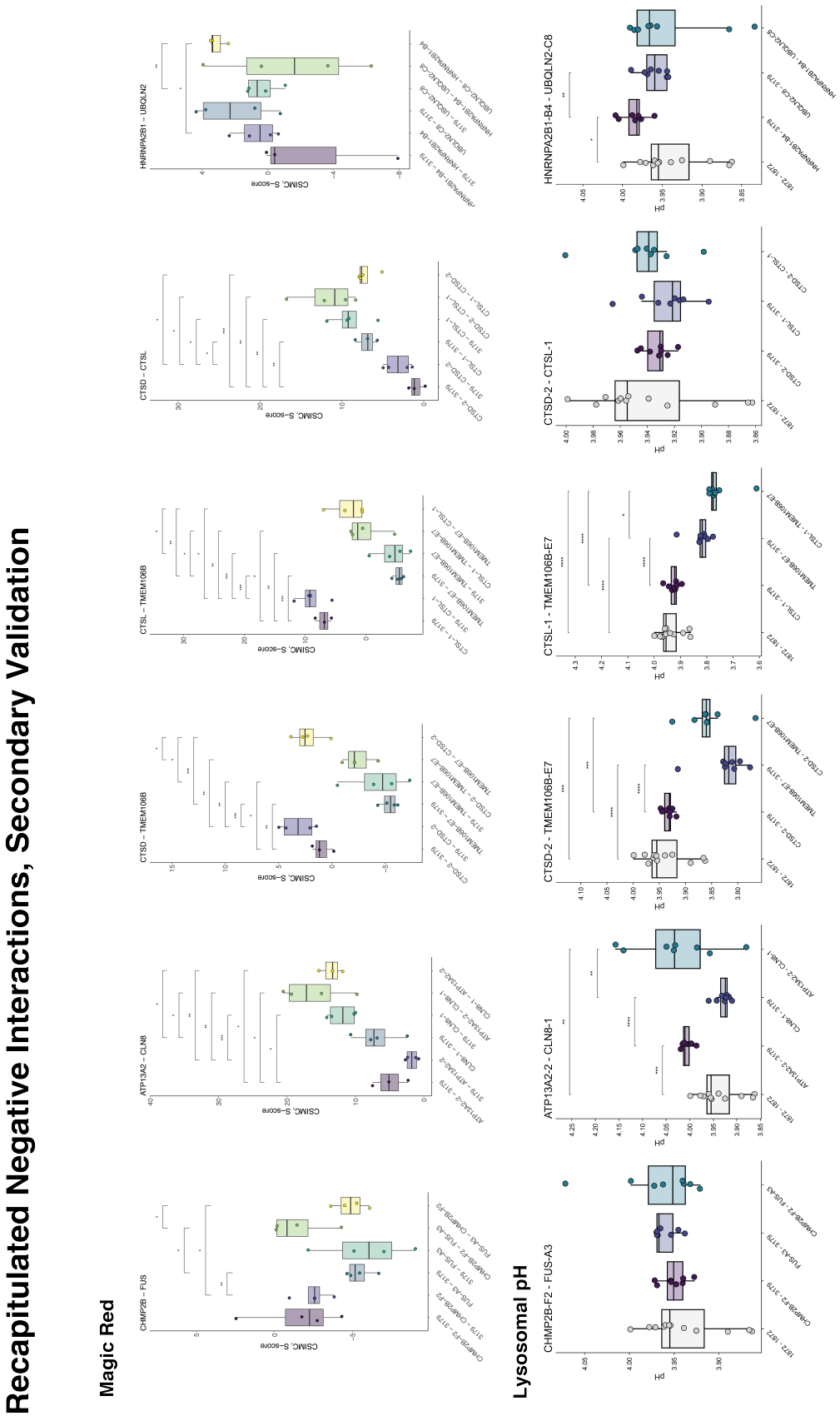


Figure 5.20: Secondary Validation, Recapitulated Negative Interactions. CHMP2B-FUS, ATP13A2-CLN8, CTSD-TMEM106B, CTSL-TMEM106B, CTSD-CTSL, and HNRNPA2B1-UBQLN2.

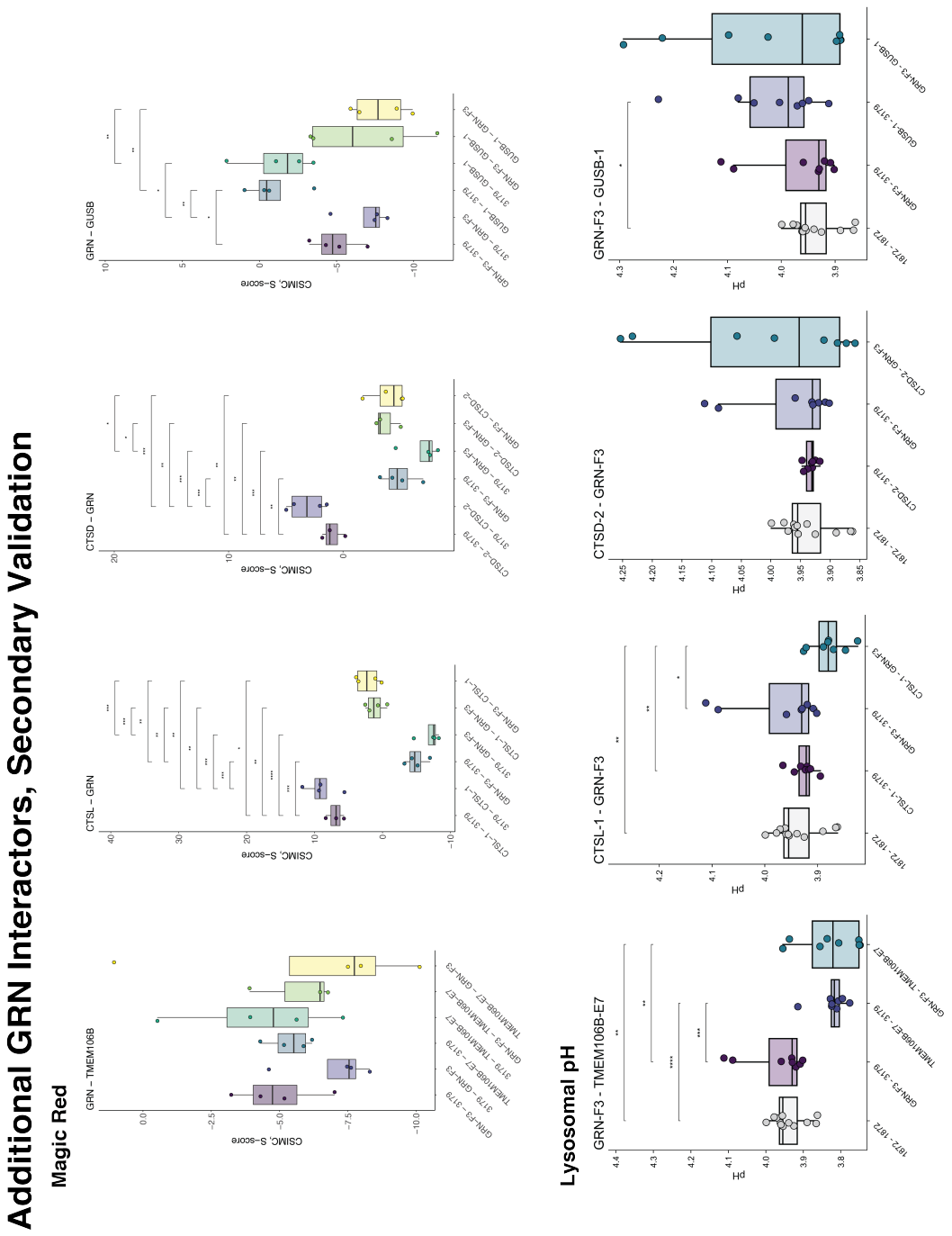


Figure 5.21: Secondary Validation, GRN Interactors. GRN-TMEM106B, CTSL-GRN, CTSD-GRN, and GRN-GUSB.

As with the primary validation results, each figure represents all hits from each major category in Table 5.2: Figure 5.16 represents the positive interactions group, Figure 5.17 represents the negative interactions group, and Figure 5.18 represents the *GRN* interactors. Interaction combinations are stacked in columns for quick comparison between the Magic Red primary S-Score plots on the top row with the lysosomal pH plots on the bottom row. All results have been pooled as a phenotypic summary in Table 5.3, along with the primary validation results.

Table 5.3: Phenotypic Summaries for all Genetic Interaction Hits

Category	**Interaction Pair**	**Interaction Screen DQ-BSA**	**Primary Validation DQ-BSA**	**Secondary Validation Magic Red**	**Secondary Validation Lyso pH**
Positive Interactions	VPS13C-1-GALC-2	high	high	low	no change
	TARDBP-E6-TMEM106B-E7	high	high	no change	very low
	TAX1BP1-2-PSAP-E5	low	low	low	no change
	CTSL-1-SNCA-2	very high	very high	high	no change
	ATP6V0A1-1-PINK1-2	low	no change	no change	high
	CLN8-1-NBR1-1	very high	very high	high	no change
Negative Interactions	CHMP2B-F2-FUS-A3	low	low	low	no change
	ATP13A2-2-CLN8-1	very high	high	very high	high
	CTSD-2-TMEM106B-E7	low	very low	no change	low
	CTSL-1-TMEM106B-E7	no change	no change	no change	very low
	CTSD-2-CTSL-1	low	low	very high	no change
	HNRNPA2B1-B4-UBQLN2-C8	very low	very low	no change	no change
GRN Interactors	GRN-F3-TMEM106B-E7	mildly low	low	low	low
	CTSL-1-GRN-F3	no change	no change	no change	low
	CTSD-2-GRN-F3	low	low	low	no change
	GRN-F3-GUSB-1	no change	low (ns)	low	no change

5.4 Discussion

In Chapter 5, I successfully demonstrated the development and optimization of Genetic Interaction Mapping in i^{3}Neurons for high-content screening and completed the first Genetic Interaction Mapping screen in human iPSC-derived Neurons. Moreover, I was able to identify key interaction hits and implement the preliminary validation of potential gene-gene interactions within my library of FTD/ALS and PD sgRNAs.

Preliminary Dual Knockdown Screening

Due to the size and scope of the target genetic interaction mapping screen, careful considerations for the plate layout, location of controls, and number of biological well replicates were made to optimize imaging parameters and downstream analysis. When considering overall virus usage and plate layout, a maximum of two well replicates per interaction could be afforded.

These early considerations resulted in a change to the analysis methods used in Chapter 4, where single-cell level data would be utilized instead of pre-averaged well-level outcomes from the high-content analysis software. Single-cell level data is difficult to work with and requires robust bioinformatics wrangling and analysis, as you are considering potentially many thousands of data points per well. However, many key conclusions were made while developing the analysis pipeline for the preliminary screen, including the need for robust outlier detection, linear drift modeling, cell- and well-level quality control, and outcome measure optimization.

Remarkably, the some of the key findings from the single KD screen (Figure 4.9) at the end of Chapter 4 were recapitulated in the preliminary dual knockdown screen, shown in Figure 5.3 and Figure 5.4. Several strong single KD phenotypes are emerging within the sgRNA library, such as *CLN8* or *ATP6V0A1* KD, which have essentially served as genetic controls for my various DQ-BSA experiments due to very consistent phenotypes on opposing ends of the assay. Additionally, we are seeing these phenotypes across multiple experiments and in multiple reciprocal combinations with non-targeting guides. The same is true for *GRN*, *PSAP*, *CTSL*,

and *TMEM106B* KD, all having provided benchmarks from the single KD experment up to and during the analysis of the main genetic interaction mapping screen, providing further evidence for their connection to lysosomal degradation pathways.

Full Genetic Interaction Mapping Screen: DQ-BSA

Key experimental design changes were implemented to make the full screen a success, most notably the switch to a "core guide" layout (Figure 5.5). The matrix design from the preliminary screen (Figure 5.2) was critically flawed beyond a single plate experiment, where plate to plate variation must be considered.

The lessons learned from the preliminary dual KD screen directly led to the experimental design changes, which provided a format in which 49 miniature genetic interaction screens could be performed. However, the optimized design also generated primary s-scores that are derived from local plate controls, allowing for cross-plate comparisons between samples linked by *genotype*. For example, core guide plate 1 (i.e. gene 1 plate) will have a gene 1 and gene 2 combination, but core guide plate 2 (i.e. gene 2 plate) will also have gene 2 and gene 1 reciprocal interaction pairs as completely independent replicates of the those seen on core guide plate 1. This is a key concept in the first interaction detection method.

In the example primary interaction hitmap for shown in Figure 5.6A, notably, the the only sgRNA KDs that normalized or flipped the primary s-score sign were *CLN8*, *TMEM106B*, and *CTSL* when combined with *GRN* KD. Two primary conclusions can be drawn from this: 1) *GRN* KD has strong negative DQ phenotype, as shown previously and across this hitmap (most combinations have negative primary s-scores), and 2) *CLN8*, *TMEM106B*, and *CTSL* either have strong positive DQ phenotypes on their own, may interact with *GRN* along some lysosomal pathway, or some combination of the two. This simple yet poignant question hits at the core of this entire project, is not entirely straightforward to address, and will require further interaction analysis and biological validation.

The secondary analysis interaction maps help provide a baseline for understanding which gene knockdowns have the greatest effects on a given core guide. In the example shown in Figure 5.6C, *ATP6V0A1*, *VPS35*, *SCARB2* combinations all

decreased the baseline GRN-GRN phenotype significantly, while *CLN8*, *CTSL*, and *PARK7* all increased the baseline GRN-GRN phenotype significantly. Referring back to the question posed with primary s-scores, the strong phenotypes seen in *ATP6V0A1* and *CLN8* KD are seen as significantly low or high, respectively, across nearly all CSIMC secondary s-score maps in Figure 5.7, Figure 5.8, Figure 5.9, and Figure 5.10, providing further evidence that single KD phenotypes must be properly considered when trying to quantify true gene-gene interactions. The secondary interaction maps efficiently demonstrate the phenotypic effects of dual KD combinations across each core guide plate, however, they do not distinguish between additive and synergistic interactions, as described in Figure 5.12. Ultimately, the primary and secondary maps are necessary tools to interpret the biological phenomena, but more in-depth analysis is required to untangle and validate any potential gene-gene interactions.

Figure 5.11 and Figure 5.13 represent the two methods I utilized to understand if large phenotypic changes or potential phenotypic rescues arising from dual gene knockdowns were due to strong single KD effects or gene-gene interactions. The secondary analysis method from Figure 5.11 utilized secondary s-scores as the base detection method for large phenotypic effects. The primary s-scores from those hit interactions could then be grouped across the entire screen, combining the duplicate wells from each core guide plate from a given interaction and further analysis via the interaction equation (Section 5.1.1). However, the method does not properly adjust for strong single KD effects and needs a better method for addressing the variation between groups within the interaction equation. Additionally, there is no correction for spatial biases like those in the tertiary analysis detection method shown in Figure 5.13. Hits from the tertiary method were ultimately chosen for downstream validation because many of the weak points in the secondary detection method were addressed, in particular the correction for spatial effects and the implementation of a custom empirical model (Figure 5.13J) for single KD and predicted double KD estimates.

The tertiary analysis detection method also allowed for the generation of a full interaction map of all combinations within the screen, shown in Figure 5.14. The dendrogram displays pairwise gene-gene interactions as a heat map (yellow = positive, blue = negative, black = no interaction), where genes clustering together represent similar interaction profiles across the screen, regardless of known function. Further analysis of these clusters is a future goal of mine, however, the visual interpretation of interactions is an efficient summary. Moreover, there are some relevant clustering patterns worth noting, such as GBA/SNCA and GRN/SQSTM1/TBK1. GBA has previously been shown to promote SNCA accumulation [188], and it is known that TBK1 phosphorylates SQSTM1/p62 and both are implicated [189, 190], along with GRN, in autophagy pathways [191].

Primary and Secondary Screen Validation

As defined in Figure 5.12, a positive or negative synergistic interaction is defined by having a higher or lower, respectively, phenotypic interaction score than expected by whatever model is being used to generate single and combinatorial knockdown estimates (Section 5.1.1). Both the primary and secondary screen validation experiments were successful in generating orthogonal phenotypic comparisons to the base DQ-BSA assay that was used in the main genetic interaction mapping screen for all of the recapitulated hits and their associated comparisons. A detailed version of these comparisons can be reviewed in Table 5.3 and all primary validation plots can be referenced in Figure 5.16, Figure 5.17, and Figure 5.18, and all and secondary validation plots in Figure 5.19, Figure 5.20, and Figure 5.21.

*For the following arguments, all phenotypic results will be grouped by interaction pair and qualitatively summarized in the following way: (**GI-DQ: Genetic Interaction DQ Result, PV-DQ: Primary Validation DQ Result, SV-MR: Secondary Validation Magic Red Result, SV-pH: Secondary Validation Lysosomal pH Result**).*

All qualitative categories are referencing the interaction pair phenotype compared to the non-targeting, or WT, phenotype. Single KDs are not considered in the qualitative results here, or in Table 5.3.

The positive interaction TARDBP-TMEM106B *(GI-DQ **high**, PV-DQ **high**, SV-MR **no change**; SV-pH **very low**)* had an interesting validation profile. In both DQ assays, the phenotype was very high, despite *TARDBP* single KD usually showing low intensity and *TMEM106B* single KD usually weakly positive. There was no change in CTSB activity, but the lysosomal pH assay showed very decreased pH. These findings would suggest that acidification may play a role here in increasing the DQ signal. Again, the preliminary lysosomal pH results indicated that pH levels were *below* that of the non-targeting controls.

The positive interaction CLN8-NBR1 *(GI-DQ **very high**, PV-DQ **very high**, SV-MR **high**, SV-pH **no change**)* also had a consistent validation profile. Both DQ-BSA assays showed a very high result, one of the highest positive interactions across the screen, and CTSB activity in Magic Red was also high compared to non-targeting controls. However, unlike the TARDBP-TMEM106B interaction, there was no significant change in lysosomal pH measurements. This indicates that the CLN8-NBR1 interaction perhaps acts on another related, but potentially lysosomal acidification-independent pathway. Strikingly, the CLN8-NBR1 DQ results were higher than *CLN8* single KD and *NBR1* has a mildly low single KD phenotype in comparison to non-targeting.

The negative interaction ATP13A2-CLN8 *(GI-DQ **very high**, PV-DQ **high**, SV-MR **very high**, SV-pH **high**)* is interesting due to a sign flip in the pH assay. Across both DQ assays, the phenotype was high, indicating an increase in proteolysis, and the results from the Magic Red assay agree as that phenotype is elevated as well. However, the lysosomal pH assay indicates that the combinatorial knockdown has a high pH as well, which would indicate alkalinized lysosomal compartments. This suggests that proteolysis and acidification readouts do not agree in this case and would an interesting interaction to follow up.

The interaction GRN-TMEM106B *(GI-DQ **mildly low**, PV-DQ **low**, SV-MR **low**, SV-pH **low**)* is also worth noting, as I have been focused on this interaction throughout my DPhil. The results across the DQ assays were in agreement, where GRN-TMEM showed low signal, backed up by the CTSB activity being low in the Magic Red assay. However, the lysosomal pH was also low, which contradicts the proteolysis results in the opposite way to the ATP13A2-CLN8 interaction. Frustratingly, the *GRN* single KD phenotype did not show as significant of an increase in pH as the *GRN* KO assays previously performed. More importantly, a remarkable trend can be seen across all interactions with *TMEM106B*, where the pH is significantly lower than the non-targeting comparison. This indicates, as in the above example with TARDBP-TMEM106B that *TMEM106B* may play a significant role in the balance of acidification in lysosomes.

The positive interaction CTSL-GRN *(GI-DQ **no change**, PV-DQ **no change**, SV-MR **no change**, SV-pH **low**)* is also in the GRN interactor group. Strikingly, there is no significant phenotype between CTSL-GRN and non-targeting controls across both DQ assays or the Magic Red assay. Lysosomal pH, however, is decreased significantly, which indicates a potential rescue across all assays. When you take into account the highly penetrant and reproducible *GRN*-related phenotypes across my entire project, in both KO and KD cases, the significance of these integrated findings becomes clear. The phenotypic rescues of CTSL-GRN compared to their single KD comparisons seen in Figure 5.18 and Figure 5.21 are distinct. Interestingly, *CTSL* single KD does not seem sufficient to rescue the lysosomal pH phenotype, as that comparison is not significant compared to non-targeting, opposed to the *TMEM106B* single KD pH phenotype.

Overall, I think that these results are indicative of a well-characterized screening validation strategy. However, my primary concerns are focused on assay improvement and optimizing several factors for repeat experiments. Firstly, it is important to note that from the screen itself to the validation experiments, I was near the absolute limit for the volume of interactions that could be imaged in a single assay due to maximizing real estate on 384 formats, which decreases overall biological replicates

per condition. Any future experimentation will greatly benefit from fewer samples and comparisons repeated on multiple plates, especially for further validation and mechanistic studies of the key interaction hits.

For example, the GRN single KD conditions did not have large effect size in the pH phenotype when compared to the GRN KO i^{3}Neurons assayed in Chapter4, despite having a consistently decreased DQ phenotype. This effect could be related to how intermediate or mild phenotypes are more precisely assayed with KO models, however, repeating these experiments and increasing the biological replicates per condition is a good first step in potentially resolving this issue. GRN remains as a strong benchmark for the KD results as a whole, as the previous work in the KO models and the validation of that lysosomal dysfunction was clear in Chapter 4.

In review of Chapter 5, several key components of my DPhil project that were developed across the findings in Chapter 3 and Chapter 4, and indeed over the past several years, were fully integrated as a functional genomics platform. This culminated in a unique genetic interaction mapping screen aimed at systematically interrogating the functional consequences of pairwise gene knockdown in genes causative for FTD/ALS and PD that function along lysosome-related pathways, and has provided a rich dataset for further mechanistic studies.

6 Discussion

Contents

6.1 Overview 157
6.2 Molecular Biology 157
6.3 Transcriptomic Interactions 157
6.4 Phenotypic Assays 158
6.5 Genetic Interaction Mapping 159
6.6 Future Work 160

6.1 Overview

The overall theme of Chapter 3 was tool generation. I was able to create new a screening-optimized CRISPRi Far-red cytosolic system, while optimizing the cloning, lentiviral delivery, and validation of CRISPRi sgRNAs for use in high-content phenotypic assays and screening. The multipurpose platform that was ultimately assembled, primarily in this chapter, enabled the high-throughput knockdown line generation necessary for the assays developed in Chapter 4 to be retrofitted and optimized for use in the high-content CRISPRi-based screens completed in Chapter 5. Indeed, other phenotypes, functional networks, or disease processes could be interrogated by this pipeline by utilizing techniques like cell paint, which analyze multiple organelle-specific readouts at once.

6.2 Molecular Biology

Some of the major accomplishments in Chapter 3 were in fundamental aspects of biology, such as the optimization of high-throughput ligation cloning which enabled me to produce and validate a sizeable sgRNA library. Moreover, the Far-Red CRISPRi system had to be optimized, first by the selection of an ideal fluorescent protein, then by completely rebuilding the tool due to lack-luster expression of iRFP670. Ultimately, this troubleshooting directly allowed for the dual KD screens performed in Chapter 5. Without an optimized second sgRNA delivery, our downstream assay options would have been greatly hindered. The drug selection cassettes also had an important role to play, allowing for the selection of sgRNA-positive i^{3}Neurons and the eventual extraction of RNA specific to each KD condition for targeted validation.

6.3 Transcriptomic Interactions

The targeted RNA sequencing was also a key success of Chapter 3, which turned a potential time-sink (sgRNA validation) into a streamlined process by drastically increaseing the sample throughput of the entire method. This series of experiments

not only validated all individual sgRNAs of the FTD/ALS and PD sublibrary, but also provided a rich dataset consisting of the transcriptomic profiles across the targeted panel of genes for each KD sample. Analysis of these profiles provided a list of potential transcriptomic interactions, shown in Table 3.3.

Three of these interactions were analyzed further, *KIF5A/LRRK2* interaction, *GCH1/CLN8* interaction, and the potential interactions between *VCP* and *ALS2*, *CLN8*, *SOD1*, and *SQSTM1*. Interestingly, *LRRK2*, the most common cause of PD [192], has been recently implicated in neural transport impairment [193], with further evidence suggesting that LRRK2 plays a key role in axonal transport [194]. KIF5A, a motor kinesin recently implicated as a cause for ALS [195], also plays a key role in axonal transport, with recent studies characterizing toxic gain-of-function mutations that induce protein aggregation [196, 197]. Of the three transcriptomic interactions analyzed in Figure 3.3, the *KIF5A/LRRK2* interaction seems to be the most promising potential connection due to this further evidence of shared functional networks. Additionally, this would be a direct overlap of FTD/ALS and PD, in this case primarily acting on pathways related to axonal transport.

6.4 Phenotypic Assays

Chapter 4 was concentrated on the development of neuronal assays that could be utilized for high-content screening. These included neuronal-specific survival and neurite tracing, transferrin recycling, lysosomal pH, and the proteolysis assay DQ-BSA. One key accomplishment from this work was my contribution to pioneering the utilization of i^{3}Neurons and CRISPRi on arrayed 96 and 384-well formats.

The two primary assays used in the downstream screening in Chapter 5 were those measuring lysosomal pH and lysosomal proteolysis (DQ-BSA), as these assays could be performed efficiently on high-content formats and were optimized for screening applications. Longitudinal neuronal imaging and neuronal survival assays occur on a scale of days, whereas the lysosomal pH and DQ-BSA assays optimized in this thesis are on a scale of hours, disregarding pre-treatements or assay loading. Based on the scale of the proposed genetic interaction mapping screen (Chapter 5)

and the aim to assess the functional interactions across our sgRNA library, these lysosomal assays required thorough optimization and confirmation of reproducibility.

The Ward Lab's *GRN* KO i^{3}Neuron cell line was an ideal model system to functionally demonstrate perturbations in the pathways related to pH and DQ-BSA. Many of the findings in Chapter 4 were derived from this line, which allowed me to optimize and automate previously low-throughput assays into high-content applications. Moreover, I was able to confirm the presence of a severe defect in *GRN* KO i^{3}Neuron lysosomal pH, which then recapitulated in the orthogonal DQ-BSA assay. This series of experiments in the *GRN* KO i^{3}Neurons culminated in the functional validation of many of our sgRNAs in the first of a series of CRISPRi-based phenotypic screens, which included a severe *GRN* KD phenotype in DQ-BSA, shown in Figure 4.9.

The results shown in Table 4.3 and Table 4.4 summarized those sgRNAs with the largest DQ-BSA phenotypes. This particular experiment was not intended to be anything more than a preliminary trial combining the DQ-BSA assay with CRISPRi sgRNAs delivered to the i^{3}Neurons for the first time. However, it marked a key branch point in my DPhil project, where most experiments before this experiment were optimization and non-CRISPRi-based, while those after this point were primarily CRISPRi-based and designed to push closer to the final genetic interaction mapping screen. The single KD screen was foundational for the entire project and marked the phenotypic debut for many sgRNAs in the screen. Even though I left out the single KD results in Table 5.3, which summarized the hit interactions across experimental validation, many of the interaction hits had their first single KD experimental "replicate" demonstrated in this preliminary screen.

6.5 Genetic Interaction Mapping

Chapter 5 demonstrated how effective the CRISPRi-based functional genomics platform can be at interrogating converging pathways. The genetic interaction mapping screen combined all the cutting-edge elements from Chapter 3 and Chapter 4, including sgRNA delivery via acoustic fluid handling, organelle-specific assays

performed at sub-cellular resolution, high-content imaging and analysis of i^{3}Neurons, complex bioinformatics analysis, and CRISPRi-based functional genomics screening.

The successful implementation and optimization of a bioinformatics analysis pipeline led to the detection of hits and the generation of the first phenotypic genetic interaction maps between the major genetic causes and risk factors of FTD/ALS and PD in iPSC-derived neurons. The top interaction hits were then validated with a repeat DQ-BSA assay and a preliminary mechanistic follow-up was performed utilizing the Magic Red and lysosomal pH assays.

Interestingly, there is emerging evidence in recent studies further connecting some of the hits reviewed in Chapter 5. *TMEM106B* was a component of the interactions TARDBP-TMEM106B and GRN-TMEM106B, and a recent study has demonstrated that *TMEM106B* modifies TDP-43 pathology [1], while overexpression of *TMEM106B* induces cell death and causes the cleavage of TDP-43 [2]. Additionally, *TMEM106B* has been implicated as an interactor of *GRN* in the clinic [3, 4], and as a regulator of lysosomal function and acidification in mice [4, 5]. Regarding the hit interactions CLN8-NBR1 and ATP13A2-CLN8, studies have demonstrated that *NBR1* interacts with *CLN8* via pathway intermediaries *BNIP3* and *BNIP3L* along mitophagy/autophagy networks [198]. While no direct links exist currently, *ATP13A2* is also classified as a CLN (CLN12) [86] with potential crossover connections to FTD/ALS via GRN and PD/Gaucher's Disease via *CLN8* [199]. It is known that *CTSL* cleaves *GRN* [5], referring to the interaction CTSL-GRN, but no current studies exist showing an interaction beyond that, certainly not to the degree of rescue shown by the data in this thesis. This may be an ideal target for follow-up studies as a priority interaction.

6.6 Future Work

In future work related to the CTSL-GRN interaction, I propose that PGRN levels in *CTSL*-depleted (CRISPRi) and inhibited cells (pharmacologically) could be ascertained to confirm if my current findings are in any way related to the cleavage process of progranulin into granulins. Additionally, I could pharmacologically

inhibit *CTSL* in *GRN* KO i^{3}Neurons, in an attempt to phenocopy the CTSL-GRN interaction independently and attempt o untangle if protease activity increased independently of pH or not in this particular interaction. Using the longitudinal neuronal survival and neurite outgrowth assay developed in Chapter 4, I could also assess if *CTSL* inhibition/knockdown promote enhanced cell viability with and without co-knockdown of GRN. Lastly, I would like to perform further protein-protein interaction analysis associated with the clusters seen in the Tertiary interaction map in Figure 5.14.

Appendices

A

Appendix for Chapter 3 Tables and Titers

Contents

A.1 List of all sgRNA sequences used for CRISPRi plasmid cloning and library generation 163
A.2 Nuclear Blue Lentivirus Library Titers and Transfer Volumes 173
A.3 Nuclear Blue sgRNA Lentivirus Library Titer Curves 177
A.4 Cytosolic Far-Red Lentivirus Library Titers and Transfer Volumes 182
A.5 Cytosolic Far-Red sgRNA Lentivirus Library Titer Curves 186
A.6 Final Targeted, Multiplexed RNA Sequencing Lentivirus Titer Table 190
A.7 Final Targeted, Multiplexed RNA Sequencing Sample Table 195
A.8 Log2 Fold Change and Significance Values from Targeted RNA Sequencing 209

A.1 List of all sgRNA sequences used for CRISPRi plasmid cloning and library generation

Table A.1: List of all sgRNA sequences used for CRISPRi plasmid cloning and library generation.

GOI	Primary Category	Subcategory	Kampmann Name	sgRNA Reference Name	Score	Sequence	Validated
CTSD	Cathepsins	FTD/ALS-related	CTSD_-_1785114.23-P1P2	CTSD-1	0.945173348	GGCGGCGGCCGGGTCGGAGA	This thesis
			CTSD_-_1784665.23-P1P2	CTSD-2	0.89146315	GCCTAGGTCTCCAGCAACAA	This thesis
CTSL	Cathepsins	FTD/ALS-related	CTSL_+_90341065.23-P1	CTSL-1	0.991087529	GGCTGCGCAGGCGCACTCCA	This thesis
			CTSL_-_90341061.23-P1	CTSL-2	0.990461469	GCGACCTCCGCAACCTTGAG	This thesis
CTSB	Cathepsins	PD GWAS	CTSB_+_11725568.23-P1P2	CTSB-1	1.017547449	GAGGGCTCCGGCAACCGCTC	This thesis
			CTSB_-_11725558.23-P1P2	CTSB-2	0.999681367	GCAGCCTGCGCGCAGCGGAG	This thesis
ALS2	FTD/ALS	-	ALS2_-_202645613.23-P1P2	ALS2-1	0.950640603	GCGCTCACCTGAAGCTCCAC	This thesis
		-	ALS2_-_202645268.23-P1P2	ALS2-2	0.880236643	GAATAGCTGGAAGGCAGCGT	This thesis
ANXA11	FTD/ALS	-	ANXA11_-_81964900.23-P1P2	ANXA11-A1	0.98210985	GACGCCGAGGCTGATCTAGG	Ward Lab, unpublished
			ANXA11_-_81965250.23-P1P2	ANXA11-B1	0.887784346	GCGGGGCACTCGGGGCACTG	
			ANXA11_-_81965296.23-P1P2	ANXA11-C1	0.838688527	GCGCCGGGCGGAAAACTCCG	
			ANXA11_-_81964867.23-P1P2	ANXA11-D1	0.829873779	GGCACCCCGACCACACATGA	

Table A.1 continued from previous page

GOI	Primary Category	Subcategory	Kampmann Name	sgRNA Reference Name	Score	Sequence	Validated
C9orf72	FTD/ALS	-	C9orf72_+_27573404.23-P1P2	C9ORF72-F1	0.902589769	GGAGTGAGGA-GGCGGCATCC	Ward Lab, unpublished
CHCHD10	FTD/ALS	-	CHCHD10_-_24109711.23-P1P2	CHCHD10-C2	0.914915516	GAGCCCCGGC-TGGCCCGAAG	Ward Lab, unpublished
CHMP2B	FTD/ALS	-	CHMP2B_-_87276493.23-P1P2	CHMP2B-F2	0.899618862	GACCTGAGCT-CCGGGTGACG	Ward Lab, unpublished
DCTN1	FTD/ALS	-	DCTN1_+_74618971.23-P1P2	DCTN1-1	1.199676387	GGCCGGCCCC-GCAGGGTCTT	This thesis
			DCTN1_+_74618911.23-P1P2	DCTN1-2	0.976343427	GCCTCACAGT-GCAGGTACGG	This thesis
FUS	FTD/ALS	-	FUS_-_31191558.23-P1P2	FUS-A3	1.391299105	GGGCCTCAAA-CGGTAGGTAA	Ward Lab, unpublished
			FUS_-_31191697.23-P1P2	FUS-C3	0.875026886	GCGCGGAGAA-GAGTAACTGG	
GRN	FTD/ALS	-	GRN_-_42422695.23-P1P2	GRN-F3	0.922267023	GTGCCCAAGG-ACCGCGGAGT	Ward Lab
HNRNPA2B1	FTD/ALS	-	HNRNPA2B1_+_26240367.23-P1P2	HNRNPA2B1-B4	0.943448121	GGCGGCGGCA-GCGGCTCTAG	Ward Lab, unpublished
KIF5A	FTD/ALS	-	KIF5A_-_57943854.23-P1P2	KIF5A-1	0.894504983	GCCGAAAGGA-CCAGACGCCC	Ward Lab, unpublished
MAPT	FTD/ALS	-	MAPT_+_43971932.23-P1P2	MAPT-G4	0.813501839	GTGTTGGTGC-CGGAGCTGGT	Ward Lab, unpublished
PFN1	FTD/ALS	-	PFN1_+_4851797.23-P1P2	PFN1-1	1.010829092	GAGCGGAGCC-GCGGTCCGGA	This thesis

Table A.1 continued from previous page

GOI	Primary Category	Subcategory	Kampmann Name	sgRNA Reference Name	Score	Sequence	Validated
			PFN1_-_4851389.23-P1P2	PFN1-2	0.960783776	GCCTGGGGCA-TAGGACCTAC	This thesis
SETX	FTD/ALS	-	SETX_+_135230337.23-P1P2	SETX-A6	1.080736025	GCCTAGAGCG-GGGCCCGGTA	Ward Lab, unpublished
SOD1	FTD/ALS	-	SOD1_-_33031987.23-P1P2	SOD1-1	1.37847727	GCTGGCCTAT-AAAGTAGTCG	This thesis
			SOD1_-_33032085.23-P1P2	SOD1-2	0.966595788	GGGCGTGGCC-TAGCGAGTTA	This thesis
TARDBP	FTD/ALS	-	TARDBP_-_11072919.23-P1P2	TARDBP-E6	1.332904599	GGGAAGTCAG-CCGTGAGACC	Ward Lab, unpublished
UBQLN2	FTD/ALS	-	UBQLN2_-_56590070.23-P1P2	UBQLN2-C8	0.955487859	GCGGTCGGAT-CACAAGGCGG	Ward Lab, unpublished
VAPB	FTD/ALS	-	VAPB_+_56964373.23-P1P2	VAPB-1	1.504657215	GCGGGGGTC-CTCTACCGGGT	This thesis
			VAPB_+_56964331.23-P1P2	VAPB-2	1.001078633	GCTACGCGGT-GCAGGCGCAG	This thesis
VCP	FTD/ALS	-	VCP_-_35072554.23-P1P2	VCP-G8	1.028575569	GTGGCTCCTG-ATCCGCGAGG	Ward Lab, unpublished
VCP_m	FTD/ALS	-	p97_i1	VCP_m-1	-	GTCTATTGTGC-CACGTTCTTCC	Anderson et al.
			VCP_+_35073081.23-P1P2	VCP_m-2	1.015310845	GAGAAGGAGC-AAGAAGTGTC	Ward Lab, unpublished
			p97_i3	VCP_m-3	-	GCTAGTCAGAA-AGTTCAGAGT	Anderson et al.
			VCP_-_35072970.23-P1P2	VCP_m-4	1.106339916	GGCTCCGGAG-TTTATCCTCC	Ward Lab, unpublished

Table A.1 continued from previous page

GOI	Primary Category	Subcategory	Kampmann Name	sgRNA Reference Name	Score	Sequence	Validated
OPTN	FTD/ALS	Autophagy Receptor	OPTN_+_13142195.23-P1P2	OPTN-D5	0.78115123	GTGACCAGGG-AACCTGCCGG	Ward Lab, unpublished
SQSTM1	FTD/ALS	Autophagy Receptor	SQSTM1_+_179233494.23-P2	SQSTM1-C6	0.887227953	GCCTGGTACG-CGGCACTCAG	Ward Lab, unpublished
TBK1	FTD/ALS	Autophagy Receptor related	TBK1_-_64845923.23-P1P2	TBK1-A7	0.904896722	GAGTGTCCTG-AGTCTCGAGG	Ward Lab, unpublished
1872	Non-targeting	-	0_i25 negative_control-10010	1872	-	GTCCACCCTT-ATCTAGGCTA	Kampmann and Ward Labs
1873	Non-targeting	-	0_i26 negative_control-10016	1873	-	GGACTAAGCG-CAAGCACCTA	
3083	Non-targeting	-	non-targeting_00249_i1	3083	-	GCAGGCCCGT-TTGCTTACGA	
3084	Non-targeting	-	non-targeting_00248_i1	3084	-	GAGTCTGGGG-AGGACATTGT	
3085	Non-targeting	-	non-targeting_00247_i1	3085	-	GCAGGCCAGA-GGCCCCGTGC	
3086	Non-targeting	-	non-targeting_00244_i1	3086	-	GACTCACGTA-GCAGTGGAAA	
3179	Non-targeting	-	non-targeting_00243_i1	3179	-	GACCCGAGAC-TGCTTCCCGG	
3180	Non-targeting	-	non-targeting_00242_i1	3180	-	GAGACGAGGA-CATGTGTAGC	
3181	Non-targeting	-	non-targeting_00239_i1	3181	-	GTACCACCCA-AACGATAACG	
NBR1	Other	Autophagy Receptor	NBR1_-_41323253.23-P1P2	NBR1-1	0.947112852	GATTCACCCC-ACAGGGATAG	This thesis

Table A.1 continued from previous page

GOI	Primary Category	Subcategory	Kampmann Name	sgRNA Reference Name	Score	Sequence	Validated
			NBR1_+_41323238.23-P1P2	NBR1-2	0.888367044	GGCTCTGCCG-CTATCCCTGT	This thesis
NDP52 (CALCOCO2)	Other	Autophagy Receptor	CALCOCO2_+_46908418.23-P1	CALCOCO2-1	1.08790595	GCAGGGACAG-CAACCAGCAG	This thesis
			CALCOCO2_+_46908402.23-P1	CALCOCO2-2	1.022300426	GCAGCGGCGC-GACAGCAACA	This thesis
TAXBP1 (TAX1BP1)	Other	Autophagy Receptor	TAX1BP1_-_27779821.23-P1P2	TAX1BP1-1	0.967945926	GAGTGGCGGA-AGAGGTTCGG	This thesis
			TAX1BP1_-_27779818.23-P1P2	TAX1BP1-2	0.926535889	GGGTAGTGGC-GGAAGAGGTT	This thesis
PSAP	Other	FTD/ALS-related	PSAP_+_73611056.23-P1P2	PSAP-E5	1.024057484	GTTAGCGCCT-GCGCTCTGGA	Ward Lab, unpublished
STX17	Other	FTD/ALS-related	STX17_+_102669102.23-P1P2	STX17-1	1.855667001	GCACCATGGC-GCTCGCACTT	This thesis
			STX17_-_102668994.23-P1P2	STX17-2	1.078870633	GGCGCCCCGG-CGGGAGGTAA	This thesis
TMEM106B	Other	FTD/ALS-related	TMEM106B_+_ 12250990.23-P1P2	TMEM106B-E7	0.963781663	GGCGGACAGG-GCCGAGGACA	Ward Lab, unpublished
CLN5	Other	Lysosomal-related CLN	CLN5_-_77566274.23-P1P2	CLN5-I17	0.946360014	GGGCACAGGG-CGCCGAGATG	Ward Lab, unpublished
ATP6V0A1	Other	PD and FTD/ALS-related	ATP6V0A1_+_40610918.23-P1P2	ATP6V0A1-1	1.181462486	GGCCAAACCC-GCACCCTCCG	This thesis
			ATP6V0A1_-_40610947.23-P1P2	ATP6V0A1-2	1.117591324	GGGTGCGGGT-TTGGCTGCGG	This thesis
OXR1	Other	PD and FTD/ALS-related	OXR1_+_107670418.23	OXR1-1	0.877891085	GCGGGAGGCG-AAAGAAAGGT	This thesis

Table A.1 continued from previous page

GOI	Primary Category	Subcategory	Kampmann Name	sgRNA Reference Name	Score	Sequence	Validated
			OXR1_+_107670110.23	OXR1-2	0.774875648	GGCCCATCAG-ACCTGACCCA	This thesis
CLN8	Other	PD GWAS	CLN8_-_1711951.23-P1P2	CLN8-1	1.214410924	GCGCGGGCGG-TGTTTGAGGC	This thesis
			CLN8_-_1712219.23-P1P2	CLN8-2	1.0179875	GGAAGCCCGG-GTGAGGGGAC	This thesis
ATP13A2 (PARK9)	PD	Familial PD	ATP13A2_-_17338380.23-P1P2	ATP13A2-1	0.919328076	GGGCTGGAGC-AGGGCTGACG	This thesis
			ATP13A2_+_17338415.23-P1P2	ATP13A2-2	0.884184373	GGGAGGGACT-GCGGCAGTGT	This thesis
LRRK2 (PARK8)	PD	Familial PD	LRRK2_+_40618865.23-P1P2	LRRK2-1	0.978845959	GCTGCTCAGG-GAACCGGCAG	This thesis
			LRRK2_+_40618843.23-P1P2	LRRK2-2	0.92624128	GCGCCGGCCA-CAGCTCCCCG	This thesis
PARK2 (Parkin)	PD	Familial PD	PARK2_+_163148768.23-P1P2	PARK2-1	0.998223787	GACCCAGGAG-AGCCGCTGGT	This thesis
			PARK2_-_163148753.23-P1P2	PARK2-2	0.945078321	GAACAGGCCC-ATGCGCGCAG	This thesis
PARK7 (DJ-1)	PD	Familial PD	PARK7_+_8022079.23-P1P2	PARK7-1	0.909088671	GTCCATGCCG-GCGAGAGGTT	This thesis
			PARK7_+_8021784.23-P1P2	PARK7-2	0.903452127	GGTACCACTC-ACCCCACACC	This thesis
PINK1 (PARK6)	PD	Familial PD	PINK1_-_20960047.23-P1P2	PINK1-1	0.858020675	GGGCCGCGGC-GCCACCATGG	This thesis
			PINK1_+_20960036.23-P1P2	PINK1-2	0.805774575	GGCCTGTCGC-ACCGCCATGG	This thesis

Table A.1 continued from previous page

GOI	Primary Category	Subcategory	Kampmann Name	sgRNA Reference Name	Score	Sequence	Validated
SNCA (PARK1)	PD	Familial PD	SNCA_+_90758294.23-P1P2	SNCA-1	0.964934719	GGGACGGCGA-CGACCAGAAG	This thesis
			SNCA_+_90758283.23-P1P2	SNCA-2	0.924212213	GACCAGAAGG-GGCCCAAGAG	This thesis
VPS13C (PARK23)	PD	Familial PD	VPS13C_-_62352597.23-P1P2	VPS13C-1	1.014147588	GGGCGCTGAG-GCACAAGGAG	This thesis
			VPS13C_-_62352585.23-P1P2	VPS13C-2	0.888175332	GCAGCACCAT-GGTGGCGCTG	This thesis
VPS35 (PARK17)	PD	Familial PD	VPS35_+_46723041.23-P1P2	VPS35-1	0.990889684	GAGGCTCTGG-GGAGTCGCCA	This thesis
			VPS35_+_46723052.23-P1P2	VPS35-2	0.948372609	GCTGCTTGCT-GCAGGCTCTG	This thesis
GBA1	PD	Familial PD and Gaucher's	GBA_-_155214411.23-P2	GBA-1	1.011781079	GCCGCGCAGT-AAGACTCTGA	This thesis
			GBA_+_155210996.23-P1	GBA-2	0.962724402	GTAGTGCCTA-TAGCTAAGGC	This thesis
CHCHD2	PD	PD GWAS	CHCHD2_-_56174016.23-P1P2	CHCHD2-1	0.881774691	GTCATTGCCC-CAGTAGAGTC	This thesis
			CHCHD2_+_56174001.23-P1P2	CHCHD2-2	0.859433449	GGGCCGTCCG-GACTCTACTG	This thesis
CRLS1	PD	PD GWAS	CRLS1_+_5986787.23-P1P2	CRLS1-1	1.020761505	GCGGCAACCA-CTCAGACACT	This thesis
			CRLS1_-_5986783.23-P1P2	CRLS1-2	1.011994521	GTAAAGTAGT-ATGGAGGCAG	This thesis
FYN	PD	PD GWAS	FYN_+_112194611.23-P1P2	FYN-1	0.965375718	GCGAGCAGCC-GCGCTGGTGG	This thesis

Table A.1 continued from previous page

GOI	Primary Category	Subcategory	Kampmann Name	sgRNA Reference Name	Score	Sequence	Validated
			FYN_-_112194589.23-P1P2	FYN-2	0.953315683	GCGGCTCCGC-TCCTGACAGA	This thesis
GALC	PD	PD GWAS	GALC_+_88459060.23-P1P2	GALC-1	0.9497777	GCCGGAGGTC-CAGAGAGTAT	This thesis
			GALC_+_88459496.23-P1P2	GALC-2	0.931158291	GGACCCACAC-AATGGCTGAG	This thesis
GCH1	PD	PD GWAS	GCH1_-_55369491.23-P1P2	GCH1-1	0.956666937	GCTGTGGCCG-GAGTCACCTG	This thesis
			GCH1_-_55369495.23-P1P2	GCH1-2	0.949593454	GGGCCGGAGT-CACCTGAGGA	This thesis
GUSB	PD	PD GWAS	GUSB_+_65447180.23-P1P2	GUSB-1	0.907780973	GGCAGACGGT-GGCCGAGCGG	This thesis
			GUSB_-_65447165.23-P1P2	GUSB-2	0.894359286	GCAGGCAACC-GCCGACCCCC	This thesis
MCCC1	PD	PD GWAS	MCCC1_-_182817269.23-P1P2	MCCC1-1	1.145435804	GCCGTGACTC-CCCAGTACAG	This thesis
			MCCC1_+_182817301.23-P1P2	MCCC1-2	1.039119069	GGGGTCACGA-GGCTTCGTAG	This thesis
NAGLU	PD	PD GWAS	NAGLU_+_40688676.23-P1P2	NAGLU-1	0.980032196	GACGCGGGGA-AGCTTCGGGG	This thesis
			NAGLU_-_40688749.23-P1P2	NAGLU-2	0.817605032	GCGCTGCCAC-CCAAATCGGG	This thesis
NEU1	PD	PD GWAS	NEU1_+_31830568.23-P1P2	NEU1-1	1.0179564	GAGTCTAGCT-GCCAGGGTCG	This thesis
			NEU1_+_31830543.23-P1P2	NEU1-2	0.933223079	GCTGCGGGGA-GAGATGACTG	This thesis

Table A.1 continued from previous page

GOI	Primary Category	Subcategory	Kampmann Name	sgRNA Reference Name	Score	Sequence	Validated
SCARB2	PD	PD GWAS	SCARB2_+_77134573.23-P1P2	SCARB2-1	0.821215967	GCCAGAGTAT-CGAGAAGGTG	This thesis
			SCARB2_-_77134528.23-P1P2	SCARB2-2	0.78391154	GAAGATGTAG-CAGCAGGGAT	This thesis
TMEM175	PD	PD GWAS	TMEM175_-_926289.23-P1P2	TMEM175-1	0.999808957	GCCGGCCGGG-CTGACTCAAG	This thesis
			TMEM175_-_926717.23-P1P2	TMEM175-2	0.873391249	GTGGGGCAGT-GACCAGTAGT	This thesis

A.2 Nuclear Blue Lentivirus Library Titers and Transfer Volumes

Table A.2: Nuclear Blue Lentivirus Library Titers and Transfer Volumes

Virus Titering Code	Plate Location	Full Virus Name	Short Virus Name	sgRNA Reference Name	Gene Target	65% Titer Transfer Volume (nL)	70% Titer Transfer Volume (nL)	75% Titer Transfer Volume (nL)	80% Titer Transfer Volume (nL)	85% Titer Transfer Volume (nL)
1	A1	1A - LRRK2-1	1A	LRRK2-1	LRRK2	301.9	366.8	456.2	590.7	826.1
2	B1	1B - LRRK2-2	1B	LRRK2-2	LRRK2	409.3	468.9	545.1	649.2	807.7
3	C1	1C - PINK1-1	1C	PINK1-1	PINK1	190.4	232.8	292.6	386.7	565.6
4	D1	1D - PINK1-2	1D	PINK1-2	PINK1	226.2	273.7	337.3	427.6	567.5
5	E1	1E - PARK2-1	1E	PARK2-1	PARK2	205.1	249.5	312.5	415.1	637.9
6	F1	1F - PARK2-2	1F	PARK2-2	PARK2	228.4	268.4	320.2	391.7	501.0
7	G1	1G - PARK7-1	1G	PARK7-1	PARK7	243.9	304.3	390.2	524.3	768.1
8	H1	1H - PARK7-2	1H	PARK7-2	PARK7	219.7	257.5	306.4	374.2	478.0
9	A2	2A - SNCA-1	2A	SNCA-1	SNCA	220.0	268.5	336.7	442.5	639.0
10	B2	2B - SNCA-2	2B	SNCA-2	SNCA	215.0	253.6	305.0	378.8	499.2
11	C2	2C - GBA-1	2C	GBA-1	GBA	275.2	332.3	415.1	554.4	879.5
12	D2	2D - GBA-2	2D	GBA-2	GBA	226.2	265.5	317.4	390.8	507.9
13	E2	2E - VPS35-1	2E	VPS35-1	VPS35	266.3	320.4	396.9	518.5	760.8
14	F2	2F - VPS35-2	2F	VPS35-2	VPS35	275.3	331.2	406.0	512.4	679.3
15	G2	2G - ATP13A2-1	2G	ATP13A2-1	ATP13A2	225.3	273.5	339.3	438.2	613.5
16	H2	2H - ATP13A2-2	2H	ATP13A2-2	ATP13A2	255.2	303.2	368.1	463.3	623.6
17	A3	3A - NAGLU-1	3A	NAGLU-1	NAGLU	255.8	303.7	366.8	456.4	598.4
18	B3	3B - NAGLU-2	3B	NAGLU-2	NAGLU	246.2	291.5	350.5	431.9	555.6
19	C3	3C - GUSB-1	3C	GUSB-1	GUSB	261.6	308.5	369.4	453.8	583.0
20	D3	3D - GUSB-2	3D	GUSB-2	GUSB	263.2	314.3	381.2	473.7	612.8
21	E3	3E - NEU1-1	3E	NEU1-1	NEU1	250.2	297.0	358.9	446.7	585.1
22	F3	3F - NEU1-2	3F	NEU1-2	NEU1	344.9	415.8	511.9	652.8	887.3
23	G3	3G - VPS13C-1	3G	VPS13C-1	VPS13C	200.4	239.4	289.8	358.7	461.0
24	H3	3H - VPS13C-2	3H	VPS13C-2	VPS13C	167.8	200.1	242.0	299.9	387.7
25	A4	4A - GCH1-1	4A	GCH1-1	GCH1	161.7	192.3	231.5	285.1	365.0
26	B4	4B - GCH1-2	4B	GCH1-2	GCH1	226.9	271.6	328.9	406.8	521.4
27	C4	4C - TMEM175-1	4C	TMEM175-1	TMEM175	215.4	258.3	314.1	390.9	505.3
28	D4	4D - TMEM175-2	4D	TMEM175-2	TMEM175	565.6	692.1	861.2	1100.4	1467.2
29	E4	4E - CTSB-1	4E	CTSB-1	CTSB	198.4	238.2	289.8	360.5	465.2
30	F4	4F - CTSB-2	4F	CTSB-2	CTSB	248.4	295.8	356.8	440.2	564.7
31	G4	4G - CTSL-1	4G	CTSL-1	CTSL	183.2	217.5	261.6	322.1	413.5
32	H4	4H - CTSL-2	4H	CTSL-2	CTSL	253.3	300.8	361.9	444.9	566.4
33	A5	5A - CTSD-1	5A	CTSD-1	CTSD	190.5	232.2	287.4	364.5	480.7
34	B5	5B - CTSD-2	5B	CTSD-2	CTSD	178.2	213.4	258.8	320.8	413.2
35	C5	5C - FYN-1	5C	FYN-1	FYN	173.3	208.1	253.9	317.9	414.7
36	D5	5D - FYN-2	5D	FYN-2	FYN	207.9	254.0	315.3	401.3	530.8
37	E5	5E - STX17-1	5E	STX17-1	STX17	232.4	272.2	323.7	395.0	504.7

Table A.2 continued from previous page

Virus Titering Code	Plate Location	Full Virus Name	Short Virus Name	sgRNA Reference Name	Gene Target	65% Titer Transfer Volume (nL)	70% Titer Transfer Volume (nL)	75% Titer Transfer Volume (nL)	80% Titer Transfer Volume (nL)	85% Titer Transfer Volume (nL)
38	F5	5F - STX17-2	5F	STX17-2	STX17	276.0	329.8	399.7	495.4	636.9
39	G5	5G - CHCHD2-1	5G	CHCHD2-1	CHCHD2	120.4	149.1	188.9	251.0	371.5
40	H5	5H - CHCHD2-2	5H	CHCHD2-2	CHCHD2	181.3	215.5	260.1	322.1	416.0
41	A6	6A - ATP6V0A1-1	6A	ATP6V0A1-1	ATP6V0A1	161.5	199.7	254.9	347.4	558.2
42	B6	6B - ATP6V0A1-2	6B	ATP6V0A1-2	ATP6V0A1	169.4	205.1	255.2	336.1	511.3
43	C6	6C - OXR1-1	6C	OXR1-1	OXR1	237.9	293.6	373.0	499.8	748.9
44	D6	6D - OXR1-2	6D	OXR1-2	OXR1	248.7	303.7	380.6	501.0	733.5
45	A7	7A - GRN-F3	7A	GRN-F3	GRN	368.4	472.6	622.8	855.1	1256.0
46	B7	7B - PSAP-E5	7B	PSAP-E5	PSAP	327.9	397.5	493.9	642.0	916.3
47	C7	7C - TMEM106B-E7	7C	TMEM106B-E7	TMEM106B	436.2	475.4	533.8	656.1	1100.0
48	D7	7D - ANXA11-A1	7D	ANXA11-A1	ANXA11	372.9	453.2	566.4	745.6	1096.7
49	E7	7E - ANXA11-B1	7E	ANXA11-B1	ANXA11	446.3	532.9	654.1	845.5	1226.1
50	F7	7F - ANXA11-C1	7F	ANXA11-C1	ANXA11	324.0	397.5	503.9	679.9	1060.5
51	G7	7G - ANXA11-D1	7G	ANXA11-D1	ANXA11	416.9	496.1	602.7	758.4	1019.2
52	H7	7H - OPTN-D5	7H	OPTN-D5	OPTN	338.7	420.1	534.4	709.9	1022.2
53	A8	8A - C9ORF72-F1	8A	C9ORF72-F1	C9ORF72	370.7	441.7	538.6	684.5	945.0
54	B8	8B - CHMP2B-F2	8B	CHMP2B-F2	CHMP2B	311.3	382.6	482.4	636.5	918.5
55	C8	8C - TARDBP-E6	8C	TARDBP-E6	TARDBP	354.7	429.8	537.1	713.4	1101.1
56	D8	8D - FUS-A3	8D	FUS-A3	FUS	437.1	512.1	629.1	876.9	1594.4
57	E8	8E - FUS-C3	8E	FUS-C3	FUS	508.0	690.1	1033.0	2042.0	-
58	F8	8F - TBK1-A7	8F	TBK1-A7	TBK1	470.7	518.2	585.1	701.3	1144.7
59	G8	8G - UBQLN2-C8	8G	UBQLN2-C8	UBQLN2	344.3	405.4	491.3	633.6	982.8
60	H8	8H - MAPT-G4	8H	MAPT-G4	MAPT	345.1	413.4	509.9	666.1	1002.2
61	A9	9A - HNRNPA2B1-B4	9A	HNRNPA2B1-B4	HNRNPA2B1	320.4	372.1	441.6	546.5	745.4
62	B9	9B - SQSTM1-C6	9B	SQSTM1-C6	SQSTM1	265.6	323.1	405.7	539.4	812.9
63	C9	9C - CHCHD10-C2	9C	CHCHD10-C2	CHCHD10	284.2	341.4	421.5	547.9	800.9
64	D9	9D - KIF5A-1	9D	KIF5A-1	KIF5A	440.7	545.4	706.8	1012.2	2030.6
65	E9	9E - VCP-G8	9E	VCP-G8	VCP	350.9	436.8	566.2	796.7	1402.9
66	F9	9F - VCP_m-1	9F	VCP_m-1	VCP	266.0	333.8	428.0	568.2	800.8
67	G9	9G - VCP_m-2	9G	VCP_m-2	VCP	302.6	371.8	468.4	618.4	900.3
68	H9	9H - VCP_m-3	9H	VCP_m-3	VCP	439.8	527.8	646.6	822.6	1127.5
69	A10	10A - VCP_m-4	10A	VCP_m-4	VCP	299.6	372.9	479.3	652.9	1004.6
70	B10	10B - CLN5	10B	CLN5-I17-1885	CLN5	262.4	344.2	469.3	680.4	1100.7
71	C10	10C - SETX	10C	SETX-A6	SETX	438.9	534.9	670.7	886.5	1313.4
72	A11	11A - 3179	11A	3179	non-targeting	401.9	488.2	614.3	827.4	1318.4
73	B11	11B - 3180	11B	3180	non-targeting	494.4	595.1	748.3	1040.7	2220.6
74	C11	11C - 3181	11C	3181	non-targeting	464.3	523.6	612.8	794.2	1400.0
75	E11	11E - 3083	11E	3083	non-targeting	501.4	599.8	762.1	1163.1	2300.0
76	F11	11F - 3084	11F	3084	non-targeting	411.6	508.4	663.1	984.4	1600.0

Table A.2 continued from previous page

Virus Titering Code	Plate Location	Full Virus Name	Short Virus Name	sgRNA Reference Name	Gene Target	65% Titer Transfer Volume (nL)	70% Titer Transfer Volume (nL)	75% Titer Transfer Volume (nL)	80% Titer Transfer Volume (nL)	85% Titer Transfer Volume (nL)
77	G11	11G - 3085	11G	3085	non-targeting	478.8	581.1	737.2	1030.6	2059.2
78	H11	11H - 3086	11H	3086	non-targeting	431.4	556.4	750.2	1098.6	1943.9
79	A12	12A - 1872	12A	1872	non-targeting	427.1	564.9	780.4	1160.3	1989.2
80	B12	12B - 1873	12B	1873	non-targeting	395.2	487.0	620.0	838.4	1295.8
81	NONE	H25 - GFP	H25	H25	GFP	312.6	398.3	526.4	742.8	1200.3
82	A1	A-1A-SOD1-1	A-1A	SOD1-1	SOD1	456.7	653.4	1066.6	-	-
83	B1	A-1B-SOD1-2	A-1B	SOD1-2	SOD1	427.3	577.3	823.6	1303.0	-
84	C1	A-1C-ALS2-1	A-1C	ALS2-1	ALS2	299.0	432.9	677.7	1197.3	-
85	D1	A-1D-ALS2-2	A-1D	ALS2-2	ALS2	449.7	588.6	806.3	1201.3	2164.2
86	E1	A-1E-DCTN1-1	A-1E	DCTN1-1	DCTN1	275.9	358.3	508.2	945.3	-
87	F1	A-1F-DCTN1-2	A-1F	DCTN1-2	DCTN1	360.6	471.5	651.5	1013.1	-
88	G1	A-1G-PFN1-1	A-1G	PFN1-1	PFN1	251.7	313.8	438.0	1521.3	-
89	H1	A-1H-PFN1-2	A-1H	PFN1-2	PFN1	477.7	636.6	965.7	-	-
90	A2	A-2A-VAPB-1	A-2A	VAPB-1	VAPB	444.2	594.2	829.6	1256.8	-
91	B2	A-2B-VAPB-2	A-2B	VAPB-2	VAPB	304.2	446.5	675.3	1058.8	1734.4
92	C2	A-2C-CALCOCO2-1	A-2C	CALCOCO2-1	NDP52/CALCOCO2	356.2	450.9	597.5	895.0	-
93	D2	A-2D-CALCOCO2-2	A-2D	CALCOCO2-2	NDP52/CALCOCO2	324.1	407.6	538.7	818.2	-
94	E2	A-2E-NBR1-1	A-2E	NBR1-1	NBR1	430.9	552.8	738.9	1084.0	2131.3
95	F2	A-2F-NBR1-2	A-2F	NBR1-2	NBR1	357.6	501.1	740.4	1286.9	2000.0
96	G2	A-2G-TAX1BP1-1	A-2G	TAX1BP1-1	TAX1BP1	662.4	888.7	1263.4	2005.1	-
97	H2	A-2H-TAX1BP1-2	A-2H	TAX1BP1-2	TAX1BP1	470.4	626.1	994.1	-	-
98	A3	A-3A-SCARB2-1	A-3A	SCARB2-1	SCARB2	518.9	718.3	1106.6	-	-
99	B3	A-3B-SCARB2-2	A-3B	SCARB2-2	SCARB2	453.0	645.8	1098.4	-	-
100	C3	A-3C-GALC-1	A-3C	GALC-1	GALC	533.3	732.8	1077.0	1802.2	-
101	D3	A-3D-GALC-2	A-3D	GALC-2	GALC	554.7	750.5	1077.5	1731.9	-
102	E3	A-3E-MCCC1-1	A-3E	MCCC1-1	MCCC1	412.6	581.5	916.4	1939.5	-
103	F3	A-3F-MCCC1-2	A-3F	MCCC1-2	MCCC1	532.2	720.2	1123.9	-	-
104	G3	A-3G-CRLS1-1	A-3G	CRLS1-1	CRLS1	504.5	701.4	1109.0	-	-
105	H3	A-3H-CRLS1-2	A-3H	CRLS1-2	CRLS1	580.8	732.9	960.2	1357.3	-
106	A4	A-4A-CLN8-1	A-4A	CLN8-1	CLN8	411.3	579.2	924.0	2206.4	-
107	B4	A-4B-CLN8-2	A-4B	CLN8-2	CLN8	563.5	813.5	1459.5	-	-

A.3 Nuclear Blue sgRNA Lentivirus Library Titer Curves

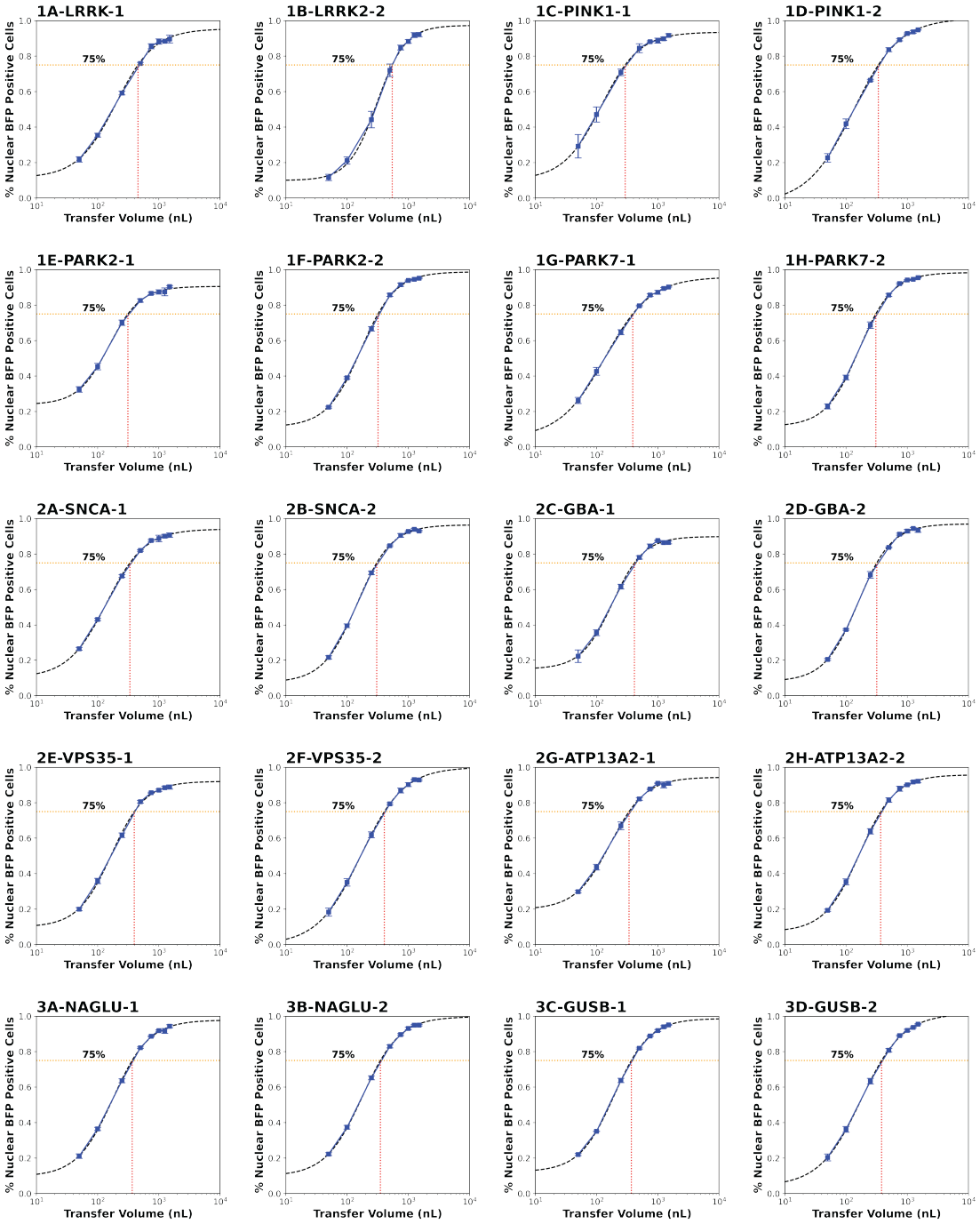


Figure A.1: Nuclear Blue Panel A: Lentivirus titer curves with interpolation.

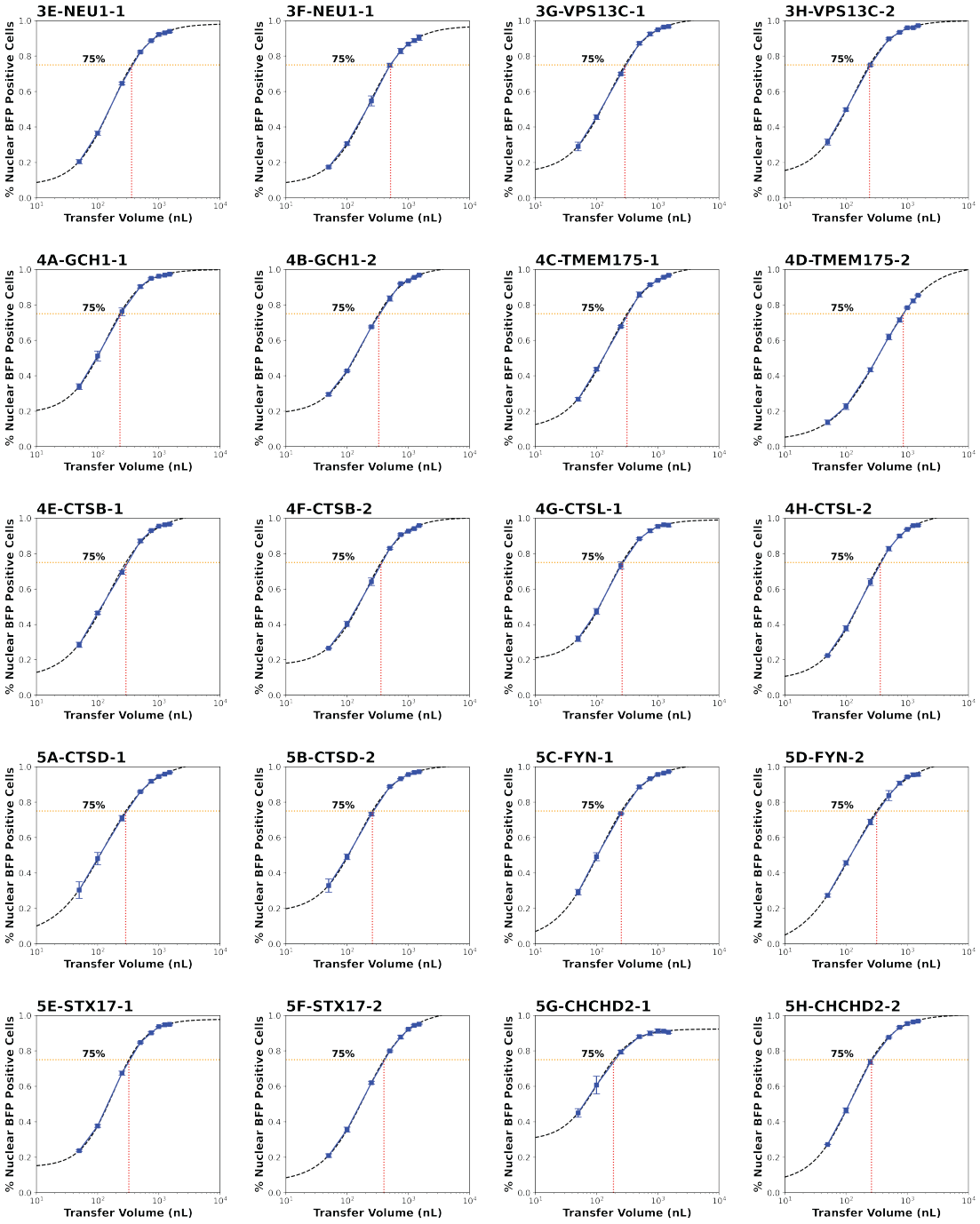


Figure A.2: Nuclear Blue Panel B: Lentivirus titer curves with interpolation.

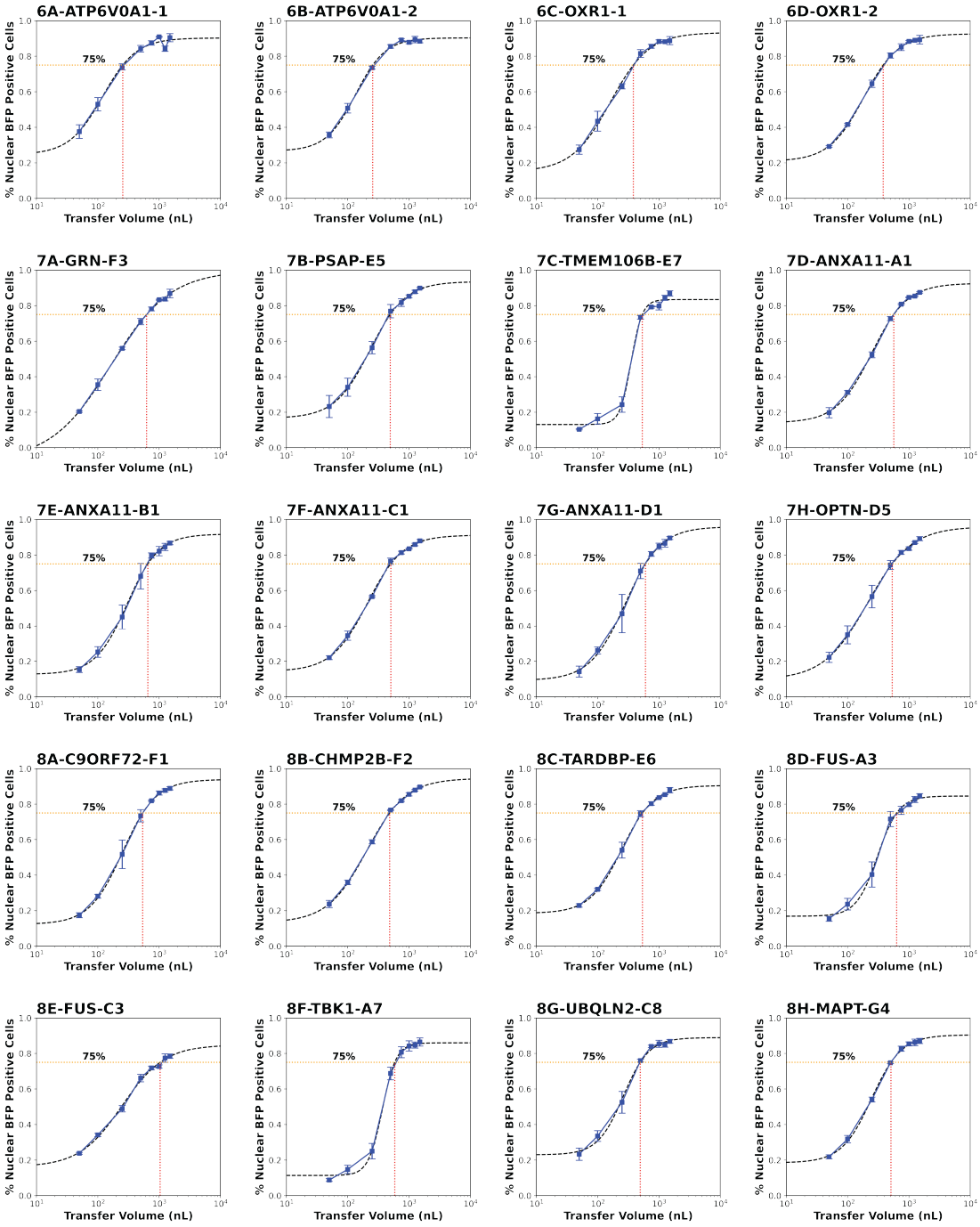


Figure A.3: Nuclear Blue Panel C: Lentivirus titer curves with interpolation.

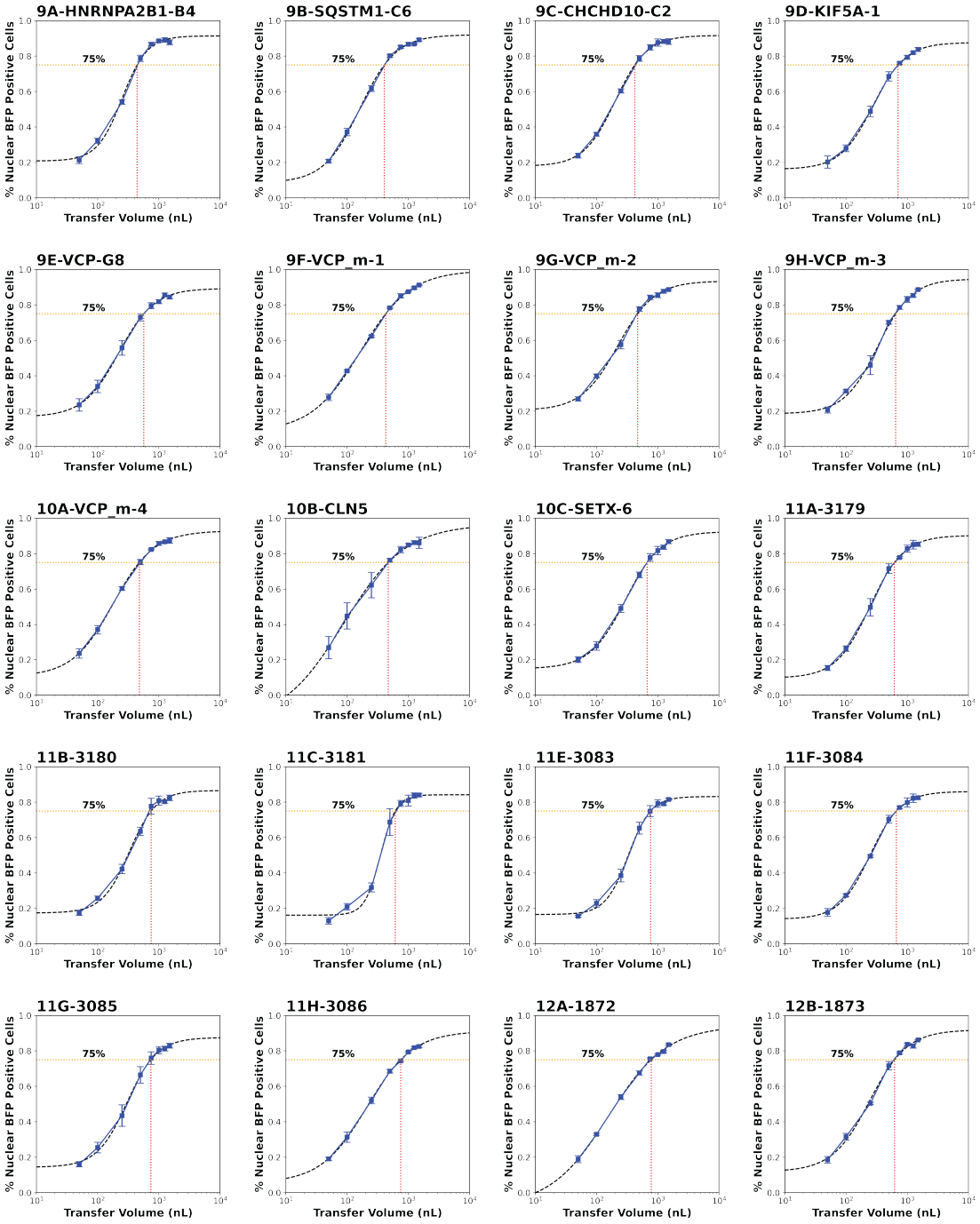


Figure A.4: Nuclear Blue Panel D: Lentivirus titer curves with interpolation.

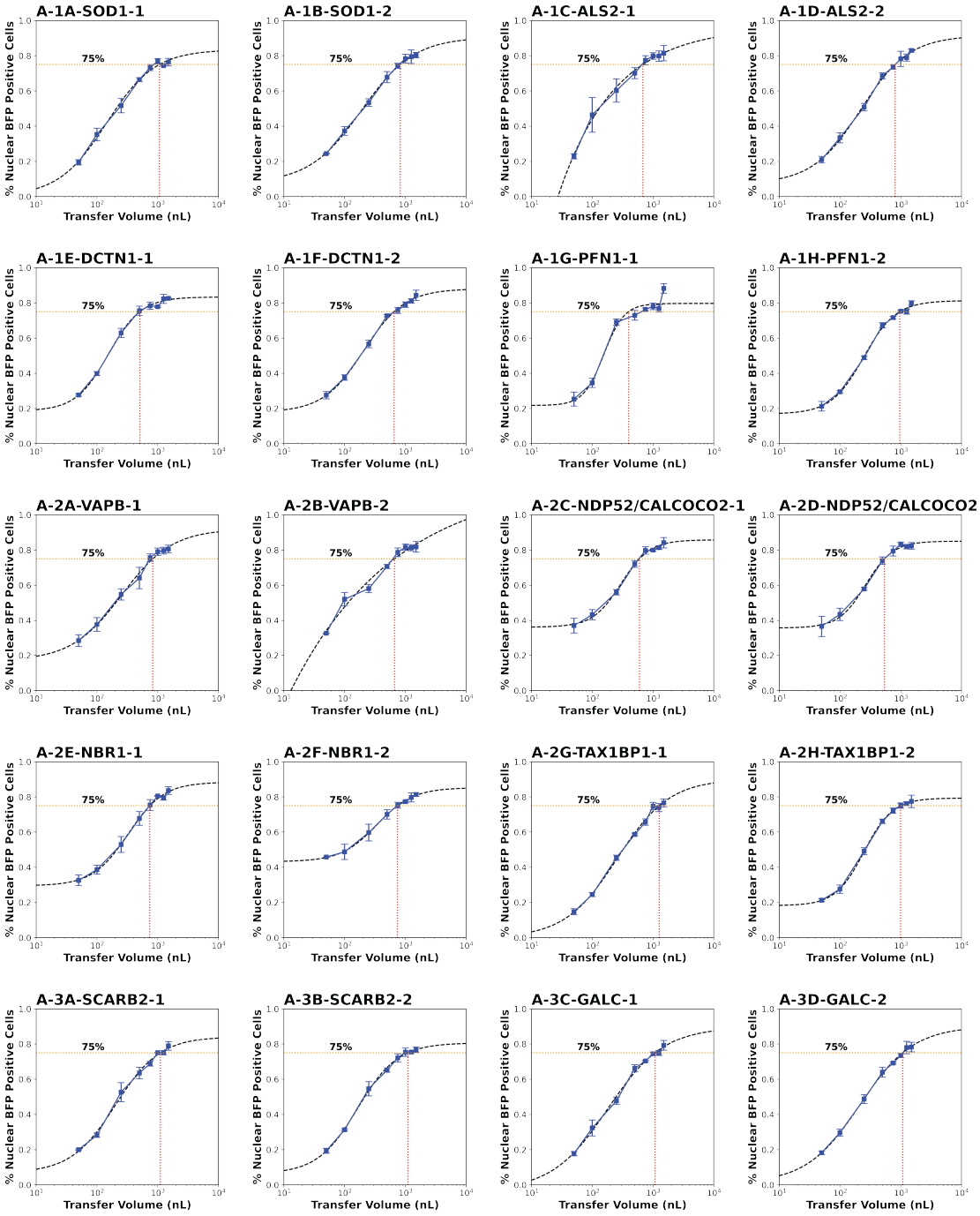


Figure A.5: Nuclear Blue Panel E: Lentivirus titer curves with interpolation.

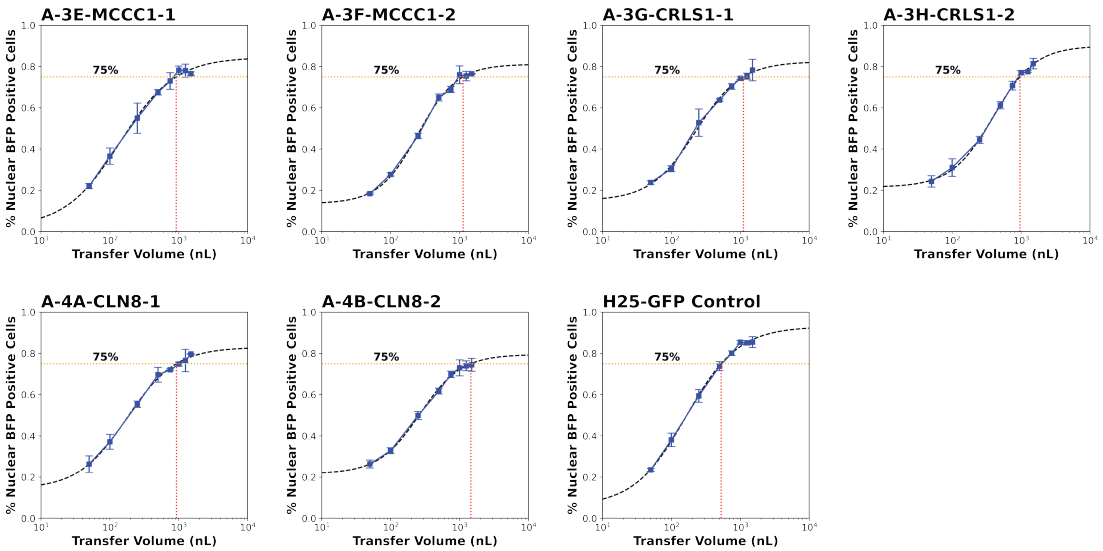


Figure A.6: Nuclear Blue Panel F: Lentivirus titer curves with interpolation.

A.4 Cytosolic Far-Red Lentivirus Library Titers and Transfer Volumes

Table A.3: Cytosolic Far-Red Lentivirus Library Titers and Transfer Volumes

Virus Titering Code	Plate Location	Full Virus Name	Short Virus Name	sgRNA Reference Name	Gene Target	65% Titer Transfer Volume (nL)	70% Titer Transfer Volume (nL)	75% Titer Transfer Volume (nL)	80% Titer Transfer Volume (nL)	85% Titer Transfer Volume (nL)
1	A1	A1 - LRRK2-1	A1	LRRK2-1	LRRK2	157.8	176.9	200.0	229.4	270.5
2	B1	B1 - LRRK2-2	B1	LRRK2-2	LRRK2	261.1	301.6	351.5	416.2	505.8
3	C1	C1 - PINK1-1	C1	PINK1-1	PINK1	108.4	124.6	144.5	170.5	207.3
4	D1	D1 - PINK1-2	D1	PINK1-2	PINK1	137.6	162.4	193.4	234.3	292.7
5	E1	E1 - PARK2-1	E1	PARK2-1	PARK2	131.6	153.5	180.8	216.7	268.2
6	F1	F1 - PARK2-2	F1	PARK2-2	PARK2	108.0	125.0	145.8	172.6	210.6
7	G1	G1 - PARK7-1	G1	PARK7-1	PARK7	181.3	202.4	228.0	261.3	308.4
8	H1	H1 - PARK7-2	H1	PARK7-2	PARK7	143.5	165.9	193.9	230.8	283.4
9	A2	A2 - SNCA-1	A2	SNCA-1	SNCA	104.5	121.5	143.2	172.7	216.1
10	B2	B2 - SNCA-2	B2	SNCA-2	SNCA	116.2	132.7	152.5	177.7	212.6
11	C2	C2 - GBA-1	C2	GBA-1	GBA	118.2	140.4	169.2	208.8	267.4
12	D2	D2 - GBA-2	D2	GBA-2	GBA	211.1	243.5	283.1	334.5	406.2
13	E2	E2 - VPS35-1	E2	VPS35-1	VPS35	127.3	147.8	172.1	202.6	244.2
14	F2	F2 - VPS35-2	F2	VPS35-2	VPS35	101.8	116.1	133.8	157.1	190.2
15	G2	G2 - ATP13A2-1	G2	ATP13A2-1	ATP13A2	157.3	177.7	202.5	234.5	279.4
16	H2	H2 - ATP13A2-2	H2	ATP13A2-2	ATP13A2	387.4	450.1	529.5	634.9	784.7
17	A3	A3 - NAGLU-1	A3	NAGLU-1	NAGLU	132.4	149.2	169.2	194.3	228.6
-	B3	A4 - NAGLU-2	A4	NAGLU-2	NAGLU	-	-	-	-	-
18	C3	C3 - GUSB-1	C3	GUSB-1	GUSB	122.7	138.8	157.5	180.7	212.0
19	D3	D3 - GUSB-2	D3	GUSB-2	GUSB	103.2	117.8	135.7	159.2	192.6
20	E3	E3 - NEU1-1	E3	NEU1-1	NEU1	105.9	122.7	142.1	165.9	197.9
21	F3	F3 - NEU1-2	F3	NEU1-2	NEU1	97.3	110.8	126.1	144.7	169.5
22	G3	G3 - VPS13C-1	G3	VPS13C-1	VPS13C	124.1	141.7	163.3	191.5	231.3
23	H3	H3 - VPS13C-2	H3	VPS13C-2	VPS13C	108.9	128.9	153.9	186.9	234.2
24	A4	A4 - GCH1-1	A4	GCH1-1	GCH1	122.4	144.6	172.8	210.9	266.3
25	B4	B4 - GCH1-2	B4	GCH1-2	GCH1	-	-	-	-	-
26	C4	C4 - TMEM175-1	C4	TMEM175-1	TMEM175	157.3	183.2	215.7	258.9	320.6
-	D4	D4 - TMEM175-2	D4	TMEM175-2	TMEM175	-	-	-	-	-
27	E4	E4 - CTSB-1	E4	CTSB-1	CTSB	206.4	239.9	281.3	335.1	411.0
28	F4	F4 - CTSB-2	F4	CTSB-2	CTSB	197.4	221.8	251.8	290.7	345.5
29	G4	G4 - CTSL-1	G4	CTSL-1	CTSL	119.3	135.5	155.1	180.3	215.8
30	H4	H4 - CTSL-2	H4	CTSL-2	CTSL	159.0	184.1	216.0	259.3	323.8
31	A5	A5 - CTSD-1	A5	CTSD-1	CTSD	1185.7	1506.4	2116.2	4306.3	-
32	B5	B5 - CTSD-2	B5	CTSD-2	CTSD	72.2	85.7	100.7	118.8	142.9
-	C5	C5 - FYN-1	C5	FYN-1	FYN	-	-	-	-	-
-	D5	D5 - FYN-2	D5	FYN-2	FYN	-	-	-	-	-
33	E5	E5 - STX17-1	E5	STX17-1	STX17	123.9	142.1	164.1	192.9	235.3

Table A.3 continued from previous page

Virus Titering Code	Plate Location	Full Virus Name	Short Virus Name	sgRNA Reference Name	Gene Target	65% Titer Transfer Volume (nL)	70% Titer Transfer Volume (nL)	75% Titer Transfer Volume (nL)	80% Titer Transfer Volume (nL)	85% Titer Transfer Volume (nL)
34	F5	F5 - STX17-2	F5	STX17-2	STX17	148.7	175.3	208.3	251.9	315.4
35	G5	G5 - CHCHD2-1	G5	CHCHD2-1	CHCHD2	87.7	100.5	115.1	133.9	162.8
36	H5	H5 - CHCHD2-2	H5	CHCHD2-2	CHCHD2	128.0	148.6	173.7	206.3	252.0
37	A6	A6 - ATP6V0A1-1	A6	ATP6V0A1-1	ATP6V0A1	90.7	106.9	126.2	150.6	184.4
38	B6	B6 - ATP6V0A1-2	B6	ATP6V0A1-2	ATP6V0A1	85.3	100.3	119.9	146.9	187.3
-	C6	C6 - OXR1-1	C6	OXR1-1	OXR1	-	-	-	-	-
-	D6	D6 - OXR1-2	D6	OXR1-2	OXR1	-	-	-	-	-
39	A7	A7 - GRN-F3	A7	GRN-F3	GRN	122.4	145.1	173.0	209.3	260.9
40	B7	B7 - PSAP-E5	B7	PSAP-E5	PSAP	86.1	105.8	129.5	160.2	203.7
41	C7	C7 - TMEM106B-E7	C7	TMEM106B-E7	TMEM106B	114.6	135.6	160.8	193.0	238.0
42	D7	D7 - ANXA11-A1	D7	ANXA11-A1	ANXA11	-	-	-	-	-
43	E7	E7 - ANXA11-B1	E7	ANXA11-B1	ANXA11	162.3	189.1	223.3	269.9	340.1
44	F7	F7 - ANXA11-C1	F7	ANXA11-C1	ANXA11	227.8	276.1	341.0	434.1	581.5
45	G7	G7 - ANXA11-D1	G7	ANXA11-D1	ANXA11	142.8	168.2	200.9	246.2	315.4
46	H7	H7 - OPTN-D5	H7	OPTN-D5	OPTN	141.5	170.4	208.7	263.0	347.9
47	A8	A8 - C9ORF72-F1	A8	C9ORF72-F1	C9ORF72	108.1	126.1	148.2	177.0	218.6
48	B8	B8 - CHMP2B-F2	B8	CHMP2B-F2	CHMP2B	101.7	120.7	145.0	178.1	227.7
49	C8	C8 - TARDBP-E6	C8	TARDBP-E6	TARDBP	71.9	83.8	98.5	117.8	145.5
50	D8	D8 - FUS-A3	D8	FUS-A3	FUS	262.6	318.7	391.4	489.8	630.5
51	E8	E8 - FUS-C3	E8	FUS-C3	FUS	110.8	128.3	150.9	181.6	227.4
52	F8	F8 - TBK1-A7	F8	TBK1-A7	TBK1	124.0	141.9	163.9	192.6	233.7
53	G8	G8 - UBQLN2-C8	G8	UBQLN2-C8	UBQLN2	105.4	121.1	140.3	165.3	200.5
54	H8	H8 - MAPT-G4	H8	MAPT-G4	MAPT	130.6	153.5	182.9	222.8	282.0
55	A9	A9 - HNRNPA2B1-B4	A9	HNRNPA2B1-B4	HNRNPA2B1	138.5	164.8	199.7	248.9	325.3
56	B9	B9 - SQSTM1-C6	B9	SQSTM1-C6	SQSTM1	157.5	184.6	217.5	260.3	321.2
57	C9	C9 - CHCHD10-C2	C9	CHCHD10-C2	CHCHD10	184.8	217.1	257.4	310.7	386.9
58	D9	D9 - KIF5A-1	D9	KIF5A-1	KIF5A	184.3	221.9	270.5	336.3	432.3
59	E9	E9 - VCP-G8	E9	VCP-G8	VCP	153.4	179.8	212.8	257.2	323.7
60	F9	F9 - VCP_m-1	F9	VCP_m-1	VCP	136.9	159.3	187.6	225.9	282.5
61	G9	G9 - VCP_m-2	G9	VCP_m-2	VCP	187.3	218.0	256.7	308.5	384.9
62	H9	H9 - VCP_m-3	H9	VCP_m-3	VCP	209.3	239.4	276.5	325.6	397.6
63	A10	A10 - VCP_m-4	A10	VCP_m-4	VCP	190.2	227.2	275.5	342.9	448.3
64	B10	B10 - CLN5	B10	CLN5-I17-1885	CLN5	288.4	339.4	404.9	494.0	626.0
65	C10	C10 - SETX	C10	SETX-A6	SETX	237.7	279.0	330.4	398.0	493.5
66	A11	A11 - 3179	A11	3179	non-targeting	224.6	269.6	325.9	400.2	505.9
67	B11	B11 - 3180	B11	3180	non-targeting	1561.7	1949.6	2513.3	3425.6	5214.2
68	C11	C11 - 3181	C11	3181	non-targeting	200.4	236.5	281.4	339.8	421.1
69	E1	E11 - 3083	E11	3083	non-targeting	232.9	276.4	330.6	401.7	502.4
70	F11	F11 - 3084	F11	3084	non-targeting	392.8	471.5	570.4	698.8	871.9

Table A.3 continued from previous page

Virus Titering Code	Plate Location	Full Virus Name	Short Virus Name	sgRNA Reference Name	Gene Target	65% Titer Transfer Volume (nL)	70% Titer Transfer Volume (nL)	75% Titer Transfer Volume (nL)	80% Titer Transfer Volume (nL)	85% Titer Transfer Volume (nL)
71	G11	G11 - 3085	G11	3085	non-targeting	203.2	229.8	262.9	307.2	373.6
72	H11	H11 - 3086	H11	3086	non-targeting	219.1	256.2	304.2	370.0	469.2
73	A12	A12 - 1872	A12	1872	non-targeting	143.0	166.9	196.9	236.7	294.0
74	B12	B12 - 1873	B12	1873	non-targeting	205.5	238.2	279.1	333.2	411.3
75	A1	A-A1-SOD1-1	A-A1	SOD1-1	SOD1	195.9	233.2	281.6	347.9	446.2
76	B1	A-B1-SOD1-2	A-B1	SOD1-2	SOD1	172.3	200.5	235.8	283.1	353.8
77	C1	A-C1-ALS2-1	A-C1	ALS2-1	ALS2	411.7	482.7	575.8	707.7	918.9
-	D1	A-D1-ALS2-2	A-D1	ALS2-2	ALS2	-	-	-	-	-
-	E1	A-E1-DCTN1-1	A-E1	DCTN1-1	DCTN1	-	-	-	-	-
-	F1	A-F1-DCTN1-2	A-F1	DCTN1-2	DCTN1	-	-	-	-	-
78	G1	A-G1-PFN1-1	A-G1	PFN1-1	PFN1	315.3	373.3	447.3	546.1	686.4
79	H1	A-H1-PFN1-2	A-H1	PFN1-2	PFN1	400.1	477.7	579.7	722.6	943.5
80	A2	A-A2-VAPB-1	A-A2	VAPB-1	VAPB	327.1	381.3	449.4	539.4	666.7
81	B2	A-B2-VAPB-2	A-B2	VAPB-2	VAPB	304.1	356.9	423.3	510.7	633.3
82	C2	A-C2-NDP52-1	A-C2	CALCOCO2-1	NDP52/CALCOCO2	583.2	678.6	792.0	929.7	1101.1
83	D2	A-D2-NDP52-2	A-D2	CALCOCO2-2	NDP52/CALCOCO2	293.1	348.7	419.8	515.3	652.8
84	E2	A-E2-NBR1-1	A-E2	NBR1-1	NBR1	321.9	378.8	452.0	551.8	700.0
85	F2	A-F2-NBR1-2	A-F2	NBR1-2	NBR1	292.3	335.5	391.8	471.8	603.3
86	G2	A-G2-TAX1BP1-1	A-G2	TAX1BP1-1	TAX1BP1	516.4	621.2	762.4	966.9	1298.2
87	H2	A-H2-TAX1BP1-2	A-H2	TAX1BP1-2	TAX1BP1	340.2	390.8	456.6	550.5	708.2
88	A3	A-A3-SCARB2-1	A-A3	SCARB2-1	SCARB2	241.1	276.9	324.1	392.7	511.7
89	B3	A-B3-SCARB2-2	A-B3	SCARB2-2	SCARB2	209.6	239.8	277.8	329.1	406.8
90	C3	A-C3-GALC-1	A-C3	GALC-1	GALC	199.1	231.4	272.3	327.7	410.4
91	D3	A-D3-GALC-2	A-D3	GALC-2	GALC	194.9	225.5	264.7	318.3	399.9
92	E3	A-E3-MCCC1-1	A-E3	MCCC1-1	MCCC1	279.6	333.6	402.5	493.8	621.5
93	F3	A-F3-MCCC1-2	A-F3	MCCC1-2	MCCC1	202.8	241.0	290.7	358.7	459.0
-	G3	A-G3-CRLS1-1	A-G3	CRLS1-1	CRLS1	-	-	-	-	-
94	H3	A-H3-CRLS1-2	A-H3	CRLS1-2	CRLS1	212.1	247.5	291.8	350.5	435.1
95	A4	A-A4-CLN8-1	A-A4	CLN8-1	CLN8	86.6	101.2	118.8	141.4	173.0
96	B4	A-B4-CLN8-2	A-B4	CLN8-2	CLN8	131.4	155.6	186.3	227.2	286.4

A.5 Cytosolic Far-Red sgRNA Lentivirus Library Titer Curves

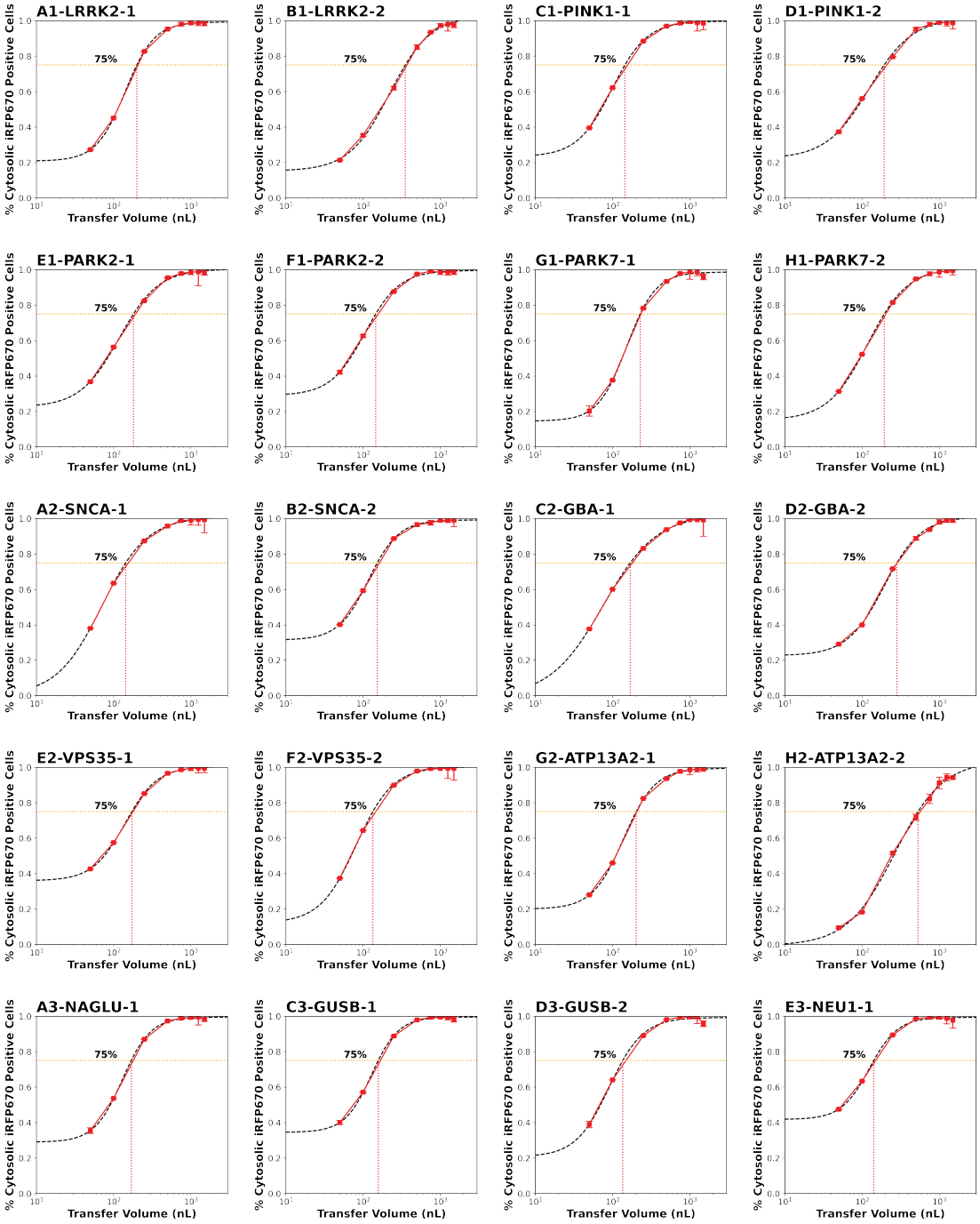


Figure A.7: Cytosolic Far-Red Panel A: Lentivirus titer curves with interpolation.

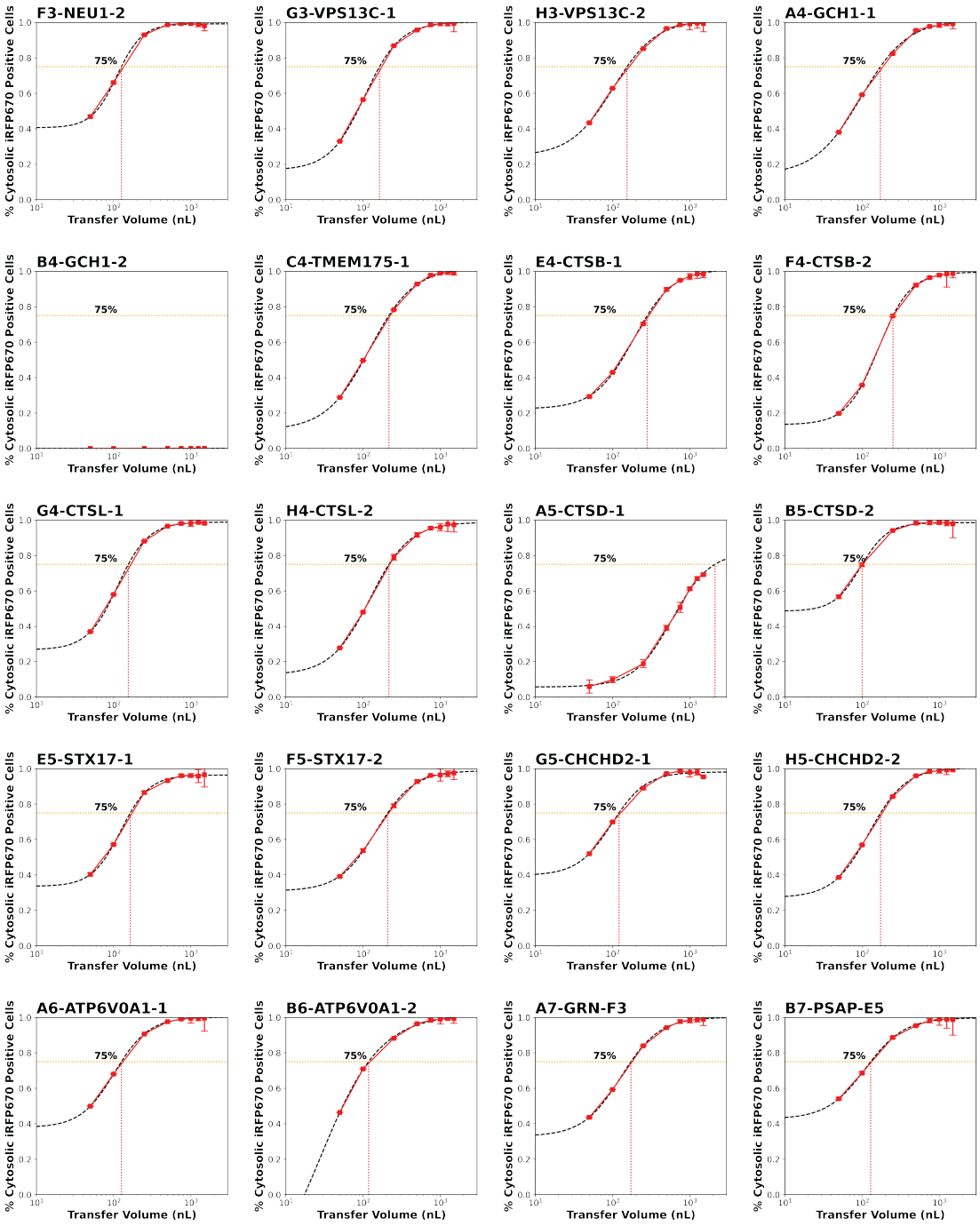


Figure A.8: Cytosolic Far-Red Panel B: Lentivirus titer curves with interpolation.

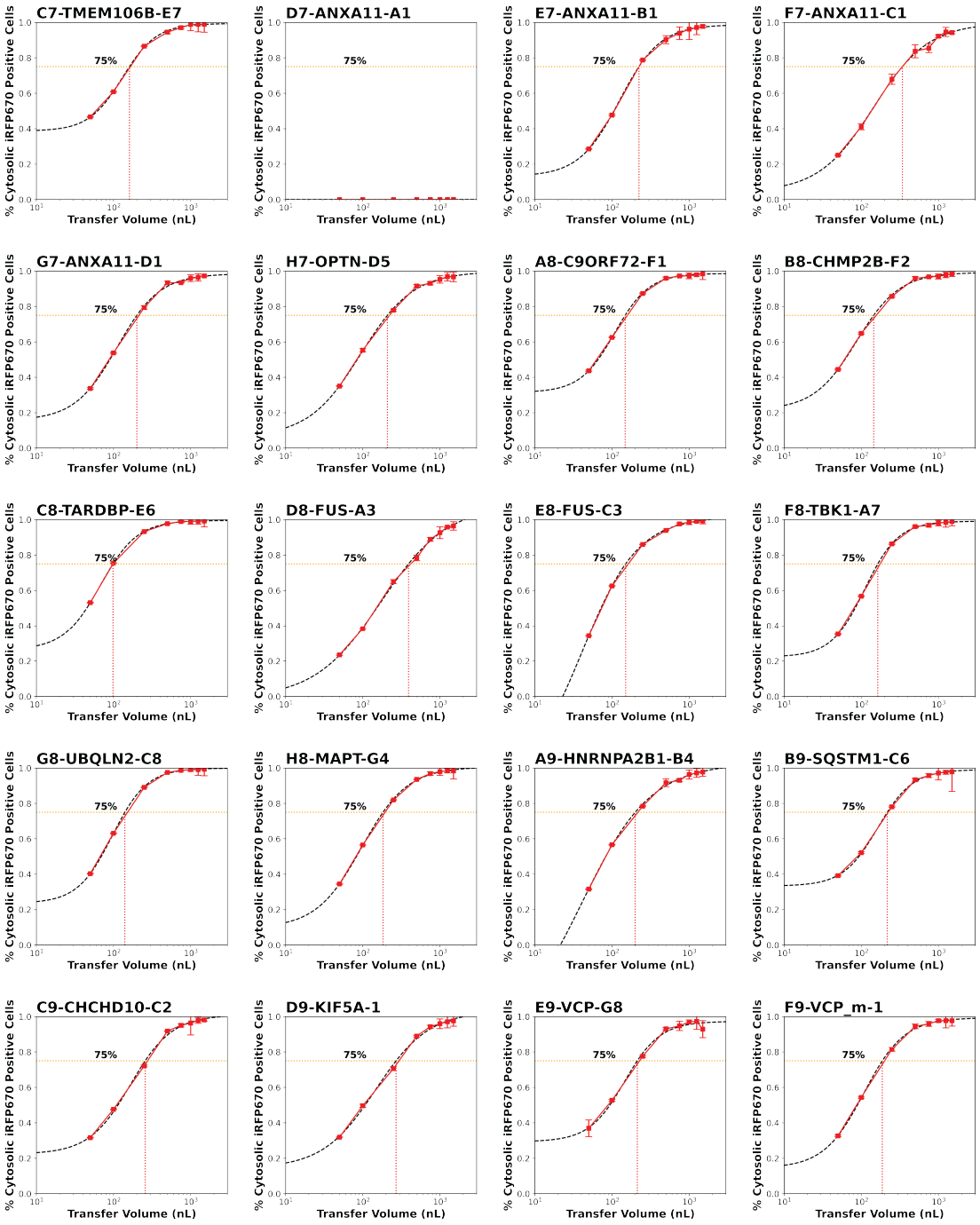


Figure A.9: Cytosolic Far-Red Panel C: Lentivirus titer curves with interpolation.

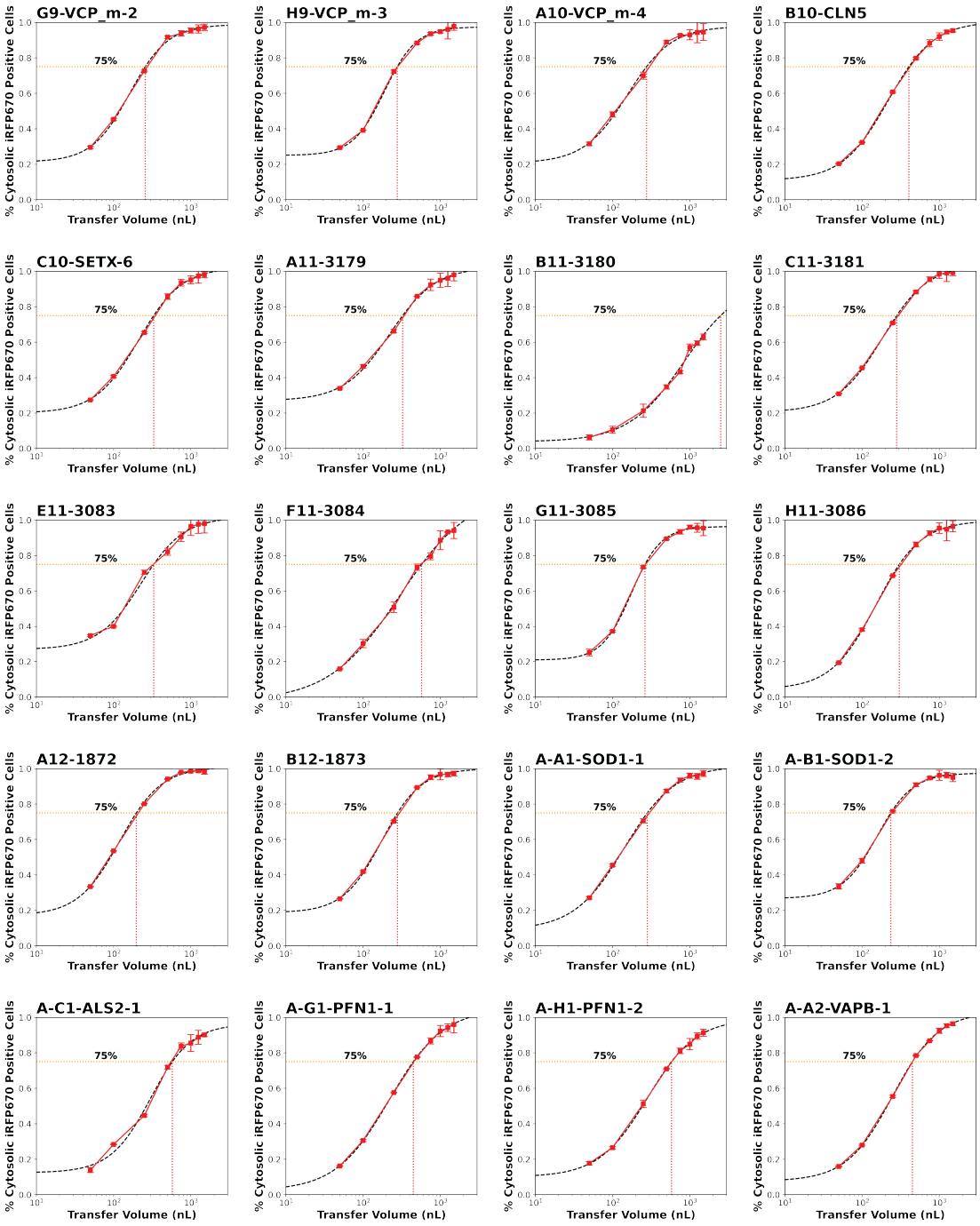


Figure A.10: Cytosolic Far-Red Panel D: Lentivirus titer curves with interpolation.

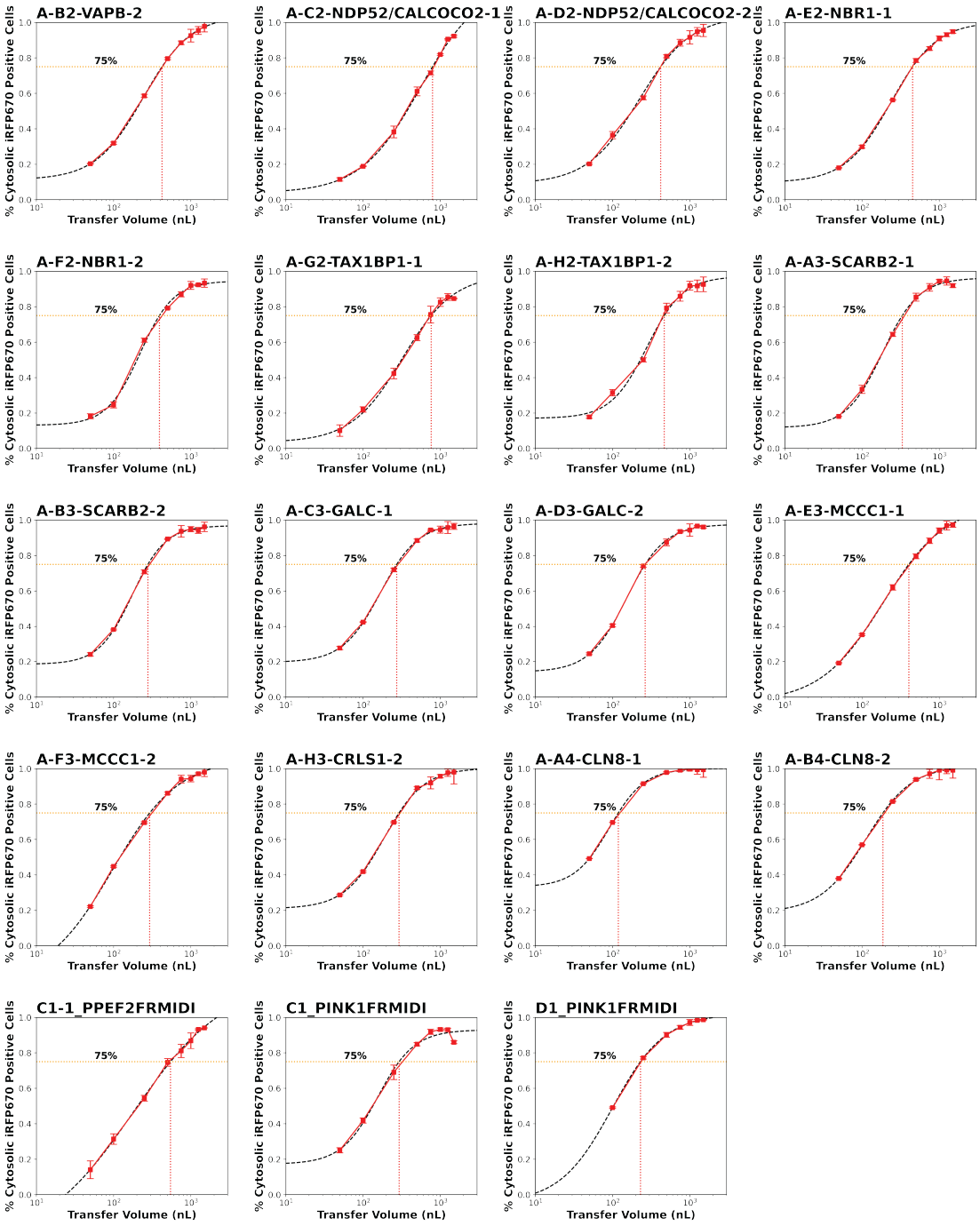


Figure A.11: Cytosolic Far-Red Panel E: Lentivirus titer curves with interpolation.

A.6 Final Targeted, Multiplexed RNA Sequencing Lentivirus Titer Table

Table A.4: Final Targeted, Multiplexed RNA Sequencing Lentivirus Titer Table

sgRNA Code	Source Well	Full Virus Name	RNA Plate 1	RNA Plate 2	RNA Plate 3	RNA Plate 4	Gene Target	75% Titer Transfer Volume (nL)
1	G5	A-1G-PFN1-1	A1	F10	D7	B4	*PFN1*	438.0
2	F6	10B - CLN5	A2	F11	D8	B5	*CLN5*	469.3
3	E4	8A - C9ORF72-F1	A3	F12	D9	B6	*C9ORF72*	538.6
4	F1	9C - CHCHD10-C2	A4	G1	D10	B7	*CHCHD10*	421.5
5	A7	1H - PARK7-2	A5	G2	D11	B8	*PARK7*	306.4
6	E6	8C - TARDBP-E6	A6	G3	D12	B9	*TARDBP*	537.1
7	G6	A-1H-PFN1-2	A7	G4	E1	B10	*PFN1*	965.7
8	D3	5H - CHCHD2-2	A8	G5	E2	B11	*CHCHD2*	260.1
9	E9	8F - TBK1-A7	A9	G6	E3	B12	*TBK1*	585.1
10	D12	7E - ANXA11-B1	A10	G7	E4	C1	*ANXA11*	654.1
11	H1	A-2G-TAX1BP1-1	A11	G8	E5	C2	*TAX1BP1*	1263.4
12	C8	5A - CTSD-1	A12	G9	E6	C3	*CTSD*	287.4
13	C3	4D - TMEM175-2	B1	G10	E7	C4	*TMEM175*	861.2
14	B2	2G - ATP13A2-1	B2	G11	E8	C5	*ATP13A2*	339.3
15	E12	9B - SQSTM1-C6	B3	G12	E9	C6	*SQSTM1*	405.7
16	H7	A-3E-MCCC1-1	B4	H1	E10	C7	*MCCC1*	916.4
17	G10	A-2D-CALCOCO2-2	B5	H2	E11	C8	*NDP52/CALCOCO2*	538.7
18	B3	2H - ATP13A2-2	B6	H3	E12	C9	*ATP13A2*	368.1
19	C11	5D - FYN-2	B7	H4	F1	C10	*FYN*	315.3
20	C10	5C - FYN-1	B8	H5	F2	C11	*FYN*	253.9
21	D9	7B - PSAP-E5	B9	H6	F3	C12	*PSAP*	493.9
22	E3	7H - OPTN-D5	B10	H7	F4	D1	*OPTN*	534.4
23	A5	1F - PARK2-2	B11	H8	F5	D2	*PARK2*	320.2
24	C12	5E - STX17-1	B12	H9	F6	D3	*STX17*	323.7
25	F8	11A - 3179	C1	H10	F7	D4	non-targeting	614.3
26	D11	7D - ANXA11-A1	C2	H11	F8	D5	*ANXA11*	566.4
27	E8	8E - FUS-C3	C3	H12	F9	D6	*FUS*	1033.0
28	G2	A-1D-ALS2-2	C4	A1	F10	D7	*ALS2*	806.3
29	D7	6D - OXR1-2	C5	A2	F11	D8	*OXR1*	380.6

Table A.4 continued from previous page

sgRNA Code	Source Well	Full Virus Name	RNA Plate 1	RNA Plate 2	RNA Plate 3	RNA Plate 4	Gene Target	75% Titer Transfer Volume (nL)
30	G8	A-2B-VAPB-2	C6	A3	F12	D9	*VAPB*	675.3
31	G9	A-2C-CALCOCO2-1	C7	A4	G1	D10	*NDP52/CALCOCO2*	597.5
32	H5	A-3C-GALC-1	C8	A5	G2	D11	*GALC*	1077.0
33	A4	1E - PARK2-1	C9	A6	G3	D12	*PARK2*	312.5
34	H11	A-4A-CLN8-1	C10	A7	G4	E1	*CLN8*	924.0
35	A10	2C - GBA-1	C11	A8	G5	E2	*GBA*	415.1
36	A6	1G - PARK7-1	C12	A9	G6	E3	*PARK7*	390.2
37	A3	1D - PINK1-2	D1	A10	G7	E4	*PINK1*	337.3
38	B8	3E - NEU1-1	D2	A11	G8	E5	*NEU1*	358.9
39	H10	A-3H-CRLS1-2	D3	A12	G9	E6	*CRLS1*	960.2
40	E10	8H - MAPT-G4	D4	B1	G10	E7	*MAPT*	509.9
41	G7	A-2A-VAPB-1	D5	B2	G11	E8	*VAPB*	829.6
42	F11	A-1A-SOD1-1	D6	B3	G12	E9	*SOD1*	1066.6
43	B10	3G - VPS13C-1	D7	B4	H1	E10	*VPS13C*	289.8
44	G12	A-2F-NBR1-2	D8	B5	H2	E11	*NBR1*	740.4
45	A1	1B - LRRK2-2	D9	B6	H3	E12	*LRRK2*	545.1
46	G1	A-1C-ALS2-1	D10	B7	H4	F1	*ALS2*	677.7
47	H12	A-4B-CLN8-2	D11	B8	H5	F2	*CLN8*	1459.5
48	H4	A-3B-SCARB2-2	D12	B9	H6	F3	*SCARB2*	1098.4
49	F9	11C - 3181	E1	B10	H7	F4	non-targeting	612.8
50	A2	1C - PINK1-1	E2	B11	H8	F5	*PINK1*	292.6
51	H6	A-3D-GALC-2	E3	B12	H9	F6	*GALC*	1077.5
52	F12	A-1B-SOD1-2	E4	C1	H10	F7	*SOD1*	823.6
53	C7	4H - CTSL-2	E5	C2	H11	F8	*CTSL*	361.9
54	H3	A-3A-SCARB2-1	E6	C3	H12	F9	*SCARB2*	1106.6
55	A8	2A - SNCA-1	E7	C4	A1	F10	*SNCA*	336.7
56	F2	9D - KIF5A-1	E8	C5	A2	F11	*KIF5A*	706.8
57	D5	6B - ATP6V0A1-2	E9	C6	A3	F12	*ATP6V0A1*	255.2
58	B1	2F - VPS35-2	E10	C7	A4	G1	*VPS35*	406.0
59	F4	9F - VCP_m-1	E11	C8	A5	G2	*VCP*	428.0

Table A.4 continued from previous page

sgRNA Code	Source Well	Full Virus Name	RNA Plate 1	RNA Plate 2	RNA Plate 3	RNA Plate 4	Gene Target	75% Titer Transfer Volume (nL)
60	D1	5F - STX17-2	E12	C9	A6	G3	*STX17*	399.7
61	E2	7G - ANXA11-D1	F1	C10	A7	G4	*ANXA11*	602.7
62	A12	2E - VPS35-1	F2	C11	A8	G5	*VPS35*	396.9
63	A9	2B - SNCA-2	F3	C12	A9	G6	*SNCA*	305.0
64	E7	8D - FUS-A3	F4	D1	A10	G7	*FUS*	629.1
65	B4	3A - NAGLU-1	F5	D2	A11	G8	*NAGLU*	366.8
66	H9	A-3G-CRLS1-1	F6	D3	A12	G9	*CRLS1*	1109.0
67	A11	2D - GBA-2	F7	D4	B1	G10	*GBA*	317.4
68	C1	4B - GCH1-2	F8	D5	B2	G11	*GCH1*	328.9
69	D10	7C - TMEM106B-E7	F9	D6	B3	G12	*TMEM106B*	533.8
70	G3	A-1E-DCTN1-1	F10	D7	B4	H1	*DCTN1*	508.2
71	F10	12A - 1872	F11	D8	B5	H2	non-targeting	780.4
72	D8	7A - GRN-F3	F12	D9	B6	H3	*GRN*	622.8
73	G11	A-2E-NBR1-1	G1	D10	B7	H4	*NBR1*	738.9
74	C4	4E - CTSB-1	G2	D11	B8	H5	*CTSB*	289.8
75	B7	3D - GUSB-2	G3	D12	B9	H6	*GUSB*	381.2
76	D6	6C - OXR1-1	G4	E1	B10	H7	*OXR1*	373.0
77	D2	5G - CHCHD2-1	G5	E2	B11	H8	*CHCHD2*	188.9
78	F5	10A - VCP_m-4	G6	E3	B12	H9	*VCP*	479.3
79	E1	7F - ANXA11-C1	G7	E4	C1	H10	*ANXA11*	503.9
80	E5	8B - CHMP2B-F2	G8	E5	C2	H11	*CHMP2B*	482.4
81	E11	9A - HNRNPA2B1-B4	G9	E6	C3	H12	*HNRNPA2B1*	441.6
82	C2	4C - TMEM175-1	G10	E7	C4	A1	*TMEM175*	314.1
83	D4	6A - ATP6V0A1-1	G11	E8	C5	A2	*ATP6V0A1*	254.9
84	B9	3F - NEU1-2	G12	E9	C6	A3	*NEU1*	511.9
85	H2	A-2H-TAX1BP1-2	H1	E10	C7	A4	*TAX1BP1*	994.1
86	G4	A-1F-DCTN1-2	H2	E11	C8	A5	*DCTN1*	651.5
87	H8	A-3F-MCCC1-2	H3	E12	C9	A6	*MCCC1*	1123.9
88	F3	9E - VCP-G8	H4	F1	C10	A7	*VCP*	566.2
89	B5	3B - NAGLU-2	H5	F2	C11	A8	*NAGLU*	350.5

Table A.4 continued from previous page

sgRNA Code	Source Well	Full Virus Name	RNA Plate 1	RNA Plate 2	RNA Plate 3	RNA Plate 4	Gene Target	75% Titer Transfer Volume (nL)
90	C9	5B - CTSD-2	H6	F3	C12	A9	*CTSD*	258.8
91	B11	3H - VPS13C-2	H7	F4	D1	A10	*VPS13C*	242.0
92	C6	4G - CTSL-1	H8	F5	D2	A11	*CTSL*	261.6
93	F7	10C - SETX	H9	F6	D3	A12	*SETX*	670.7
94	B6	3C - GUSB-1	H10	F7	D4	B1	*GUSB*	369.4
95	B12	4A - GCH1-1	H11	F8	D5	B2	*GCH1*	231.5
96	C5	4F - CTSB-2	H12	F9	D6	B3	*CTSB*	356.8
97	I1	11F - 3084	-	-	-	-	non-targeting	663.1
98	I2	11G - 3085	-	-	-	-	non-targeting	737.2
99	I3	12B - 1873	-	-	-	-	non-targeting	620.0
100	I4	9G - VCP_m-2	-	-	-	-	*VCP*	468.4
101	I5	9H - VCP_m-3	-	-	-	-	*VCP*	646.6

A.7 Final Targeted, Multiplexed RNA Sequencing Sample Table

Table A.5: Final Targeted, Multiplexed RNA Sequencing Sample Table.

Unique Sample Identifier	RNA Plate Position	sgRNA Code	Replicate	Sample Plate	RNA Plate	RiboGreen Plate	ABS Value	ng/uL	RIN or RIN^e
A02-2-1	A02	2	1	200224-1B	200304-1B	RIBO1	16479	12.845	7.7
A04-4-1	A04	4	1	200224-1B	200304-1B	RIBO1	7982	6.222	8.5
A06-6-1	A06	6	1	200224-1B	200304-1B	RIBO1	6210	4.841	8.3
A08-8-1	A08	8	1	200224-1B	200304-1B	RIBO1	7278	5.673	8.5
A09-9-1	A09	9	1	200224-1B	200304-1B	RIBO1	2342	1.826	8.6
A09-097_1B-1	A09	097_1B	1	200224-1B	200304-1B EXTRA	RIBO6	11548	9.711	9.2
A12-12-1	A12	12	1	200224-1B	200304-1B	RIBO1	5062	3.946	7.9
B01-13-1	B01	13	1	200224-1B	200304-1B	RIBO1	9329	7.272	8.8
B02-14-1	B02	14	1	200224-1B	200304-1B	RIBO1	10898	8.495	8.6
B03-15-1	B03	15	1	200224-1B	200304-1B	RIBO1	5703	4.445	0
B04-16-1	B04	16	1	200224-1B	200304-1B	RIBO1	7916	6.170	9.5
B05-17-1	B05	17	1	200224-1B	200304-1B	RIBO1	11687	9.110	8.9
B06-18-1	B06	18	1	200224-1B	200304-1B	RIBO1	4116	3.208	8.8
B07-19-1	B07	19	1	200224-1B	200304-1B	RIBO1	4979	3.881	8.7
B08-20-1	B08	20	1	200224-1B	200304-1B	RIBO1	7206	5.617	9
B09-21-1	B09	21	1	200224-1B	200304-1B	RIBO1	6070	4.731	8.8
B10-22-1	B10	22	1	200224-1B	200304-1B	RIBO1	5583	4.352	9.3
B11-23-1	B11	23	1	200224-1B	200304-1B	RIBO1	13631	10.625	8.4
B12-24-1	B12	24	1	200224-1B	200304-1B	RIBO1	10668	8.316	7.8
C01-25-1	C01	25	1	200224-1B	200304-1B	RIBO1	7347	5.727	8.8
C03-27-1	C03	27	1	200224-1B	200304-1B	RIBO1	8973	6.994	8.9
C04-28-1	C04	28	1	200224-1B	200304-1B	RIBO1	11427	8.907	8.9
C05-29-1	C05	29	1	200224-1B	200304-1B	RIBO1	11121	8.669	8.7
C10-34-1	C10	34	1	200224-1B	200304-1B	RIBO1	6209	4.840	9.1
C11-35-1	C11	35	1	200224-1B	200304-1B	RIBO1	4565	3.558	0
C12-36-1	C12	36	1	200224-1B	200304-1B	RIBO1	6781	5.286	8.6
D01-37-1	D01	37	1	200224-1B	200304-1B	RIBO1	2580	2.011	8.2
D03-39-1	D03	39	1	200224-1B	200304-1B	RIBO1	13520	10.539	9
D06-42-1	D06	42	1	200224-1B	200304-1B	RIBO1	5328	4.153	8.6

Table A.5 continued from previous page

Unique Sample Identifier	RNA Plate Position	sgRNA Code	Replicate	Sample Plate	RNA Plate	RiboGreen Plate	ABS Value	ng/uL	RIN or RIN[e]
D08-44-1	D08	44	1	200224-1B	200304-1B	RIBO1	3840	2.993	8.9
D09-45-1	D09	45	1	200224-1B	200304-1B	RIBO1	3491	2.721	8.8
D10-46-1	D10	46	1	200224-1B	200304-1B	RIBO1	6525	5.086	9
D11-47-1	D11	47	1	200224-1B	200304-1B	RIBO1	9964	7.767	9.5
D12-48-1	D12	48	1	200224-1B	200304-1B	RIBO1	8523	6.644	9.2
E01-49-1	E01	49	1	200224-1B	200304-1B	RIBO1	6665	5.195	8.8
E02-50-1	E02	50	1	200224-1B	200304-1B	RIBO1	14410	11.232	8.9
E03-51-1	E03	51	1	200224-1B	200304-1B	RIBO1	13795	10.753	8.8
E04-52-1	E04	52	1	200224-1B	200304-1B	RIBO1	9550	7.444	9.2
E05-53-1	E05	53	1	200224-1B	200304-1B	RIBO1	6984	5.444	9.4
E07-55-1	E07	55	1	200224-1B	200304-1B	RIBO1	5326	4.152	8.8
E10-58-1	E10	58	1	200224-1B	200304-1B	RIBO1	4103	3.198	8.3
F01-61-1	F01	61	1	200224-1B	200304-1B	RIBO1	15057	11.737	8.5
F02-62-1	F02	62	1	200224-1B	200304-1B	RIBO1	15374	11.984	9
F04-64-1	F04	64	1	200224-1B	200304-1B	RIBO1	9758	7.606	9.1
F06-66-1	F06	66	1	200224-1B	200304-1B	RIBO1	10775	8.399	8.8
F07-67-1	F07	67	1	200224-1B	200304-1B	RIBO1	7336	5.718	7.9
F08-68-1	F08	68	1	200224-1B	200304-1B	RIBO1	12466	9.717	9.1
F09-69-1	F09	69	1	200224-1B	200304-1B	RIBO1	8501	6.626	8.9
F10-70-1	F10	70	1	200224-1B	200304-1B	RIBO1	9708	7.567	9.4
F11-71-1	F11	71	1	200224-1B	200304-1B	RIBO1	6038	4.707	8.9
G01-73-1	G01	73	1	200224-1B	200304-1B	RIBO2	14001	11.826	9.2
G03-75-1	G03	75	1	200224-1B	200304-1B	RIBO2	14017	11.839	8.8
G04-76-1	G04	76	1	200224-1B	200304-1B	RIBO2	6960	5.879	8.8
G05-77-1	G05	77	1	200224-1B	200304-1B	RIBO2	10486	8.857	8.8
G06-78-1	G06	78	1	200224-1B	200304-1B	RIBO2	3266	2.759	9.5
G07-79-1	G07	79	1	200224-1B	200304-1B	RIBO2	10740	9.071	9.6
G09-81-1	G09	81	1	200224-1B	200304-1B	RIBO2	1831	1.547	9.1
G10-82-1	G10	82	1	200224-1B	200304-1B	RIBO2	8891	7.510	9.6
G12-84-1	G12	84	1	200224-1B	200304-1B	RIBO2	8468	7.152	9

Table A.5 continued from previous page

Unique Sample Identifier	RNA Plate Position	sgRNA Code	Replicate	Sample Plate	RNA Plate	RiboGreen Plate	ABS Value	ng/uL	RIN or RIN^e
H02-86-1	H02	86	1	200224-1B	200304-1B	RIBO2	12426	10.496	9.5
H03-87-1	H03	87	1	200224-1B	200304-1B	RIBO2	9866	8.333	9.4
H05-89-1	H05	89	1	200224-1B	200304-1B	RIBO2	3378	2.853	9.7
H08-92-1	H08	92	1	200224-1B	200304-1B	RIBO2	9334	7.884	9.3
H09-93-1	H09	93	1	200224-1B	200304-1B	RIBO2	6180	5.220	8.7
H10-94-1	H10	94	1	200224-1B	200304-1B	RIBO2	6247	5.276	8.4
H12-96-1	H12	96	1	200224-1B	200304-1B	RIBO2	3245	2.741	7.9
A01-28-2	A01	28	2	200224-2A	200304-2A	RIBO2	11657	9.846	9.2
A02-29-2	A02	29	2	200224-2A	200304-2A	RIBO2	8344	7.048	8.6
A03-30-2	A03	30	2	200224-2A	200304-2A	RIBO2	10815	9.135	8.6
A04-31-2	A04	31	2	200224-2A	200304-2A	RIBO2	15475	13.071	8.9
A05-32-2	A05	32	2	200224-2A	200304-2A	RIBO2	9742	8.228	8.9
A06-33-2	A06	33	2	200224-2A	200304-2A	RIBO2	16193	13.677	8.6
A07-34-2	A07	34	2	200224-2A	200304-2A	RIBO2	12613	10.653	8.4
A08-35-2	A08	35	2	200224-2A	200304-2A	RIBO2	11409	9.637	8.6
A09-36-2	A09	36	2	200224-2A	200304-2A	RIBO2	12007	10.142	9.6
A10-097_2A-2	A10	097_2A	2	200224-2A	200304-2A EXTRA	RIBO6	13330	11.210	8.6
A11-38-2	A11	38	2	200224-2A	200304-2A	RIBO2	6122	5.171	9.1
A12-39-2	A12	39	2	200224-2A	200304-2A	RIBO2	9442	7.975	9.3
B01-40-2	B01	40	2	200224-2A	200304-2A	RIBO2	10224	8.636	8
B02-41-2	B02	41	2	200224-2A	200304-2A	RIBO2	12946	10.935	9.1
B03-42-2	B03	42	2	200224-2A	200304-2A	RIBO2	11719	9.898	8.9
B04-43-2	B04	43	2	200224-2A	200304-2A	RIBO2	9343	7.891	9.3
B05-44-2	B05	44	2	200224-2A	200304-2A	RIBO2	5967	5.040	9.3
B06-45-2	B06	45	2	200224-2A	200304-2A	RIBO2	2410	2.036	9.5
B07-46-2	B07	46	2	200224-2A	200304-2A	RIBO2	13982	11.810	9.2
B09-48-2	B09	48	2	200224-2A	200304-2A	RIBO2	5148	4.348	9.6
B10-49-2	B10	49	2	200224-2A	200304-2A	RIBO2	7702	6.505	9.5
B11-50-2	B11	50	2	200224-2A	200304-2A	RIBO2	7916	6.686	9.3
B12-51-2	B12	51	2	200224-2A	200304-2A	RIBO2	10734	9.066	9.3

Table A.5 continued from previous page

Unique Sample Identifier	RNA Plate Position	sgRNA Code	Replicate	Sample Plate	RNA Plate	RiboGreen Plate	ABS Value	ng/uL	RIN or RIN[e]
C01-52-2	C01	52	2	200224-2A	200304-2A	RIBO2	12115	10.233	9.2
C02-53-2	C02	53	2	200224-2A	200304-2A	RIBO2	14905	12.589	9
C03-54-2	C03	54	2	200224-2A	200304-2A	RIBO2	9506	8.029	9.4
C04-55-2	C04	55	2	200224-2A	200304-2A	RIBO2	7620	6.436	9.4
C05-56-2	C05	56	2	200224-2A	200304-2A	RIBO2	7551	6.378	9.2
C06-57-2	C06	57	2	200224-2A	200304-2A	RIBO2	2611	2.205	7.7
C07-58-2	C07	58	2	200224-2A	200304-2A	RIBO2	8491	7.172	9.5
C09-60-2	C09	60	2	200224-2A	200304-2A	RIBO2	9981	8.430	9.6
C10-61-2	C10	61	2	200224-2A	200304-2A	RIBO2	6879	5.810	9.6
C10-099_2A-2	C10	099_2A	2	200224-2A	200304-2A EXTRA	RIBO6	7246	6.093	9
C11-62-2	C11	62	2	200224-2A	200304-2A	RIBO2	6255	5.283	9.6
C12-63-2	C12	63	2	200224-2A	200304-2A	RIBO2	6176	5.217	9.3
D01-64-2	D01	64	2	200224-2A	200304-2A	RIBO2	9327	7.878	9.4
D02-65-2	D02	65	2	200224-2A	200304-2A	RIBO2	11975	10.115	9.4
D03-66-2	D03	66	2	200224-2A	200304-2A	RIBO2	8271	6.986	9.4
D04-67-2	D04	67	2	200224-2A	200304-2A	RIBO2	3175	2.682	9
D05-68-2	D05	68	2	200224-2A	200304-2A	RIBO2	6882	5.813	9.2
D06-69-2	D06	69	2	200224-2A	200304-2A	RIBO2	4261	3.599	9.4
D08-71-2	D08	71	2	200224-2A	200304-2A	RIBO2	264	0.223	8.4
D09-72-2	D09	72	2	200224-2A	200304-2A	RIBO2	9007	7.608	9.6
D11-74-2	D11	74	2	200224-2A	200304-2A	RIBO2	4421	3.734	9.7
D12-75-2	D12	75	2	200224-2A	200304-2A	RIBO2	8323	7.030	9.6
E01-76-2	E01	76	2	200224-2A	200304-2A	RIBO3	6547	5.329	8.7
E02-77-2	E02	77	2	200224-2A	200304-2A	RIBO3	7062	5.748	9.3
E03-78-2	E03	78	2	200224-2A	200304-2A	RIBO3	11782	9.590	9.1
E04-79-2	E04	79	2	200224-2A	200304-2A	RIBO3	9909	8.065	9.1
E05-80-2	E05	80	2	200224-2A	200304-2A	RIBO3	2044	1.664	9.4
E06-81-2	E06	81	2	200224-2A	200304-2A	RIBO3	2516	2.048	9.2
E07-82-2	E07	82	2	200224-2A	200304-2A	RIBO3	3420	2.784	9.5
E08-83-2	E08	83	2	200224-2A	200304-2A	RIBO3	3197	2.602	9.5

Table A.5 continued from previous page

Unique Sample Identifier	RNA Plate Position	sgRNA Code	Replicate	Sample Plate	RNA Plate	RiboGreen Plate	ABS Value	ng/uL	RIN or RIN[e]
E09-84-2	E09	84	2	200224-2A	200304-2A	RIBO3	6336	5.157	9.6
E10-85-2	E10	85	2	200224-2A	200304-2A	RIBO3	6203	5.049	9.6
E11-86-2	E11	86	2	200224-2A	200304-2A	RIBO3	6827	5.557	9.7
E12-87-2	E12	87	2	200224-2A	200304-2A	RIBO3	12014	9.779	9.4
F01-88-2	F01	88	2	200224-2A	200304-2A	RIBO3	9809	7.984	8.7
F02-89-2	F02	89	2	200224-2A	200304-2A	RIBO3	7585	6.174	9.1
F03-90-2	F03	90	2	200224-2A	200304-2A	RIBO3	10726	8.730	9.1
F04-91-2	F04	91	2	200224-2A	200304-2A	RIBO3	7513	6.115	9.1
F05-92-2	F05	92	2	200224-2A	200304-2A	RIBO3	4536	3.692	9.3
F06-93-2	F06	93	2	200224-2A	200304-2A	RIBO3	4583	3.730	9.2
F07-94-2	F07	94	2	200224-2A	200304-2A	RIBO3	7183	5.846	8.8
F08-95-2	F08	95	2	200224-2A	200304-2A	RIBO3	8009	6.519	9.8
F09-96-2	F09	96	2	200224-2A	200304-2A	RIBO3	7307	5.947	9.6
F10-1-2	F10	1	2	200224-2A	200304-2A	RIBO3	8825	7.183	9.4
F11-2-2	F11	2	2	200224-2A	200304-2A	RIBO3	10263	8.353	9.6
F12-3-2	F12	3	2	200224-2A	200304-2A	RIBO3	7965	6.483	9.7
G01-4-2	G01	4	2	200224-2A	200304-2A	RIBO3	13331	10.850	9.3
G02-5-2	G02	5	2	200224-2A	200304-2A	RIBO3	10308	8.390	9.2
G03-6-2	G03	6	2	200224-2A	200304-2A	RIBO3	11899	9.685	9.3
G04-7-2	G04	7	2	200224-2A	200304-2A	RIBO3	9360	7.618	9.3
G05-8-2	G05	8	2	200224-2A	200304-2A	RIBO3	5113	4.162	8.5
G06-9-2	G06	9	2	200224-2A	200304-2A	RIBO3	4240	3.451	9.2
G07-10-2	G07	10	2	200224-2A	200304-2A	RIBO3	5220	4.249	8.7
G08-11-2	G08	11	2	200224-2A	200304-2A	RIBO3	9893	8.052	7.7
G09-12-2	G09	12	2	200224-2A	200304-2A	RIBO3	7479	6.087	9.5
G10-13-2	G10	13	2	200224-2A	200304-2A	RIBO3	8285	6.743	9.7
G11-14-2	G11	14	2	200224-2A	200304-2A	RIBO3	6262	5.097	9.4
H01-16-2	H01	16	2	200224-2A	200304-2A	RIBO3	19422	15.808	8.8
H02-17-2	H02	17	2	200224-2A	200304-2A	RIBO3	12940	10.532	9.2
H03-18-2	H03	18	2	200224-2A	200304-2A	RIBO3	12012	9.777	9.1

Table A.5 continued from previous page

Unique Sample Identifier	RNA Plate Position	sgRNA Code	Replicate	Sample Plate	RNA Plate	RiboGreen Plate	ABS Value	ng/uL	RIN or RIN[e]
H04-19-2	H04	19	2	200224-2A	200304-2A	RIBO3	14732	11.991	9.1
H05-20-2	H05	20	2	200224-2A	200304-2A	RIBO3	13212	10.754	9
H06-21-2	H06	21	2	200224-2A	200304-2A	RIBO3	10217	8.316	8.7
H07-22-2	H07	22	2	200224-2A	200304-2A	RIBO3	7709	6.275	9.1
H08-23-2	H08	23	2	200224-2A	200304-2A	RIBO3	10768	8.764	9.5
H09-24-2	H09	24	2	200224-2A	200304-2A	RIBO3	12975	10.561	9
H10-25-2	H10	25	2	200224-2A	200304-2A	RIBO3	12441	10.126	9.4
H11-26-2	H11	26	2	200224-2A	200304-2A	RIBO3	11306	9.202	-
H12-27-2	H12	27	2	200224-2A	200304-2A	RIBO3	14391	11.713	7
A01-55-3	A01	55	3	200224-3A	200304-3A	RIBO3	6890	5.608	8.7
A02-56-3	A02	56	3	200224-3A	200304-3A	RIBO3	9101	7.408	9.1
A03-57-3	A03	57	3	200224-3A	200304-3A	RIBO3	11977	9.748	9
A04-58-3	A04	58	3	200224-3A	200304-3A	RIBO3	14089	11.467	8.8
A05-59-3	A05	59	3	200224-3A	200304-3A	RIBO3	10403	8.467	8.8
A06-60-3	A06	60	3	200224-3A	200304-3A	RIBO3	14284	11.626	9.1
A07-61-3	A07	61	3	200224-3A	200304-3A	RIBO3	10752	8.751	8.8
A08-62-3	A08	62	3	200224-3A	200304-3A	RIBO3	12432	10.119	8.9
A09-63-3	A09	63	3	200224-3A	200304-3A	RIBO3	10742	8.743	9.3
A10-64-3	A10	64	3	200224-3A	200304-3A	RIBO3	14356	11.685	8.6
A11-65-3	A11	65	3	200224-3A	200304-3A	RIBO3	2207	1.796	8.9
A12-66-3	A12	66	3	200224-3A	200304-3A	RIBO3	15768	12.834	8.3
B01-67-3	B01	67	3	200224-3A	200304-3A	RIBO3	10553	8.589	8.9
B02-68-3	B02	68	3	200224-3A	200304-3A	RIBO3	10220	8.318	9.1
B03-69-3	B03	69	3	200224-3A	200304-3A	RIBO3	11811	9.613	8.7
B04-70-3	B04	70	3	200224-3A	200304-3A	RIBO3	9560	7.781	9.3
B05-71-3	B05	71	3	200224-3A	200304-3A	RIBO3	9928	8.081	9.2
B06-72-3	B06	72	3	200224-3A	200304-3A	RIBO3	8119	6.608	9.2
B07-73-3	B07	73	3	200224-3A	200304-3A	RIBO3	13489	10.979	8.8
B08-74-3	B08	74	3	200224-3A	200304-3A	RIBO3	14489	11.793	8.8
B09-75-3	B09	75	3	200224-3A	200304-3A	RIBO3	7608	6.192	9.1

Table A.5 continued from previous page

Unique Sample Identifier	RNA Plate Position	sgRNA Code	Replicate	Sample Plate	RNA Plate	RiboGreen Plate	ABS Value	ng/uL	RIN or RIN^e
B10-76-3	B10	76	3	200224-3A	200304-3A	RIBO3	10733	8.736	9.2
B11-77-3	B11	77	3	200224-3A	200304-3A	RIBO3	12301	10.012	8.7
C01-79-3	C01	79	3	200224-3A	200304-3A	RIBO4	11529	9.220	8.9
C02-80-3	C02	80	3	200224-3A	200304-3A	RIBO4	13518	10.811	9.2
C03-81-3	C03	81	3	200224-3A	200304-3A	RIBO4	13500	10.796	9.1
C04-82-3	C04	82	3	200224-3A	200304-3A	RIBO4	13763	11.006	9.2
C05-83-3	C05	83	3	200224-3A	200304-3A	RIBO4	9465	7.569	9.1
C06-84-3	C06	84	3	200224-3A	200304-3A	RIBO4	13329	10.659	8.9
C07-85-3	C07	85	3	200224-3A	200304-3A	RIBO4	11292	9.030	9
C08-86-3	C08	86	3	200224-3A	200304-3A	RIBO4	7778	6.220	9.2
C09-87-3	C09	87	3	200224-3A	200304-3A	RIBO4	10316	8.250	9.3
C10-88-3	C10	88	3	200224-3A	200304-3A	RIBO4	12709	10.164	8.3
C11-89-3	C11	89	3	200224-3A	200304-3A	RIBO4	12210	9.764	9.2
C11-099_3A-3	C11	099_3A	3	200224-3A	200304-3A EXTRA	RIBO6	10684	8.985	9.1
C12-90-3	C12	90	3	200224-3A	200304-3A	RIBO4	8430	6.742	9.2
D01-91-3	D01	91	3	200224-3A	200304-3A	RIBO4	7753	6.200	9.3
D02-92-3	D02	92	3	200224-3A	200304-3A	RIBO4	12919	10.331	9.2
D03-93-3	D03	93	3	200224-3A	200304-3A	RIBO4	13656	10.921	8.9
D04-94-3	D04	94	3	200224-3A	200304-3A	RIBO4	8254	6.601	9.3
D05-95-3	D05	95	3	200224-3A	200304-3A	RIBO4	7033	5.624	9.3
D06-96-3	D06	96	3	200224-3A	200304-3A	RIBO4	7325	5.858	8.8
D07-1-3	D07	1	3	200224-3A	200304-3A	RIBO4	8224	6.577	9.3
D08-2-3	D08	2	3	200224-3A	200304-3A	RIBO4	7274	5.817	9.2
D09-3-3	D09	3	3	200224-3A	200304-3A	RIBO4	9575	7.657	9.3
D10-4-3	D10	4	3	200224-3A	200304-3A	RIBO4	7428	5.940	9.3
D11-5-3	D11	5	3	200224-3A	200304-3A	RIBO4	11326	9.058	9.2
D12-6-3	D12	6	3	200224-3A	200304-3A	RIBO4	9679	7.740	9.3
E01-7-3	E01	7	3	200224-3A	200304-3A	RIBO4	9193	7.352	9.6
E02-8-3	E02	8	3	200224-3A	200304-3A	RIBO4	12202	9.758	9.3
E04-10-3	E04	10	3	200224-3A	200304-3A	RIBO4	13993	11.190	8.4

Table A.5 continued from previous page

Unique Sample Identifier	RNA Plate Position	sgRNA Code	Replicate	Sample Plate	RNA Plate	RiboGreen Plate	ABS Value	ng/uL	RIN or RIN[e]
E05-11-3	E05	11	3	200224-3A	200304-3A	RIBO4	7726	6.179	9.5
E06-12-3	E06	12	3	200224-3A	200304-3A	RIBO4	7804	6.241	9.5
E08-14-3	E08	14	3	200224-3A	200304-3A	RIBO4	4214	3.370	9.1
E09-15-3	E09	15	3	200224-3A	200304-3A	RIBO4	8643	6.912	8.7
E10-16-3	E10	16	3	200224-3A	200304-3A	RIBO4	8239	6.589	9.4
E11-17-3	E11	17	3	200224-3A	200304-3A	RIBO4	9748	7.796	9.2
F01-19-3	F01	19	3	200224-3A	200304-3A	RIBO4	13365	10.688	9.2
F02-20-3	F02	20	3	200224-3A	200304-3A	RIBO4	11373	9.095	8.9
F03-21-3	F03	21	3	200224-3A	200304-3A	RIBO4	10750	8.597	8.6
F04-22-3	F04	22	3	200224-3A	200304-3A	RIBO4	7135	5.706	9.2
F05-23-3	F05	23	3	200224-3A	200304-3A	RIBO4	8397	6.715	9.2
F06-24-3	F06	24	3	200224-3A	200304-3A	RIBO4	10188	8.147	9.3
F07-25-3	F07	25	3	200224-3A	200304-3A	RIBO4	7426	5.939	9.4
F08-26-3	F08	26	3	200224-3A	200304-3A	RIBO4	10068	8.052	9.2
F09-27-3	F09	27	3	200224-3A	200304-3A	RIBO4	13015	10.408	9.1
F10-28-3	F10	28	3	200224-3A	200304-3A	RIBO4	11420	9.133	9.1
F11-29-3	F11	29	3	200224-3A	200304-3A	RIBO4	8596	6.874	9.1
F12-30-3	F12	30	3	200224-3A	200304-3A	RIBO4	9121	7.294	9.4
G01-31-3	G01	31	3	200224-3A	200304-3A	RIBO4	12213	9.767	9.4
G02-32-3	G02	32	3	200224-3A	200304-3A	RIBO4	14129	11.299	9.4
G03-33-3	G03	33	3	200224-3A	200304-3A	RIBO4	18196	14.552	9.1
G04-34-3	G04	34	3	200224-3A	200304-3A	RIBO4	15189	12.147	9.2
G05-35-3	G05	35	3	200224-3A	200304-3A	RIBO4	10750	8.597	9.1
G06-36-3	G06	36	3	200224-3A	200304-3A	RIBO4	6587	5.268	9.3
G07-37-3	G07	37	3	200224-3A	200304-3A	RIBO4	11766	9.409	9.1
G08-38-3	G08	38	3	200224-3A	200304-3A	RIBO4	10769	8.612	9.4
G09-39-3	G09	39	3	200224-3A	200304-3A	RIBO4	9597	7.675	9.3
G10-40-3	G10	40	3	200224-3A	200304-3A	RIBO4	11510	9.205	9.1
G11-41-3	G11	41	3	200224-3A	200304-3A	RIBO4	10574	8.456	9.2
G12-42-3	G12	42	3	200224-3A	200304-3A	RIBO4	14204	11.359	9

Table A.5 continued from previous page

Unique Sample Identifier	RNA Plate Position	sgRNA Code	Replicate	Sample Plate	RNA Plate	RiboGreen Plate	ABS Value	ng/uL	RIN or RIN^e
H01-43-3	H01	43	3	200224-3A	200304-3A	RIBO4	8782	7.023	9.4
H02-44-3	H02	44	3	200224-3A	200304-3A	RIBO4	12407	9.922	9.4
H03-45-3	H03	45	3	200224-3A	200304-3A	RIBO4	14748	11.794	9.1
H04-46-3	H04	46	3	200224-3A	200304-3A	RIBO4	15463	12.366	9.2
H05-47-3	H05	47	3	200224-3A	200304-3A	RIBO4	12038	9.627	9.2
H06-48-3	H06	48	3	200224-3A	200304-3A	RIBO4	12343	9.871	9.1
H08-50-3	H08	50	3	200224-3A	200304-3A	RIBO4	13602	10.878	8.8
H09-51-3	H09	51	3	200224-3A	200304-3A	RIBO4	11165	8.929	8.8
H10-52-3	H10	52	3	200224-3A	200304-3A	RIBO4	12966	10.369	8.9
H11-53-3	H11	53	3	200224-3A	200304-3A	RIBO4	12625	10.096	8
H12-54-3	H12	54	3	200224-3A	200304-3A	RIBO4	13740	10.988	8.7
A01-82-4	A01	82	4	200224-4B	200304-4B	RIBO5	9016	7.441	8.9
A02-83-4	A02	83	4	200224-4B	200304-4B	RIBO5	3989	3.292	7.4
A03-84-4	A03	84	4	200224-4B	200304-4B	RIBO5	10070	8.311	9.2
A04-85-4	A04	85	4	200224-4B	200304-4B	RIBO5	11281	9.310	9
A05-86-4	A05	86	4	200224-4B	200304-4B	RIBO5	6713	5.540	8.9
A06-87-4	A06	87	4	200224-4B	200304-4B	RIBO5	9911	8.179	8.5
A07-88-4	A07	88	4	200224-4B	200304-4B	RIBO5	9195	7.589	8.1
A08-89-4	A08	89	4	200224-4B	200304-4B	RIBO5	10814	8.925	9.1
A09-90-4	A09	90	4	200224-4B	200304-4B	RIBO5	6898	5.693	9
A10-91-4	A10	91	4	200224-4B	200304-4B	RIBO5	6396	5.279	8.8
A12-93-4	A12	93	4	200224-4B	200304-4B	RIBO5	10526	8.687	8.9
B01-94-4	B01	94	4	200224-4B	200304-4B	RIBO5	6626	5.468	7.9
B02-95-4	B02	95	4	200224-4B	200304-4B	RIBO5	6719	5.545	8.2
B03-96-4	B03	96	4	200224-4B	200304-4B	RIBO5	6726	5.551	9
B06-3-4	B06	3	4	200224-4B	200304-4B	RIBO5	8359	6.899	9.3
B07-4-4	B07	4	4	200224-4B	200304-4B	RIBO5	10350	8.542	9.1
B08-5-4	B08	5	4	200224-4B	200304-4B	RIBO5	7310	6.033	8.8
B10-7-4	B10	7	4	200224-4B	200304-4B	RIBO5	7405	6.111	9.1
B11-8-4	B11	8	4	200224-4B	200304-4B	RIBO5	6537	5.395	8.9

Table A.5 continued from previous page

Unique Sample Identifier	RNA Plate Position	sgRNA Code	Replicate	Sample Plate	RNA Plate	RiboGreen Plate	ABS Value	ng/uL	RIN or RIN[e]
B12-9-4	B12	9	4	200224-4B	200304-4B	RIBO5	7970	6.578	9.2
C01-10-4	C01	10	4	200224-4B	200304-4B	RIBO5	7665	6.326	9.1
C02-11-4	C02	11	4	200224-4B	200304-4B	RIBO5	9675	7.985	9.6
C05-14-4	C05	14	4	200224-4B	200304-4B	RIBO5	10690	8.822	9.1
C06-15-4	C06	15	4	200224-4B	200304-4B	RIBO5	9079	7.493	9.3
C08-17-4	C08	17	4	200224-4B	200304-4B	RIBO5	7445	6.144	8.9
C09-18-4	C09	18	4	200224-4B	200304-4B	RIBO5	6722	5.548	8.9
C10-19-4	C10	19	4	200224-4B	200304-4B	RIBO5	8564	7.068	8.9
C11-20-4	C11	20	4	200224-4B	200304-4B	RIBO5	9852	8.131	9.3
D01-22-4	D01	22	4	200224-4B	200304-4B	RIBO5	12082	9.971	9.4
D02-23-4	D02	23	4	200224-4B	200304-4B	RIBO5	8378	6.914	8.4
D03-24-4	D03	24	4	200224-4B	200304-4B	RIBO5	11831	9.764	9.3
D04-25-4	D04	25	4	200224-4B	200304-4B	RIBO5	3084	2.545	9.1
D05-26-4	D05	26	4	200224-4B	200304-4B	RIBO5	2595	2.142	9.5
D06-27-4	D06	27	4	200224-4B	200304-4B	RIBO5	8170	6.743	9.3
D07-28-4	D07	28	4	200224-4B	200304-4B	RIBO5	10384	8.570	9.1
D08-29-4	D08	29	4	200224-4B	200304-4B	RIBO5	6911	5.704	9.4
D09-30-4	D09	30	4	200224-4B	200304-4B	RIBO5	8295	6.846	9.4
D10-31-4	D10	31	4	200224-4B	200304-4B	RIBO5	11801	9.739	9.1
D11-32-4	D11	32	4	200224-4B	200304-4B	RIBO5	9911	8.179	8.6
D12-33-4	D12	33	4	200224-4B	200304-4B	RIBO5	11107	9.166	8.5
E01-34-4	E01	34	4	200224-4B	200304-4B	RIBO5	4032	3.328	8.6
E03-36-4	E03	36	4	200224-4B	200304-4B	RIBO5	10610	8.756	9.3
E04-37-4	E04	37	4	200224-4B	200304-4B	RIBO5	11276	9.306	8.9
E05-38-4	E05	38	4	200224-4B	200304-4B	RIBO5	5443	4.492	9.1
E06-39-4	E06	39	4	200224-4B	200304-4B	RIBO5	1469	1.212	8.1
E07-40-4	E07	40	4	200224-4B	200304-4B	RIBO5	8870	7.320	8.9
E08-41-4	E08	41	4	200224-4B	200304-4B	RIBO5	10647	8.787	9.5
E09-42-4	E09	42	4	200224-4B	200304-4B	RIBO5	8905	7.349	9.2
E10-43-4	E10	43	4	200224-4B	200304-4B	RIBO5	6355	5.245	9

Table A.5 continued from previous page

Unique Sample Identifier	RNA Plate Position	sgRNA Code	Replicate	Sample Plate	RNA Plate	RiboGreen Plate	ABS Value	ng/uL	RIN or RIN[e]
E11-44-4	E11	44	4	200224-4B	200304-4B	RIBO5	5088	4.199	9.3
F01-46-4	F01	46	4	200224-4B	200304-4B	RIBO5	8128	6.708	9
F02-47-4	F02	47	4	200224-4B	200304-4B	RIBO5	8036	6.632	9.3
F04-49-4	F04	49	4	200224-4B	200304-4B	RIBO5	8059	6.651	8.9
F05-50-4	F05	50	4	200224-4B	200304-4B	RIBO5	6836	5.642	9
F06-51-4	F06	51	4	200224-4B	200304-4B	RIBO5	10711	8.840	9.2
F07-52-4	F07	52	4	200224-4B	200304-4B	RIBO5	13277	10.957	9
F08-53-4	F08	53	4	200224-4B	200304-4B	RIBO5	10621	8.765	9.3
F09-54-4	F09	54	4	200224-4B	200304-4B	RIBO5	13183	10.880	9.3
F10-55-4	F10	55	4	200224-4B	200304-4B	RIBO5	13809	11.396	9.1
F11-56-4	F11	56	4	200224-4B	200304-4B	RIBO5	6793	5.606	8.9
F12-57-4	F12	57	4	200224-4B	200304-4B	RIBO5	12322	10.169	9.3
G01-58-4	G01	58	4	200224-4B	200304-4B	RIBO6	15223	12.802	9.2
G02-59-4	G02	59	4	200224-4B	200304-4B	RIBO6	11117	9.349	9.3
G03-60-4	G03	60	4	200224-4B	200304-4B	RIBO6	14613	12.289	9.2
G04-61-4	G04	61	4	200224-4B	200304-4B	RIBO6	11235	9.448	9.4
G05-62-4	G05	62	4	200224-4B	200304-4B	RIBO6	10639	8.947	9.1
G06-63-4	G06	63	4	200224-4B	200304-4B	RIBO6	4719	3.968	9.1
G07-64-4	G07	64	4	200224-4B	200304-4B	RIBO6	8910	7.493	9.1
G08-65-4	G08	65	4	200224-4B	200304-4B	RIBO6	10392	8.739	9.2
G09-66-4	G09	66	4	200224-4B	200304-4B	RIBO6	9665	8.128	9.3
G10-67-4	G10	67	4	200224-4B	200304-4B	RIBO6	5525	4.646	9.1
G11-68-4	G11	68	4	200224-4B	200304-4B	RIBO6	9766	8.213	9.2
H01-70-4	H01	70	4	200224-4B	200304-4B	RIBO6	10307	8.667	8.5
H02-71-4	H02	71	4	200224-4B	200304-4B	RIBO6	9381	7.889	9.4
H03-72-4	H03	72	4	200224-4B	200304-4B	RIBO6	15005	12.618	9.4
H04-73-4	H04	73	4	200224-4B	200304-4B	RIBO6	13207	11.106	9.4
H05-74-4	H05	74	4	200224-4B	200304-4B	RIBO6	3232	2.718	9.2
H06-75-4	H06	75	4	200224-4B	200304-4B	RIBO6	8441	7.098	9.2
H07-76-4	H07	76	4	200224-4B	200304-4B	RIBO6	1360	1.144	8.7

Table A.5 continued from previous page

Unique Sample Identifier	RNA Plate Position	sgRNA Code	Replicate	Sample Plate	RNA Plate	RiboGreen Plate	ABS Value	ng/uL	RIN or RIN[e]
H08-77-4	H08	77	4	200224-4B	200304-4B	RIBO6	7919	6.659	9.2
H09-78-4	H09	78	4	200224-4B	200304-4B	RIBO6	8795	7.396	9.4
H10-79-4	H10	79	4	200224-4B	200304-4B	RIBO6	8722	7.335	8.9
H11-80-4	H11	80	4	200224-4B	200304-4B	RIBO6	9756	8.204	8.8
H12-81-4	H12	81	4	200224-4B	200304-4B	RIBO6	10823	9.101	9.2
A01-1-5	A01	1	5	200224-1A	200305-1A	RIBO7	11636	6.974	9.5
A03-3-5	A03	3	5	200224-1A	200305-1A	RIBO7	6375	3.821	9
A03-097_1A-5	A03	097_1A	5	200224-1A	200305-1A EXTRA	RIBO8	9993	6.341	9.1
A05-5-5	A05	5	5	200224-1A	200305-1A	RIBO7	5073	3.041	8.5
A05-099_1A-5	A05	099_1A	5	200224-1A	200305-1A EXTRA	RIBO8	15843	10.053	9.5
A06-6-5	A06	6	5	200224-1A	200305-1A	RIBO7	6502	3.897	9.3
A07-7-5	A07	7	5	200224-1A	200305-1A	RIBO7	7801	4.676	9.3
A09-9-5	A09	9	5	200224-1A	200305-1A	RIBO7	11912	7.140	9.3
A10-10-5	A10	10	5	200224-1A	200305-1A	RIBO7	10026	6.009	9.3
A11-11-5	A11	11	5	200224-1A	200305-1A	RIBO7	7712	4.622	8.9
A12-12-5	A12	12	5	200224-1A	200305-1A	RIBO7	10101	6.054	8.7
B01-13-5	B01	13	5	200224-1A	200305-1A	RIBO7	12108	7.257	9.4
B03-15-5	B03	15	5	200224-1A	200305-1A	RIBO7	9616	5.763	9.1
B04-16-5	B04	16	5	200224-1A	200305-1A	RIBO7	7022	4.209	9.1
B06-18-5	B06	18	5	200224-1A	200305-1A	RIBO7	4979	2.984	8.8
B09-21-5	B09	21	5	200224-1A	200305-1A	RIBO7	7302	4.377	9.2
C02-26-5	C02	26	5	200224-1A	200305-1A	RIBO7	4932	2.956	9.2
C06-30-5	C06	30	5	200224-1A	200305-1A	RIBO7	3614	2.166	8.5
C07-31-5	C07	31	5	200224-1A	200305-1A	RIBO7	5214	3.125	8.9
C08-32-5	C08	32	5	200224-1A	200305-1A	RIBO7	2493	1.494	8.4
C09-33-5	C09	33	5	200224-1A	200305-1A	RIBO7	10996	6.591	9.2
C11-35-5	C11	35	5	200224-1A	200305-1A	RIBO7	6315	3.785	8.9
D01-37-5	D01	37	5	200224-1A	200305-1A	RIBO7	4459	2.673	9.3
D02-38-5	D02	38	5	200224-1A	200305-1A	RIBO7	4467	2.677	8.8
D04-40-5	D04	40	5	200224-1A	200305-1A	RIBO7	2639	1.582	8.8

Table A.5 continued from previous page

Unique Sample Identifier	RNA Plate Position	sgRNA Code	Replicate	Sample Plate	RNA Plate	RiboGreen Plate	ABS Value	ng/uL	RIN or RIN[e]
D05-41-5	D05	41	5	200224-1A	200305-1A	RIBO7	1335	0.800	9.3
D07-43-5	D07	43	5	200224-1A	200305-1A	RIBO7	7140	4.279	9.3
D09-45-5	D09	45	5	200224-1A	200305-1A	RIBO7	9750	5.844	9.4
D11-47-5	D11	47	5	200224-1A	200305-1A	RIBO7	11056	6.627	9.2
D12-48-5	D12	48	5	200224-1A	200305-1A	RIBO7	11503	6.894	9.4
E01-49-5	E01	49	5	200224-1A	200305-1A	RIBO7	4244	2.544	9
E06-54-5	E06	54	5	200224-1A	200305-1A	RIBO7	920	0.551	0
E08-56-5	E08	56	5	200224-1A	200305-1A	RIBO7	8993	5.390	9.3
E09-57-5	E09	57	5	200224-1A	200305-1A	RIBO7	6758	4.050	9.1
E11-59-5	E11	59	5	200224-1A	200305-1A	RIBO7	4651	2.788	9.3
E12-60-5	E12	60	5	200224-1A	200305-1A	RIBO7	5985	3.587	9.3
F03-63-5	F03	63	5	200224-1A	200305-1A	RIBO7	7998	4.794	9.7
F05-65-5	F05	65	5	200224-1A	200305-1A	RIBO7	10441	6.258	9.5
F09-69-5	F09	69	5	200224-1A	200305-1A	RIBO7	6079	3.644	9.5
F10-70-5	F10	70	5	200224-1A	200305-1A	RIBO7	9625	5.769	9.7
F12-72-5	F12	72	5	200224-1A	200305-1A	RIBO7	8714	5.223	9.6
G02-74-5	G02	74	5	200224-1A	200305-1A	RIBO8	6155	3.906	9.5
G08-80-5	G08	80	5	200224-1A	200305-1A	RIBO8	7674	4.870	9.7
G11-83-5	G11	83	5	200224-1A	200305-1A	RIBO8	7896	5.011	9.6
H01-85-5	H01	85	5	200224-1A	200305-1A	RIBO8	13629	8.648	9.7
H04-88-5	H04	88	5	200224-1A	200305-1A	RIBO8	6656	4.224	9.1
H06-90-5	H06	90	5	200224-1A	200305-1A	RIBO8	8115	5.149	9.6
H07-91-5	H07	91	5	200224-1A	200305-1A	RIBO8	8376	5.315	9.7
H08-92-5	H08	92	5	200224-1A	200305-1A	RIBO8	11594	7.357	9.7
H11-95-5	H11	95	5	200224-1A	200305-1A	RIBO8	11016	6.990	9.6

A.8 Log2 Fold Change and Significance Values from Targeted RNA Sequencing

Table A.6: Log_2 Fold Change and Significance Values from Targeted RNA Sequencing.

Gene	sgRNA	Mean Counts	log2FoldChange	padj
ALS2	ALS2_1	98.84	-1.92	2.72746E-26
ALS2	ALS2_2	98.84	-0.32	0.916415443
ANXA11	ANXA11_A1	6.33	-1.81	0.505029277
ANXA11	ANXA11_B1	6.33	-3.08	0.064842454
ANXA11	ANXA11_C1	6.33	-2.70	0.113397288
ANXA11	ANXA11_D1	6.33	-3.21	0.081693014
ATP13A2	ATP13A2_1	802.36	-2.16	1.06199E-20
ATP13A2	ATP13A2_2	802.36	-2.77	5.06562E-36
ATP6V0A1	ATP6V0A1_1	1425.30	-5.22	9.2588E-143
ATP6V0A1	ATP6V0A1_2	1425.30	-4.36	1.5432E-116
C9ORF72	C9ORF72_F1	404.15	-3.62	4.8421E-116
CALCOCO2	CALCOCO2_1	162.61	-7.06	2.38776E-30
CALCOCO2	CALCOCO2_2	162.61	-5.68	5.87877E-33
CHCHD10	CHCHD10_C2	396.43	-2.83	2.81013E-63
CHCHD2	CHCHD2_1	17.10	-0.63	0.99327396
CHCHD2	CHCHD2_2	17.10	-1.09	0.993118508
CHMP2B	CHMP2B_F2	158.83	-2.74	6.47869E-68
CLN5	CLN5_I17_1885	133.27	-4.50	6.2454E-30
CLN8	CLN8_1	31.60	-4.71	3.06489E-10
CLN8	CLN8_2	31.60	-1.84	2.98805E-07
CRLS1	CRLS1_1	256.58	-0.36	0.662964159
CRLS1	CRLS1_2	256.58	-1.51	2.8811E-16
CTSB	CTSB_1	773.93	-6.02	5.8006E-119
CTSB	CTSB_2	773.93	-7.76	1.3054E-105
CTSD	CTSD_1	174.09	-4.33	1.05025E-16
CTSD	CTSD_2	174.09	-3.72	7.83791E-16
CTSL	CTSL_1	143.23	-1.87	2.85557E-25
CTSL	CTSL_2	143.23	-3.68	2.80884E-49
DCTN1	DCTN1_1	2599.92	-0.08	0.985987221
DCTN1	DCTN1_2	2599.92	-0.04	0.992017486
FUS	FUS_A3	2797.23	-0.91	2.88737E-17
FUS	FUS_C3	2797.23	-0.68	1.43111E-09
FYN	FYN_1	900.73	-0.24	0.988225715
FYN	FYN_2	900.73	-0.10	0.910457315
GALC	GALC_1	253.68	-2.49	1.57334E-47
GALC	GALC_2	253.68	-6.20	1.99581E-26
GBA	GBA_1	258.55	-0.54	0.032782335
GBA	GBA_2	258.55	-0.59	0.010608809
GCH1	GCH1_1	42.04	-3.73	6.22362E-20
GCH1	GCH1_2	42.04	-1.95	3.37905E-13
GRN	GRN_F3	292.26	-6.49	2.86479E-75
GUSB	GUSB_1	61.97	-4.16	3.61932E-17
GUSB	GUSB_2	61.97	-3.38	1.53457E-19
HNRNPA2B1	HNRNPA2B1_B4	3938.56	-1.14	3.53491E-27
KIF5A	KIF5A_1	2124.93	-6.12	0
LRRK2	LRRK2_2	28.47	-0.33	0.860562304

Table A.6 continued from previous page

Gene	sgRNA	Mean Counts	log2FoldChange	padj
MAPT	MAPT_G4	1813.89	-5.47	2.35952E-88
MCCC1	MCCC1_1	130.28	-3.80	3.2176E-42
MCCC1	MCCC1_2	130.28	-2.94	1.69803E-35
NAGLU	NAGLU_1	23.21	-3.49	4.50807E-08
NAGLU	NAGLU_2	23.21	0.18	0.969175441
NBR1	NBR1_1	489.13	-3.68	2.7608E-110
NBR1	NBR1_2	489.13	-4.38	6.0126E-161
NEU1	NEU1_1	196.82	-1.80	2.18745E-29
NEU1	NEU1_2	196.82	-2.69	4.42851E-62
OPTN	OPTN_D5	383.80	-4.11	4.78385E-89
OXR1	OXR1_1	732.29	-0.09	0.969354305
OXR1	OXR1_2	732.29	0.09	0.921931447
PARK2	PARK2_1	21.37	-3.19	6.20776E-13
PARK2	PARK2_2	21.37	-5.92	3.33935E-07
PARK7	PARK7_1	1558.12	-0.85	0.001001063
PARK7	PARK7_2	1558.12	-3.06	6.39927E-51
PFN1	PFN1_1	2540.02	-1.96	9.98659E-09
PFN1	PFN1_2	2540.02	-1.86	4.37408E-10
PINK1	PINK1_1	343.23	-2.78	3.23063E-19
PINK1	PINK1_2	343.23	-4.47	1.22236E-38
PSAP	PSAP_E5	3539.88	-1.70	2.29695E-06
SCARB2	SCARB2_1	1941.84	-2.46	4.31828E-54
SCARB2	SCARB2_2	1941.84	-4.49	4.6959E-153
SETX	SETX_A6	274.35	-2.38	4.86701E-48
SNCA	SNCA_1	1303.24	-2.62	1.95798E-54
SNCA	SNCA_2	1303.24	-2.71	3.50955E-58
SOD1	SOD1_1	828.09	-3.54	1.84716E-50
SOD1	SOD1_2	828.09	-2.82	1.94997E-30
SQSTM1	SQSTM1_C6	635.05	-0.52	0.002244608
STX17	STX17_1	129.06	-0.82	0.000425103
STX17	STX17_2	129.06	-5.34	1.38177E-41
TARDBP	TARDBP_E6	1607.05	-0.97	1.31475E-17
TAX1BP1	TAX1BP1_1	479.37	-5.21	1.16008E-94
TAX1BP1	TAX1BP1_2	479.37	-4.72	4.0535E-135
TBK1	TBK1_A7	133.58	-2.96	1.00053E-50
TMEM106B	TMEM106B_E7	248.10	-3.94	9.2672E-107
TMEM175	TMEM175_1	283.16	-4.53	8.2839E-102
TMEM175	TMEM175_2	283.16	-0.01	0.990560539
VAPB	VAPB_1	514.36	-3.43	7.5369E-124
VAPB	VAPB_2	514.36	-3.34	5.7251E-117
VCP	VCP_G8	2044.81	-2.43	1.05486E-47
VCP	VCP_m_1	2044.81	-0.31	0.996105053
VCP	VCP_m_4	2044.81	-0.41	0.651691289
VPS13C	VPS13C_1	392.11	-3.81	4.03825E-76
VPS13C	VPS13C_2	392.11	-0.66	0.005894339
VPS35	VPS35_1	957.08	-3.05	1.0409E-184
VPS35	VPS35_2	957.08	-3.73	1.1218E-249

B

Appendix for Chapter 5 Primary and Secondary Analysis Maps

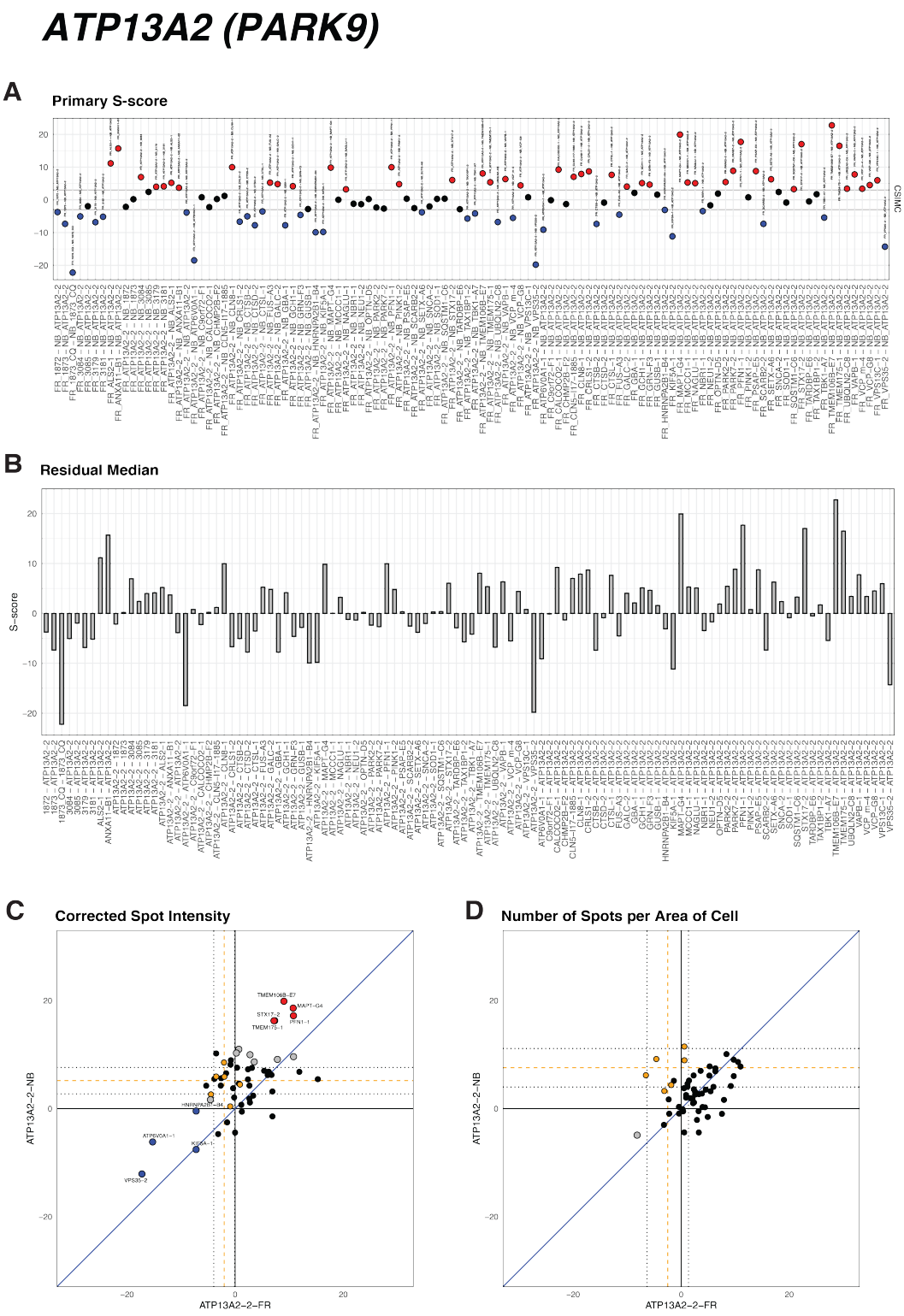


Figure B.1: *ATP13A2*: Primary and Secondary Analysis Genetic Interaction Maps.

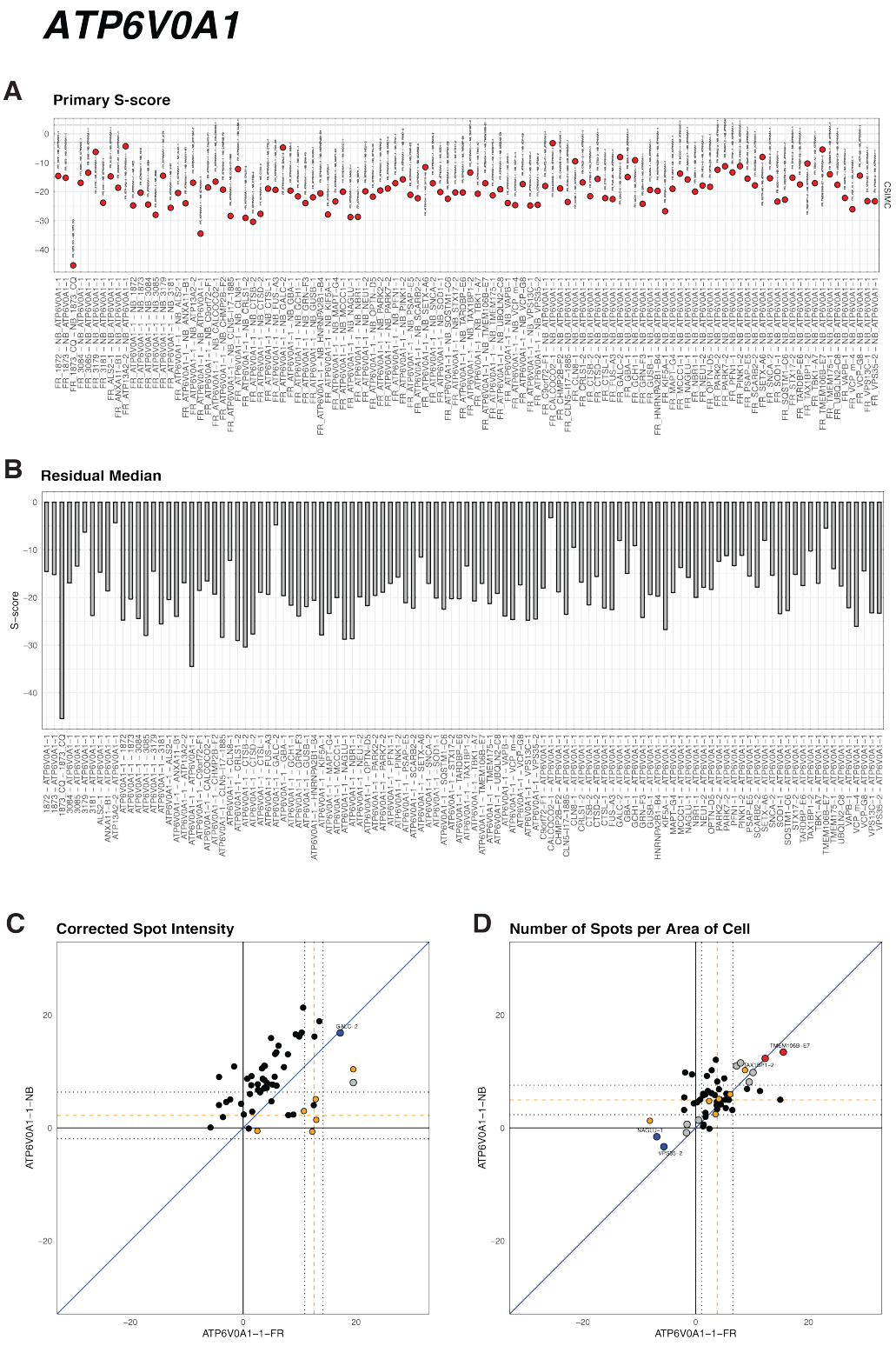


Figure B.2: *ATP6V0A1*: Primary and Secondary Analysis Genetic Interaction Maps.

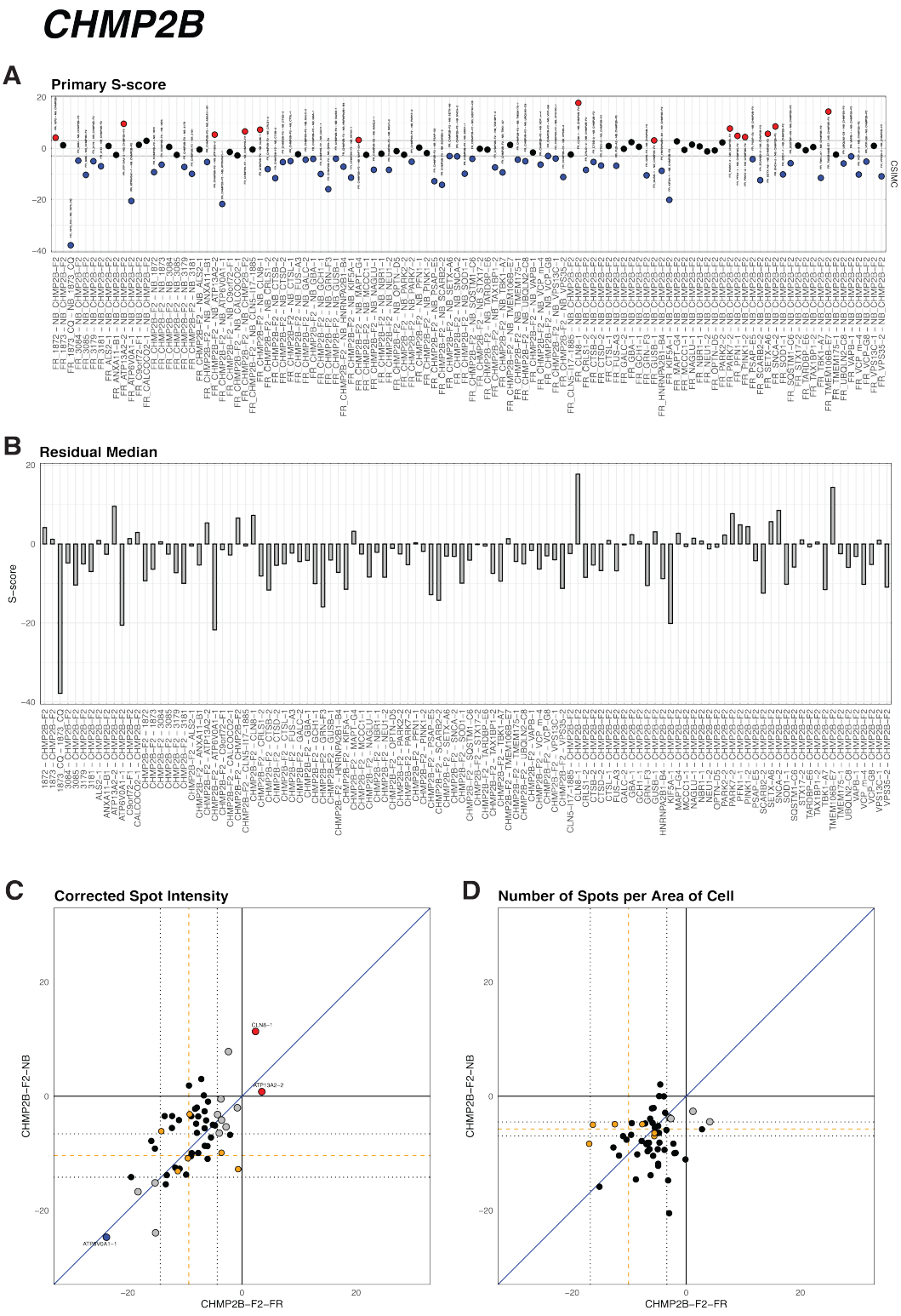


Figure B.3: *CHMP2B*: Primary and Secondary Analysis Genetic Interaction Maps.

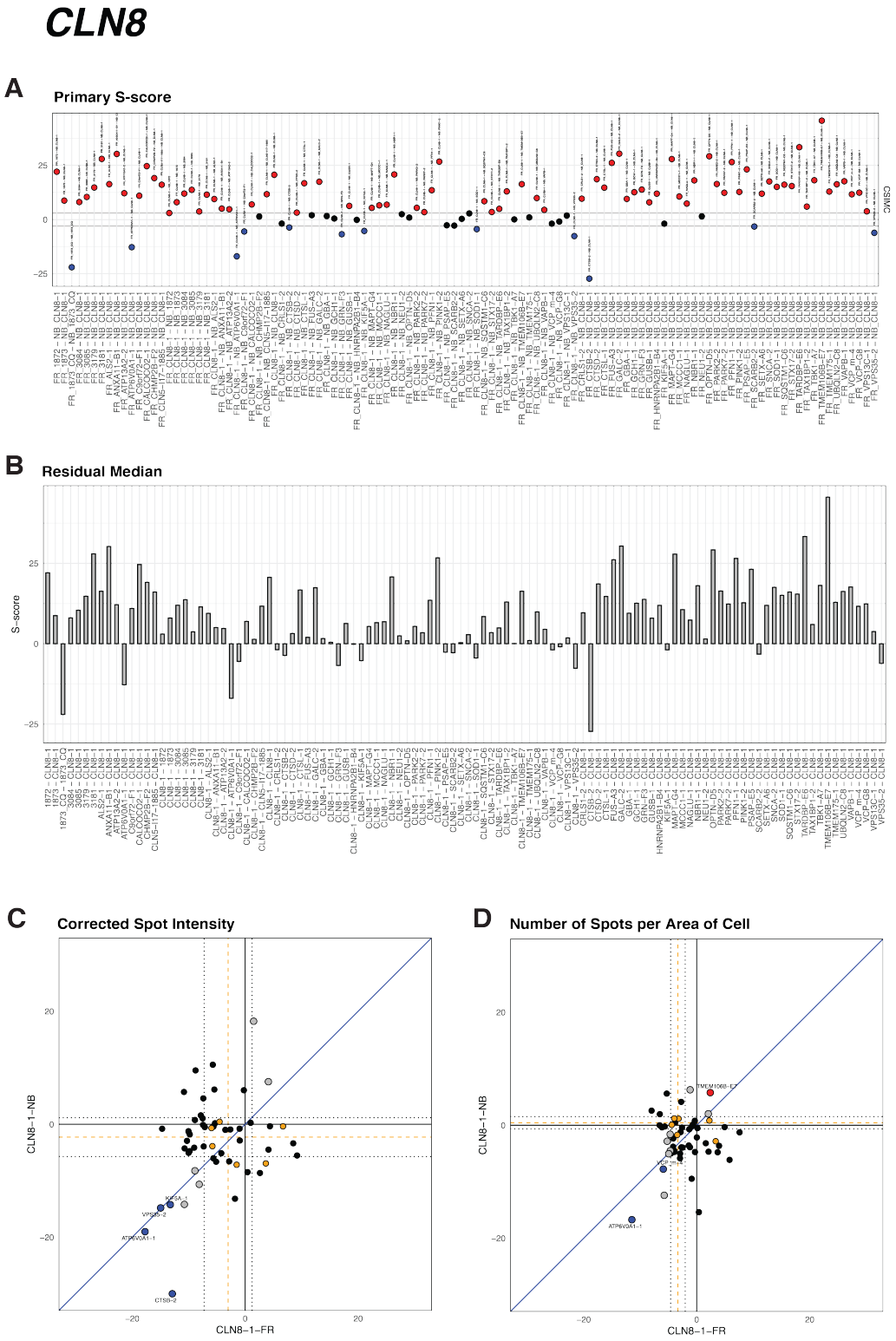


Figure B.4: *CLN8*: Primary and Secondary Analysis Genetic Interaction Maps.

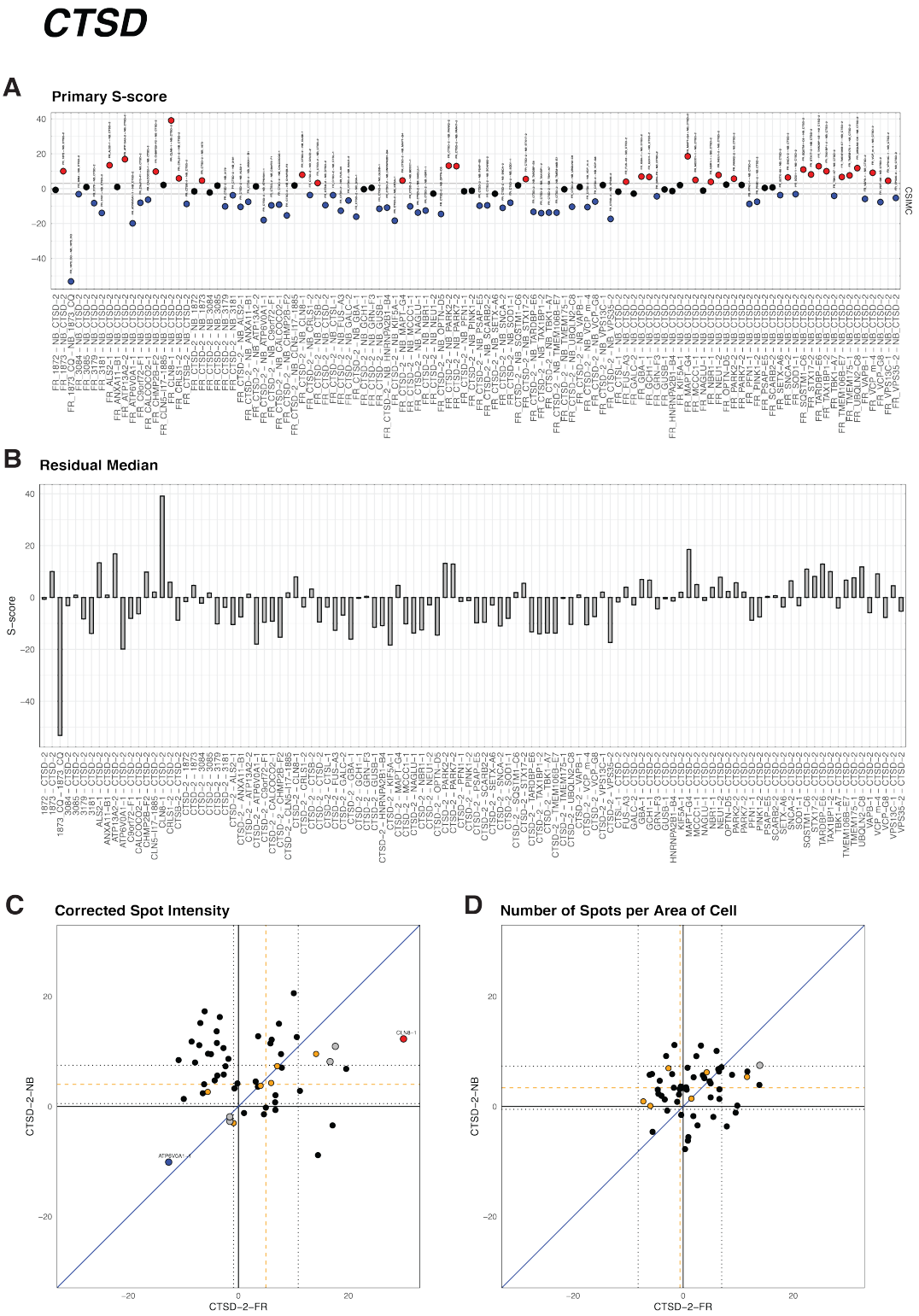


Figure B.5: *CTSD*: Primary and Secondary Analysis Genetic Interaction Maps.

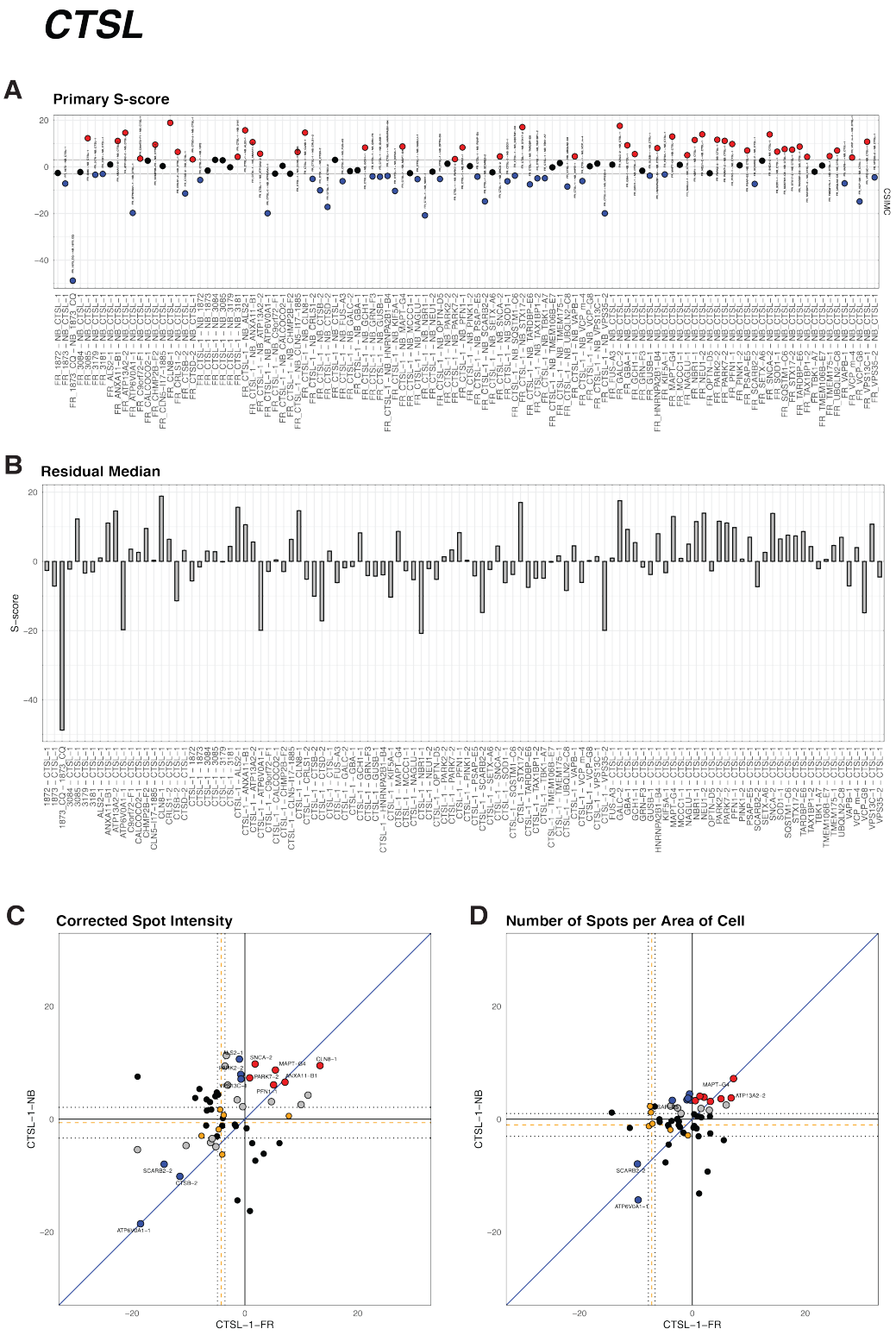


Figure B.6: *CTSL*: Primary and Secondary Analysis Genetic Interaction Maps.

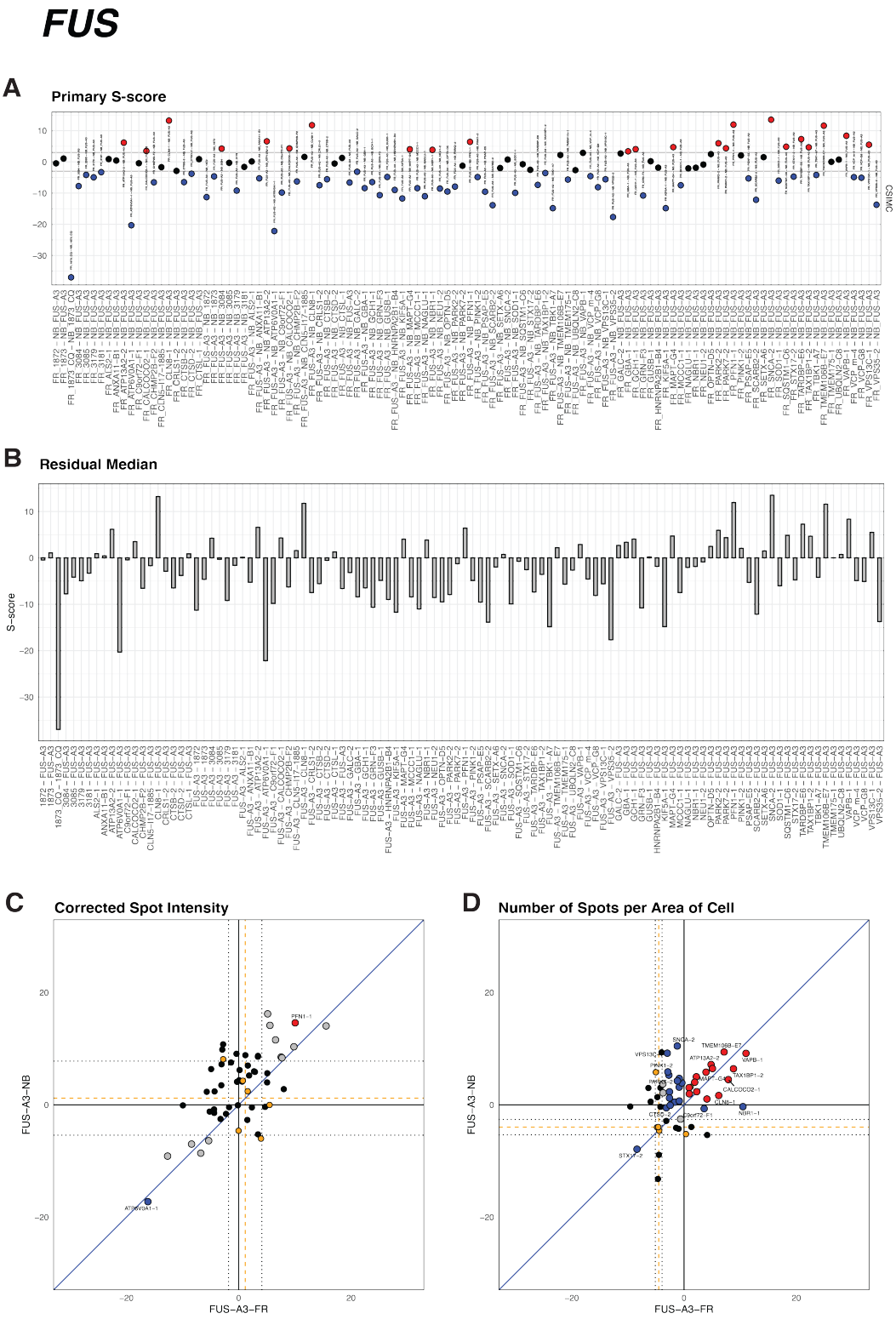


Figure B.7: *FUS*: Primary and Secondary Analysis Genetic Interaction Maps.

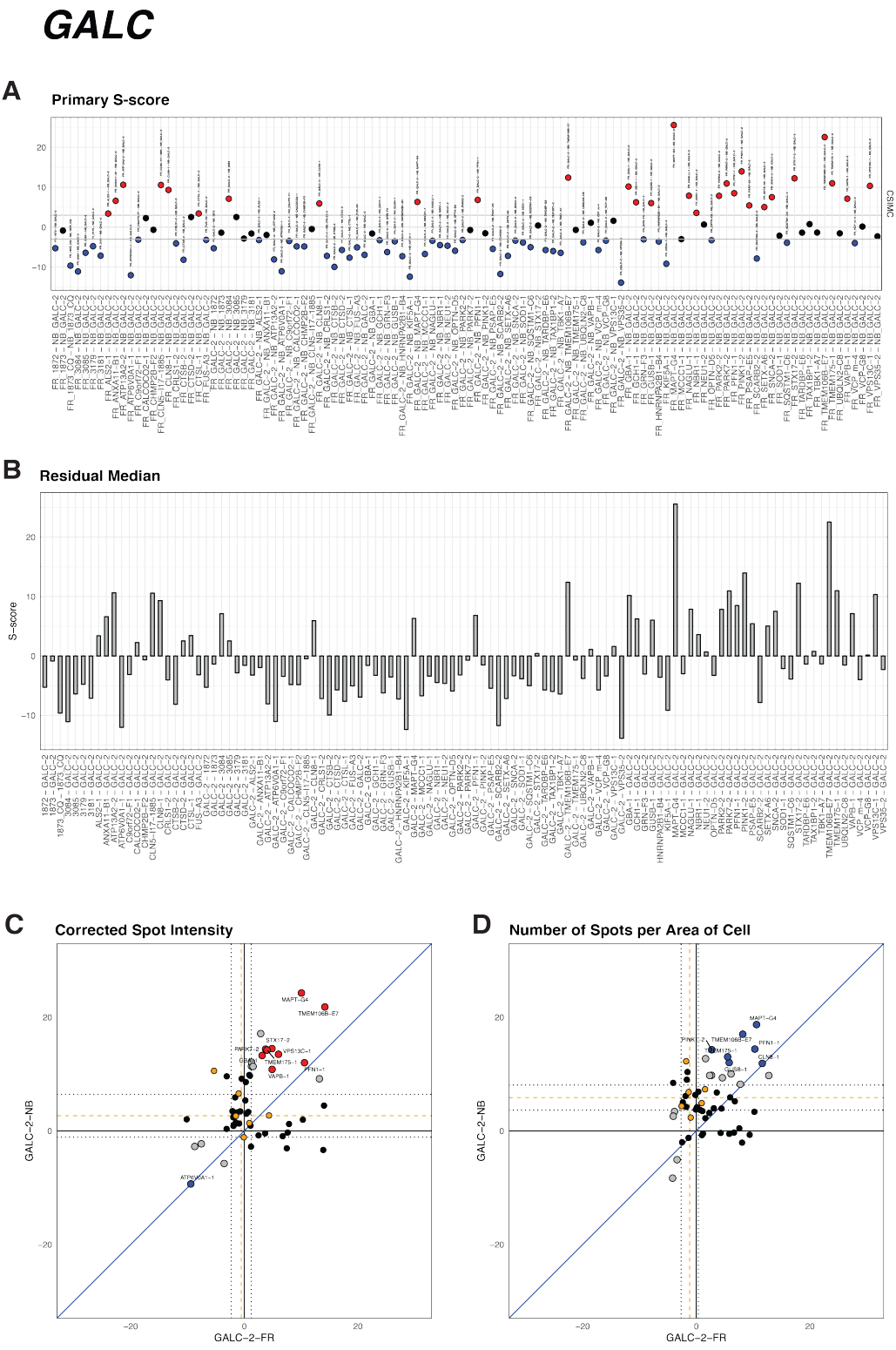


Figure B.8: *GALC*: Primary and Secondary Analysis Genetic Interaction Maps.

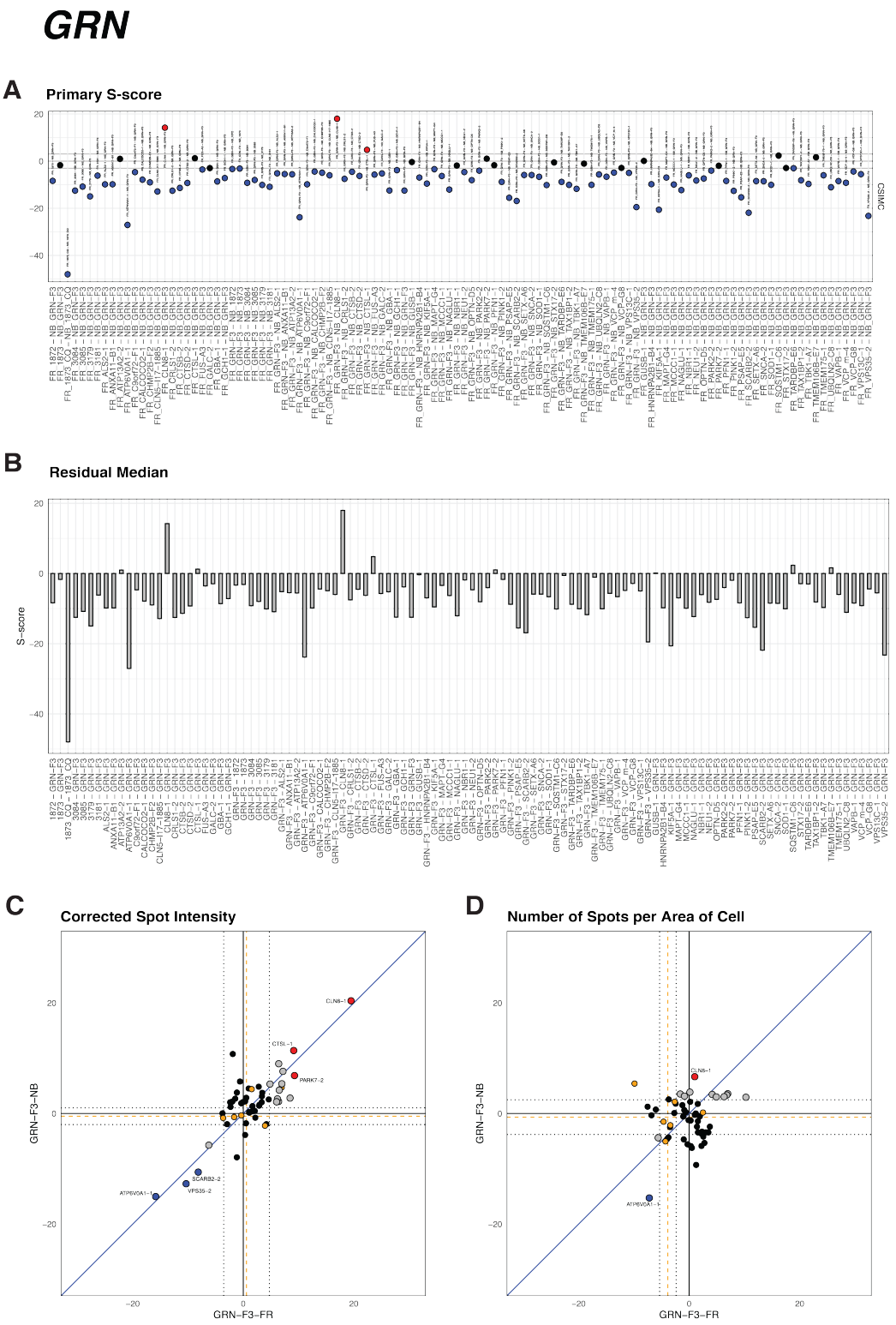


Figure B.9: *GRN*: Primary and Secondary Analysis Genetic Interaction Maps.

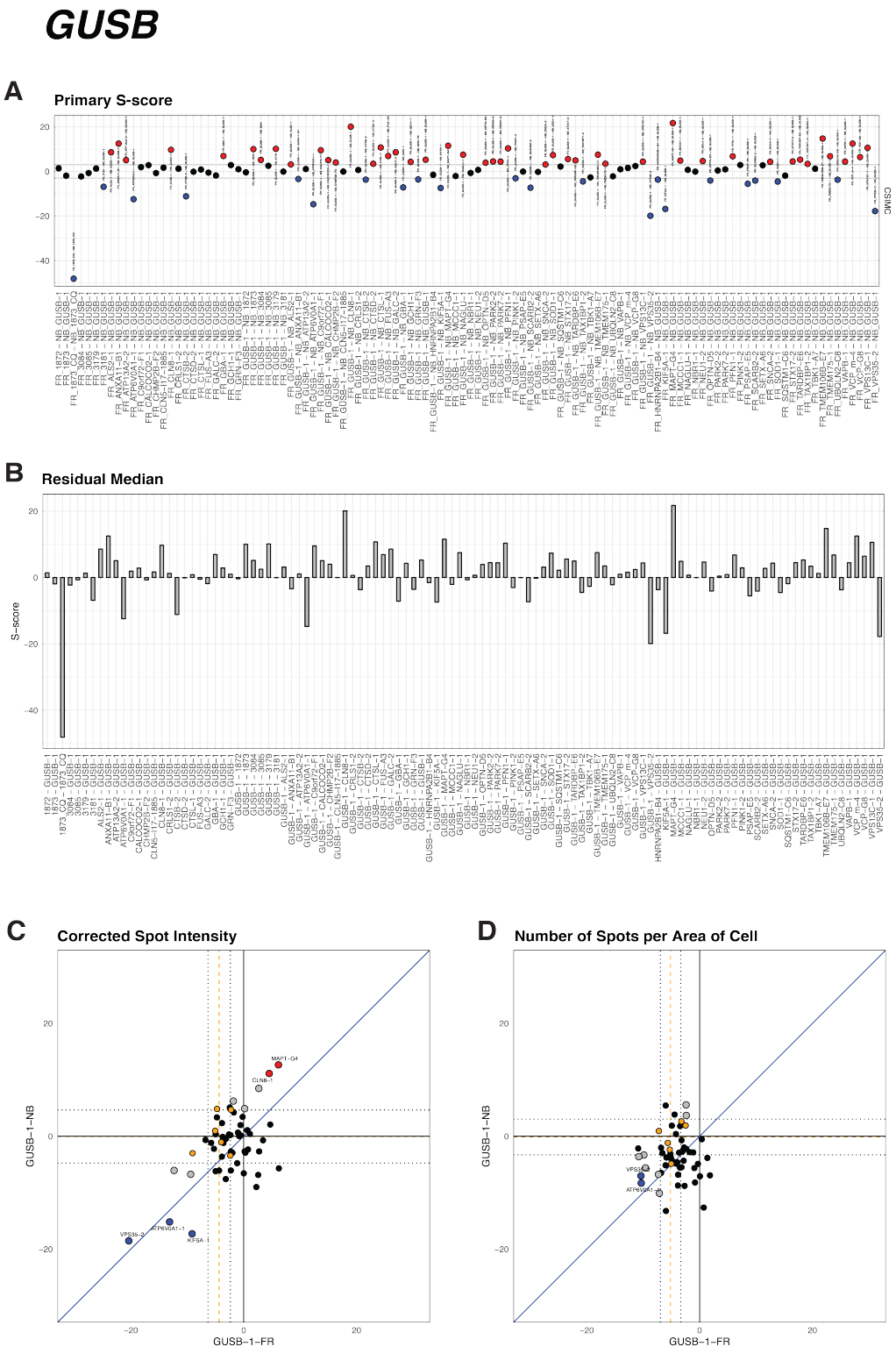


Figure B.10: *GUSB*: Primary and Secondary Analysis Genetic Interaction Maps.

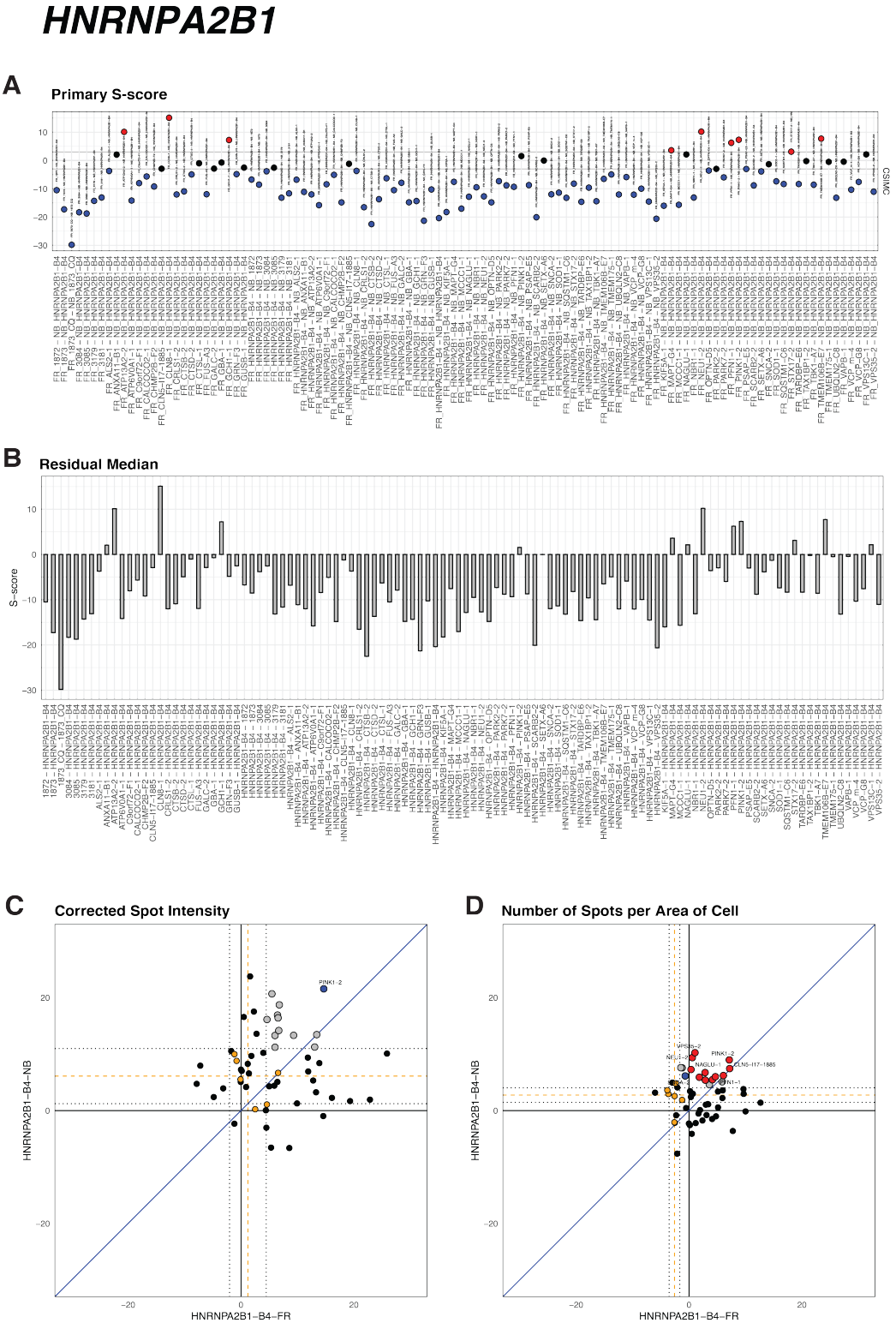


Figure B.11: *HNRNPA2B1*: Primary and Secondary Analysis Genetic Interaction Maps.

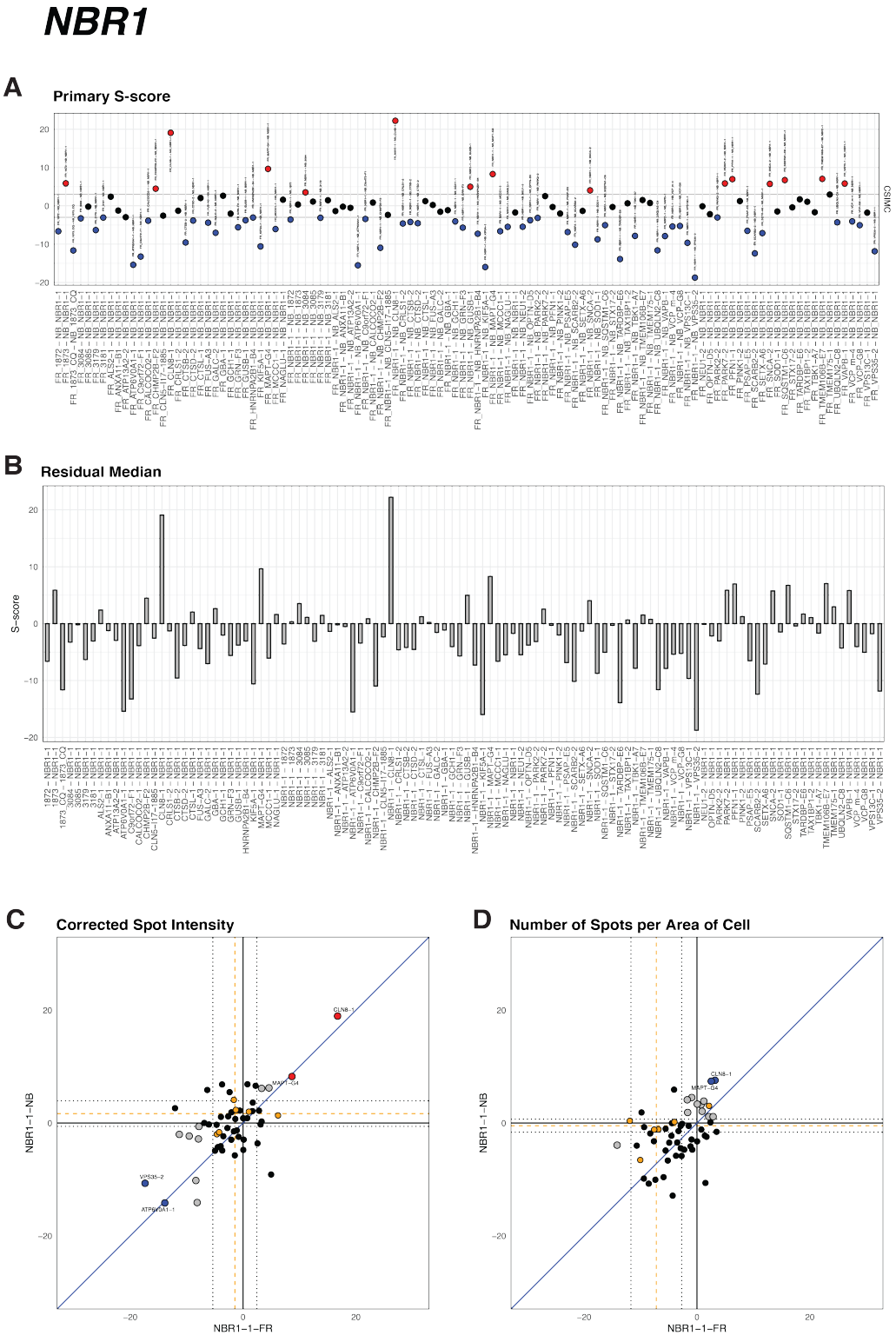


Figure B.12: *NBR1*: Primary and Secondary Analysis Genetic Interaction Maps.

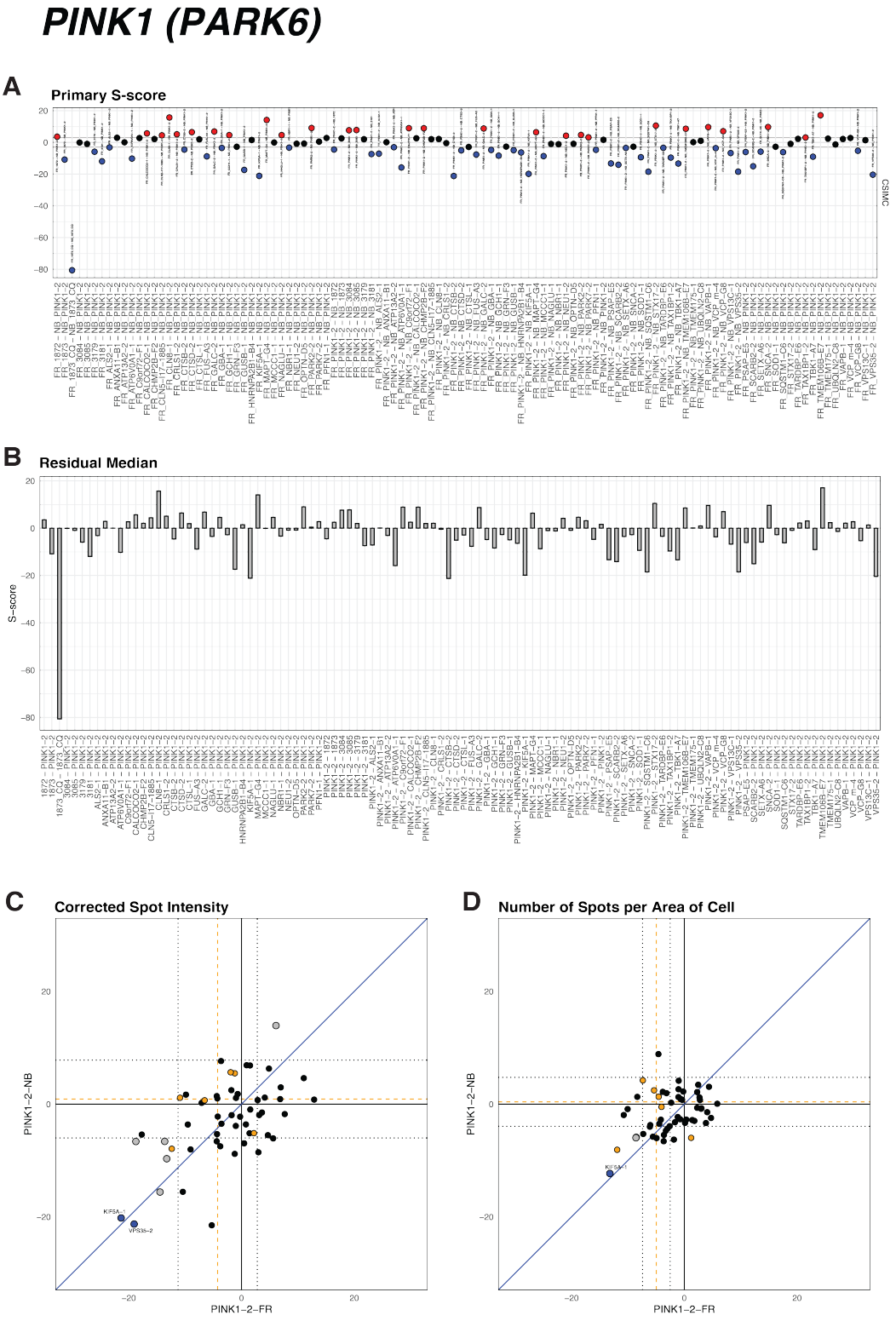


Figure B.13: *PINK1 (PARK6)*: Primary and Secondary Analysis Genetic Interaction Maps.

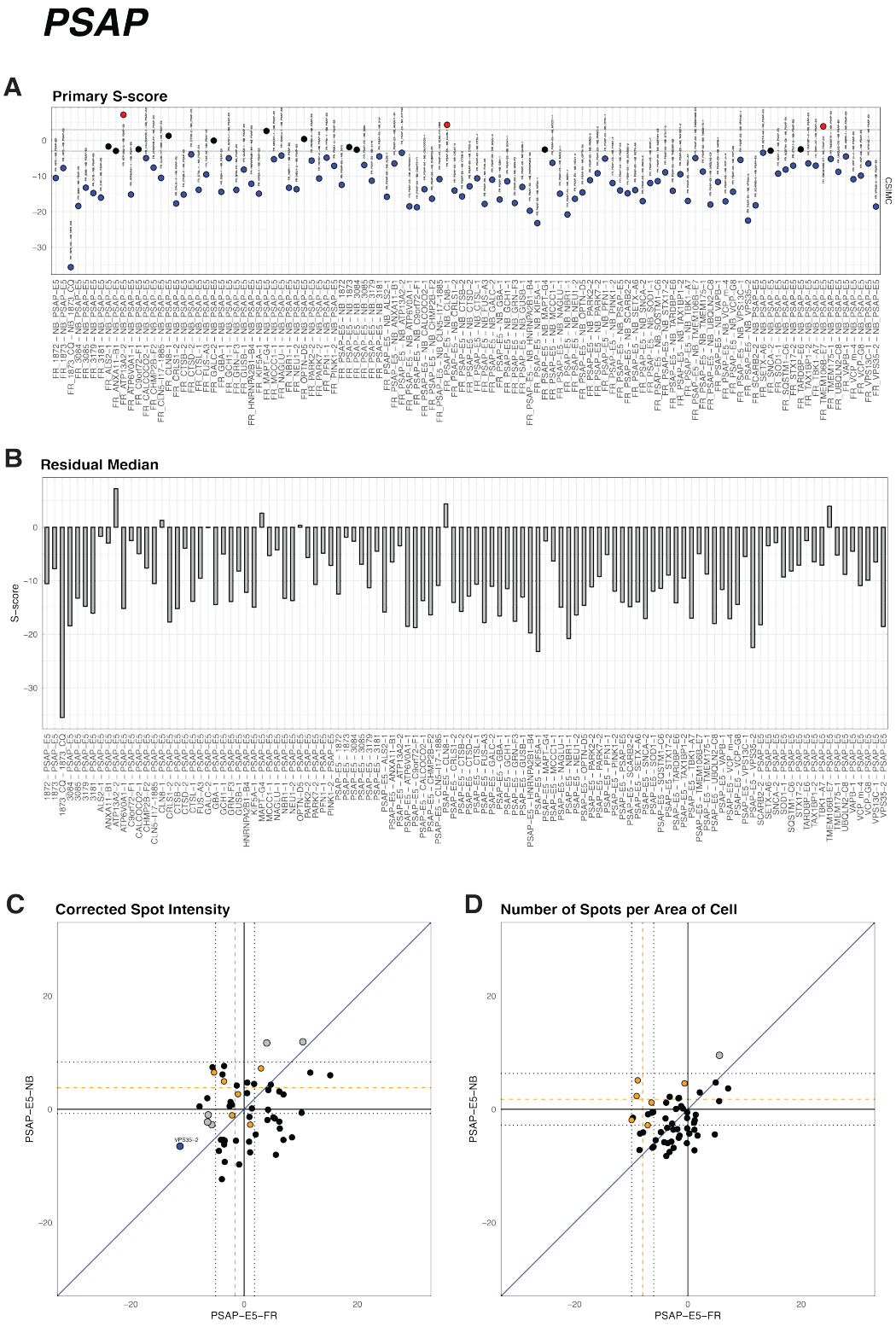


Figure B.14: *PSAP*: Primary and Secondary Analysis Genetic Interaction Maps.

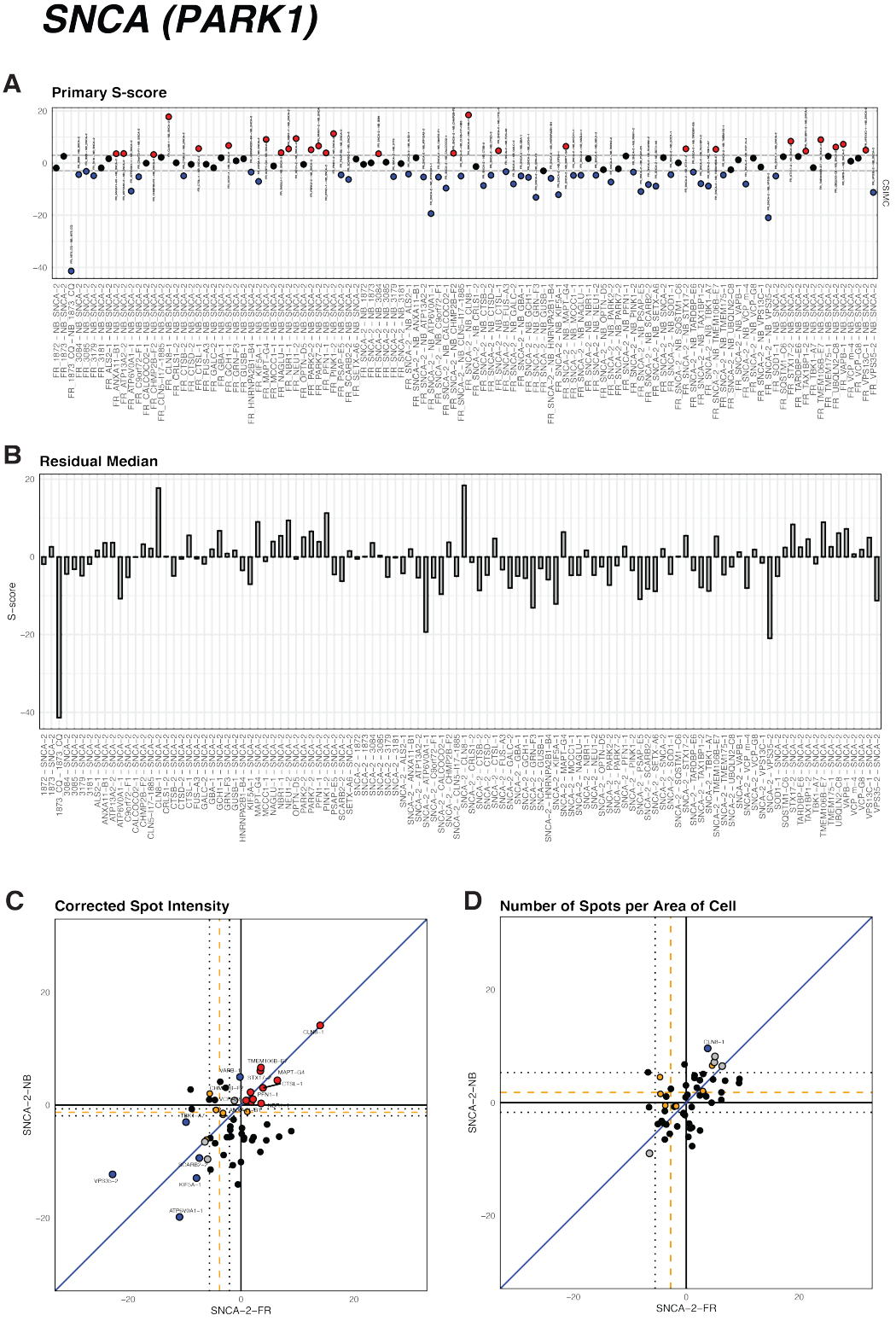


Figure B.15: *SNCA (PARK1)*: Primary and Secondary Analysis Genetic Interaction Maps.

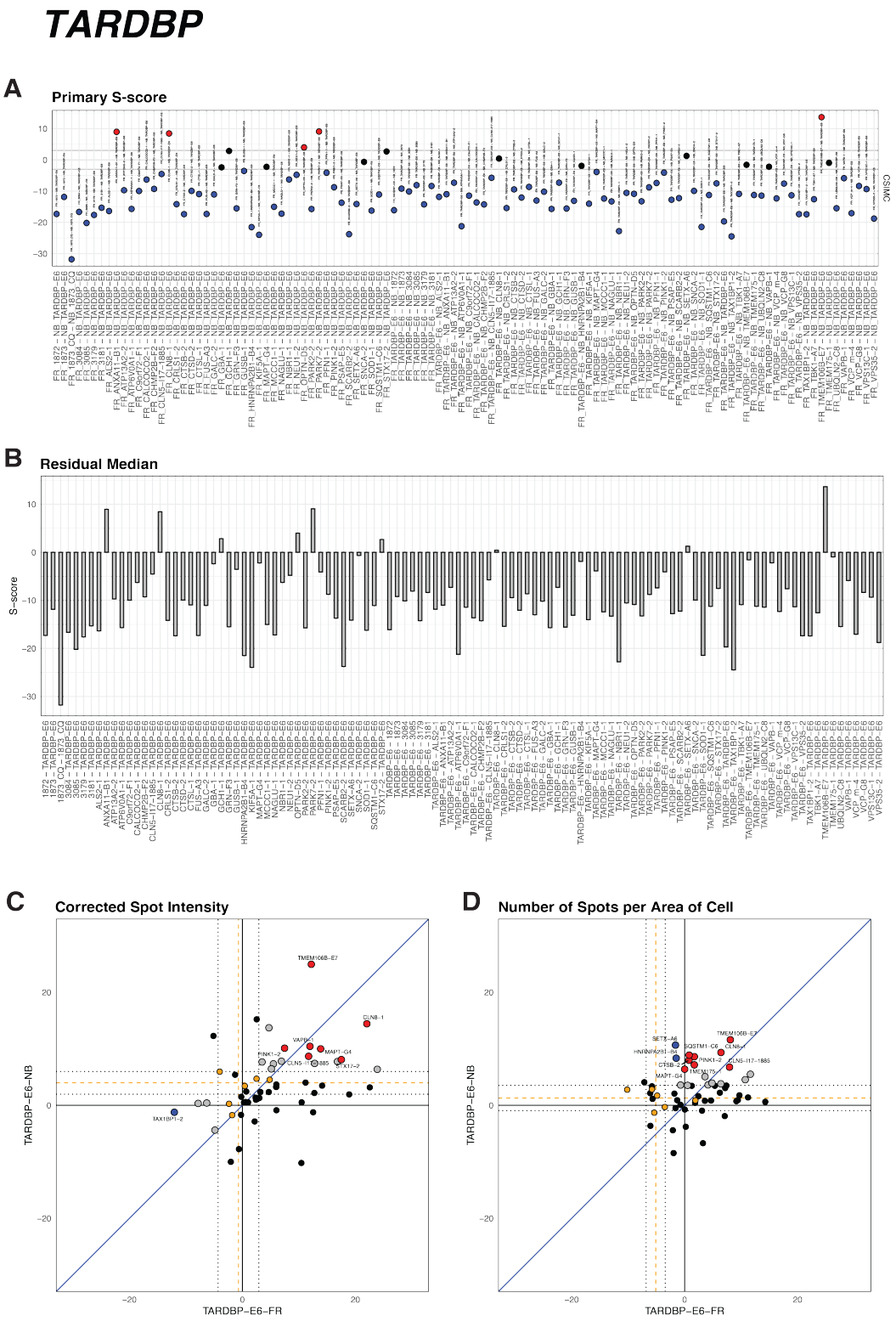


Figure B.16: *TARDBP*: Primary and Secondary Analysis Genetic Interaction Maps.

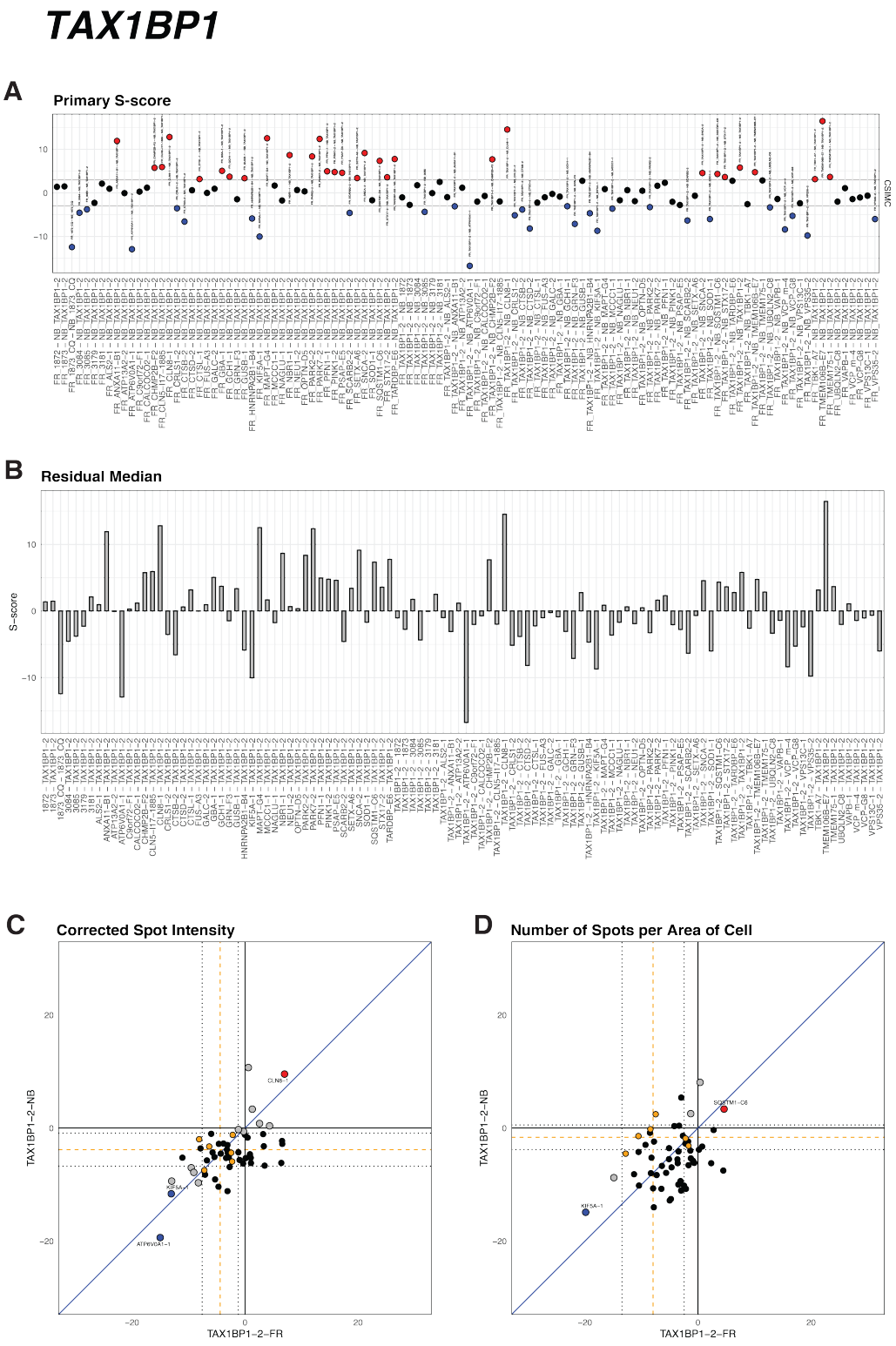


Figure B.17: *TAX1BP1*: Primary and Secondary Analysis Genetic Interaction Maps.

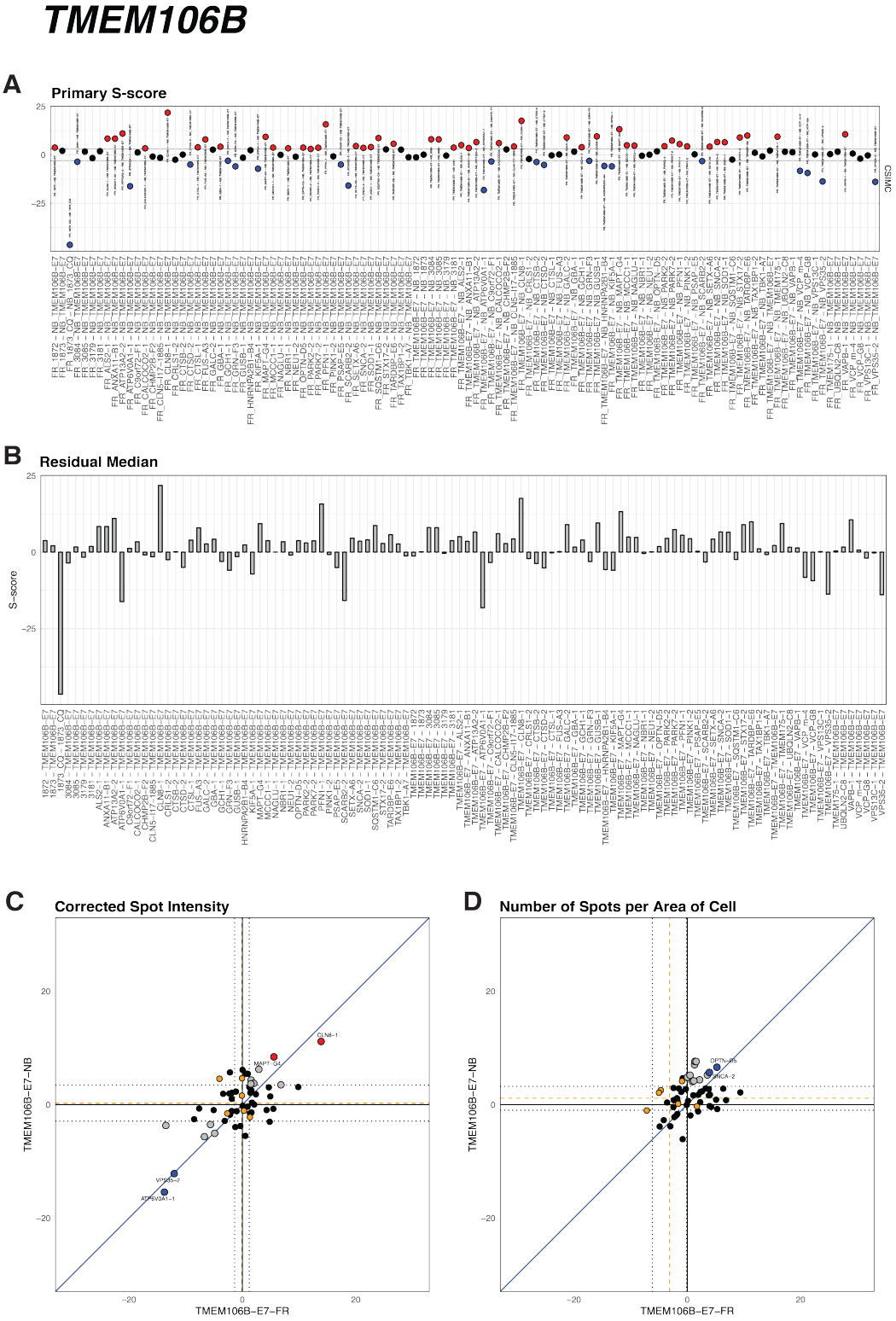


Figure B.18: *TMEM106B*: Primary and Secondary Analysis Genetic Interaction Maps.

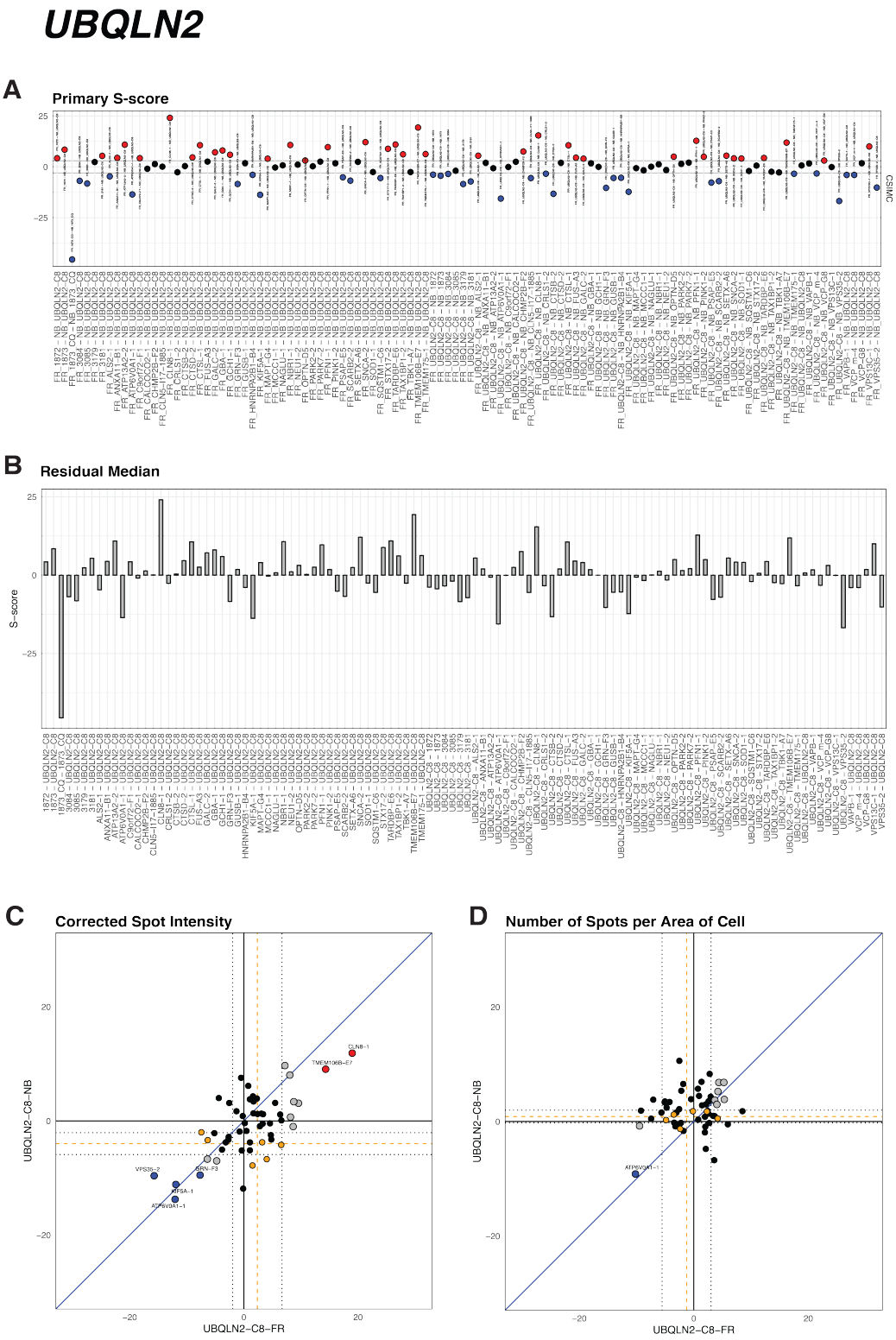


Figure B.19: *UBQLN2*: Primary and Secondary Analysis Genetic Interaction Maps.

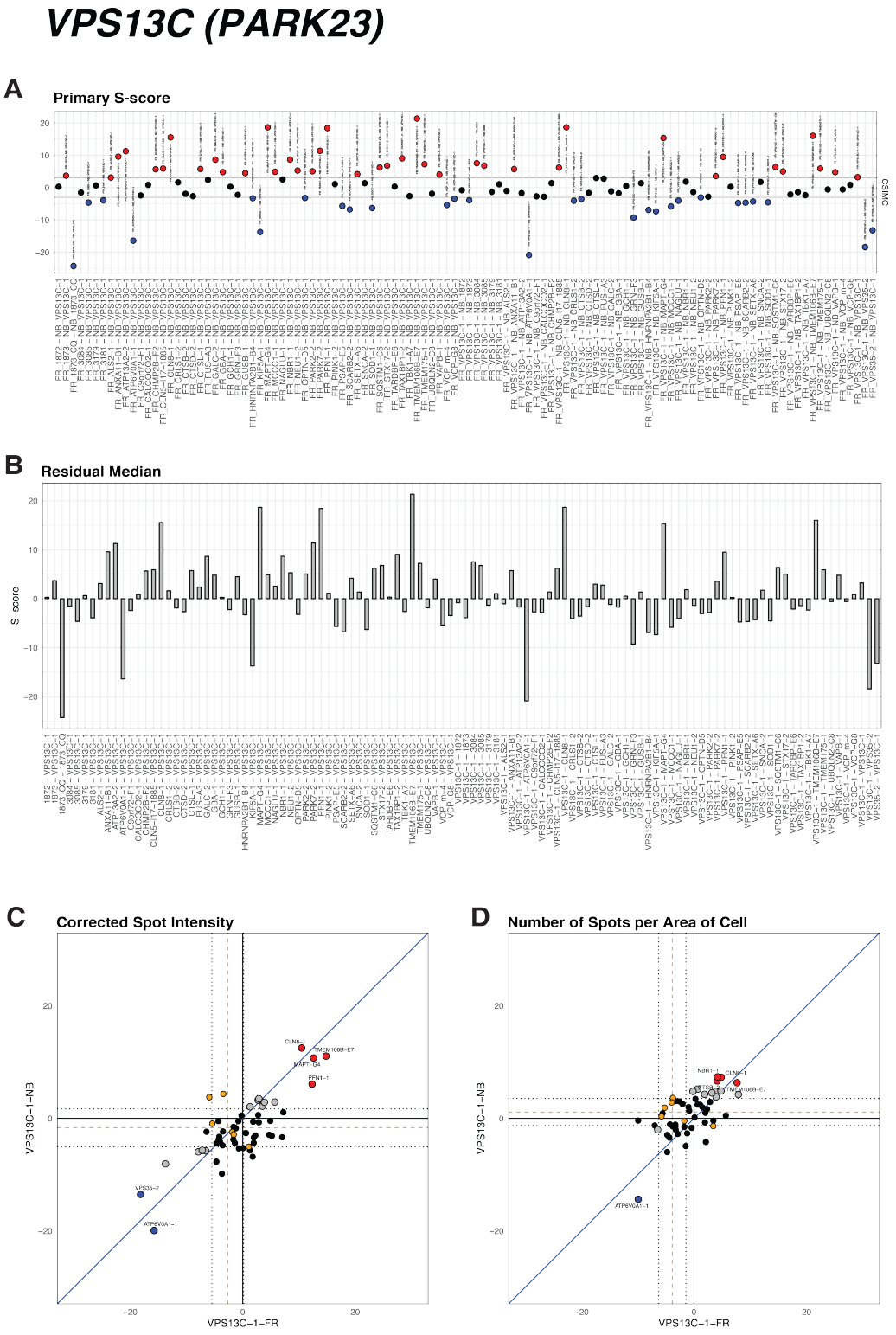


Figure B.20: *VPS13C (PARK23)*: Primary and Secondary Analysis Genetic Interaction Maps.

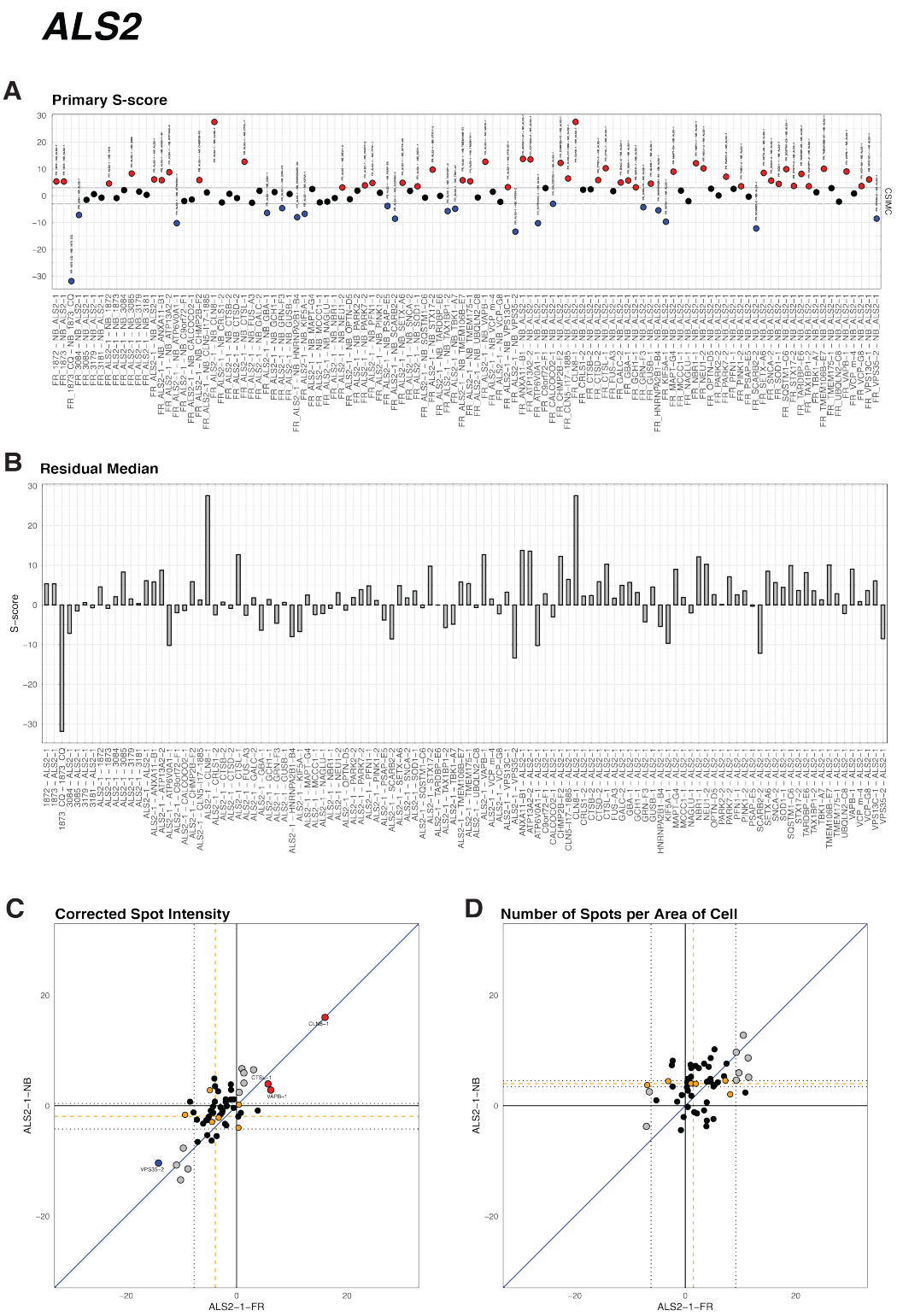


Figure B.21: *ALS2*: Primary and Secondary Analysis Genetic Interaction Maps.

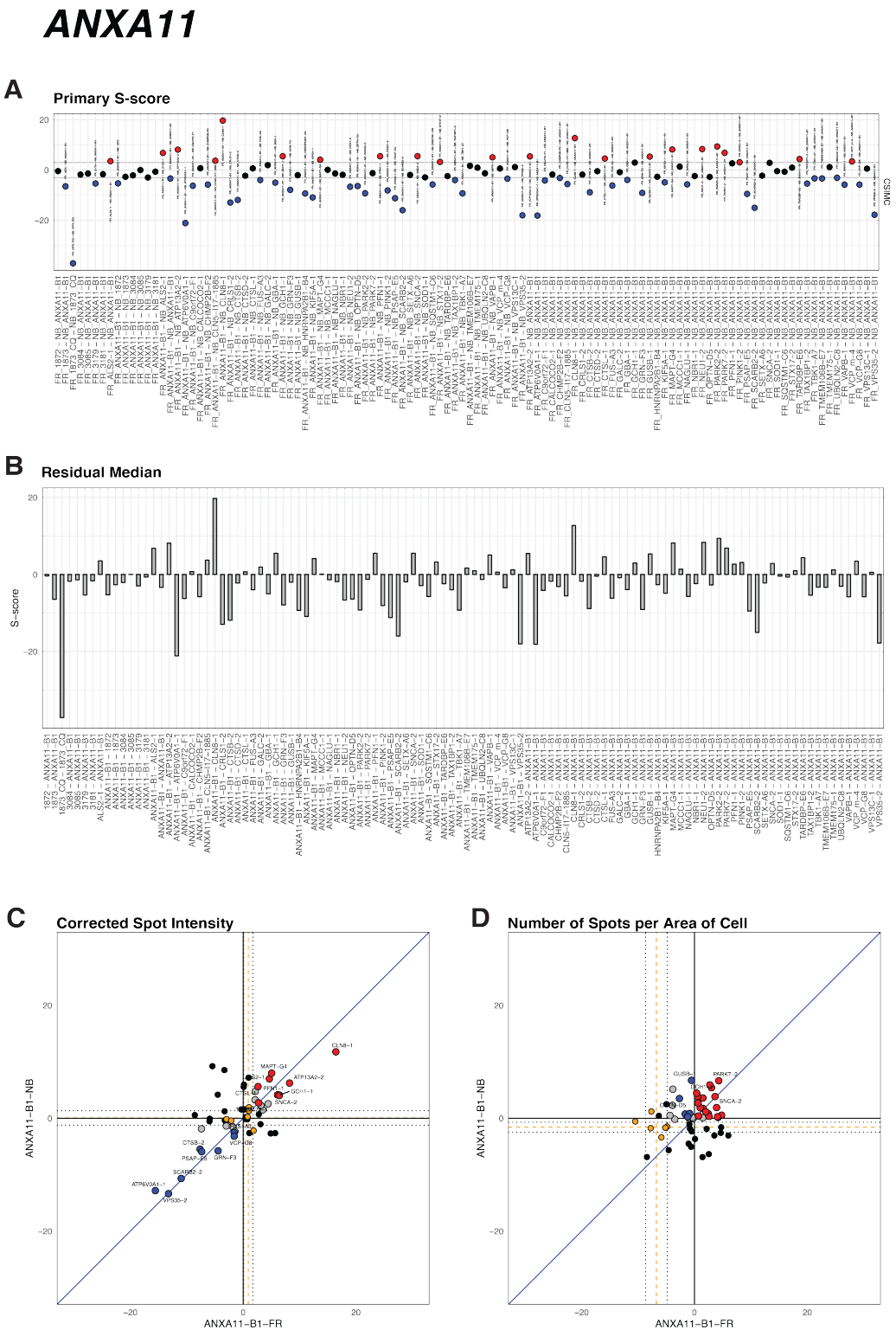


Figure B.22: *ANXA11*: Primary and Secondary Analysis Genetic Interaction Maps.

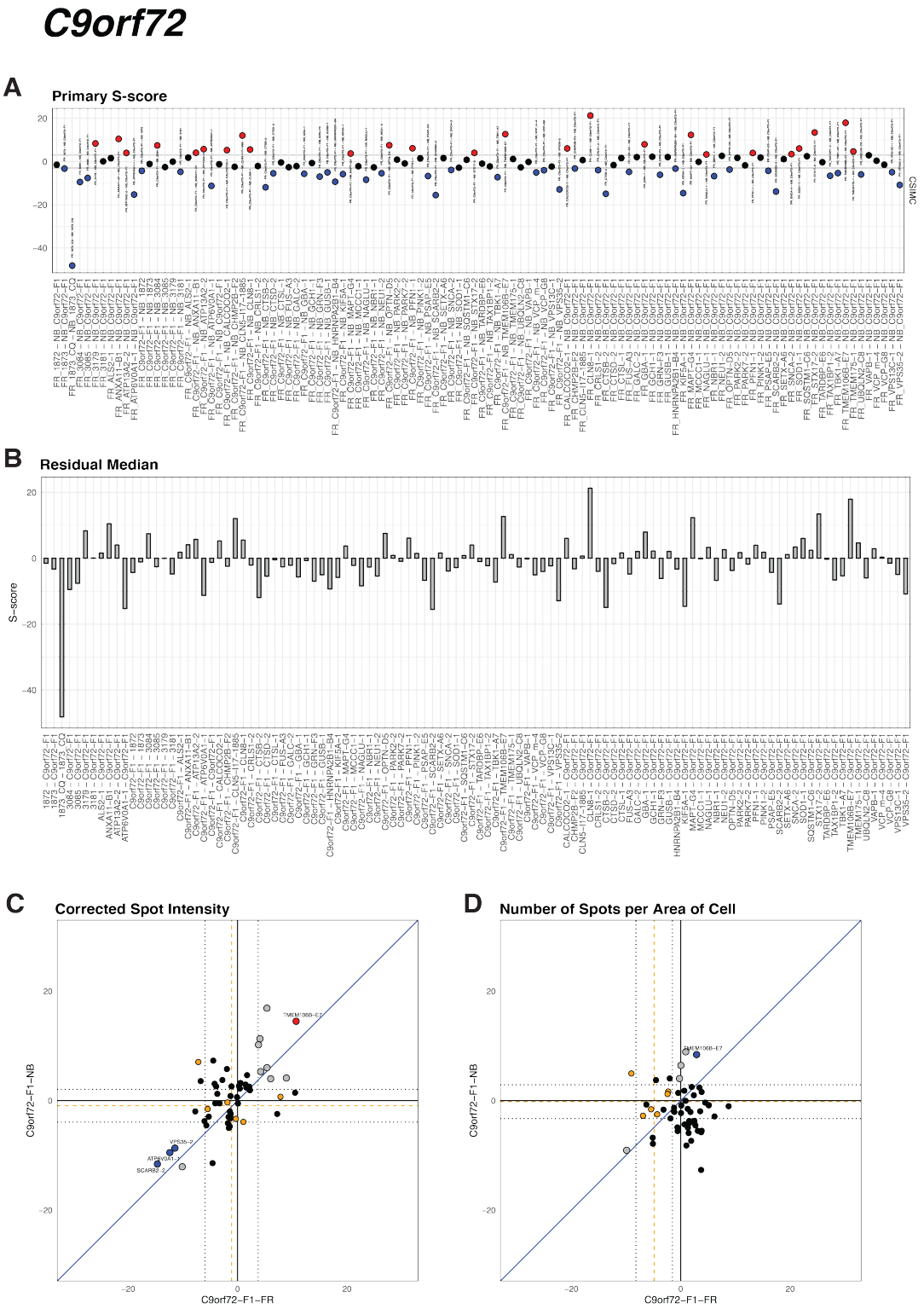


Figure B.23: *C9orf72*: Primary and Secondary Analysis Genetic Interaction Maps.

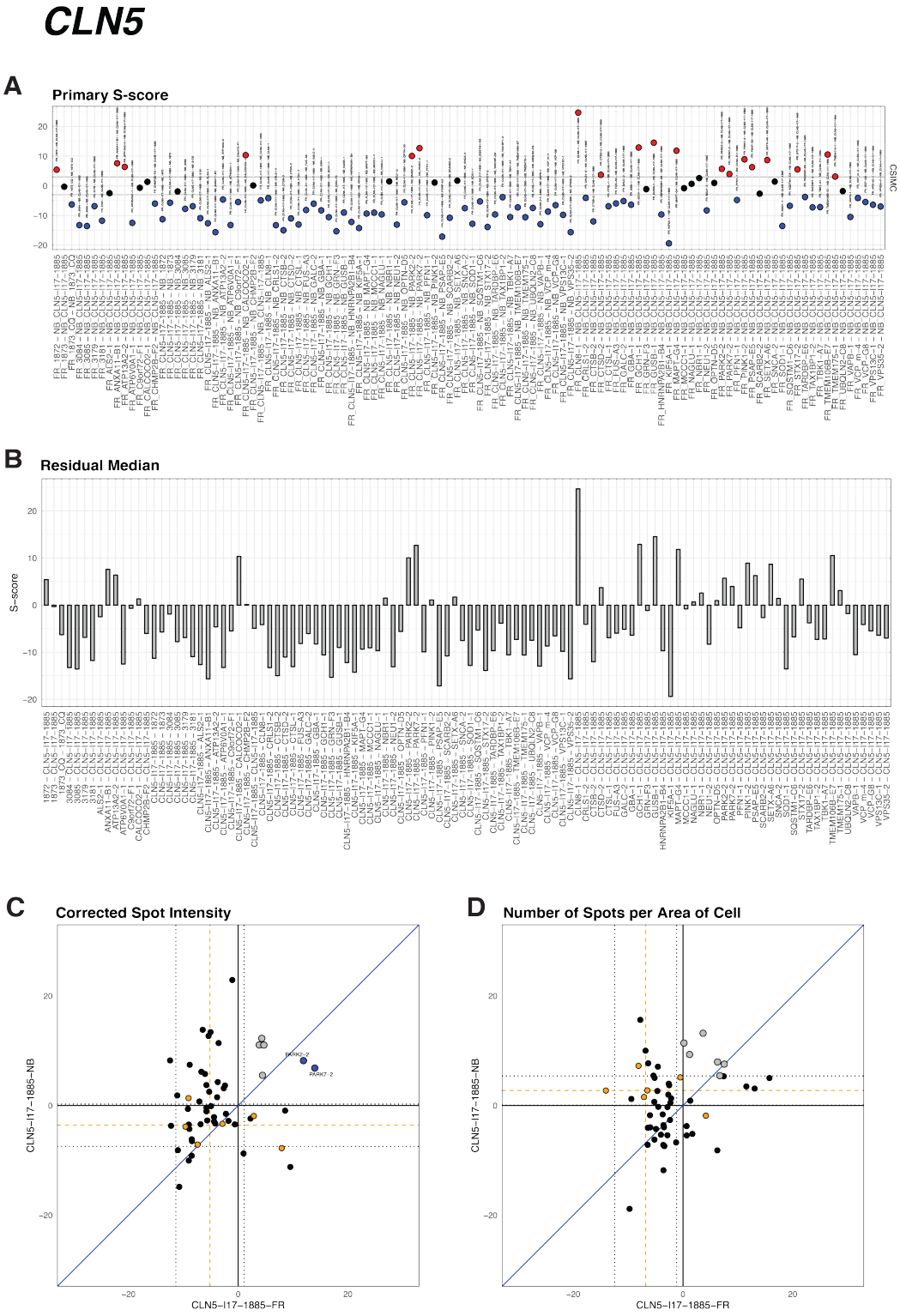


Figure B.24: *CLN5*: Primary and Secondary Analysis Genetic Interaction Maps.

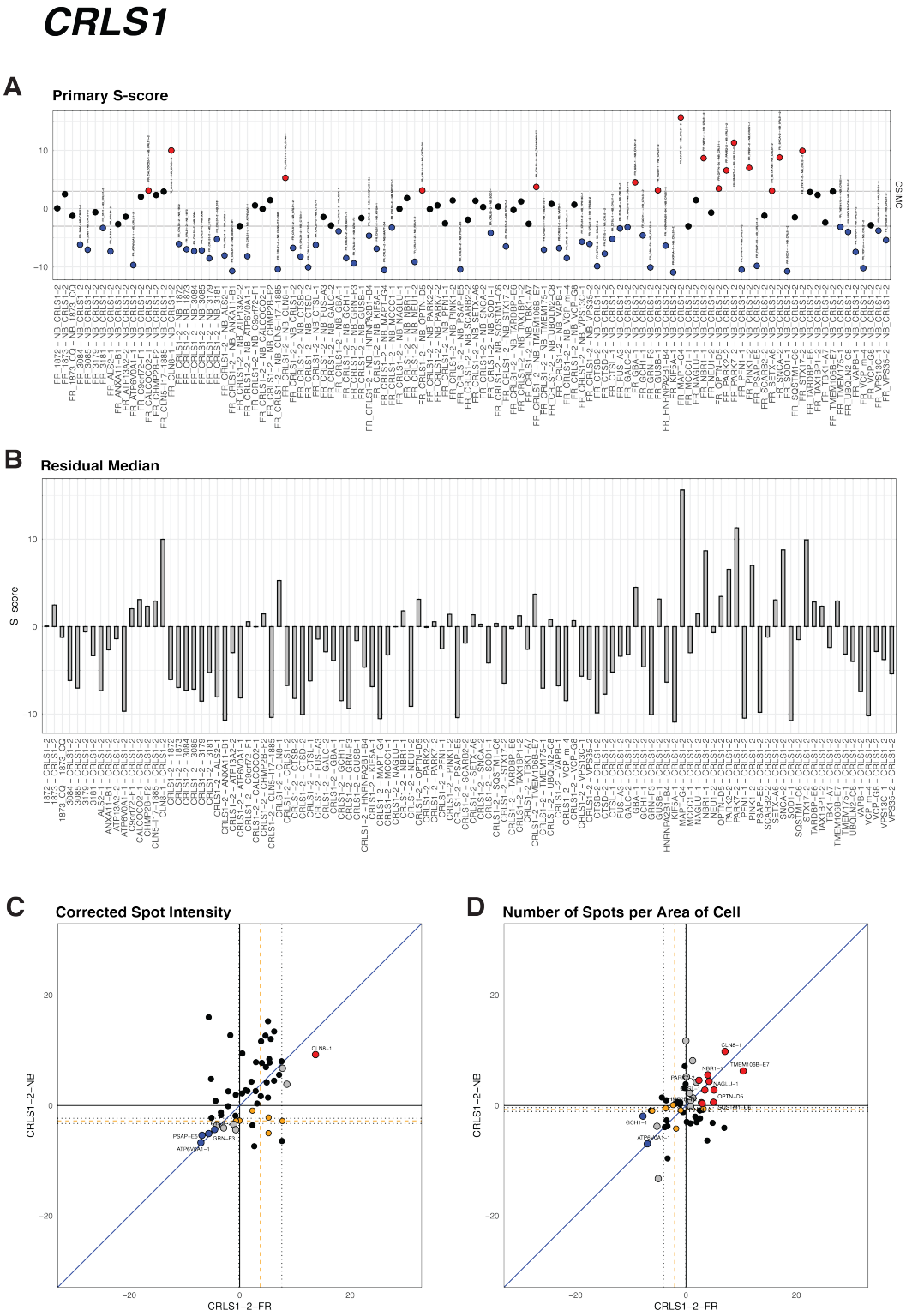


Figure B.25: *CRLS1*: Primary and Secondary Analysis Genetic Interaction Maps.

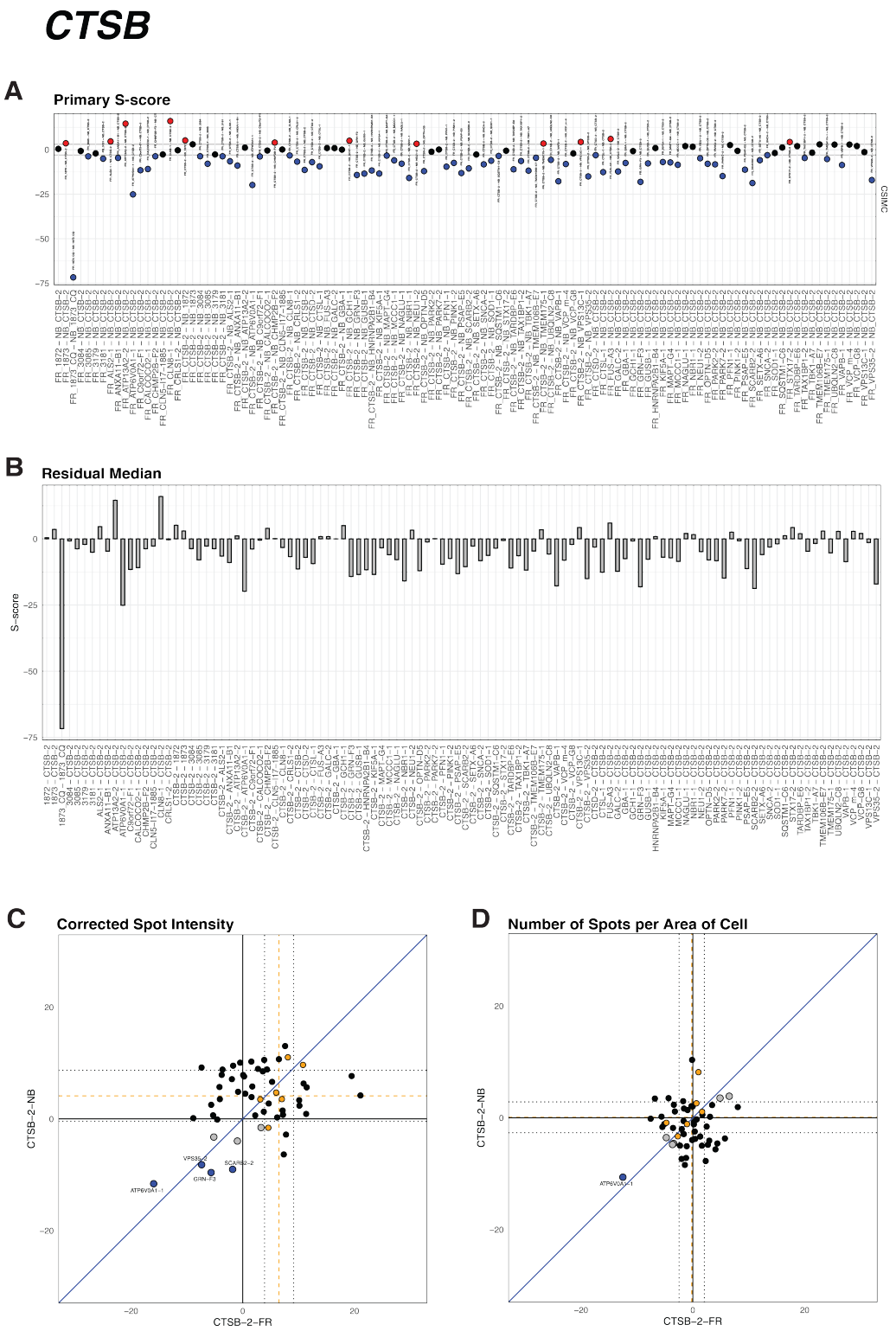


Figure B.26: *CTSB*: Primary and Secondary Analysis Genetic Interaction Maps.

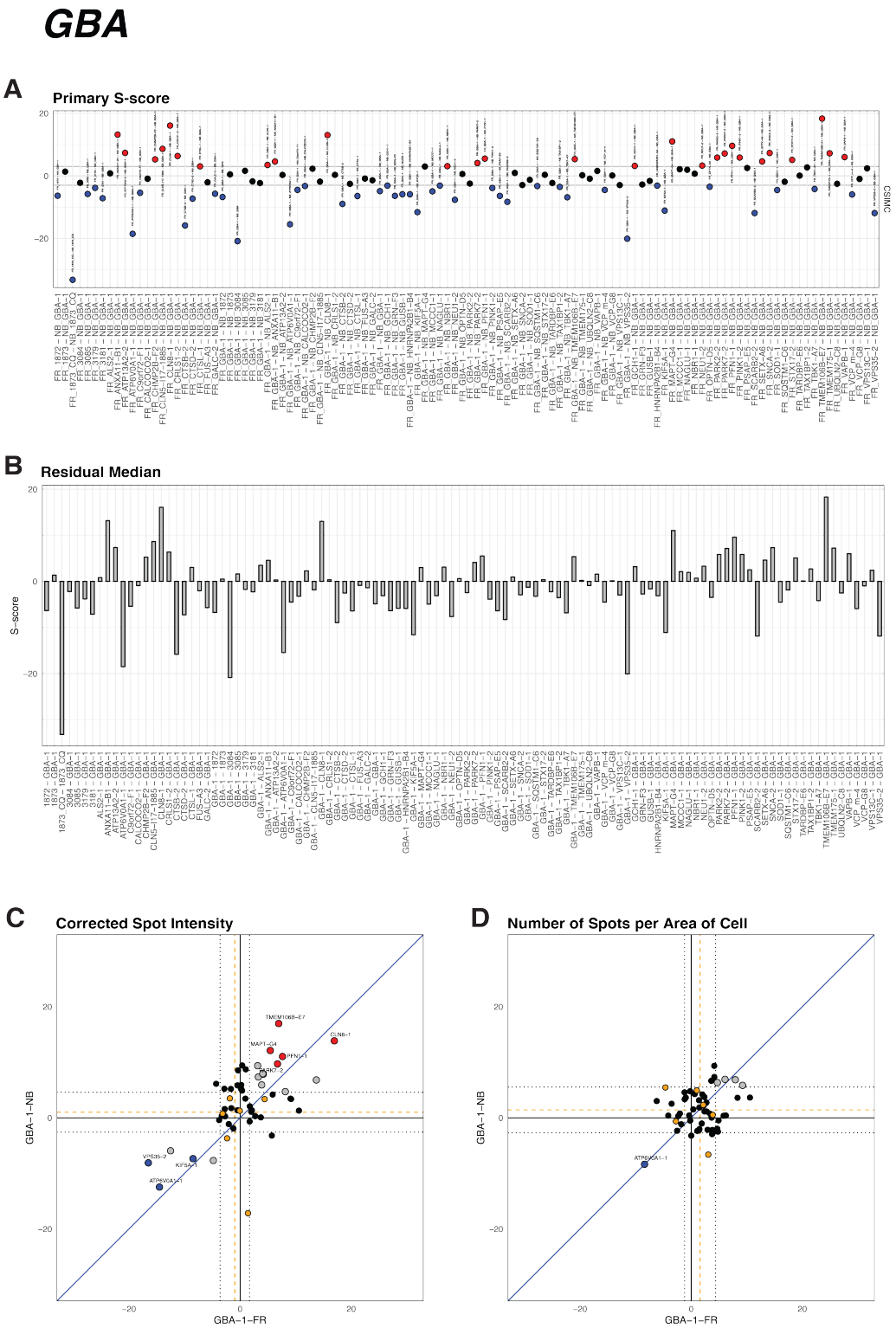


Figure B.27: *GBA*: Primary and Secondary Analysis Genetic Interaction Maps.

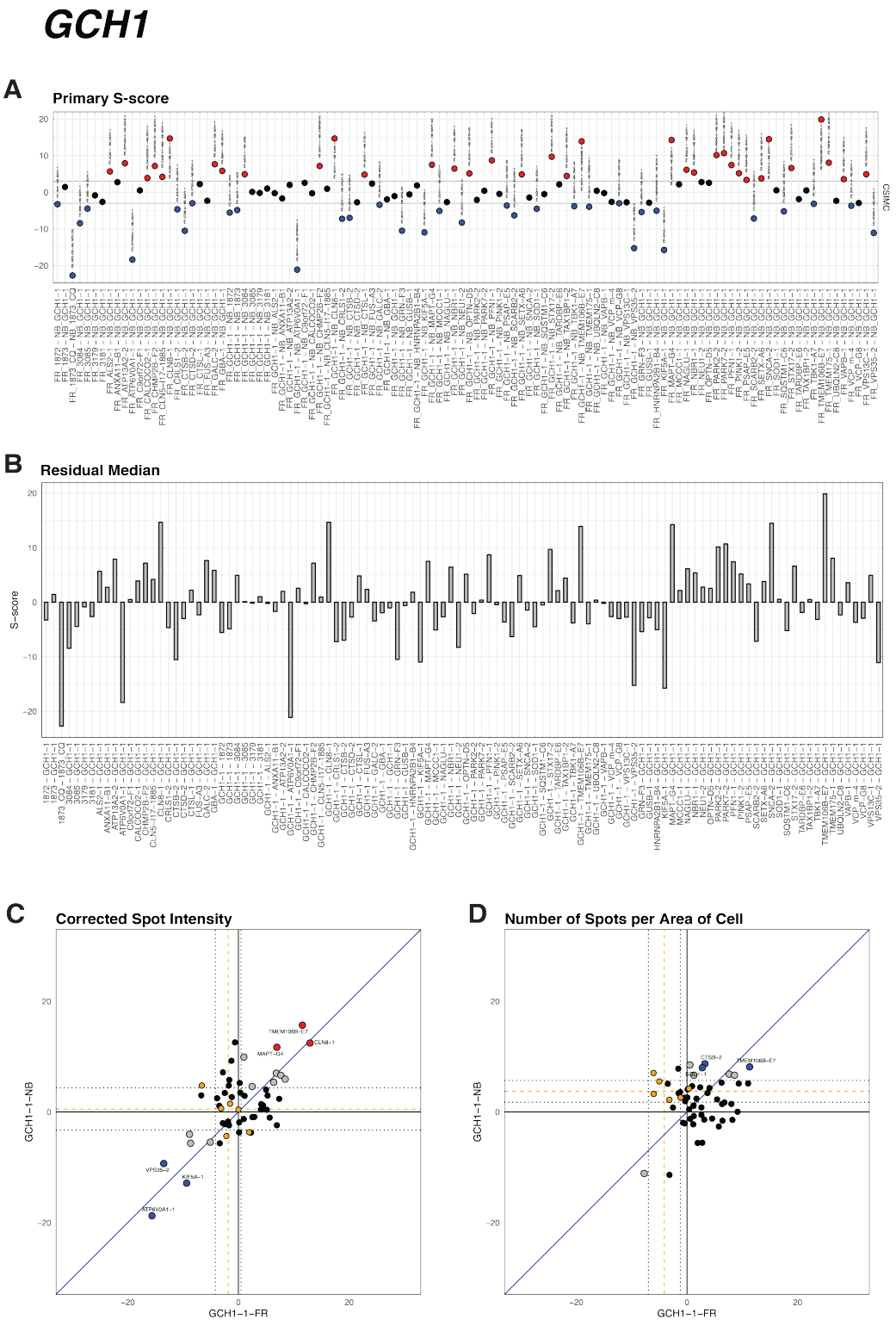


Figure B.28: *GCH1*: Primary and Secondary Analysis Genetic Interaction Maps.

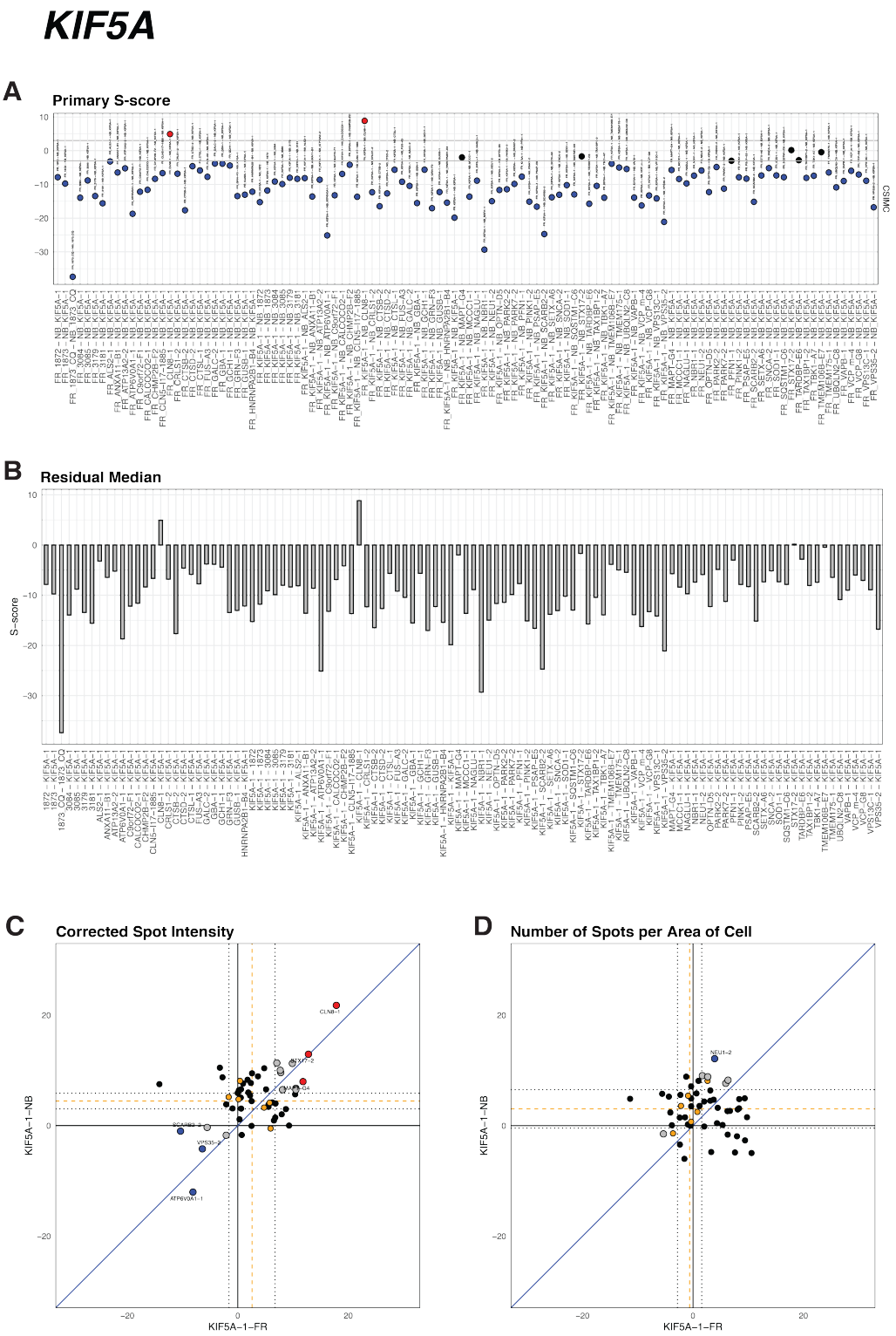


Figure B.29: *KIF5A*: Primary and Secondary Analysis Genetic Interaction Maps.

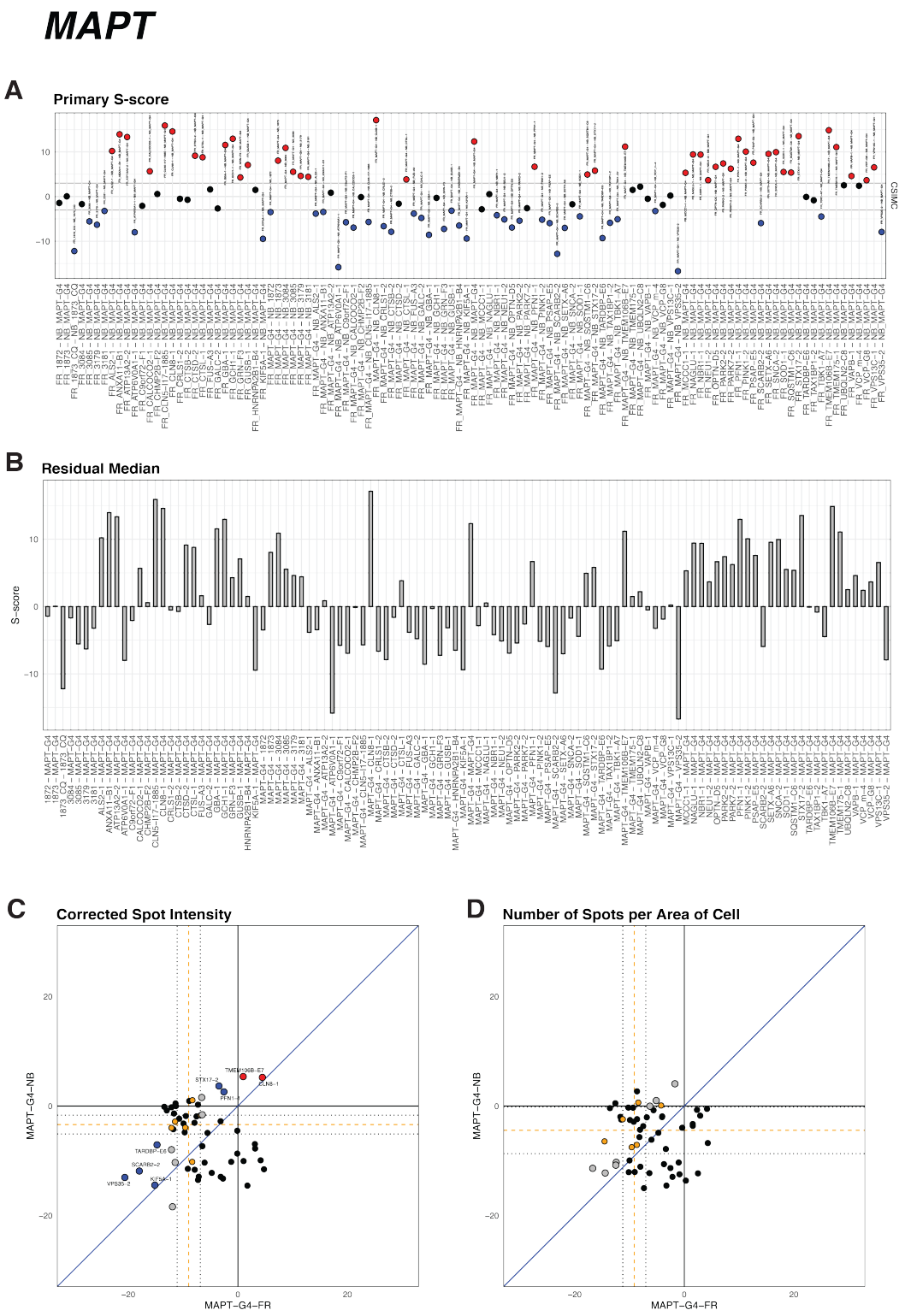


Figure B.30: *MAPT*: Primary and Secondary Analysis Genetic Interaction Maps.

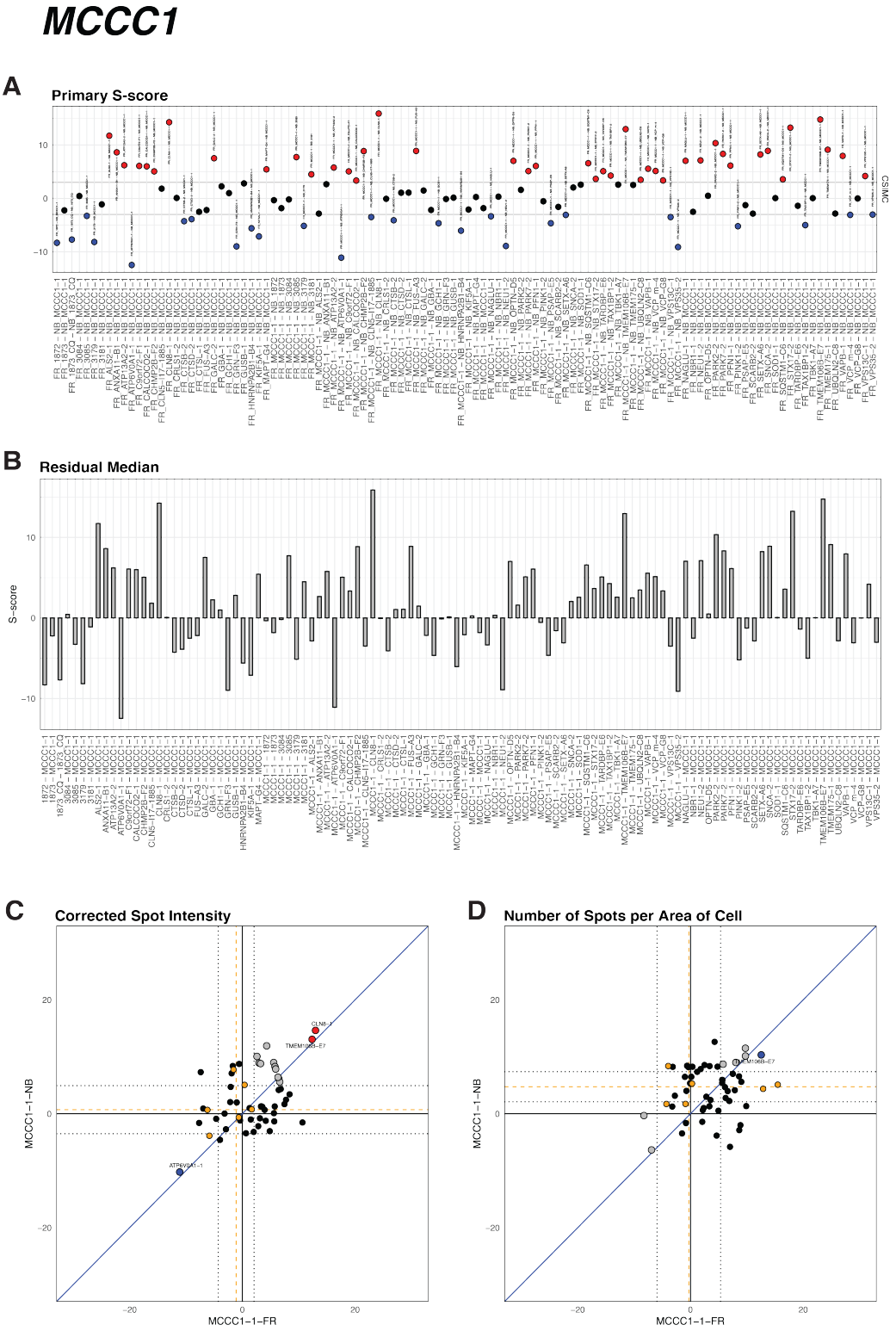


Figure B.31: *MCCC1*: Primary and Secondary Analysis Genetic Interaction Maps.

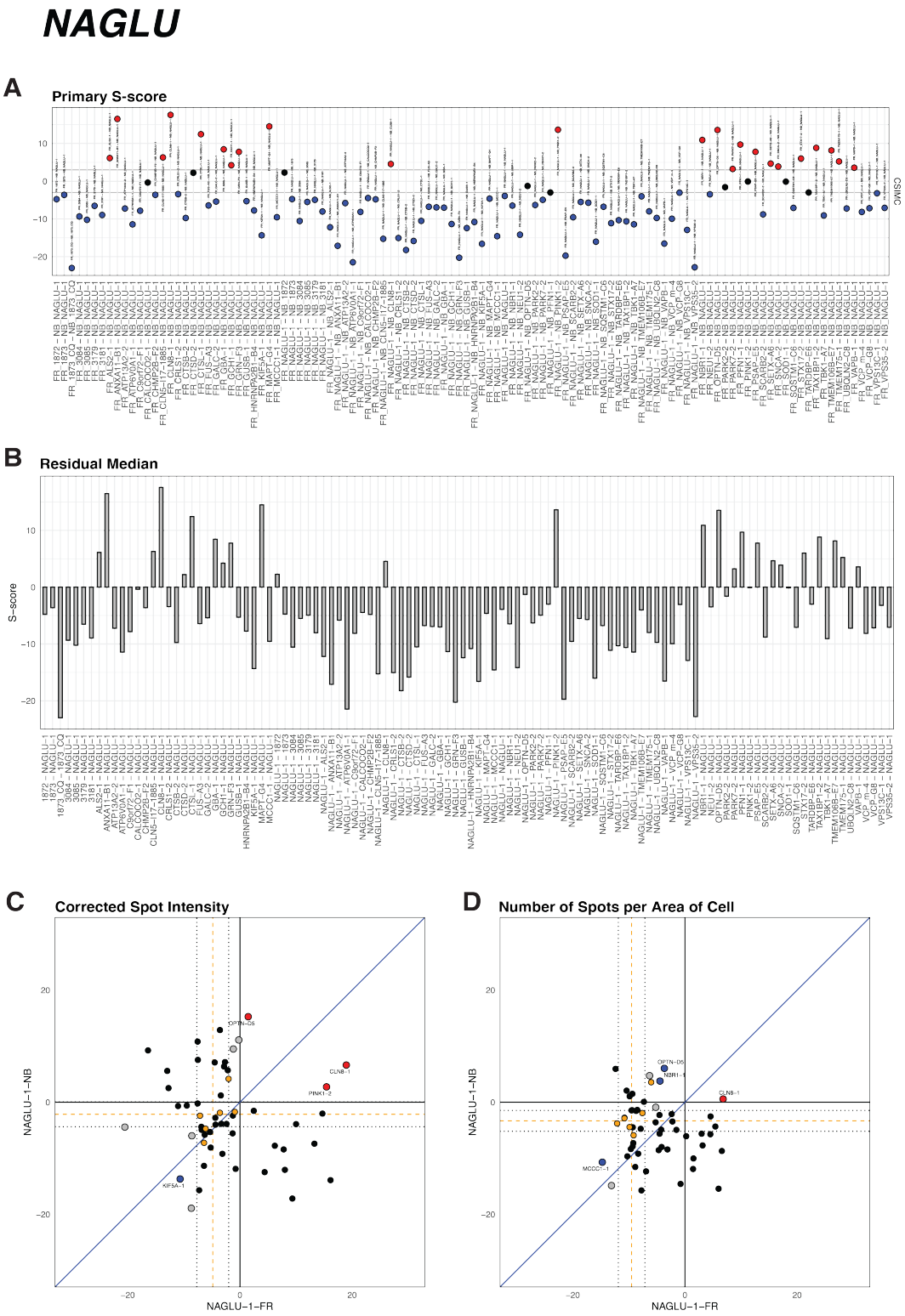


Figure B.32: *NAGLU*: Primary and Secondary Analysis Genetic Interaction Maps.

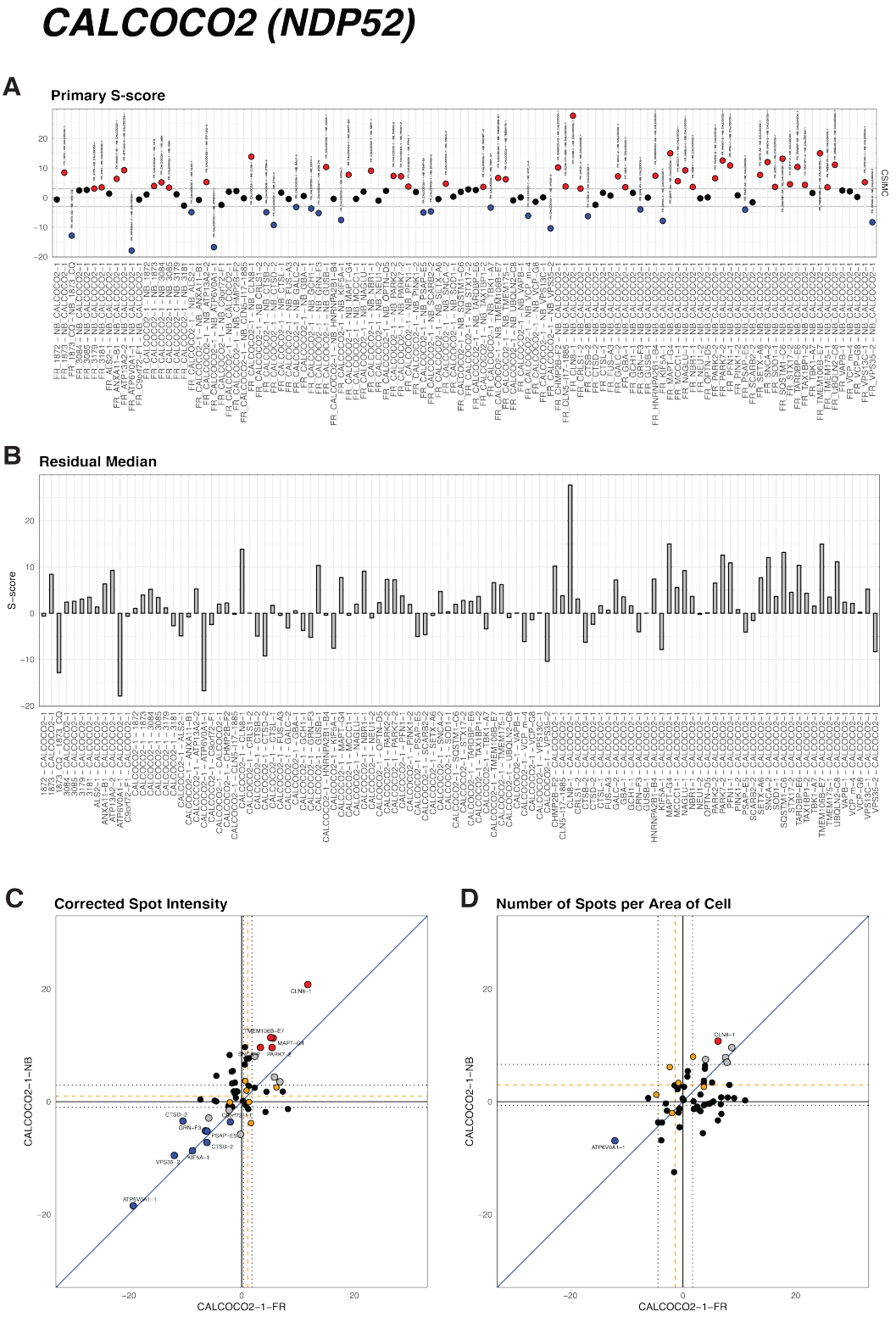


Figure B.33: *NDP52 (CALCOCO2)*: Primary and Secondary Analysis Genetic Interaction Maps.

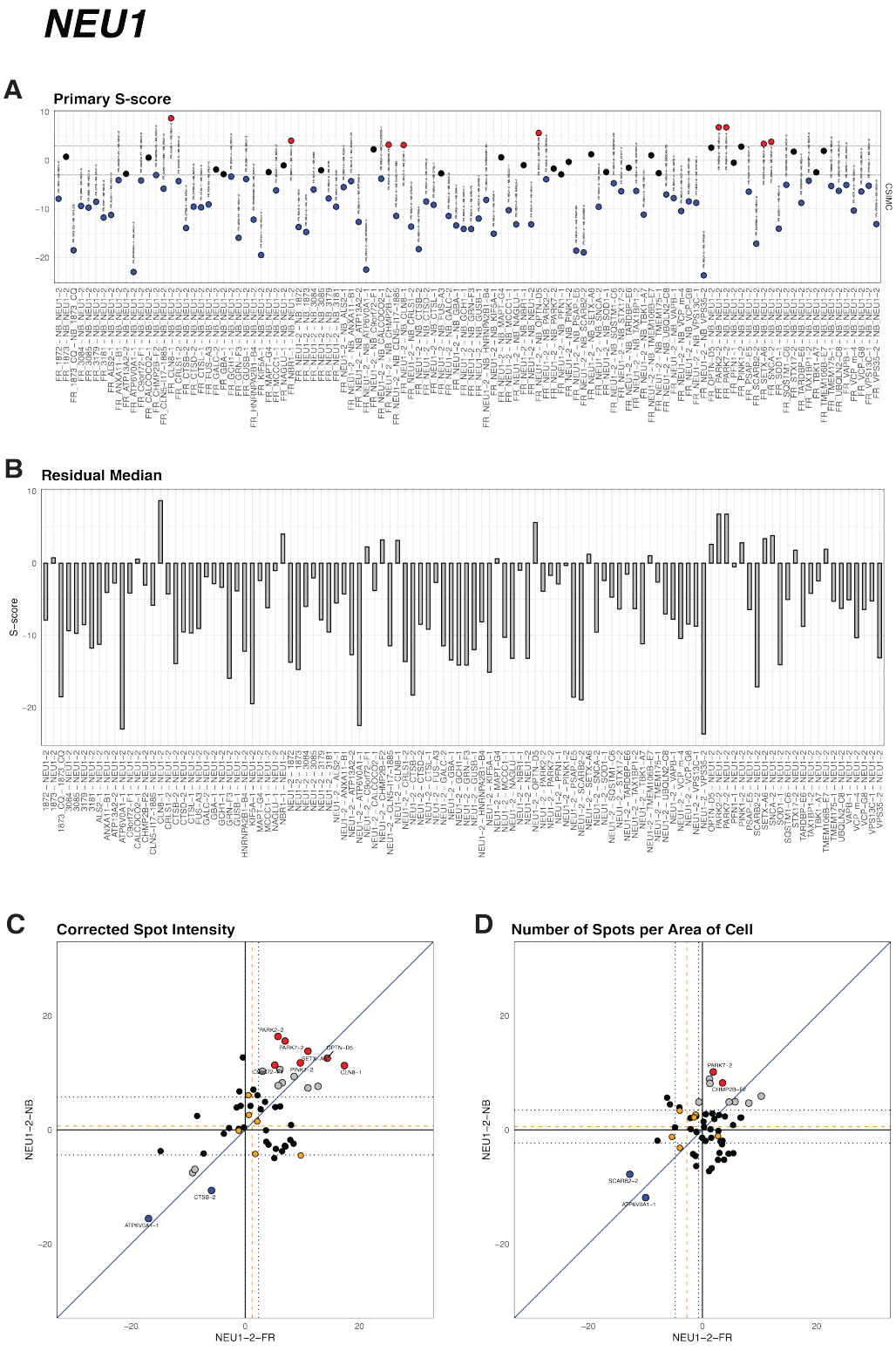


Figure B.34: *NEU1*: Primary and Secondary Analysis Genetic Interaction Maps.

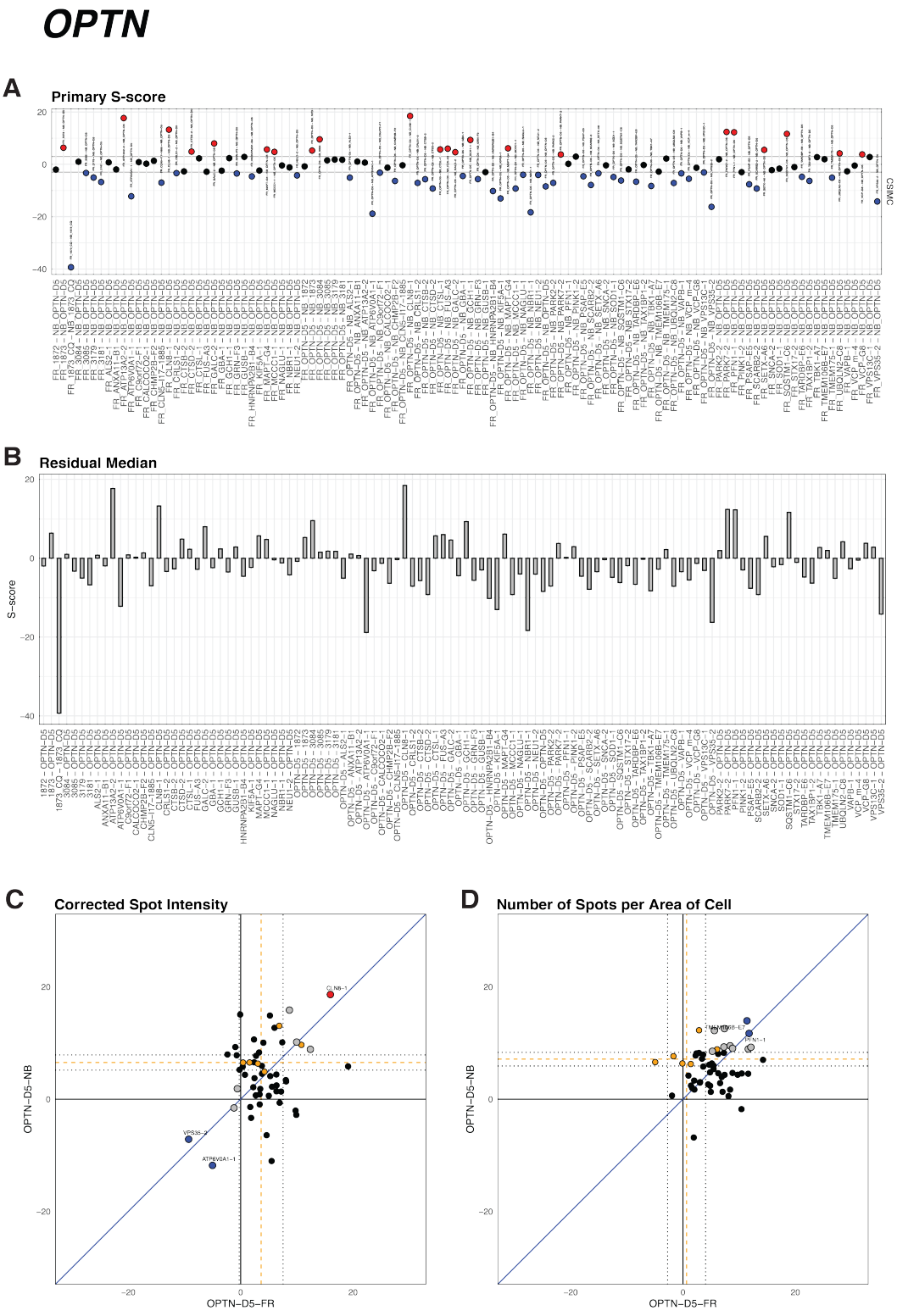


Figure B.35: *OPTN*: Primary and Secondary Analysis Genetic Interaction Maps.

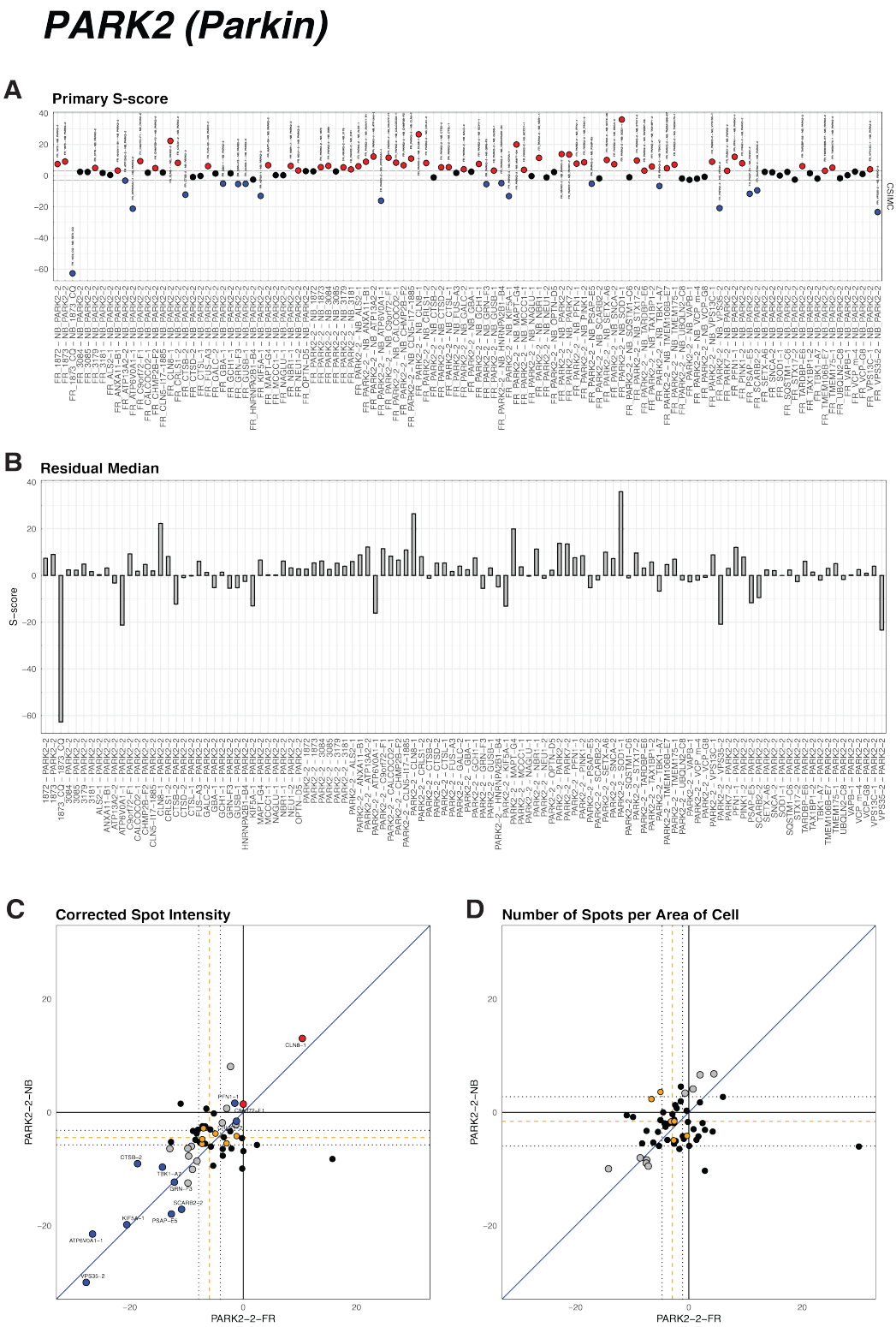


Figure B.36: *PARK2 (Parkin)*: Primary and Secondary Analysis Genetic Interaction Maps.

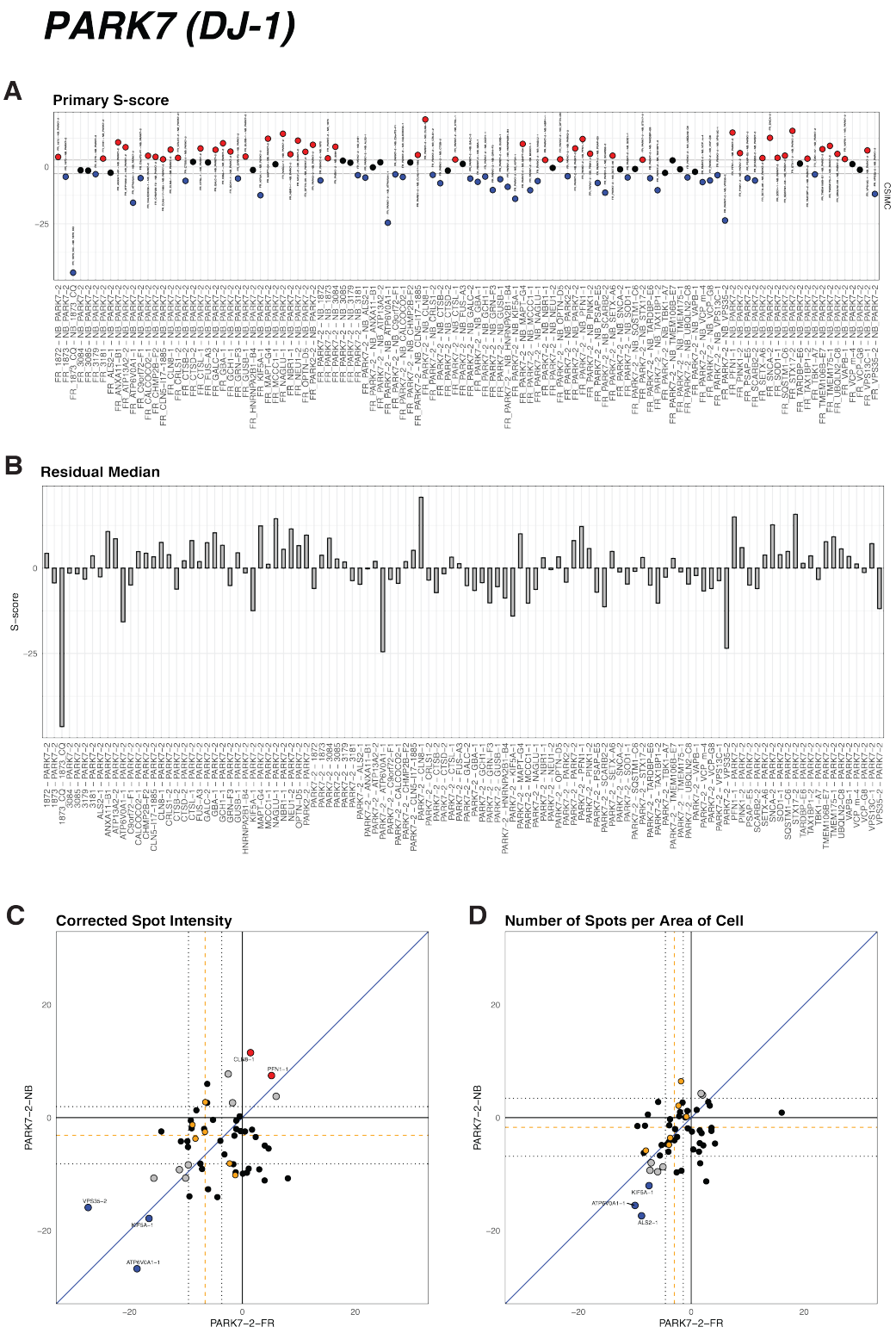


Figure B.37: *PARK7 (DJ-1)*: Primary and Secondary Analysis Genetic Interaction Maps.

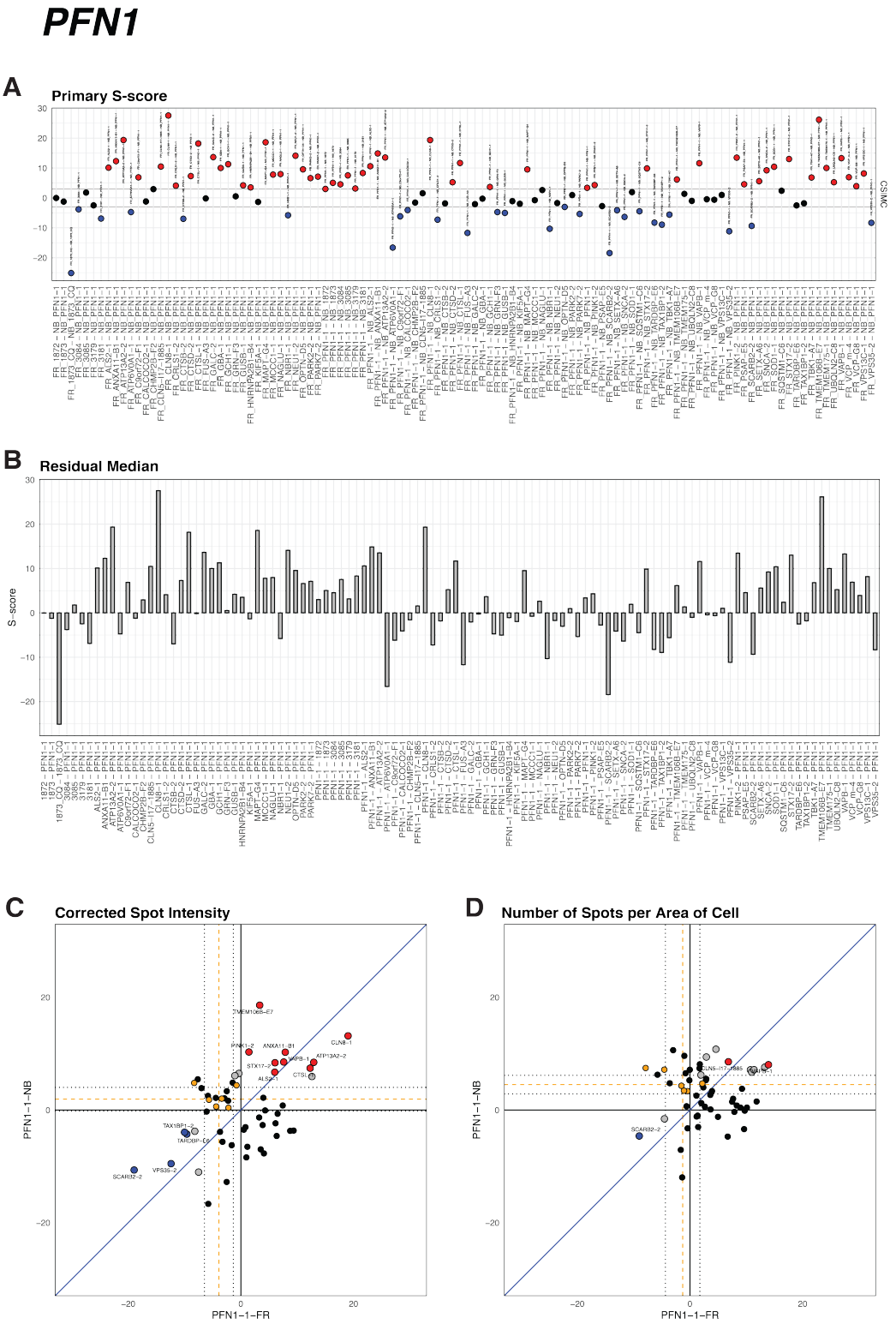


Figure B.38: *PFN1*: Primary and Secondary Analysis Genetic Interaction Maps.

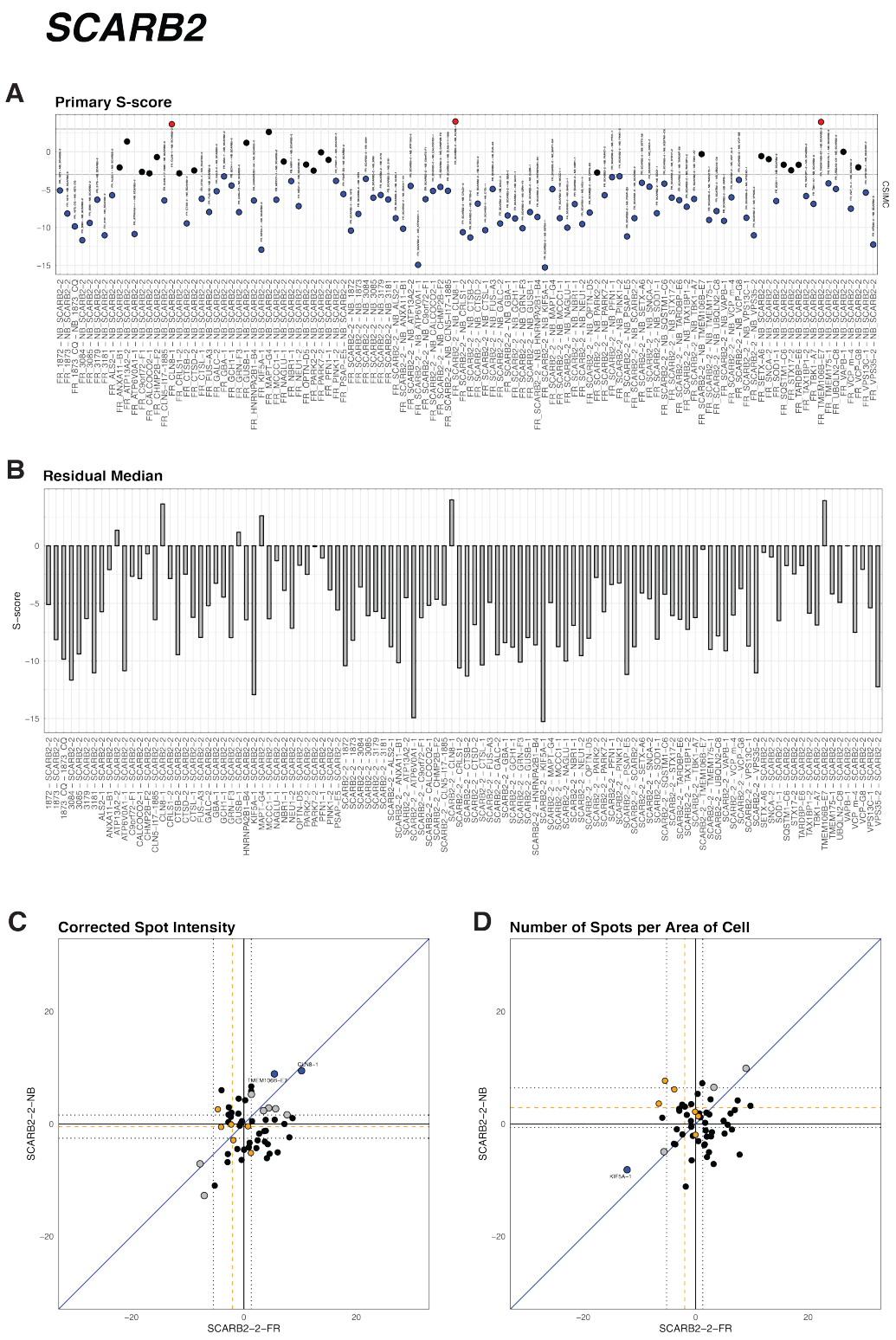


Figure B.39: *SCARB2*: Primary and Secondary Analysis Genetic Interaction Maps.

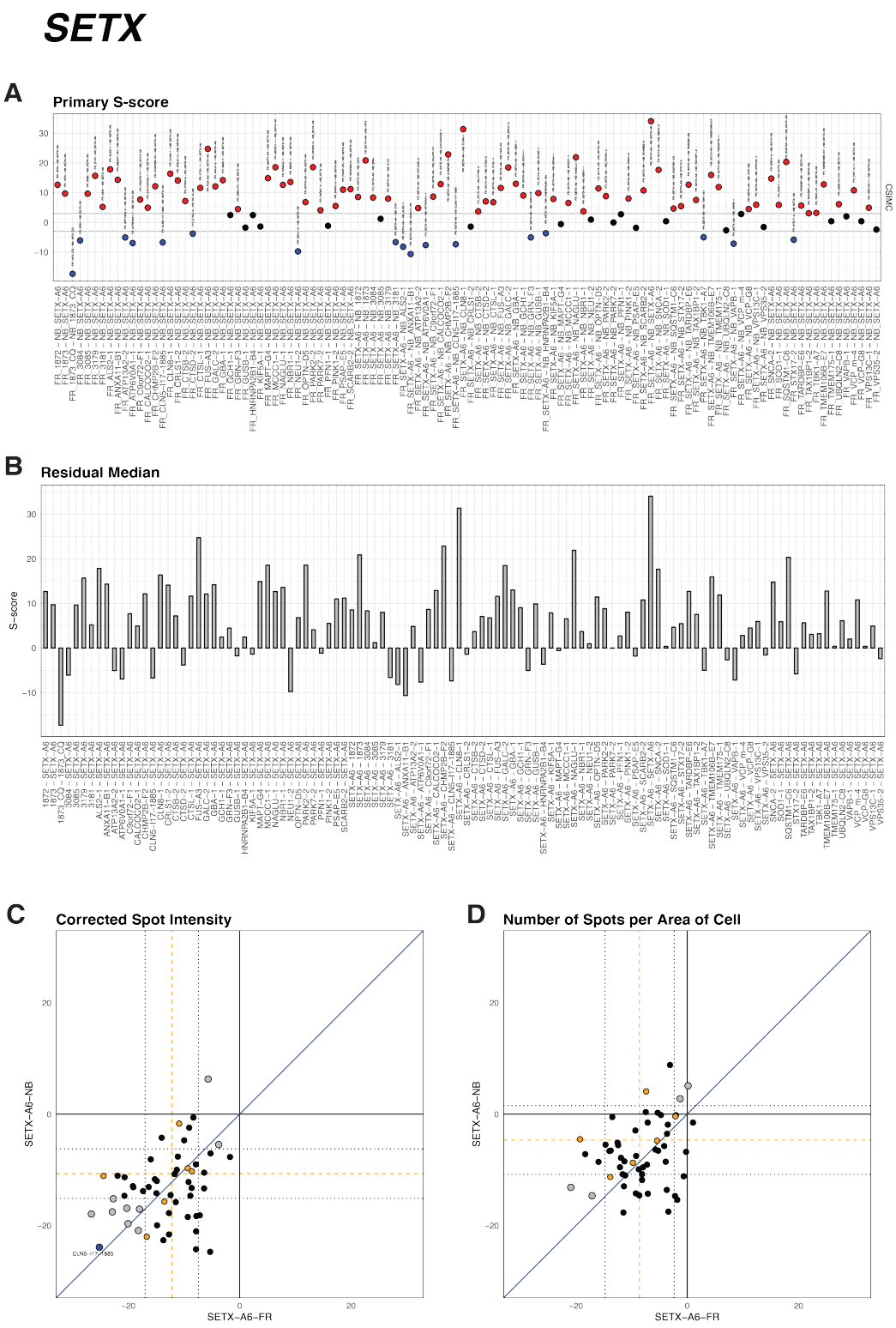


Figure B.40: *SETX*: Primary and Secondary Analysis Genetic Interaction Maps.

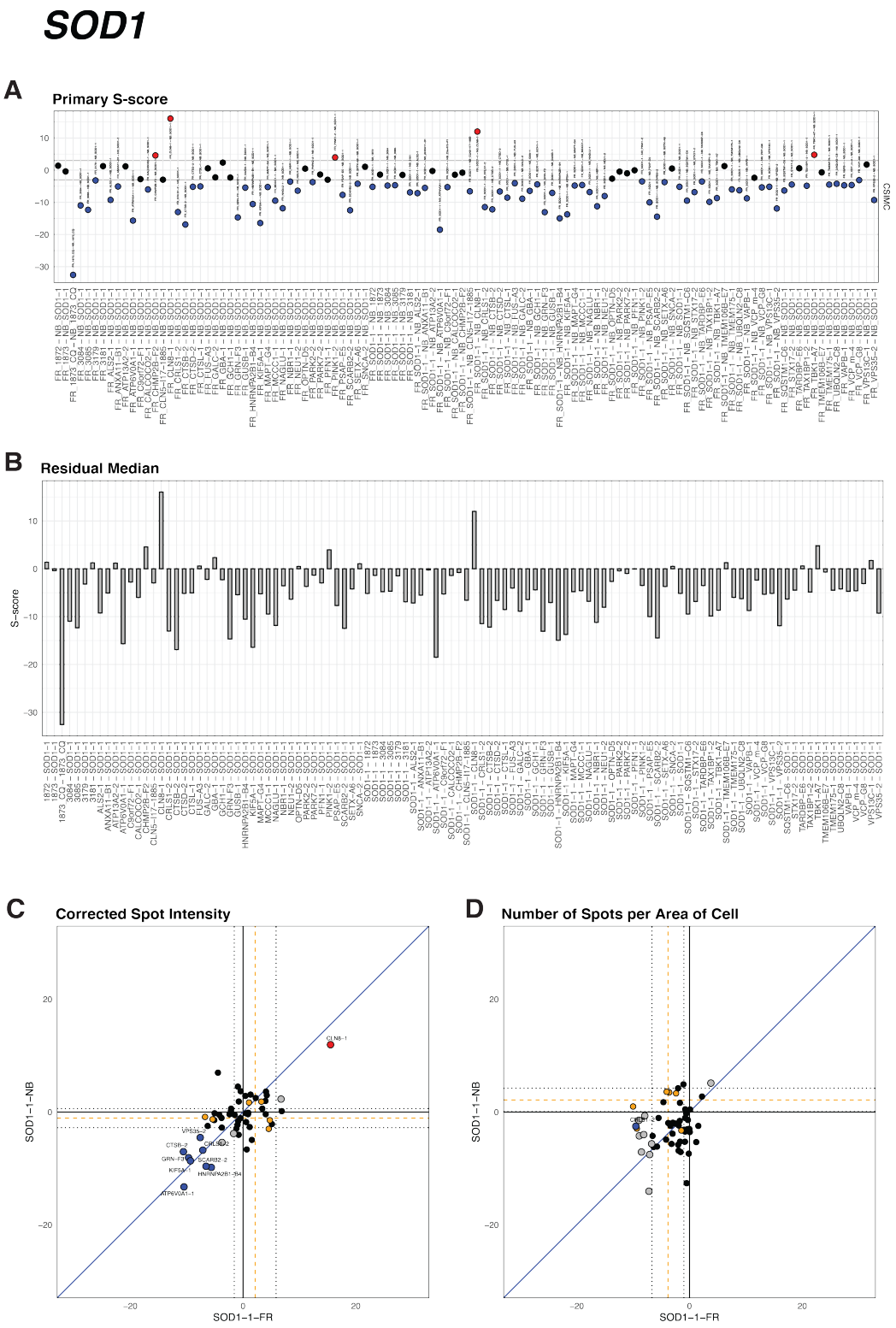


Figure B.41: *SOD1*: Primary and Secondary Analysis Genetic Interaction Maps.

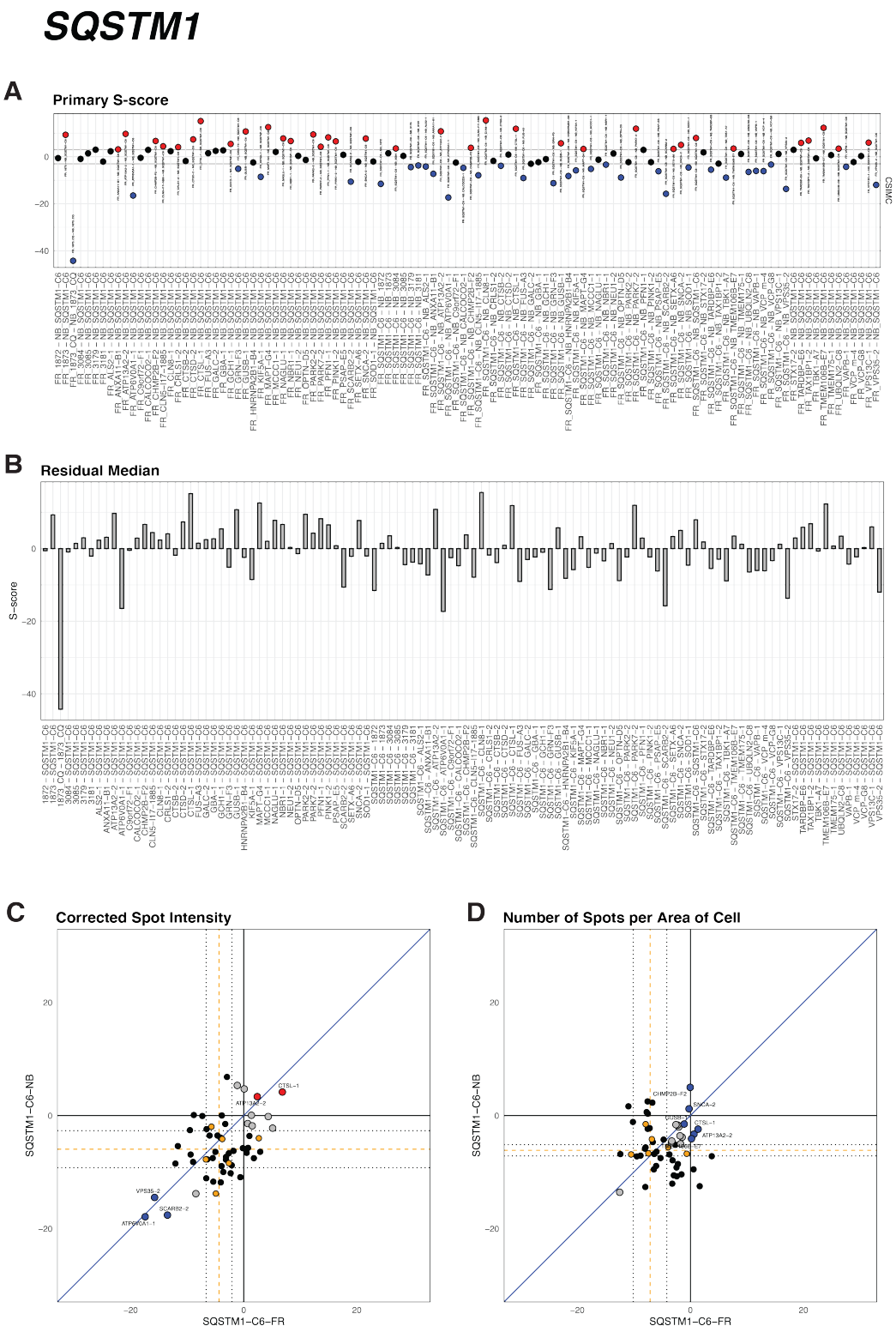


Figure B.42: *SQSTM1*: Primary and Secondary Analysis Genetic Interaction Maps.

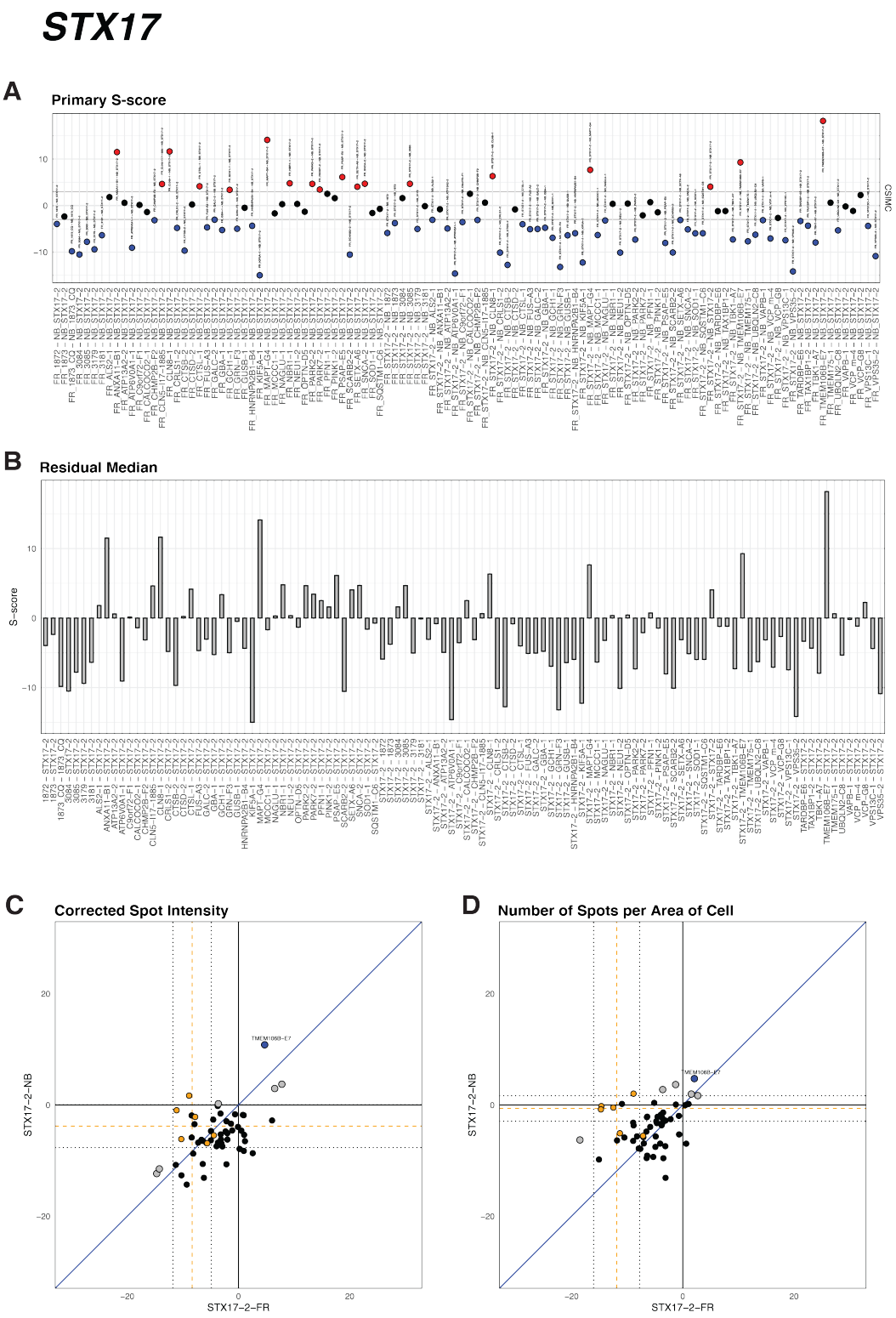


Figure B.43: *STX17*: Primary and Secondary Analysis Genetic Interaction Maps.

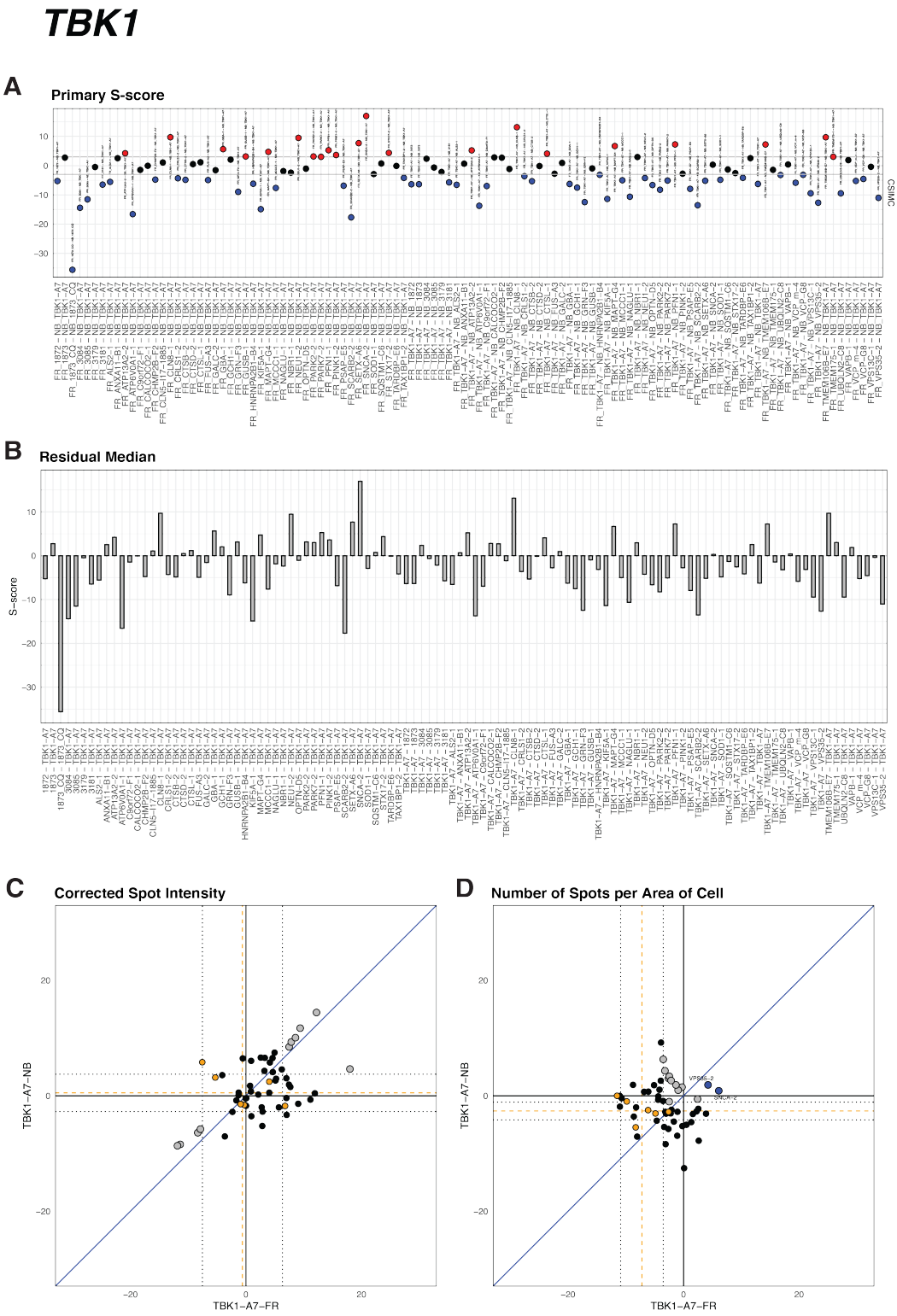


Figure B.44: *TBK1*: Primary and Secondary Analysis Genetic Interaction Maps.

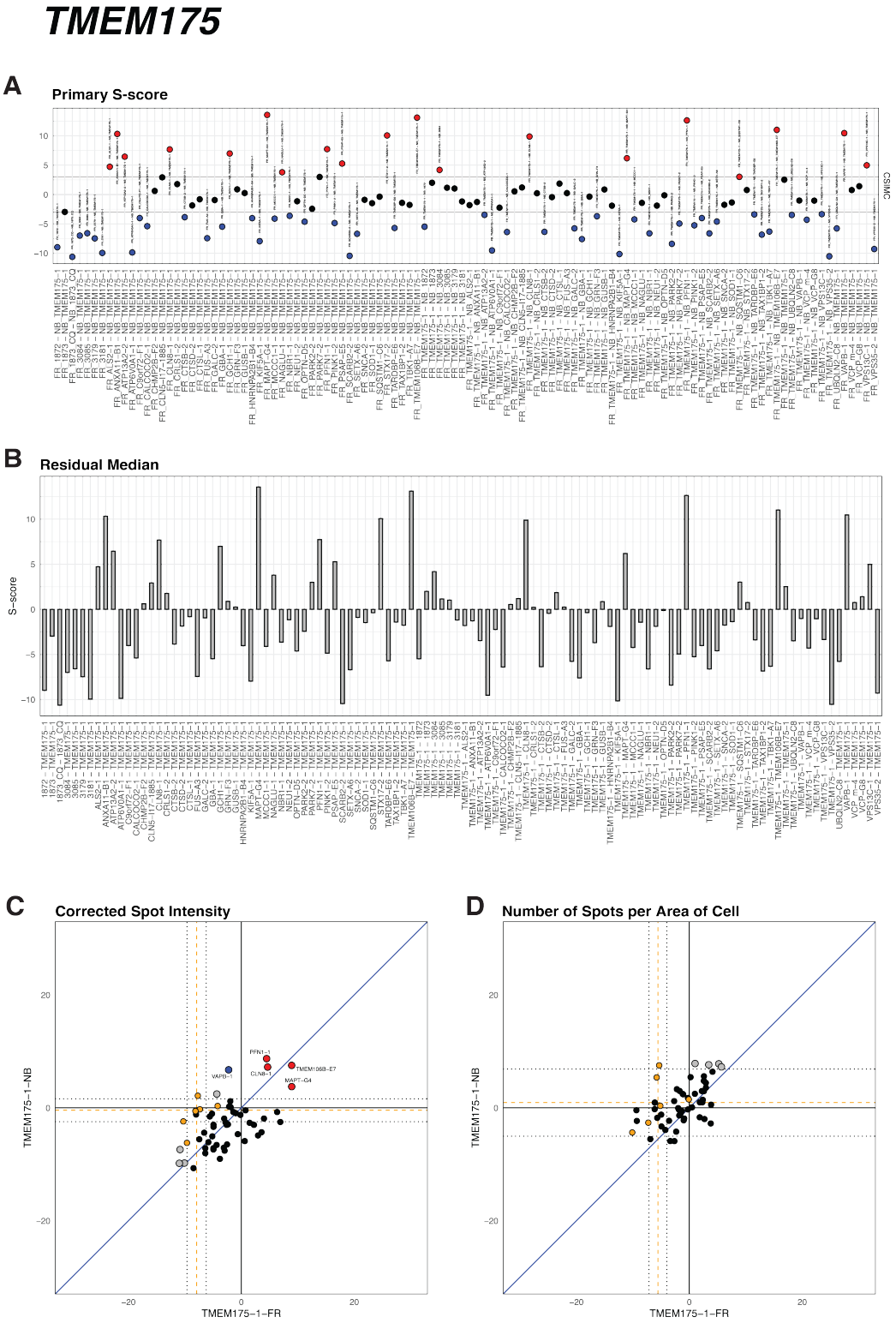


Figure B.45: *TMEM175*: Primary and Secondary Analysis Genetic Interaction Maps.

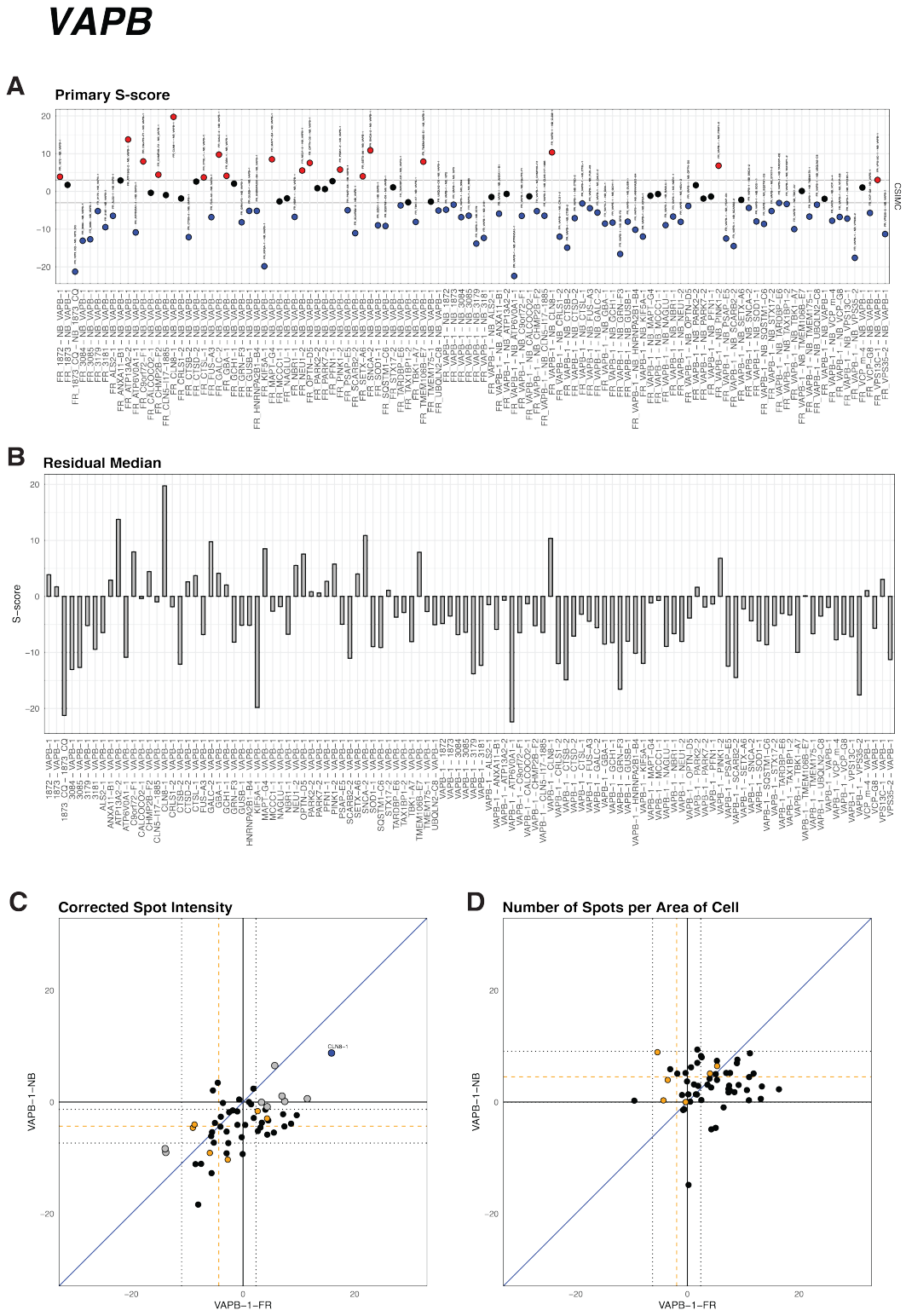


Figure B.46: *VAPB*: Primary and Secondary Analysis Genetic Interaction Maps.

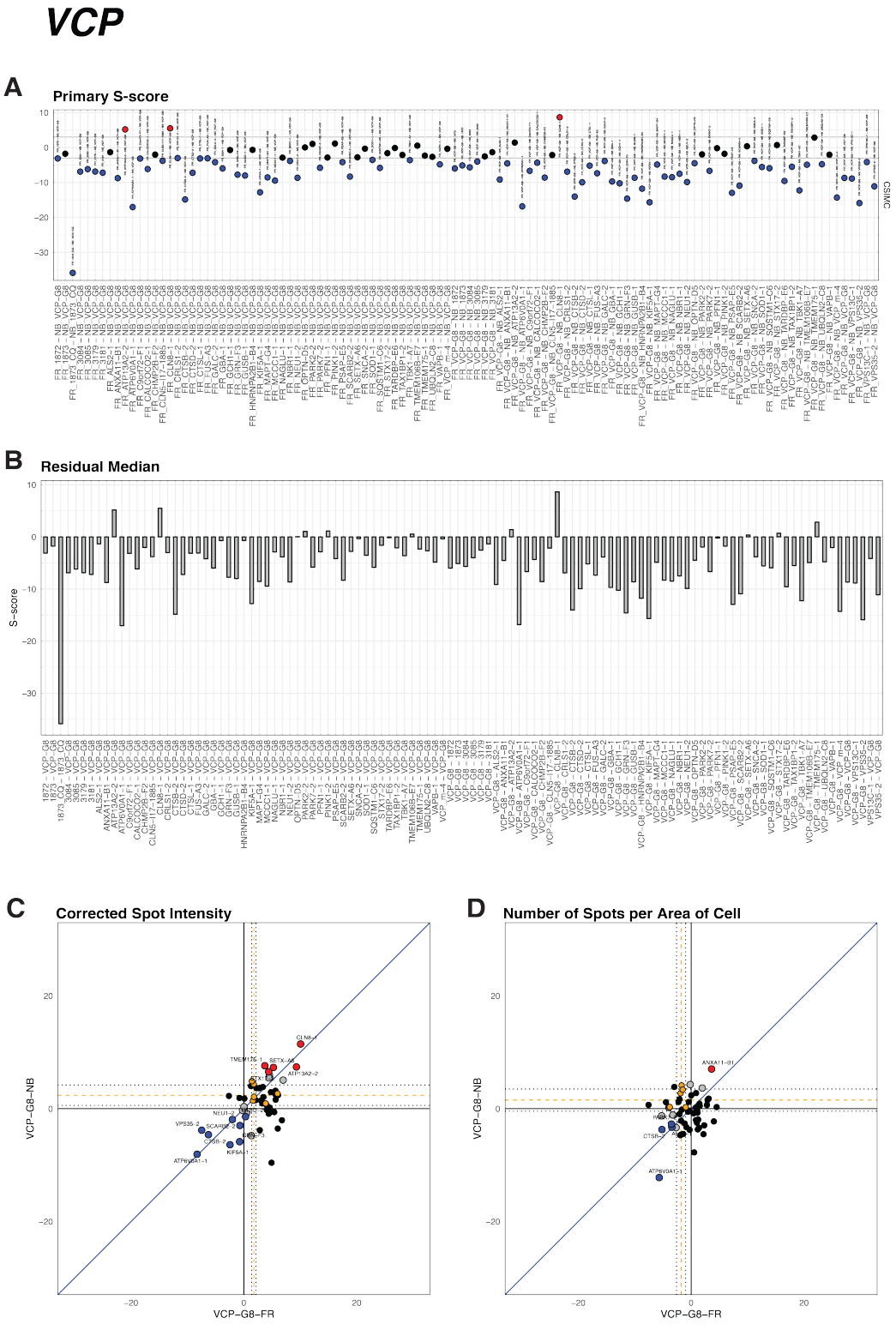


Figure B.47: *VCP*: Primary and Secondary Analysis Genetic Interaction Maps.

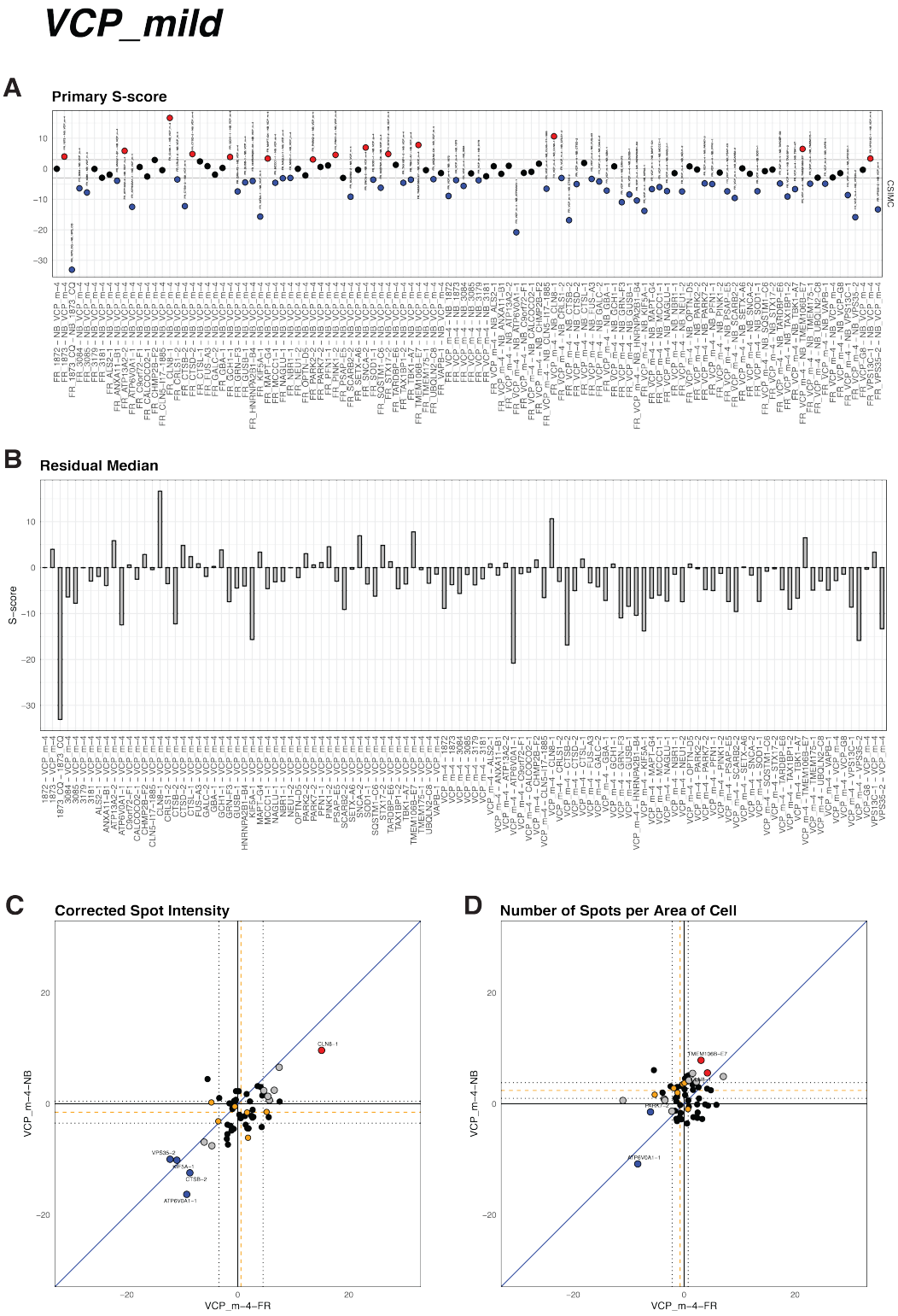


Figure B.48: *VCP_mild*: Primary and Secondary Analysis Genetic Interaction Maps.

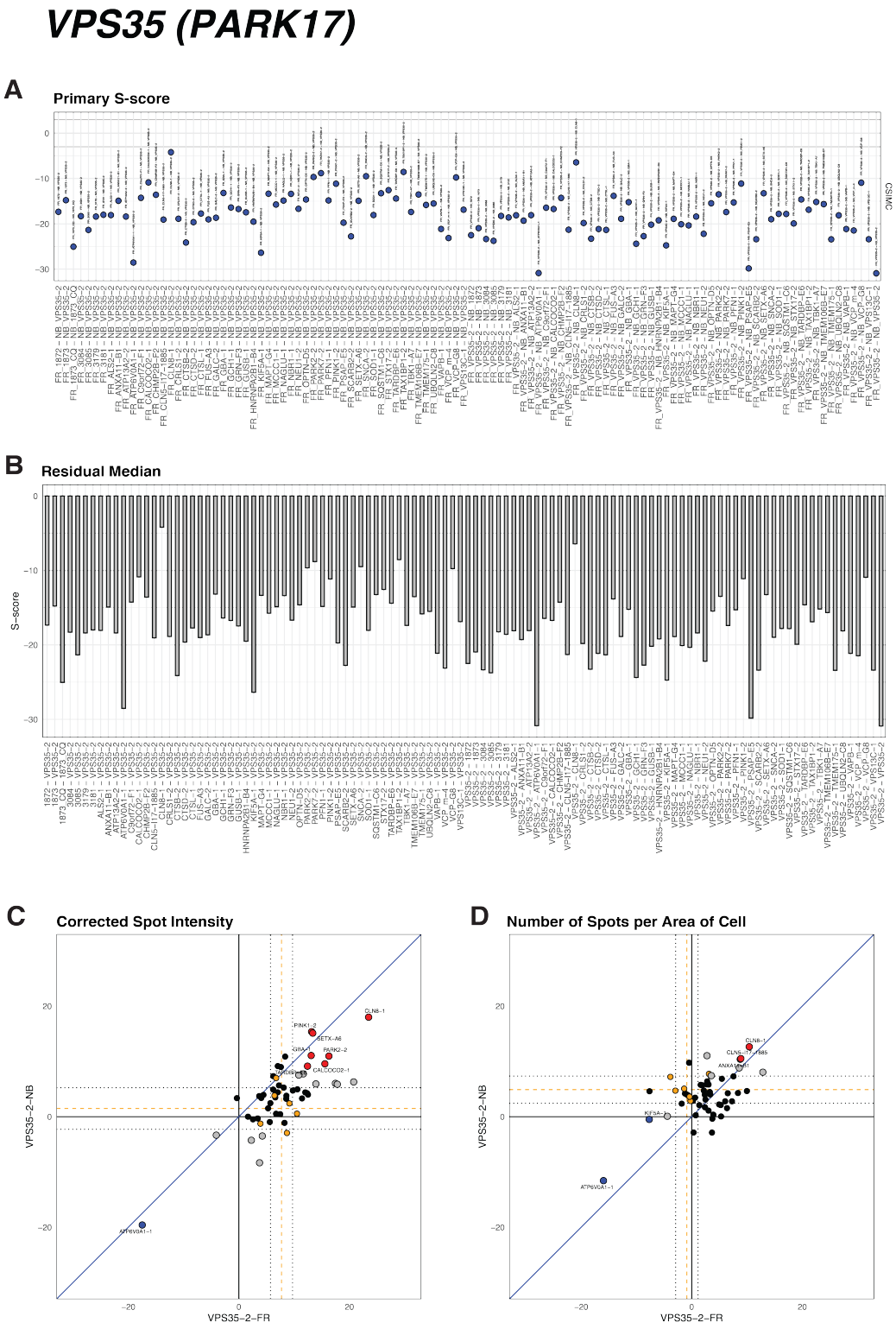


Figure B.49: *VPS35 (PARK17)*: Primary and Secondary Analysis Genetic Interaction Maps.

C

Appendix for Chapter 5 Tables

Contents

C.1 Genetic Interaction Mapping Screen Hit Table 262

C.1 Genetic Interaction Mapping Screen Hit Table

Table C.1: Table of all interaction screening hits; hits that recapitulated in the validation screen are labeled (blue=negative, red=positive, grey=other).

Gene1	Gene2	Combination Reference	Category	Interaction Score
ATP13A2-2	CLN8-1	ATP13A2-2,CLN8-1	SC_2.5_percent	-0.096
CTSL-1	TMEM106B-E7	CTSL-1,TMEM106B-E7	SC_2.5_percent	-0.092
CTSB-2	CTSL-1	CTSB-2,CTSL-1	SC_2.5_percent	-0.074
ATP6V0A1-1	CLN8-1	ATP6V0A1-1,CLN8-1	SC_2.5_percent	-0.072
TMEM106B-E7	VCP-G8	TMEM106B-E7,VCP-G8	SC_2.5_percent	-0.068
CTSD-2	TMEM106B-E7	CTSD-2,TMEM106B-E7	SC_2.5_percent	-0.066
ATP6V0A1-1	VPS35-2	ATP6V0A1-1,VPS35-2	SC_2.5_percent	-0.063
CLN8-1	STX17-2	CLN8-1,STX17-2	SC_2.5_percent	-0.058
PARK2-2	TMEM106B-E7	PARK2-2,TMEM106B-E7	SC_2.5_percent	-0.058
ANXA11-B1	TMEM106B-E7	ANXA11-B1,TMEM106B-E7	SC_2.5_percent	-0.057
PFN1-1	TARDBP-E6	PFN1-1,TARDBP-E6	SC_2.5_percent	-0.052
CLN8-1	NEU1-2	CLN8-1,NEU1-2	SC_2.5_percent	-0.051
HNRNPA2B1-B4	MCCC1-1	HNRNPA2B1-B4,MCCC1-1	SC_2.5_percent	-0.048
TMEM106B-E7	VPS35-2	TMEM106B-E7,VPS35-2	SC_2.5_percent	-0.044
ATP6V0A1-1	NBR1-1	ATP6V0A1-1,NBR1-1	SC_2.5_percent	-0.044
ATP13A2-2	VPS35-2	ATP13A2-2,VPS35-2	SC_2.5_percent	-0.042
MCCC1-1	NBR1-1	MCCC1-1,NBR1-1	SC_2.5_percent	-0.041
SQSTM1-C6	UBQLN2-C8	SQSTM1-C6,UBQLN2-C8	SC_2.5_percent	-0.041
GUSB-1	VPS35-2	GUSB-1,VPS35-2	SC_2.5_percent	-0.041
GALC-2	SQSTM1-C6	GALC-2,SQSTM1-C6	SC_2.5_percent	-0.041
CHMP2B-F2	HNRNPA2B1-B4	CHMP2B-F2,HNRNPA2B1-B4	SC_2.5_percent	-0.040
ATP6V0A1-1	CTSL-1	ATP6V0A1-1,CTSL-1	SC_2.5_percent	-0.040
PARK2-2	TBK1-A7	PARK2-2,TBK1-A7	SC_2.5_percent	-0.040
CALCOCO2-1	CTSD-2	CALCOCO2-1,CTSD-2	SC_2.5_percent	-0.039
NEU1-2	SETX-A6	NEU1-2,SETX-A6	SC_2.5_percent	-0.039
PARK2-2	PSAP-E5	PARK2-2,PSAP-E5	SC_2.5_percent	-0.038
ALS2-1	CALCOCO2-1	ALS2-1,CALCOCO2-1	SC_2.5_percent	-0.038
CTSB-2	GUSB-1	CTSB-2,GUSB-1	SC_2.5_percent	-0.038
TAX1BP1-2	VCP_m-4	TAX1BP1-2,VCP_m-4	SC_2.5_percent	-0.038
PFN1-1	TAX1BP1-2	PFN1-1,TAX1BP1-2	SC_2.5_percent	-0.037
MAPT-G4	TARDBP-E6	MAPT-G4,TARDBP-E6	SC_2.5_percent	-0.037
CLN8-1	SETX-A6	CLN8-1,SETX-A6	SC_2.5_percent	-0.037
STX17-2	TMEM175-1	STX17-2,TMEM175-1	SC_2.5_percent	-0.036
GCH1-1	SQSTM1-C6	GCH1-1,SQSTM1-C6	SC_2.5_percent	-0.036
CTSL-1	VCP-G8	CTSL-1,VCP-G8	SC_2.5_percent	-0.036
PARK7-2	VCP-G8	PARK7-2,VCP-G8	SC_2.5_percent	-0.036
ATP6V0A1-1	VPS13C-1	ATP6V0A1-1,VPS13C-1	SC_2.5_percent	-0.036
GUSB-1	UBQLN2-C8	GUSB-1,UBQLN2-C8	SC_2.5_percent	-0.036
KIF5A-1	PINK1-2	KIF5A-1,PINK1-2	SC_2.5_percent	-0.035
TBK1-A7	UBQLN2-C8	TBK1-A7,UBQLN2-C8	SC_2.5_percent	-0.035
PINK1-2	PSAP-E5	PINK1-2,PSAP-E5	SC_2.5_percent	-0.035
CLN5	PFN1-1	CLN5,PFN1-1	SC_2.5_percent	-0.035
GUSB-1	KIF5A-1	GUSB-1,KIF5A-1	SC_2.5_percent	-0.035
CTSD-2	GALC-2	CTSD-2,GALC-2	SC_2.5_percent	-0.035
ANXA11-B1	CHMP2B-F2	ANXA11-B1,CHMP2B-F2	SC_2.5_percent	-0.035
CLN5	TARDBP-E6	CLN5,TARDBP-E6	SC_2.5_percent	-0.034
CTSD-2	CTSL-1	CTSD-2,CTSL-1	SC_2.5_percent	-0.034
CTSD-2	VCP-G8	CTSD-2,VCP-G8	SC_2.5_percent	-0.034
ATP13A2-2	TARDBP-E6	ATP13A2-2,TARDBP-E6	SC_2.5_percent	-0.033
ALS2-1	TBK1-A7	ALS2-1,TBK1-A7	SC_2.5_percent	-0.033
CTSD-2	GUSB-1	CTSD-2,GUSB-1	SC_2.5_percent	-0.032
ANXA11-B1	CRLS1-2	ANXA11-B1,CRLS1-2	SC_2.5_percent	-0.032
ATP13A2-2	SNCA-2	ATP13A2-2,SNCA-2	SC_2.5_percent	-0.032
NBR1-1	PSAP-E5	NBR1-1,PSAP-E5	SC_2.5_percent	-0.032
ATP13A2-2	SETX-A6	ATP13A2-2,SETX-A6	SC_2.5_percent	-0.032
GBA-1	SQSTM1-C6	GBA-1,SQSTM1-C6	SC_2.5_percent	-0.031
PFN1-1	SNCA-2	PFN1-1,SNCA-2	SC_2.5_percent	-0.031
CTSD-2	SNCA-2	CTSD-2,SNCA-2	SC_2.5_percent	-0.031

Table C.1 continued from previous page

Gene1	Gene2	Combination Reference	Category	Interaction Score
FUS-A3	STX17-2	FUS-A3,STX17-2	SC_2.5_percent	-0.031
GUSB-1	PFN1-1	GUSB-1,PFN1-1	SC_2.5_percent	-0.031
SQSTM1-C6	VAPB-1	SQSTM1-C6,VAPB-1	SC_2.5_percent	-0.030
PSAP-E5	UBQLN2-C8	PSAP-E5,UBQLN2-C8	SC_2.5_percent	-0.030
ALS2-1	UBQLN2-C8	ALS2-1,UBQLN2-C8	SC_2.5_percent	-0.030
NEU1-2	SCARB2-2	NEU1-2,SCARB2-2	SC_2.5_percent	-0.030
ATP13A2-2	NEU1-2	ATP13A2-2,NEU1-2	SC_2.5_percent	-0.030
CLN8-1	TMEM175-1	CLN8-1,TMEM175-1	SC_2.5_percent	-0.030
PARK2-2	VPS35-2	PARK2-2,VPS35-2	SC_2.5_percent	-0.029
CRLS1-2	PFN1-1	CRLS1-2,PFN1-1	SC_2.5_percent	-0.029
GALC-2	VCP_m-4	GALC-2,VCP_m-4	SC_2.5_percent	-0.029
MCCC1-1	NAGLU-1	MCCC1-1,NAGLU-1	SC_2.5_percent	-0.029
CRLS1-2	PSAP-E5	CRLS1-2,PSAP-E5	SC_2.5_percent	-0.029
NBR1-1	VCP-G8	NBR1-1,VCP-G8	SC_2.5_percent	-0.029
PARK7-2	SETX-A6	PARK7-2,SETX-A6	SC_2.5_percent	-0.029
PARK7-2	PSAP-E5	PARK7-2,PSAP-E5	SC_2.5_percent	-0.029
CHMP2B-F2	FUS-A3	CHMP2B-F2,FUS-A3	SC_2.5_percent	-0.029
NEU1-2	VCP-G8	NEU1-2,VCP-G8	SC_2.5_percent	-0.029
CRLS1-2	GALC-2	CRLS1-2,GALC-2	SC_2.5_percent	-0.029
NBR1-1	VPS35-2	NBR1-1,VPS35-2	SC_2.5_percent	-0.028
ATP13A2-2	KIF5A-1	ATP13A2-2,KIF5A-1	SC_2.5_percent	-0.028
ATP13A2-2	UBQLN2-C8	ATP13A2-2,UBQLN2-C8	SC_2.5_percent	-0.028
PINK1-2	SQSTM1-C6	PINK1-2,SQSTM1-C6	SC_2.5_percent	-0.028
OPTN-D5	TMEM106B-E7	OPTN-D5,TMEM106B-E7	SC_2.5_percent	-0.028
CRLS1-2	HNRNPA2B1-B4	CRLS1-2,HNRNPA2B1-B4	SC_2.5_percent	-0.028
PSAP-E5	SNCA-2	PSAP-E5,SNCA-2	SC_2.5_percent	-0.027
CTSL-1	SOD1-1	CTSL-1,SOD1-1	SC_2.5_percent	-0.027
CLN5-I17-1885	CTSL-1	CLN5-I17-1885,CTSL-1	SC_2.5_percent	-0.027
ATP6V0A1-1	CHMP2B-F2	ATP6V0A1-1,CHMP2B-F2	SC_2.5_percent	-0.026
CTSD-2	GBA-1	CTSD-2,GBA-1	SC_2.5_percent	-0.026
CLN8-1	CRLS1-2	CLN8-1,CRLS1-2	SC_2.5_percent	-0.026
ANXA11-B1	FUS-A3	ANXA11-B1,FUS-A3	SC_2.5_percent	-0.026
MAPT-G4	MCCC1-1	MAPT-G4,MCCC1-1	SC_2.5_percent	-0.026
OPTN-D5	PARK2-2	OPTN-D5,PARK2-2	SC_2.5_percent	-0.026
NAGLU-1	VPS13C-1	NAGLU-1,VPS13C-1	SC_2.5_percent	-0.026
PFN1-1	SETX-A6	PFN1-1,SETX-A6	SC_2.5_percent	-0.026
STX17-2	VPS13C-1	STX17-2,VPS13C-1	SC_2.5_percent	-0.026
GALC-2	SOD1-1	GALC-2,SOD1-1	SC_2.5_percent	-0.026
ATP13A2-2	TAX1BP1-2	ATP13A2-2,TAX1BP1-2	SC_2.5_percent	-0.025
PARK2-2	TARDBP-E6	PARK2-2,TARDBP-E6	SC_2.5_percent	-0.025
HNRNPA2B1-B4	UBQLN2-C8	HNRNPA2B1-B4,UBQLN2-C8	SC_2.5_percent	-0.025
ATP13A2-2	HNRNPA2B1-B4	ATP13A2-2,HNRNPA2B1-B4	SC_2.5_percent	-0.025
CTSL-1	MCCC1-1	CTSL-1,MCCC1-1	SC_2.5_percent	-0.025
CLN8-1	CTSB-2	CLN8-1,CTSB-2	SC_2.5_percent	-0.025
GUSB-1	PINK1-2	GUSB-1,PINK1-2	SC_2.5_percent	-0.025
STX17-2	VAPB-1	STX17-2,VAPB-1	SC_2.5_percent	-0.025
ALS2-1	PFN1-1	ALS2-1,PFN1-1	SC_2.5_percent	-0.025
TARDBP-E6	TMEM106B-E7	TARDBP-E6,TMEM106B-E7	SC_2.5_percent	0.025
CTSD-2	VCP_m-4	CTSD-2,VCP_m-4	SC_2.5_percent	0.025
CTSD-2	VAPB-1	CTSD-2,VAPB-1	SC_2.5_percent	0.025
CHMP2B-F2	MCCC1-1	CHMP2B-F2,MCCC1-1	SC_2.5_percent	0.025
PFN1-1	UBQLN2-C8	PFN1-1,UBQLN2-C8	SC_2.5_percent	0.025
GCH1-1	TARDBP-E6	GCH1-1,TARDBP-E6	SC_2.5_percent	0.025
MAPT-G4	VPS13C-1	MAPT-G4,VPS13C-1	SC_2.5_percent	0.026
PINK1-2	VCP-G8	PINK1-2,VCP-G8	SC_2.5_percent	0.026
ATP13A2-2	GCH1-1	ATP13A2-2,GCH1-1	SC_2.5_percent	0.026
CLN5-I17-1885	GRN-F3	CLN5-I17-1885,GRN-F3	SC_2.5_percent	0.026
CTSL-1	STX17-2	CTSL-1,STX17-2	SC_2.5_percent	0.026
CRLS1-2	KIF5A-1	CRLS1-2,KIF5A-1	SC_2.5_percent	0.027
MAPT-G4	SQSTM1-C6	MAPT-G4,SQSTM1-C6	SC_2.5_percent	0.027
CTSD-2	STX17-2	CTSD-2,STX17-2	SC_2.5_percent	0.027
C9orf72-F1	GUSB-1	C9orf72-F1,GUSB-1	SC_2.5_percent	0.027
TAX1BP1-2	TBK1-A7	TAX1BP1-2,TBK1-A7	SC_2.5_percent	0.027
SOD1-1	VCP-G8	SOD1-1,VCP-G8	SC_2.5_percent	0.028
NBR1-1	SQSTM1-C6	NBR1-1,SQSTM1-C6	SC_2.5_percent	0.028

Table C.1 continued from previous page

Gene1	Gene2	Combination Reference	Category	Interaction Score
CTSL-1	PFN1-1	CTSL-1,PFN1-1	SC_2.5_percent	0.028
OPTN-D5	PSAP-E5	OPTN-D5,PSAP-E5	SC_2.5_percent	0.028
GCH1-1	OPTN-D5	GCH1-1,OPTN-D5	SC_2.5_percent	0.028
C9orf72-F1	PINK1-2	C9orf72-F1,PINK1-2	SC_2.5_percent	0.028
SQSTM1-C6	TAX1BP1-2	SQSTM1-C6,TAX1BP1-2	SC_2.5_percent	0.028
CTSL-1	HNRNPA2B1-B4	CTSL-1,HNRNPA2B1-B4	SC_2.5_percent	0.028
C9orf72-F1	OPTN-D5	C9orf72-F1,OPTN-D5	SC_2.5_percent	0.029
GRN-F3	NBR1-1	GRN-F3,NBR1-1	SC_2.5_percent	0.029
C9orf72-F1	MCCC1-1	C9orf72-F1,MCCC1-1	SC_2.5_percent	0.030
CLN5-I17-1885	SCARB2-2	CLN5-I17-1885,SCARB2-2	SC_2.5_percent	0.030
MCCC1-1	TMEM106B-E7	MCCC1-1,TMEM106B-E7	SC_2.5_percent	0.030
VAPB-1	VCP_m-4	VAPB-1,VCP_m-4	SC_2.5_percent	0.030
ALS2-1	NBR1-1	ALS2-1,NBR1-1	SC_2.5_percent	0.030
ATP13A2-2	MCCC1-1	ATP13A2-2,MCCC1-1	SC_2.5_percent	0.030
SNCA-2	VAPB-1	SNCA-2,VAPB-1	SC_2.5_percent	0.031
FUS-A3	VPS13C-1	FUS-A3,VPS13C-1	SC_2.5_percent	0.031
ATP6V0A1-1	SCARB2-2	ATP6V0A1-1,SCARB2-2	SC_2.5_percent	0.031
CTSL-1	SQSTM1-C6	CTSL-1,SQSTM1-C6	SC_2.5_percent	0.032
CLN8-1	GRN-F3	CLN8-1,GRN-F3	SC_2.5_percent	0.032
CRLS1-2	GBA-1	CRLS1-2,GBA-1	SC_2.5_percent	0.032
CTSL-1	PARK7-2	CTSL-1,PARK7-2	SC_2.5_percent	0.032
SQSTM1-C6	VPS13C-1	SQSTM1-C6,VPS13C-1	SC_2.5_percent	0.033
UBQLN2-C8	VCP-G8	UBQLN2-C8,VCP-G8	SC_2.5_percent	0.033
CLN5	PARK7-2	CLN5,PARK7-2	SC_2.5_percent	0.033
ATP6V0A1-1	HNRNPA2B1-B4	ATP6V0A1-1,HNRNPA2B1-B4	SC_2.5_percent	0.033
NAGLU-1	PFN1-1	NAGLU-1,PFN1-1	SC_2.5_percent	0.034
CTSB-2	VPS13C-1	CTSB-2,VPS13C-1	SC_2.5_percent	0.034
SNCA-2	UBQLN2-C8	SNCA-2,UBQLN2-C8	SC_2.5_percent	0.034
CHMP2B-F2	SQSTM1-C6	CHMP2B-F2,SQSTM1-C6	SC_2.5_percent	0.035
ALS2-1	ATP6V0A1-1	ALS2-1,ATP6V0A1-1	SC_2.5_percent	0.035
NEU1-2	TBK1-A7	NEU1-2,TBK1-A7	SC_2.5_percent	0.035
CLN5	CTSD-2	CLN5,CTSD-2	SC_2.5_percent	0.035
PSAP-E5	TAX1BP1-2	PSAP-E5,TAX1BP1-2	SC_2.5_percent	0.036
STX17-2	VCP-G8	STX17-2,VCP-G8	SC_2.5_percent	0.036
C9orf72-F1	PARK2-2	C9orf72-F1,PARK2-2	SC_2.5_percent	0.036
TAX1BP1-2	VPS35-2	TAX1BP1-2,VPS35-2	SC_2.5_percent	0.036
GBA-1	NBR1-1	GBA-1,NBR1-1	SC_2.5_percent	0.036
ALS2-1	ANXA11-B1	ALS2-1,ANXA11-B1	SC_2.5_percent	0.036
CTSL-1	GRN-F3	CTSL-1,GRN-F3	SC_2.5_percent	0.036
ATP6V0A1-1	PINK1-2	ATP6V0A1-1,PINK1-2	SC_2.5_percent	0.036
MCCC1-1	VAPB-1	MCCC1-1,VAPB-1	SC_2.5_percent	0.037
GALC-2	VPS13C-1	GALC-2,VPS13C-1	SC_2.5_percent	0.037
OPTN-D5	VCP-G8	OPTN-D5,VCP-G8	SC_2.5_percent	0.038
GUSB-1	VPS13C-1	GUSB-1,VPS13C-1	SC_2.5_percent	0.038
CRLS1-2	VCP-G8	CRLS1-2,VCP-G8	SC_2.5_percent	0.040
GBA-1	SETX-A6	GBA-1,SETX-A6	SC_2.5_percent	0.040
CLN5	GCH1-1	CLN5,GCH1-1	SC_2.5_percent	0.040
ALS2-1	CHMP2B-F2	ALS2-1,CHMP2B-F2	SC_2.5_percent	0.040
ATP13A2-2	PSAP-E5	ATP13A2-2,PSAP-E5	SC_2.5_percent	0.041
CTSB-2	FUS-A3	CTSB-2,FUS-A3	SC_2.5_percent	0.041
HNRNPA2B1-B4	PINK1-2	HNRNPA2B1-B4,PINK1-2	SC_2.5_percent	0.041
CTSL-1	SNCA-2	CTSL-1,SNCA-2	SC_2.5_percent	0.042
OPTN-D5	PFN1-1	OPTN-D5,PFN1-1	SC_2.5_percent	0.043
SOD1-1	VPS35-2	SOD1-1,VPS35-2	SC_2.5_percent	0.046
GRN-F3	GUSB-1	GRN-F3,GUSB-1	SC_2.5_percent	0.047
NEU1-2	PARK7-2	NEU1-2,PARK7-2	SC_2.5_percent	0.049
CLN5	PARK2-2	CLN5,PARK2-2	SC_2.5_percent	0.049
CTSD-2	SCARB2-2	CTSD-2,SCARB2-2	SC_2.5_percent	0.050
PARK2-2	PINK1-2	PARK2-2,PINK1-2	SC_2.5_percent	0.051
OPTN-D5	PARK7-2	OPTN-D5,PARK7-2	SC_2.5_percent	0.051
ATP6V0A1-1	SETX-A6	ATP6V0A1-1,SETX-A6	SC_2.5_percent	0.053
SCARB2-2	SETX-A6	SCARB2-2,SETX-A6	SC_2.5_percent	0.053
CTSD-2	SQSTM1-C6	CTSD-2,SQSTM1-C6	SC_2.5_percent	0.055
ATP13A2-2	VCP-G8	ATP13A2-2,VCP-G8	SC_2.5_percent	0.055
ALS2-1	CTSB-2	ALS2-1,CTSB-2	SC_2.5_percent	0.056

Table C.1 continued from previous page

Gene1	Gene2	Combination Reference	Category	Interaction Score
ATP6V0A1-1	PSAP-E5	ATP6V0A1-1,PSAP-E5	SC_2.5_percent	0.056
GALC-2	PINK1-2	GALC-2,PINK1-2	SC_2.5_percent	0.059
CLN8-1	NBR1-1	CLN8-1,NBR1-1	SC_2.5_percent	0.070
SNCA-2	VCP-G8	SNCA-2,VCP-G8	PD_related	-
GBA-1	PARK7-2	GBA-1,PARK7-2	PD_related	-
PARK7-2	NBR1-1	NBR1-1,PARK7-2	PD_related	-
CTSB-2	GRN-F3	CTSB-2,GRN-F3	GRN_related	-
CTSD-2	GRN-F3	CTSD-2,GRN-F3	GRN_related	-
GRN-F3	PSAP-E5	GRN-F3,PSAP-E5	GRN_related	-
GRN-F3	TMEM106B-E7	GRN-F3,TMEM106B-E7	GRN_related	-
TARDBP-E6,VPS35-2	TARDBP-E6	VPS35-2	334_49_prev_method	-
CTSB-2	PARK2-2	CTSB-2,PARK2-2	334_49_prev_method	-
C9orf72-F1	CTSB-2	C9orf72-F1,CTSB-2	334_49_prev_method	-
CALCOCO2-1	CTSB-2	CALCOCO2-1,CTSB-2	334_49_prev_method	-
CTSB-2	OPTN-D5	CTSB-2,OPTN-D5	334_49_prev_method	-
GUSB-1	SETX-A6	GUSB-1,SETX-A6	334_49_prev_method	-
NBR1-1	OPTN-D5	NBR1-1,OPTN-D5	334_49_prev_method	-
CTSB-2	PARK7-2	CTSB-2,PARK7-2	334_49_prev_method	-
CTSD-2	SETX-A6	CTSD-2,SETX-A6	334_49_prev_method	-
CTSB-2	PINK1-2	CTSB-2,PINK1-2	334_49_prev_method	-
GUSB-1	PARK2-2	GUSB-1,PARK2-2	334_49_prev_method	-
ATP6V0A1-1	TARDBP-E6	ATP6V0A1-1,TARDBP-E6	334_49_prev_method	-
HNRNPA2B1-B4	TARDBP-E6	HNRNPA2B1-B4,TARDBP-E6	334_49_prev_method	-
PINK1-2	VAPB-1	PINK1-2,VAPB-1	334_49_prev_method	-
ATP13A2-2	PFN1-1	ATP13A2-2,PFN1-1	334_49_prev_method	-
ATP13A2-2	VAPB-1	ATP13A2-2,VAPB-1	334_49_prev_method	-
STX17-2	TARDBP-E6	STX17-2,TARDBP-E6	334_49_prev_method	-
NEU1-2	TARDBP-E6	NEU1-2,TARDBP-E6	334_49_prev_method	-
ANXA11-B1	TARDBP-E6	ANXA11-B1,TARDBP-E6	334_49_prev_method	-
TARDBP-E6	VAPB-1	TARDBP-E6,VAPB-1	334_49_prev_method	-

References

[1] Fei Mao, John L. Robinson, Travis Unger, Marijan Posavi, Defne A. Amado, et al. "TMEM106B modifies TDP-43 pathology in human ALS brain and cell-based models of TDP-43 proteinopathy". In: *Acta Neuropathologica* 142.4 (2021), pp. 629–642.

[2] Hiroaki Suzuki and Masaaki Matsuoka. "The Lysosomal Trafficking Transmembrane Protein 106B Is Linked to Cell Death*". In: *Journal of Biological Chemistry* 291.41 (2016), pp. 21448–21460.

[3] N Finch, M M Carrasquillo, M Baker, N J Rutherford, G Coppola, et al. "TMEM106B regulates progranulin levels and the penetrance of FTLD in GRN mutation carriers". In: *Neurology* 76.5 (2011), pp. 467–474.

[4] Zoe A Klein, Hideyuki Takahashi, Mengxiao Ma, Massimiliano Stagi, Melissa Zhou, et al. "Loss of TMEM106B Ameliorates Lysosomal and Frontotemporal Dementia-Related Phenotypes in Progranulin-Deficient Mice." English. In: *Neuron* 95.2 (July 2017), 281–296.e6.

[5] Xiaolai Zhou, Lirong Sun, Owen Adam Brady, Kira A Murphy, and Fenghua Hu. "Elevated TMEM106B levels exaggerate lipofuscin accumulation and lysosomal dysfunction in aged mice with progranulin deficiency". English. In: *Acta Neuropathologica Communications* 5.1 (Jan. 2017), pp. 1–11.

[6] Marka van Blitterswijk, Bianca Mullen, Alexandra M Nicholson, Kevin F Bieniek, Michael G Heckman, et al. "TMEM106B protects C9ORF72 expansion carriers against frontotemporal dementia". English. In: *Acta Neuropathologica* 127.3 (Jan. 2014), pp. 397–406.

[7] J. Paul Luzio, Paul R. Pryor, and Nicholas A. Bright. "Lysosomes: fusion and function". In: *Nature Reviews Molecular Cell Biology* 8.8 (2007), pp. 622–632.

[8] J. Ross Buchan, Regina-Maria Kolaitis, J. Paul Taylor, and Roy Parker. "Eukaryotic Stress Granules Are Cleared by Autophagy and Cdc48/VCP Function". In: *Cell* 153.7 (2013), pp. 1461–1474.

[9] Anna M. Blokhuis, Max Koppers, Ewout J. N. Groen, Dianne M. A. van den Heuvel, Stefano Dini Modigliani, et al. "Comparative interactomics analysis of different ALS-associated proteins identifies converging molecular pathways". In: *Acta Neuropathologica* 132.2 (2016), pp. 175–196.

[10] Jee Bang, Salvatore Spina, and Bruce L Miller. "Frontotemporal dementia". English. In: *The Lancet* 386.10004 (Oct. 2015), pp. 1672–1682.

[11] Renata Teles Vieira, Leonardo Caixeta, Sergio Machado, Adriana Cardoso Silva, Antonio Egidio Nardi, et al. *Epidemiology of early-onset dementia: a review of the literature*. Tech. rep. June 2013, pp. 1–8.

[12] Terri L Petkau and Blair R Leavitt. "Progranulin in neurodegenerative disease". English. In: *Trends in Neurosciences* 37.7 (July 2014), pp. 388–398.

[13] T W Chow, B L Miller, V N Hayashi, and D H Geschwind. "Inheritance of frontotemporal dementia." English. In: *Archives of neurology* 56.7 (July 1999), pp. 817–822.

[14] Catarina Falcão Campos, Marta Gromicho, Hilmi Uysal, Julian Grosskreutz, Magdalena Kuzma-Kozakiewicz5, et al. "Family history of neurodegenerative disorders in patients with amyotrophic lateral sclerosis: population-based case–control study". In: *Journal of Neurology, Neurosurgery & Psychiatry* 91.6 (2020), pp. 671–672.

[15] Matt Baker, Ian R Mackenzie, Stuart M Pickering-Brown, Jennifer Gass, Rosa Rademakers, et al. "Mutations in progranulin cause tau-negative frontotemporal dementia linked to chromosome 17". In: *Nature* 442.7105 (July 2006), pp. 916–919.

[16] Katherine R Smith, John Damiano, Silvana Franceschetti, Stirling Carpenter, Laura Canafoglia, et al. "Strikingly Different Clinicopathological Phenotypes Determined by Progranulin-Mutation Dosage". English. In: *The American Journal of Human Genetics* 90.6 (June 2012), pp. 1102–1107.

[17] M.E. Ward, A. Taubes, R. Chen, B.L. Miller, C.F. Sephton, et al. "Early retinal neurodegeneration and impaired Ran-mediated nuclear import of TDP-43 in progranulin-deficient FTLD". English. In: *Journal of Experimental Medicine* 211.10 (2014), pp. 1937–1945.

[18] M.E. Ward, R. Chen, H.-Y. Huang, C. Ludwig, M. Telpoukhovskaia, et al. "Individuals with progranulin haploinsufficiency exhibit features of neuronal ceroid lipofuscinosis". English. In: *Science Translational Medicine* 9.385 (2017), eaah5642.

[19] Dmitri Tolkatchev, Suneil Malik, Anna Vinogradova, Ping Wang, Zhigang Chen, et al. "Structure dissection of human progranulin identifies well-folded granulin/epithelin modules with unique functional activities". English. In: *Protein Science* 17.4 (Apr. 2008), pp. 711–724.

[20] Jennifer Gass, Wing C Lee, Casey Cook, Nicole Finch, Caroline Stetler, et al. "Progranulin regulates neuronal outgrowth independent of Sortilin". English. In: *Molecular Neurodegeneration* 7.1 (2012), p. 33.

[21] B Cenik, C F Sephton, B Kutluk Cenik, J Herz, and G Yu. "Progranulin: A Proteolytically Processed Protein at the Crossroads of Inflammation and Neurodegeneration". English. In: *Journal of Biological Chemistry* 287.39 (Sept. 2012), pp. 32298–32306.

[22] Zhiheng He, Colin H P Ong, Jaroslava Halper, and Andrew Bateman. "Progranulin is a mediator of the wound response". English. In: *Nature Medicine* 9.2 (Jan. 2003), pp. 225–229.

[23] Clarissa Valdez, Yvette C Wong, Michael Schwake, Guojun Bu, Zbigniew K Wszolek, et al. "Progranulin-mediated deficiency of cathepsin D results in FTD and NCL-like phenotypes in neurons derived from FTD patients". English. In: *Human Molecular Genetics* (Sept. 2017), pp. 1–12.

[24] Alessandro Simonati and Ruth E. Williams. “Neuronal Ceroid Lipofuscinosis: The Multifaceted Approach to the Clinical Issues, an Overview”. In: *Frontiers in Neurology* 13 (2022), p. 811686.

[25] Haoxing Xu and Dejian Ren. “Lysosomal Physiology”. In: *Annual Review of Physiology* 77.1 (2015), pp. 57–80.

[26] Laura Canafoglia, Michela Morbin, Vidmer Scaioli, Davide Pareyson, Ludovico D’Incerti, et al. “Recurrent generalized seizures, visual loss, and palinopsia as phenotypic features of neuronal ceroid lipofuscinosis due to progranulin gene mutation”. English. In: *Epilepsia* 55.6 (Apr. 2014), e56–e59.

[27] Lonneke ML de Lau and Monique MB Breteler. “Epidemiology of Parkinson’s disease”. In: *The Lancet Neurology* 5.6 (2006), pp. 525–535.

[28] E. Ray Dorsey and Bastiaan R. Bloem. “The Parkinson Pandemic—A Call to Action”. In: *JAMA Neurology* 75.1 (2017), p. 9.

[29] Sigurlaug Sveinbjornsdottir. “The clinical symptoms of Parkinson’s disease”. In: *Journal of Neurochemistry* 139.S1 (2016), pp. 318–324.

[30] Dennis W Dickson, Heiko Braak, John E Duda, Charles Duyckaerts, Thomas Gasser, et al. “Neuropathological assessment of Parkinson’s disease: refining the diagnostic criteria”. In: *The Lancet Neurology* 8.12 (2009), pp. 1150–1157.

[31] Glenda M. Halliday, Janice L. Holton, Tamas Revesz, and Dennis W. Dickson. “Neuropathology underlying clinical variability in patients with synucleinopathies”. In: *Acta Neuropathologica* 122.2 (2011), pp. 187–204.

[32] I.G. McKeith, D. Galasko, K. Kosaka, E.K. Perry, D.W. Dickson, et al. “Consensus guidelines for the clinical and pathologic diagnosis of dementia with Lewy bodies (DLB)”. In: *Neurology* 47.5 (1996), pp. 1113–1124.

[33] Christine Klein and Ana Westenberger. “Genetics of Parkinson’s Disease”. In: *Cold Spring Harbor Perspectives in Medicine* 2.1 (2012), a008888.

[34] Douglas J. Gelb, Eugene Oliver, and Sid Gilman. “Diagnostic Criteria for Parkinson Disease”. In: *Archives of Neurology* 56.1 (1999), pp. 33–39.

[35] Olivier Rascol, Pierre Payoux, Fabienne Ory, Joaquim J. Ferreira, Christine Brefel-Courbon, et al. “Limitations of current Parkinson’s disease therapy”. In: *Annals of Neurology* 53.S3 (2003), S3–S15.

[36] Tanvi Pingale and Girdhari Lal Gupta. “Current and emerging therapeutic targets for Parkinson’s disease”. In: *Metabolic Brain Disease* 36.1 (2021), pp. 13–27.

[37] Sumit Das, Zach Zhang, and Lee Cyn Ang. “Clinicopathological overlap of neurodegenerative diseases: A comprehensive review”. In: *Journal of Clinical Neuroscience* 78 (2020), pp. 30–33.

[38] A Kertesz, P McMonagle, and S Jesso. “Extrapyramidal syndromes in frontotemporal degeneration”. English. In: *Journal of Molecular Neuroscience* 45.3 (Nov. 2011), pp. 336–342.

[39] Douglas P Wightman, Jeanne E Savage, Elleke Tissink, Cato Romero, Iris E Jansen, et al. “The genetic overlap between Alzheimer’s disease, amyotrophic lateral sclerosis, Lewy body dementia, and Parkinson’s disease”. In: (2022).

[40] R.L. Wallings, S.W. Humble, M.E. Ward, and R. Wade-Martins. "Lysosomal Dysfunction at the Centre of Parkinson's Disease and Frontotemporal Dementia/Amyotrophic Lateral Sclerosis". In: *Trends in Neurosciences* 42.12 (2019), pp. 899–912.

[41] Alexander P. Marsh. "Molecular mechanisms of proteinopathies across neurodegenerative disease: a review". In: *Neurological Research and Practice* 1.1 (2019), p. 35.

[42] Celine Deneubourg, Mauricio Ramm, Luke J. Smith, Olga Baron, Kritarth Singh, et al. "The spectrum of neurodevelopmental, neuromuscular and neurodegenerative disorders due to defective autophagy". In: *Autophagy* 18.3 (2022), pp. 496–517.

[43] Michael T. Hayes. "Parkinson's Disease and Parkinsonism". In: *The American Journal of Medicine* 132.7 (2019), pp. 802–807.

[44] Eduardo Tolosa, Gregor Wenning, and Werner Poewe. "The diagnosis of Parkinson's disease". In: *The Lancet Neurology* 5.1 (2006), pp. 75–86.

[45] A Cannas, P Solla, G Borghero, G L Floris, A Chio, et al. "C9ORF72 intermediate repeat expansion in patients affected by atypical parkinsonian syndromes or Parkinson's disease complicated by psychosis or dementia in a Sardinian population". English. In: *J Neurol* 262.11 (Nov. 2015), pp. 2498–2503.

[46] José Fidel Baizabal-Carvallo and Joseph Jankovic. "Parkinsonism, movement disorders and genetics in frontotemporal dementia". English. In: *Nature Reviews Neurology* 12.3 (2016), pp. 175–185.

[47] Manuel Menéndez-González, Tania Álvarez-Avellón, José M Salas-Pacheco, Benito De Celis-Alonso, Kathryn A Wyman-Chick, et al. "Frontotemporal Lobe Degeneration as Origin of Scans Without Evidence of Dopaminergic Deficit". In: *Frontiers in Neurology* 9 (2018), p. 146.

[48] Hee Kyung Park, Kee Hyung Park, Bora Yoon, Jae-Hong Lee, Seong Hye Choi, et al. "Clinical characteristics of parkinsonism in frontotemporal dementia according to subtypes". English. In: *Journal of the Neurological Sciences* 372 (Jan. 2017), pp. 51–56.

[49] Alexander V Lebedev, Eric Westman, Andrew Simmons, Aleksandra Lebedeva, Franã Oise J Siepel, et al. "Large-scale resting state network correlates of cognitive impairment in Parkinson's disease and related dopaminergic deficits". In: *Frontiers in Systems Neuroscience* 8.13 (2014), p. 1121.

[50] Tammaryn Lashley, Jonathan D Rohrer, Simon Mead, and Tamas Revesz. "Review: an update on clinical, genetic and pathological aspects of frontotemporal lobar degenerations." English. In: *Neuropathology and applied neurobiology* 41.7 (Dec. 2015), pp. 858–881.

[51] Diana Chang, Mike A Nalls, Ingileif B Hallgrímsdóttir, Julie Hunkapiller, Marcel van der Brug, et al. "A meta-analysis of genome-wide association studies identifies 17 new Parkinson's disease risk loci." English. In: *Nature Publishing Group* 49.10 (Oct. 2017), pp. 1511–1516.

[52] Laurie A Robak, Iris E Jansen, Jeroen van Rooij, André G Uitterlinden, Robert Kraaij, et al. "Excessive burden of lysosomal storage disorder gene variants in Parkinson's disease." English. In: *Brain* 140.12 (Dec. 2017), pp. 3191–3203.

[53] E Dagan, I Schlesinger, M Ayoub, A Mory, M Nassar, et al. "The contribution of Niemann-Pick SMPD1 mutations to Parkinson disease in Ashkenazi Jews". English. In: *Parkinsonism & related disorders* 21.9 (2015), pp. 1067–1071.

[54] Shuo-Chien Ling, Magdalini Polymenidou, and Don W Cleveland. "Converging Mechanisms in ALS and FTD: Disrupted RNA and Protein Homeostasis". In: *Neuron* 79.3 (Aug. 2013), pp. 416–438.

[55] Joseph Amick and Shawn M Ferguson. "C9orf72: At the intersection of lysosome cell biology and neurodegenerative disease." English. In: *Traffic (Copenhagen, Denmark)* 18.5 (May 2017), pp. 267–276.

[56] Joseph Amick, Agnes Roczniak-Ferguson, and Shawn M Ferguson. "C9orf72 binds SMCR8, localizes to lysosomes, and regulates mTORC1 signaling". English. In: *Molecular Biology of the Cell* 27.20 (Oct. 2016). Ed. by Julie Brill, pp. 3040–3051.

[57] Chao Wang, Maria A Telpoukhovskaia, Ben A Bahr, Xu Chen, and Li Gan. "Endo-lysosomal dysfunction: a converging mechanism in neurodegenerative diseases". English. In: *Current Opinion in Neurobiology* 48 (Feb. 2018), pp. 52–58.

[58] Hung Phuoc Nguyen, Christine Van Broeckhoven, and Julie van der Zee. "ALS Genes in the Genomic Era and their Implications for FTD." English. In: *Trends in genetics : TIG* 34.6 (June 2018), pp. 404–423.

[59] Kurt J. De Vos and Majid Hafezparast. "Neurobiology of axonal transport defects in motor neuron diseases: Opportunities for translational research?" In: *Neurobiology of Disease* 105 (2017), pp. 283–299.

[60] Raffaele Ferrari, Demis A Kia, James E Tomkins, John Hardy, Nicholas W Wood, et al. "Stratification of candidate genes for Parkinson's disease using weighted protein-protein interaction network analysis." English. In: *BMC genomics* 19.1 (June 2018), p. 452.

[61] Chengyuan Mao, Herui Wang, Haiyang Luo, Shuyu Zhang, Huisha Xu, et al. "CHCHD10 is involved in the development of Parkinson's disease caused by CHCHD2 loss-of-function mutation p.T61I". English. In: *Neurobiology of aging* 75 (Mar. 2019), pp. 38–41.

[62] Ralph A. Nixon. "The aging lysosome: An essential catalyst for late-onset neurodegenerative diseases". In: *Biochimica et Biophysica Acta (BBA) - Proteins and Proteomics* 1868.9 (2020), p. 140443.

[63] Patricia García-Sanz, Lorena Orgaz, José M Fuentes, Carlos Vicario, and Rosario Moratalla. "Cholesterol and multilamellar bodies: Lysosomal dysfunction in GBA-Parkinson disease." English. In: *Autophagy* 14.4 (2018), pp. 717–718.

[64] Giulietta M. Riboldi and Alessio B. Di Fonzo. "GBA, Gaucher Disease, and Parkinson's Disease: From Genetic to Clinic to New Therapeutic Approaches". In: *Cells* 8.4 (2019), p. 364.

[65] Tania F Gendron and Leonard Petrucelli. "Disease Mechanisms of C9ORF72Repeat Expansions". English. In: *Cold Spring Harbor Perspectives in Medicine* 8.4 (Apr. 2018), a024224.

[66] Tobias B. Haack, Erika Ignatius, Javier Calvo-Garrido, Arcangela Iuso, Pirjo Isohanni, et al. "Absence of the Autophagy Adaptor SQSTM1/p62 Causes Childhood-Onset Neurodegeneration with Ataxia, Dystonia, and Gaze Palsy". In: *The American Journal of Human Genetics* 99.3 (Sept. 2016), pp. 735–743.

[67] Yin Xu, Sheng Zhang, and Hui Zheng. "The cargo receptor SQSTM1 ameliorates neurofibrillary tangle pathology and spreading through selective targeting of pathological MAPT (microtubule associated protein tau)." English. In: *Autophagy* (Oct. 2018), pp. 1–16.

[68] Christy O.Y. Hung and Frederick J. Livesey. "Altered γ-Secretase Processing of APP Disrupts Lysosome and Autophagosome Function in Monogenic Alzheimer's Disease". In: *Cell Reports* 25.13 (2018), 3647–3660.e2.

[69] Ju-Hyun Lee, Mary Kate McBrayer, Devin M Wolfe, Luke J Haslett, Asok Kumar, et al. "Presenilin 1 Maintains Lysosomal Ca2+ Homeostasis via TRPML1 by Regulating vATPase-Mediated Lysosome Acidification". English. In: *CellReports* 12.9 (Sept. 2015), pp. 1430–1444.

[70] Chiara Fedeli, Riccardo Filadi, Alice Rossi, Cristina Mammucari, and Paola Pizzo. "PSEN2 (presenilin 2) mutants linked to familial Alzheimer disease impair autophagy by altering Ca2+ homeostasis". In: *Autophagy* 15.12 (2019), pp. 2044–2062.

[71] Zoë P. Van Acker, Marine Bretou, and Wim Annaert. "Endo-lysosomal dysregulations and late-onset Alzheimer's disease: impact of genetic risk factors". In: *Molecular Neurodegeneration* 14.1 (2019), p. 20.

[72] Kathleen M Cunningham, Kirstin Maulding, Kai Ruan, Mumine Senturk, Jonathan C Grima, et al. "TFEB/Mitf links impaired nuclear import to autophagolysosomal dysfunction in C9-ALS". In: *eLife* 9 (2020), e59419.

[73] Mickael Decressac and Anders Björklund. "TFEB: Pathogenic role and therapeutic target in Parkinson disease". In: *Autophagy* 9.8 (2013), pp. 1244–1246.

[74] Phillippa J Carling, Brent J Ryan, William McGuinness, Shikha Kataria, Stewart W Humble, et al. "Multiparameter phenotypic screening for endogenous TFEB and TFE3 translocation identifies novel chemical series modulating lysosome function". In: *Autophagy* (2022), pp. 1–14.

[75] Zhongya Gu, Huan Cao, Chengchao Zuo, Yaqi Huang, Jinfeng Miao, et al. "TFEB in Alzheimer's disease: From molecular mechanisms to therapeutic implications". In: *Neurobiology of Disease* 173 (2022), p. 105855.

[76] Erin T. Williams, Xi Chen, P. Anthony Otero, and Darren J. Moore. "Understanding the contributions of VPS35 and the retromer in neurodegenerative disease". In: *Neurobiology of Disease* 170 (2022), p. 105768.

[77] A Zimprich, A Benet-Pages, W Struhal, E Graf, S H Eck, et al. "A mutation in VPS35, encoding a subunit of the retromer complex, causes late-onset Parkinson disease". English. In: *Am J Hum Genet* 89.1 (July 2011), pp. 168–175.

[78] Carles Vilariño-Güell, Christian Wider, Owen, Justus, Jennifer, et al. "VPS35 Mutations in Parkinson Disease". English. In: *The American Journal of Human Genetics* 89.1 (2011), pp. 162–167.

[79] Gina Puska, Mirjam I Lutz, Kinga Molnar, Günther Regelsberger, Gerda Ricken, et al. "Lysosomal response in relation to α-synuclein pathology differs between Parkinson's disease and multiple system atrophy." English. In: *Neurobiol Dis* 114 (June 2018), pp. 140–152.

[80] Sander Beel, Matthieu Moisse, Markus Damme, Louis De Muynck, Wim Robberecht, et al. "Progranulin functions as a cathepsin D chaperone to stimulate axonal outgrowth in vivo". English. In: *Human Molecular Genetics* 26.15 (Apr. 2017), pp. 2850–2863.

[81] Johannes van den Boom and Hemmo Meyer. "VCP/p97-Mediated Unfolding as a Principle in Protein Homeostasis and Signaling". English. In: *Molecular cell* 69.2 (Jan. 2018), pp. 182–194.

[82] Hugo, Elizabeth, Helen, Evangelia Emmanoulidou, Ying Zheng, et al. "ER Stress and Autophagic Perturbations Lead to Elevated Extracellular α-Synuclein in GBA-N370S Parkinson's iPSC-Derived Dopamine Neurons". English. In: *Stem Cell Reports* 6.3 (2016), pp. 342–356.

[83] Y V Taguchi, J Liu, J Ruan, J Pacheco, X Zhang, et al. "Glucosylsphingosine Promotes alpha-Synuclein Pathology in Mutant GBA-Associated Parkinson's Disease". English. In: *The Journal of neuroscience : the official journal of the Society for Neuroscience* 37.40 (Oct. 2017), pp. 9617–9631.

[84] Chuong B Do, Joyce Y Tung, Elizabeth Dorfman, Amy K Kiefer, Emily M Drabant, et al. "Web-Based Genome-Wide Association Study Identifies Two Novel Loci and a Substantial Genetic Component for Parkinson's Disease". English. In: *PLoS Genet* 7.6 (2011). Ed. by Greg Gibson, e1002141.

[85] Alfredo Ramirez, André Heimbach, Jan Gründemann, Barbara Stiller, Dan Hampshire, et al. "Hereditary parkinsonism with dementia is caused by mutations in ATP13A2, encoding a lysosomal type 5 P-type ATPase". English. In: *Nature genetics* 38.10 (2006), pp. 1184–1191.

[86] Jose Bras, Alain Verloes, Susanne A. Schneider, Sara E. Mole, and Rita J. Guerreiro. "Mutation of the parkinsonism gene ATP13A2 causes neuronal ceroid-lipofuscinosis". In: *Human Molecular Genetics* 21.12 (2012), pp. 2646–2650.

[87] Anastasia G Henry, Soheil Aghamohammadzadeh, Harry Samaroo, Yi Chen, Kewa Mou, et al. "Pathogenic LRRK2 mutations, through increased kinase activity, produce enlarged lysosomes with reduced degradative capacity and increase ATP13A2 expression." English. In: *Hum Mol Genet* 24.21 (Nov. 2015), pp. 6013–6028.

[88] S Sato, M Koike, M Funayama, J Ezaki, T Fukuda, et al. "Lysosomal Storage of Subunit c of Mitochondrial ATP Synthase in Brain-Specific Atp13a2-Deficient Mice". English. In: *Am J Pathol* 186.12 (Dec. 2016), pp. 3074–3082.

[89] Tine Holemans, Danny Mollerup Sørensen, Sarah Van Veen, Shaun Martin, Diane Hermans, et al. "A lipid switch unlocks Parkinson's disease-associated ATP13A2". English. In: *Proceedings of the National Academy of Sciences* 112.29 (2015), pp. 9040–9045.

[90] Faisal Fecto, Jianhua Yan, S Pavan Vemula, Erdong Liu, Yi Yang, et al. "SQSTM1 mutations in familial and sporadic amyotrophic lateral sclerosis." English. In: *Archives of neurology* 68.11 (Nov. 2011), pp. 1440–1446.

[91] Makito Hirano, Yusaku Nakamura, Kazumasa Saigoh, Hikaru Sakamoto, Shuichi Ueno, et al. "Mutations in the gene encoding p62 in Japanese patients with amyotrophic lateral sclerosis." English. In: *Neurology* 80.5 (Jan. 2013), pp. 458–463.

[92] Elisa Rubino, Innocenzo Rainero, Adriano Chiò, Ekaterina Rogaeva, Daniela Galimberti, et al. "SQSTM1 mutations in frontotemporal lobar degeneration and amyotrophic lateral sclerosis." English. In: *Neurology* 79.15 (Oct. 2012), pp. 1556–1562.

[93] Isabelle Le Ber, Agnès Camuzat, Rita Guerreiro, Kawtar Bouya-Ahmed, Jose Bras, et al. "SQSTM1 mutations in French patients with frontotemporal dementia or frontotemporal dementia with amyotrophic lateral sclerosis." English. In: *JAMA Neurology* 70.11 (Nov. 2013), pp. 1403–1410.

[94] Julia K Götzl, Christina M Lang, Christian Haass, and Anja Capell. "Impaired protein degradation in FTLD and related disorders." English. In: *Ageing Research Reviews* 32 (Dec. 2016), pp. 122–139.

[95] Giles D J Watts, Jill Wymer, Margaret J Kovach, Sarju G Mehta, Steven Mumm, et al. "Inclusion body myopathy associated with Paget disease of bone and frontotemporal dementia is caused by mutant valosin-containing protein." English. In: *Nature genetics* 36.4 (Apr. 2004), pp. 377–381.

[96] Janel O Johnson, Jessica Mandrioli, Michael Benatar, Yevgeniya Abramzon, Vivianna M Van Deerlin, et al. "Exome sequencing reveals VCP mutations as a cause of familial ALS." English. In: *Neuron* 68.5 (Dec. 2010), pp. 857–864.

[97] Emilie Tresse, Florian A Salomons, Jouni Vesa, Laura C Bott, Virginia Kimonis, et al. "VCP/p97 is essential for maturation of ubiquitin-containing autophagosomes and this function is impaired by mutations that cause IBMPFD". English. In: *Autophagy* 6.2 (Oct. 2014), pp. 217–227.

[98] Nam Chul Kim, Emilie Tresse, Regina-Maria Kolaitis, Amandine Molliex, Ruth E Thomas, et al. "VCP is essential for mitochondrial quality control by PINK1/Parkin and this function is impaired by VCP mutations." English. In: *Neuron* 78.1 (Apr. 2013), pp. 65–80.

[99] Ana C Bento, Claudia C Bippes, Corina Kohler, Charles Hemion, Stephan Frank, et al. "UBXD1 is a mitochondrial recruitment factor for p97/VCP and promotes mitophagy." English. In: *Sci Rep* 8.1 (Aug. 2018), p. 12415.

[100] Chrisovalantis Papadopoulos, Philipp Kirchner, Monika Bug, Daniel Grum, Lisa Koerver, et al. "VCP/p97 cooperates with YOD1, UBXD1 and PLAA to drive clearance of ruptured lysosomes by autophagy." English. In: *EMBO J* 36.2 (Jan. 2017), pp. 135–150.

[101] Chi-Hong Wu, Claudia Fallini, Nicola Ticozzi, Pamela J Keagle, Peter C Sapp, et al. "Mutations in the profilin 1 gene cause familial amyotrophic lateral sclerosis." English. In: *Nature* 488.7412 (Aug. 2012), pp. 499–503.

[102] Mina Nekouei, Parviz Ghezellou, Atousa Aliahmadi, Sareh Arjmand, Mahmoud Kiaei, et al. "Changes in biophysical characteristics of PFN1 due to mutation causing amyotrophic lateral sclerosis." English. In: *Metabolic brain disease* 33.6 (Dec. 2018), pp. 1975–1984.

[103] Yoshinori Tanaka, Takashi Nonaka, Genjiro Suzuki, Fuyuki Kametani, and Masato Hasegawa. "Gain-of-function profilin 1 mutations linked to familial amyotrophic lateral sclerosis cause seed-dependent intracellular TDP-43 aggregation." English. In: *Human Molecular Genetics* 25.7 (Apr. 2016), pp. 1420–1433.

[104] C P Webster, E F Smith, C S Bauer, A Moller, G M Hautbergue, et al. "The C9orf72 protein interacts with Rab1a and the ULK1 complex to regulate initiation of autophagy". English. In: *EMBO J* 35.15 (Aug. 2016), pp. 1656–1676.

[105] Chantal Sellier, Maria-Letizia Campanari, Camille Julie Corbier, Angeline Gaucherot, Isabelle Kolb-Cheynel, et al. "Loss of C9ORF72 impairs autophagy and synergizes with polyQ Ataxin-2 to induce motor neuron dysfunction and cell death." English. In: *EMBO J* 35.12 (June 2016), pp. 1276–1297.

[106] Y Aoki, R Manzano, Y Lee, R Dafinca, M Aoki, et al. "C9orf72 and RAB7L1 regulate vesicle trafficking in amyotrophic lateral sclerosis and frontotemporal dementia". English. In: *Brain* 140.4 (Apr. 2017), pp. 887–897.

[107] S Almeida, E Gascon, H Tran, H J Chou, T F Gendron, et al. "Modeling key pathological features of frontotemporal dementia with C9ORF72 repeat expansion in iPSC-derived human neurons". English. In: *Acta Neuropathol* 126.3 (Sept. 2013), pp. 385–399.

[108] Maneka Chitiprolu, Chantal Jagow, Veronique Tremblay, Emma Bondy-Chorney, Geneviève Paris, et al. "A complex of C9ORF72 and p62 uses arginine methylation to eliminate stress granules by autophagy." English. In: *Nature Communications* 9.1 (July 2018), p. 2794.

[109] C Bussi, J M Peralta Ramos, D S Arroyo, J I Gallea, P Ronchi, et al. "Alpha-synuclein fibrils recruit TBK1 and OPTN to lysosomal damage sites and induce autophagy in microglial cells". English. In: *J Cell Sci* 131.23 (Nov. 2018), jcs226241.

[110] Rebecca Wallings, Natalie Connor-Robson, and Richard Wade-Martins. "LRRK2 interacts with the vacuolar-type H+-ATPase pump a1 subunit to regulate lysosomal function." English. In: *Human Molecular Genetics* (Apr. 2019).

[111] Sarah Jinn, Robert E Drolet, Paige E Cramer, Andus Hon-Kit Wong, Dawn M Toolan, et al. "TMEM175 deficiency impairs lysosomal and mitochondrial function and increases α-synuclein aggregation." English. In: *Proceedings of the National Academy of Sciences of the United States of America* 114.9 (Feb. 2017), pp. 2389–2394.

[112] Carla F Bento, Avraham Ashkenazi, Maria Jimenez Sanchez, and David C Rubinsztein. "The Parkinson's disease-associated genes ATP13A2 and SYT11 regulate autophagy via a common pathway." English. In: *Nature Communications* 7.1 (June 2016), p. 11803.

[113] D A Salazar, V J Butler, A R Argouarch, T Y Hsu, A Mason, et al. "The Progranulin Cleavage Products, Granulins, Exacerbate TDP-43 Toxicity and Increase TDP-43 Levels". English. In: *The Journal of neuroscience : the official journal of the Society for Neuroscience* 35.25 (June 2015), pp. 9315–9328.

[114] Q Xia, H Wang, Z Hao, C Fu, Q Hu, et al. "TDP-43 loss of function increases TFEB activity and blocks autophagosome-lysosome fusion". English. In: *EMBO J* 35.2 (Jan. 2016), pp. 121–142.

[115] C J Holler, G Taylor, Q Deng, and T Kukar. "Intracellular Proteolysis of Progranulin Generates Stable, Lysosomal Granulins that Are Haploinsufficient in Patients with Frontotemporal Dementia Caused by GRN Mutations". English. In: *eNeuro* 4.4 (2017), ENEURO.0100–17.2017.

[116] Yoshinori Tanaka, Genjiro Suzuki, Takashi Matsuwaki, Masato Hosokawa, Geidy Serrano, et al. "Progranulin regulates lysosomal function and biogenesis through acidification of lysosomes." English. In: *Hum Mol Genet* 26.5 (Mar. 2017), pp. 969–988.

[117] Emma L Clayton, Carmelo Milioto, Bhavana Muralidharan, Frances E Norona, James R Edgar, et al. "Frontotemporal dementia causative CHMP2B impairs neuronal endolysosomal traffic-rescue by TMEM106B knockdown". English. In: *Brain* 141.12 (2018), pp. 3428–3442.

[118] Kazutoshi Takahashi and Shinya Yamanaka. "Induction of Pluripotent Stem Cells from Mouse Embryonic and Adult Fibroblast Cultures by Defined Factors". In: *Cell* 126.4 (2006), pp. 663–676.

[119] Fuguo Jiang and Jennifer A. Doudna. "CRISPR–Cas9 Structures and Mechanisms". In: *Annual Review of Biophysics* 46.1 (2015), pp. 1–25.

[120] Y Ishino, H Shinagawa, K Makino, M Amemura, and A Nakata. "Nucleotide sequence of the iap gene, responsible for alkaline phosphatase isozyme conversion in Escherichia coli, and identification of the gene product". In: *Journal of Bacteriology* 169.12 (1987), pp. 5429–5433.

[121] Frank Hille and Emmanuelle Charpentier. "CRISPR-Cas: biology, mechanisms and relevance". In: *Philosophical Transactions of the Royal Society B: Biological Sciences* 371.1707 (2016), p. 20150496.

[122] Luciano A. Marraffini. "CRISPR-Cas immunity in prokaryotes". In: *Nature* 526.7571 (2015), pp. 55–61.

[123] Francisco J. M. Mojica and Francisco Rodriguez-Valera. "The discovery of CRISPR in archaea and bacteria". In: *The FEBS Journal* 283.17 (2016), pp. 3162–3169.

[124] Alexander Bolotin, Benoit Quinquis, Alexei Sorokin, and S. Dusko Ehrlich. "Clustered regularly interspaced short palindrome repeats (CRISPRs) have spacers of extrachromosomal origin". In: *Microbiology* 151.8 (2005), pp. 2551–2561.

[125] Giedrius Gasiunas, Rodolphe Barrangou, Philippe Horvath, and Virginijus Siksnys. "Cas9–crRNA ribonucleoprotein complex mediates specific DNA cleavage for adaptive immunity in bacteria". In: *Proceedings of the National Academy of Sciences* 109.39 (2012), E2579–E2586.

[126] Martin Jinek, Krzysztof Chylinski, Ines Fonfara, Michael Hauer, Jennifer A. Doudna, et al. "A Programmable Dual-RNA–Guided DNA Endonuclease in Adaptive Bacterial Immunity". In: *Science* 337.6096 (2012), pp. 816–821.

[127] Le Cong, F. Ann Ran, David Cox, Shuailiang Lin, Robert Barretto, et al. "Multiplex Genome Engineering Using CRISPR/Cas Systems". In: *Science* 339.6121 (2013), pp. 819–823.

[128] Irina Gostimskaya. "CRISPR–Cas9: A History of Its Discovery and Ethical Considerations of Its Use in Genome Editing". In: *Biochemistry (Moscow)* 87.8 (2022), pp. 777–788.

[129] Lei S. Qi, Matthew H. Larson, Luke A. Gilbert, Jennifer A. Doudna, Jonathan S. Weissman, et al. "Repurposing CRISPR as an RNA-Guided Platform for Sequence-Specific Control of Gene Expression". In: *Cell* 152.5 (2013), pp. 1173–1183.

[130] Andrew Fire, SiQun Xu, Mary K. Montgomery, Steven A. Kostas, Samuel E. Driver, et al. "Potent and specific genetic interference by double-stranded RNA in Caenorhabditis elegans". In: *Nature* 391.6669 (1998), pp. 806–811.

[131] Luke A. Gilbert, Matthew H. Larson, Leonardo Morsut, Zairan Liu, Gloria A. Brar, et al. "CRISPR-Mediated Modular RNA-Guided Regulation of Transcription in Eukaryotes". In: *Cell* 154.2 (2013), pp. 442–451.

[132] Luke A. Gilbert, Max A. Horlbeck, Britt Adamson, Jacqueline E. Villalta, Yuwen Chen, et al. "Genome-Scale CRISPR-Mediated Control of Gene Repression and Activation". In: *Cell* 159.3 (2014), pp. 647–661.

[133] Bastiaan Evers, Katarzyna Jastrzebski, Jeroen P M Heijmans, Wipawadee Grernrum, Roderick L Beijersbergen, et al. "CRISPR knockout screening outperforms shRNA and CRISPRi in identifying essential genes". In: *Nature Biotechnology* 34.6 (2016), pp. 631–633.

[134] Alan Cabera, Hailey I. Edelstein, Fokion Glykofrydis, Kasey S. Love, Sebastian Palacios, et al. "The sound of silence: Transgene silencing in mammalian cell engineering". In: *Cell Systems* 13.12 (2022), pp. 950–973.

[135] Kazutoshi Takahashi, Koji Tanabe, Mari Ohnuki, Megumi Narita, Tomoko Ichisaka, et al. "Induction of Pluripotent Stem Cells from Adult Human Fibroblasts by Defined Factors". In: *Cell* 131.5 (2007), pp. 861–872.

[136] Junying Yu, Maxim A. Vodyanik, Kim Smuga-Otto, Jessica Antosiewicz-Bourget, Jennifer L. Frane, et al. "Induced Pluripotent Stem Cell Lines Derived from Human Somatic Cells". In: *Science* 318.5858 (2007), pp. 1917–1920.

[137] Yingsha Zhang, ChangHui Pak, Yan Han, Henrik Ahlenius, Zhenjie Zhang, et al. "Rapid Single-Step Induction of Functional Neurons from Human Pluripotent Stem Cells". In: *Neuron* 78.5 (June 2013), pp. 785–798.

[138] C. Wang, M.E. Ward, R. Chen, K. Liu, T.E. Tracy, et al. "Scalable Production of iPSC-Derived Human Neurons to Identify Tau-Lowering Compounds by High-Content Screening". English. In: *Stem Cell Reports* 9.4 (2017), pp. 1221–1233.

[139] M.S. Fernandopulle, R. Prestil, C. Grunseich, C. Wang, L. Gan, et al. "Transcription Factor–Mediated Differentiation of Human iPSCs into Neurons". In: *Current Protocols in Cell Biology* 79.1 (2018).

[140] R. Tian, M.A. Gachechiladze, C.H. Ludwig, M.T. Laurie, J.Y. Hong, et al. "CRISPR Interference-Based Platform for Multimodal Genetic Screens in Human iPSC-Derived Neurons". In: *Neuron* 104.2 (2019), 239–255.e12.

[141] A Saric, S Grinstein, and S A Freeman. "Measurement of Autolysosomal pH by Dual-Wavelength Ratio Imaging". In: *Molecular Characterization of Autophagic Responses, Part B*. Vol. 588. Molecular Characterization of Autophagic Responses, Part B. Molecular Characterization of Autophagic Responses, Part B, 2017, pp. 15–29.

[142] Alexander Agrotis and Robin Ketteler. "A new age in functional genomics using CRISPR/Cas9 in arrayed library screening". In: *Frontiers in Genetics* 6 (2015), p. 300.

[143] Dan Yu, Zhiqiang Dong, William Clay Gustafson, Rubén Ruiz-González, Luca Signor, et al. "Rational design of a monomeric and photostable far-red fluorescent protein for fluorescence imaging in vivo". In: *Protein Science* 25.2 (2016), pp. 308–315.

[144] Erik A Rodriguez, Geraldine N Tran, Larry A Gross, Jessica L Crisp, Xiaokun Shu, et al. "A far-red fluorescent protein evolved from a cyanobacterial phycobiliprotein". In: *Nature Methods* 13.9 (2016), pp. 763–769.

[145] Daria M Shcherbakova and Vladislav V Verkhusha. "Near-infrared fluorescent proteins for multicolor in vivo imaging". English. In: *Nature Methods* 10.8 (June 2013), pp. 751–754.

[146] Olesya V. Stepanenko, Olga V. Stepanenko, Irina M. Kuznetsova, Daria M. Shcherbakova, Vladislav V. Verkhusha, et al. "Interaction of Biliverdin Chromophore with Near-Infrared Fluorescent Protein BphP1-FP Engineered from Bacterial Phytochrome". In: *International Journal of Molecular Sciences* 18.5 (2017), p. 1009.

[147] Felipe Montecinos-Franjola, John Y Lin, and Erik A Rodriguez. "Fluorescent proteins for in vivo imaging, where's the biliverdin?" In: *Biochemical Society Transactions* 48.6 (2020), pp. 2657–2667.

[148] Ziqing Liu, Olivia Chen, J Blake Joseph Wall, Michael Zheng, Yang Zhou, et al. "Systematic comparison of 2A peptides for cloning multi-genes in a polycistronic vector". English. In: *Sci Rep* 7.1 (May 2017), pp. 663–9.

[149] Yuancheng Wang, Feng Wang, Sheng Xu, Riyuan Wang, Wenjing Chen, et al. "Optimization of a 2A self-cleaving peptide-based multigene expression system for efficient expression of upstream and downstream genes in silkworm." English. In: *Molecular Genetics and Genomics* 294.4 (Aug. 2019), pp. 849–859.

[150] Max A Horlbeck, Luke A Gilbert, Jacqueline E Villalta, Britt Adamson, Ryan A Pak, et al. "Compact and highly active next-generation libraries for CRISPR-mediated gene repression and activation". In: *eLife* 5 (2016), e19760.

[151] A.S. Artyukhov, E.B. Dashinimaev, V.O. Tsvetkov, A.P. Bolshakov, E.V. Konovalova, et al. "New genes for accurate normalization of qRT-PCR results in study of iPS and iPS-derived cells". In: *Gene* 626 (2017), pp. 234–240.

[152] Agilent. "Comparison of RIN and RINe algorithms for the Agilent 2100 Bioanalyzer and the Agilent 2200 TapeStation systems". In: *Agilent Technical Overview* (2012).

[153] Daniel J. Anderson, Ronan Le Moigne, Stevan Djakovic, Brajesh Kumar, Julie Rice, et al. "Targeting the AAA ATPase p97 as an Approach to Treat Cancer through Disruption of Protein Homeostasis". In: *Cancer Cell* 28.5 (2015), pp. 653–665.

[154] Max Karlsson, Cheng Zhang, Loren Méar, Wen Zhong, Andreas Digre, et al. "A single–cell type transcriptomics map of human tissues". In: *Science Advances* 7.31 (2021), eabh2169.

[155] Mathias Uhlén, Linn Fagerberg, Björn M. Hallström, Cecilia Lindskog, Per Oksvold, et al. "Tissue-based map of the human proteome". In: *Science* 347.6220 (2015), p. 1260419.

[156] Giovanni De Marco, Annarosa Lomartire, Umberto Manera, Antonio Canosa, Maurizio Grassano, et al. "Effects of intracellular calcium accumulation on proteins encoded by the major genes underlying amyotrophic lateral sclerosis". In: *Scientific Reports* 12.1 (2022), p. 395.

[157] James C. Dodge. "Lipid Involvement in Neurodegenerative Diseases of the Motor System: Insights from Lysosomal Storage Diseases". In: *Frontiers in Molecular Neuroscience* 10 (2017), p. 356.

[158] Emyr Lloyd-Evans, Anthony J Morgan, Xingxuan He, David A Smith, Elena Elliot-Smith, et al. "Niemann-Pick disease type C1 is a sphingosine storage disease that causes deregulation of lysosomal calcium". In: *Nature Medicine* 14.11 (Oct. 2008), pp. 1247–1255.

[159] Xueyi Li, Clive Standley, Ellen Sapp, Antonio Valencia, Zheng-Hong Qin, et al. "Mutant huntingtin impairs vesicle formation from recycling endosomes by interfering with Rab11 activity." English. In: *Molecular and cellular biology* 29.22 (Nov. 2009), pp. 6106–6116.

[160] Hang Zhou, Tingting Cao, Tian Liu, Shijie Liu, Lu Chen, et al. "Super-resolution Segmentation Network for Reconstruction of Packed Neurites". In: *Neuroinformatics* (2022), pp. 1–13.

[161] Shivesh Chaudhary, Sihoon Moon, and Hang Lu. "Fast, efficient, and accurate neuro-imaging denoising via supervised deep learning". In: *Nature Communications* 13.1 (2022), p. 5165.

[162] Dominique F Leitner and James R Connor. "Functional roles of transferrin in the brain." English. In: *Biochimica et biophysica acta* 1820.3 (Mar. 2012), pp. 393–402.

[163] S A Schneider and K P Bhatia. "Syndromes of Neurodegeneration With Brain Iron Accumulation". English. In: *Seminars in Pediatric Neurology* 19.2 (June 2012), pp. 57–66.

[164] Pavle Matak, Andrija Matak, Sarah Moustafa, Dipendra K Aryal, Eric J Benner, et al. "Disrupted iron homeostasis causes dopaminergic neurodegeneration in mice." English. In: *Proceedings of the National Academy of Sciences of the United States of America* 113.13 (Mar. 2016), pp. 3428–3435.

[165] Anthony O. Fedele and Christopher G. Proud. "Chloroquine and bafilomycin A mimic lysosomal storage disorders and impair mTORC1 signalling". In: *Bioscience Reports* 40.4 (2020), BSR20200905.

[166] Shuyan Lu, Tae Sung, Nianwei Lin, Robert T. Abraham, and Bart A. Jessen. "Lysosomal adaptation: How cells respond to lysosomotropic compounds". In: *PLoS ONE* 12.3 (2017), e0173771.

[167] A.V. Prabhu, I. Kang, R. De Pace, C.A. Wassif, H. Fujiwara, et al. "A human iPSC-derived inducible neuronal model of Niemann-Pick disease, type C1". In: *BMC Biology* 19.1 (2021).

[168] Tania López-Hernández, Dmytro Puchkov, Eberhard Krause, Tanja Maritzen, and Volker Haucke. "Endocytic regulation of cellular ion homeostasis controls lysosome biogenesis". In: *Nature Cell Biology* 22.7 (2020), pp. 815–827.

[169] Xiangli Zhao, Rossella Liberti, Jinlong Jian, Wenyu Fu, Aubryanna Hettinghouse, et al. "Progranulin associates with Rab2 and is involved in autophagosome-lysosome fusion in Gaucher disease". In: *Journal of Molecular Medicine* 99.11 (2021), pp. 1639–1654.

[170] Mike A Nalls, Cornelis Blauwendraat, Costanza L Vallerga, Karl Heilbron, Sara Bandres-Ciga, et al. "Identification of novel risk loci, causal insights, and heritable risk for Parkinson's disease: a meta-analysis of genome-wide association studies". In: *The Lancet Neurology* 18.12 (2019), pp. 1091–1102.

[171] Mike A Nalls, Cornelis Blauwendraat, Costanza L Vallerga, Karl Heilbron, Sara Bandres-Ciga, et al. "Parkinson's disease genetics: identifying novel risk loci, providing causal insights and improving estimates of heritable risk." English. In: *bioRxiv* (Jan. 2019), pp. 1–29.

[172] Xiaolai Zhou, Daniel H. Paushter, Tuancheng Feng, Lirong Sun, Thomas Reinheckel, et al. "Lysosomal processing of progranulin". In: *Molecular Neurodegeneration* 12.1 (2017), p. 62.

[173] Chris W. Lee, Jeannette N. Stankowski, Jeannie Chew, Casey N. Cook, Ying-Wai Lam, et al. "The lysosomal protein cathepsin L is a progranulin protease". In: *Molecular Neurodegeneration* 12.1 (2017), p. 55.

[174] Xin Zheng, Fei Chu, Bernard L. Mirkin, Thangirala Sudha, Shaker A. Mousa, et al. "Role of the proteolytic hierarchy between cathepsin L, cathepsin D and caspase-3 in regulation of cellular susceptibility to apoptosis and autophagy". In: *Biochimica et Biophysica Acta (BBA) - Molecular Cell Research* 1783.12 (2008), pp. 2294–2300.

[175] Manuel Schweighauser, Diana Arseni, Mehtap Bacioglu, Melissa Huang, Sofia Lövestam, et al. "Age-dependent formation of TMEM106B amyloid filaments in human brains". In: *Nature* 605.7909 (2022), pp. 310–314.

[176] Andrew Chang, Xinyu Xiang, Jing Wang, Carolyn Lee, Tamta Arakhamia, et al. "Homotypic fibrillization of TMEM106B across diverse neurodegenerative diseases". In: *Cell* 185.8 (2022), 1346–1355.e15.

[177] Yi Xiao Jiang, Qin Cao, Michael R. Sawaya, Romany Abskharon, Peng Ge, et al. "Amyloid fibrils in FTLD-TDP are composed of TMEM106B and not TDP-43". In: *Nature* 605.7909 (2022), pp. 304–309.

[178] Jolien Perneel and Rosa Rademakers. "Identification of TMEM106B amyloid fibrils provides an updated view of TMEM106B biology in health and disease." In: *Acta neuropathologica* (2022), pp. 1–13.

[179] Katie E. Copley and James Shorter. "Flying under the radar: TMEM106B(120–254) fibrils break out in diverse neurodegenerative disorders". In: *Cell* 185.8 (2022), pp. 1290–1292.

[180] Jason H Moore. "A global view of epistasis". In: *Nature Genetics* 37.1 (2005), pp. 13–14.

[181] Sean R. Collins, Assen Roguev, and Nevan J. Krogan. "Chapter 9 Quantitative Genetic Interaction Mapping Using the E-MAP Approach". In: *Methods in Enzymology* 470 (2010), pp. 205–231.

[182] Júlia Domingo, Pablo Baeza-Centurion, and Ben Lehner. "The Causes and Consequences of Genetic Interactions (Epistasis)". In: *Annual Review of Genomics and Human Genetics* 20.1 (2019), pp. 1–28.

[183] Assen Roguev, Dale Talbot, Gian Luca Negri, Michael Shales, Gerard Cagney, et al. "Quantitative genetic-interaction mapping in mammalian cells". In: *Nature Methods* 10.5 (2013), pp. 432–437.

[184] Michael C. Bassik, Martin Kampmann, Robert Jan Lebbink, Shuyi Wang, Marco Y. Hein, et al. "A Systematic Mammalian Genetic Interaction Map Reveals Pathways Underlying Ricin Susceptibility". In: *Cell* 152.4 (2013), pp. 909–922.

[185] Sean R Collins, Maya Schuldiner, Nevan J Krogan, and Jonathan S Weissman. "A strategy for extracting and analyzing large-scale quantitative epistatic interaction data". In: *Genome Biology* 7.7 (2006), R63.

[186] Dan Du, Assen Roguev, David E Gordon, Meng Chen, Si-Han Chen, et al. "Genetic interaction mapping in mammalian cells using CRISPR interference". In: *Nature Methods* 14.6 (2017), pp. 577–580.

[187] Ke Li, Lin Yang, Cheng Zhang, Yang Niu, Wei Li, et al. "HPS6 interacts with dynactin p150Glued to mediate retrograde trafficking and maturation of lysosomes." English. In: *Journal of Cell Science* 127.Pt 21 (Nov. 2014), pp. 4574–4588.

[188] Ting-Ting Du, Le Wang, Chun-Li Duan, Ling-Ling Lu, Jian-Liang Zhang, et al. "GBA deficiency promotes SNCA/α-synuclein accumulation through autophagic inhibition by inactivated PPP2A". In: *Autophagy* 11.10 (2015), pp. 1803–1820.

[189] David Schlütermann, Niklas Berleth, Jana Deitersen, Nora Wallot-Hieke, Olena Friesen, et al. "FIP200 controls the TBK1 activation threshold at SQSTM1/p62-positive condensates". In: *Scientific Reports* 11.1 (2021), p. 13863.

[190] Jennilee M. Davidson, Roger S. Chung, and Albert Lee. "The converging roles of sequestosome-1/p62 in the molecular pathways of amyotrophic lateral sclerosis (ALS) and frontotemporal dementia (FTD)". In: *Neurobiology of Disease* 166 (2022), p. 105653.

[191] Michael C. Chang, Karpagam Srinivasan, Brad A. Friedman, Eric Suto, Zora Modrusan, et al. "Progranulin deficiency causes impairment of autophagy and TDP-43 accumulation". In: *Journal of Experimental Medicine* 214.9 (2017), pp. 2611–2628.

[192] Qin Rui, Haibo Ni, Di Li, Rong Gao, and Gang Chen. "The Role of LRRK2 in Neurodegeneration of Parkinson Disease". In: *Current Neuropharmacology* 16.9 (2018), pp. 1348–1357.

[193] Joseph M. Thomas, Tianxia Li, Wei Yang, Fengtian Xue, Paul S. Fishman, et al. "68 and FX2149 Attenuate Mutant LRRK2-R1441C-Induced Neural Transport Impairment". In: *Frontiers in Aging Neuroscience* 8 (2017), p. 337.

[194] Charlotte F. Brzozowski, Baraa A. Hijaz, Vijay Singh, Nolwazi Z. Gcwensa, Kaela Kelly, et al. "Inhibition of LRRK2 kinase activity promotes anterograde axonal transport and presynaptic targeting of α-synuclein". In: *Acta Neuropathologica Communications* 9.1 (2021), p. 180.

[195] Aude Nicolas, Kevin P. Kenna, Alan E. Renton, Nicola Ticozzi, Faraz Faghri, et al. "Genome-wide Analyses Identify KIF5A as a Novel ALS Gene". In: *Neuron* 97.6 (2018), 1268–1283.e6.

[196] Devesh C Pant, Janani Parameswaran, Lu Rao, Isabel Loss, Ganesh Chilukuri, et al. "ALS-linked KIF5A ΔExon27 mutant causes neuronal toxicity through gain-of-function". In: *EMBO reports* 23.8 (2022), e54234.

[197] Desiree M. Baron, Adam R. Fenton, Sara Saez-Atienzar, Anthony Giampetruzzi, Aparna Sreeram, et al. "ALS-associated KIF5A mutations abolish autoinhibition resulting in a toxic gain of function". In: *Cell Reports* 39.1 (2022), p. 110598.

[198] Rosa Passantino, Caterina Cascio, Irene Deidda, Giacoma Galizzi, Domenica Russo, et al. "Identifying protein partners of CLN8, an ER-resident protein involved in neuronal ceroid lipofuscinosis". In: *Biochimica et Biophysica Acta (BBA) - Molecular Cell Research* 1833.3 (2013), pp. 529–540.

[199] Susan L. Cotman, Amel Karaa, John F. Staropoli, and Katherine B. Sims. "Neuronal Ceroid Lipofuscinosis: Impact of Recent Genetic Advances and Expansion of the Clinicopathologic Spectrum". In: *Current Neurology and Neuroscience Reports* 13.8 (2013), p. 366.